



1-1-2019

Antennas And Wave Propagation In Wireless Body Area Networks: Design And Evaluation Techniques

Ala Alemaryeen

[How does access to this work benefit you? Let us know!](#)

Follow this and additional works at: <https://commons.und.edu/theses>



Part of the [Electrical and Computer Engineering Commons](#)

Recommended Citation

Alemaryeen, Ala, "Antennas And Wave Propagation In Wireless Body Area Networks: Design And Evaluation Techniques" (2019). *Theses and Dissertations*. 2304.

<https://commons.und.edu/theses/2304>

This Dissertation is brought to you for free and open access by the Theses, Dissertations, and Senior Projects at UND Scholarly Commons. It has been accepted for inclusion in Theses and Dissertations by an authorized administrator of UND Scholarly Commons. For more information, please contact und.common@library.und.edu.

ANTENNAS AND WAVE PROPAGATION IN WIRELESS BODY AREA
NETWORKS: DESIGN AND EVALUATION TECHNIQUES

by

Ala Ali Alemaryeen

Bachelor of Electrical Engineering, Mutah University, 2012

Master of Science, University of North Dakota, 2015

A Dissertation

Submitted to the Graduate Faculty

of the

University of North Dakota

In partial fulfillment of the requirements

for the degree of

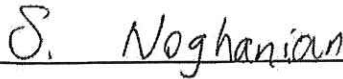
Doctor of Philosophy

Grand Forks, North Dakota

May
2019

Copyright 2019 Ala Alemaryeen

This dissertation, submitted by Ala Alemaryeen in partial fulfillment of the requirements for the Degree of Doctor of Philosophy in Electrical Engineering from the University of North Dakota, has been read by the Faculty Advisory Committee under whom the work has been done, and is hereby approved.



Sima Noghmanian, Chairperson



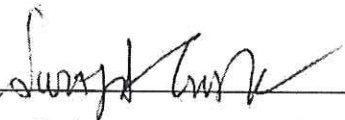
Reza Fazel-Rezai, Committee Member



Kouhyar Tavakolian, Committee Member



Colin Combs, Committee Member



Surojit Gupta, Member at Large

This dissertation is being submitted by the appointed advisory committee as having met all of the requirements of the Graduate School at the University of North Dakota and is hereby approved.



Dr. Chris Nelson
Dean of the School of Graduate Studies



Date

PERMISSION

Title Antennas and Wave Propagation in Wireless Body Area Networks:
 Design and Evaluation Techniques

Department Electrical Engineering

Degree Doctor of Philosophy

In presenting this dissertation in partial fulfillment of the requirements for a graduate degree from the University of North Dakota, I agree that the library of this University shall make it freely available for inspection. I further agree that permission for extensive copying for scholarly purposes may be granted by the professor who supervised my dissertation work or, in her absence, by the Chairperson of the department or the dean of the Graduate School. It is understood that any copying or publication or other use of this thesis or part thereof for financial gain shall not be allowed without my written permission. It is also understood that due recognition shall be given to me and to the University of North Dakota in any scholarly use which may be made of any material in my dissertation.

Ala Alemaryeen

May 2019

TABLE OF CONTENTS

List of Figures	viii
List of Tables	xiii
Abbreviations	xv
Acknowledgments	xvi
List of Publications and Awards	xxv
Abstract	xxvii
CHAPTER 1 Introduction	1
1.1 Research Motivation and Objectives	1
1.2 Design Constraints, Requirements, and Challenges	4
1.3 Overview of the Thesis	13
CHAPTER 2 Design of Flexible Wearable Antenna	16
2.1 Introduction.....	16
2.2 Background.....	18
2.3 Antenna Topology and Materials.....	23
2.4 Performance of Wearable Antennas in Free-space.....	25
2.4.1 Performance of Wearable Antennas in Planar Configuration.....	25
2.4.2 Performance of Wearable Antennas under Crumpling Effects.....	30
2.5 Performance of Wearable Antennas on Human Body Models.....	40
2.5.1 Frequency Detuning.....	41
2.5.2 Radiation Characteristics	43
2.5.3 Analysis of Specific Absorption Rate (SAR)	44
2.6 Summary	47
CHAPTER 3 Design of Textile Wearable Antenna	48
3.1 Introduction.....	48
3.2 Background.....	50
3.3 Antenna Topology and Materials.....	53
3.4 Performance of Wearable Antennas in Free-space.....	55
3.4.1 Performance of Wearable Antennas in Planar Configuration.....	55
3.4.2 Performance of AMC Antenna under Structural Deformation Effects	58
3.5 Performance of Wearable Antennas on Human Body Models.....	62

3.5.1	Performance of Wearable Antennas in Planar Configuration.....	64
3.5.2	Performance of Wearable Antennas in Bending Configuration	66
3.5.3	SAR Validation.....	69
3.5.4	Experimental Analysis of Antennas Performance on Body Phantom	71
3.6	Application of Magneto-Dielectric Material in Wearable Antenna Design .	73
3.6.1	Background.....	73
3.6.2	Antenna Topology and Materials.....	77
3.6.3	Performance of Antennas in Planar Configuration.....	77
3.6.4	Structural Deformation Effects	78
3.6.5	Human Body Effects.....	83
3.7	Application of Layered Substrate in Wearable Antenna Design	84
3.7.1	Antenna Topology and Materials.....	84
3.7.2	Results and Discussion	86
3.8	Summary	87
CHAPTER 4 Design of Implantable Antenna.....		89
4.1	Introduction.....	89
4.2	Background.....	90
4.3	Implantable Antenna Design and Simulation Setups.....	92
4.4	Results and Discussion	94
4.5	Transmission Link Evaluation	96
4.6	Summary	98
CHAPTER 5 Investigated Wireless Body Area Network Applications		99
5.1	Introduction.....	99
5.2	Respiratory Rate Measurement using UWB Radar System	100
5.2.1	Background.....	100
5.2.2	Experimental Setups	102
5.2.3	UWB Radar Configuration	103
5.2.4	Antenna Selection	108
5.2.5	Evaluation of the Proposed Radar System in a Controlled Environment....	108
5.2.6	Respiratory Rate Measurement with Human Subjects	118
5.3	An Accurate Phase-Based Localization Method of RFID Tag.....	123

5.3.1	Background	123
5.3.2	System Overview	127
5.3.3	Results and Discussion	129
5.4	Summary	134
CHAPTER 6 Conclusions, Contributions, and Future Work.....		136
6.1	Research Conclusions and Challenges.....	136
6.1.1	Wearable Antenna Design	136
6.1.2	Implantable Antenna Design.....	140
6.1.3	Investigated Wireless Body Area Network Applications	141
6.2	Future Work	142
References	145
Appendix A	154

LIST OF FIGURES

Fig. 1.1: Examples of non-invasive wearable devices [2]-[5].	2
Fig. 1.2: Examples of invasive implantable devices [6].	2
Fig. 1.3: Classifications of wireless body area communication.	3
Fig. 1.4: Constraints and requirements of wearable and implantable antennas design.	4
Fig. 1.5: (a) Rectangular [16], (b) cylindrical [17], and (c) spherical [18] body models.	6
Fig. 1.6: Human body model of Ella; (a) 3D, (b) side, and (c) front views [19].	7
Fig. 1.7: Physical skin phantoms; (a) solid [21], (b) semisolid [22], and (c) liquid [23].	8
Fig. 1.8: Simulated S_{11} of wearable antenna in free-space and on body phantom.	13
Fig. 2.1: AMC antennas based on (a) textile [33] and (b) flexible materials [39].	18
Fig. 2.2: Fabricated prototypes; (a) folded antenna and AMC and (b) AMC antenna [41].	19
Fig. 2.3: Fabricated prototype; (a) front view, (b) rear view and (c) entire antenna [42].	20
Fig. 2.4: (a) Fabricated prototype and (b) antenna under bending conditions [40].	21
Fig. 2.5: Flexible antenna mounted on the human chest [43].	21
Fig. 2.6: (a) Fabricated AMC antenna and (b) flexibility test [44].	22
Fig. 2.7: (a) AMC structure and (b) proposed antenna [34].	22
Fig. 2.8: Configuration of CPW-fed monopole antenna (right) and dimension details (left).	23
Fig. 2.9: Configuration of AMC unit cell (right) and dimension details (left).	24
Fig. 2.10: Photograph of fabricated (a) monopole, (b) AMC reflector, and (c) AMC antenna.	24
Fig. 2.11: Reflection phase diagram of AMC unit cell.	25
Fig. 2.12: Simulated and measured S_{11} of (a) monopole and (b) AMC antennas in free-space.	28
Fig. 2.13: Co-pol radiation of monopole antenna at 2.45 GHz in (a) E-plane and (b) H-plane.	30
Fig. 2.14: Co-pol radiation of AMC antenna at 2.45 GHz in (a) E-plane and (b) H-plane.	30

Fig. 2.15: S_{11} of crumpled monopole antenna based on simulation (S) and measurement (M) results in E-plane; (a) case1 and (b) case2.	32
Fig. 2.16: S_{11} of crumpled monopole antenna based on simulation (S) and measurement (M) results in H-plane; (a) case1 and (b) case2.....	33
Fig. 2.17: Monopole current distribution; (a) flat form, and (b) crumpling case 4 in H-plane....	34
Fig. 2.18: Co-pol radiation at 2.45 GHz of monopole antenna crumpled in E-plane; (a) case1_E-plane, (b) case1_H-plane, (c) case2_E-plane, (d) case2_H-plane.	35
Fig. 2.19: Co-pol radiation at 2.45 GHz of monopole antenna crumpled in H-plane; (a) case1_E-plane, (b) case1_H-plane, (c) case2_E-plane, (d) case2_H-plane.	36
Fig. 2.20: Simulated S_{11} of crumpled AMC antenna (a) series 1 and (b) series 2.	38
Fig. 2.21: Simulation (S) and measurement (M) results of crumpled AMC antenna of (E) E-plane crumpling and measurement results of (H) H-plane crumpling in case 2 from series 2. .	38
Fig. 2.22: S_{11} of (a) monopole and (b) AMC antennas on different body models.	42
Fig. 2.23: S_{11} (a) monopole and (b) AMC antennas at different separation distances.	43
Fig. 2.24: Simulated averaged SAR (W/Kg) at 2.45 GHz for monopole antenna (left) and AMC antenna (right); (a) 1 g, and (b) 10 g.	46
Fig. 3.1: Textile (a) stretch AMC antenna [56] and (b) hexagonal AMC structure [50].	51
Fig. 3.2: Photograph of circular AMC textile antenna [36].	51
Fig. 3.3: (a) A textile slot antenna integrating (b) a square patch AMC structure [58].....	52
Fig. 3.4: AMC antenna using (a) felt/zelt [38] and (b) jeans/conductive plates [37].....	52
Fig. 3.5: Configuration of CPW-fed monopole antenna (right) and dimension details (left).	54
Fig. 3.6: Configuration of AMC unit cell (right) and dimension details (left).....	54
Fig. 3.7: Photograph of the fabricated (a) monopole and (b) AMC antennas.	54

Fig. 3.8: Reflection phase diagram of AMC unit cell.	55
Fig. 3.9: Measured S_{11} of monopole and AMC antennas in free-space.	56
Fig. 3.10: Simulated and measured S_{11} of (a) monopole and (b) AMC antennas in free-space.	57
Fig. 3.11: Co-pol radiation of monopole antenna at 5.8 GHz in (a) E-plane and (b) H-plane.	59
Fig. 3.12: (a) co-pol radiation in E-plane, (b) cross-pol radiation in E-plane, (c) co-pol radiation in H-plane, and (d) cross-pol radiation in H-plane of AMC antenna at 5.8 GHz.	59
Fig. 3.13: Photograph depicting (a) bending configurations and (b) S_{11} measurement setup.	60
Fig. 3.14: S_{11} results of bent AMC antenna in (a) E-plane and (b) H-plane directions.	61
Fig. 3.15: (a) Crumpling profiles and (b) S_{11} measurement results of crumpled AMC antenna.	62
Fig. 3.16: Cross sections (a) Cubic BM_layered, (b) Cylindrical BM_layered, (c) Cubic BM_equivalent, (d) Cylindrical BM_equivalent, and (e) Ella; dimensions are in <i>mm</i>	64
Fig. 3.17: Simulated S_{11} of flat (a) monopole and (b) AMC antennas.	65
Fig. 3.18: Simulated S_{11} of bent monopole antenna in (a) E-plane and (b) H-plane directions.	67
Fig. 3.19: Simulated S_{11} of bent AMC antenna in (a) E-plane and (b) H-plane directions.	68
Fig. 3.20: Muscle phantom dielectric property measurements; (a) setup and (b) results.	72
Fig. 3.21: Measured S_{11} of flat (a) monopole and (b) AMC antennas on body phantom.	73
Fig. 3.22: Microstrip antenna with (a) superstrate, (b) AMC ground, and (c) MD material [73].	75
Fig. 3.23: (a) Side and top views of single antenna and (b) antenna array [74].	76
Fig. 3.24: Simulated S_{11} of antennas in free-space.	78
Fig. 3.25: (a) Monopole1, (b) monopole2, and (c) AMC antennas bent in E-plane.	79
Fig. 3.26: (a) Monopole1, (b) monopole2, and (c) AMC antennas bent in H-plane.	79
Fig. 3.27: S_{11} of bent (a) monopole1, (b) monopole2, and (c) AMC antennas in E-plane.	80
Fig. 3.28: S_{11} of bent (a) monopole1, (b) monopole2, and (c) AMC antennas in H-plane.	81

Fig. 3.29: S_{11} of monopole_MD_GP.....	83
Fig. 3.30: Studied layered substrate sequences.	85
Fig. 3.31: S_{11} of studied monopole antenna configurations.	86
Fig. 3.32: Simulated co-pol (left) and cross-pol (right) radiations of MA configurations in (a) E-plane and (b) H-plane at f_r	87
Fig. 4.1: (a) Geometry of implanted antenna and (b) In vitro measurement setup [32].....	90
Fig. 4.2: (a) Geometry of implanted antenna and (b) fabricated prototype [75]......	91
Fig. 4.3: Geometry of implanted antenna proposed in (a) [13] and (b) [76]......	92
Fig. 4.4: Proposed antenna; (a) conformal form and (b) implanted in layered body model.	93
Fig. 4.5: Configuration of the proposed capsule antenna in planar form.	93
Fig. 4.6: Capsule antenna; (a) considering the battery and (b) inside Ella model.	94
Fig. 4.7: (a) S_{11} and (b) gain of capsule antenna for different configurations.	95
Fig. 4.8: Simulation setup of coupling strength for external half wavelength dipole.	96
Fig. 4.9: Different implanting depths (d); (a) coupling strength and (b) realized gain.	97
Fig. 4.10: Coupling strength results for different free-space distances (s).	97
Fig. 5.1: Experimental setup for measuring the movement of a controlled moving unit.	103
Fig. 5.2: The UWB radar is measuring respiratory rate from one subject.	103
Fig. 5.3: PulseON ® 410 hardware functional block diagram [48].	105
Fig. 5.4: PulseON ® 410 generated waveform in (a) frequency and (b) time domains [48].	105
Fig. 5.5: PulseON ® 410 transmit gain setting vs. transmit power [101].	107
Fig. 5.6: Characteristics of bandpass filter applied by PulseON ® 410 transceiver [101].	107
Fig. 5.7: Dimension details of (a) antenna 1, (b) antenna 3, and (c) antenna 2 given in <i>cm</i>	108
Fig. 5.8: Result of frequency analysis of data received by the radar sensing system.	110

Fig. 5.9: Absolute error values of radar-based measurement results using three different antennas for different (a) frequencies, (b) displacements, and (c) measurement distances.....	111
Fig. 5.10: S_{11} of antennas; (a) [0-18] GHz and (b) [3.1-5.2] GHz frequency band.....	112
Fig. 5.11: (a) Co- and (b) cross-polarization of antennas' E-plane.....	113
Fig. 5.12: (a) Co- and (b) cross-polarization of antennas' H-plane.....	114
Fig. 5.13: Antenna gains versus frequency.	114
Fig. 5.14: Phase center variations vs. frequency of antenna 3 along (a) <i>y-axis</i> and (b) <i>z-axis</i> ...	117
Fig. 5.15: Maximum standard deviation of calculations of the phase center location.	117
Fig. 5.16: Comparison of monostatic and bistatic radars using antennas (a) 1, (b) 2, and (c) 3.	119
Fig. 5.17: Results of cardboard and metallic targets using antennas (a) 1, (b) 2, and (c) 3.	120
Fig. 5.18: Example result of respiratory rate measurement of test subject (S6).	122
Fig. 5.19: Respiration-rates of two test subjects for four different scanning times.....	123
Fig. 5.20: Classification of indoor positioning technologies.....	126
Fig. 5.21: Localization using single antenna; (a) measurement and (b) simulation setups.....	128
Fig. 5.22: Localization using antenna array; (a) measurement and (b) simulation setups.	128
Fig. 5.23: Phase results of (a) case 1, (b) case 2, and (c) case 3.....	131
Fig. 5.24: Phase results of case 4; (a) antenna1, (b) antenna2, (c) antenna3, and (d) antenna4.	132
Fig. 5.25: Phase results of case 5; (a) antenna1, (b) antenna2, (c) antenna3, and (d) antenna4.	133
Fig. 5.26: Simulated transmission coefficients of antenna array elements.	134

LIST OF TABLES

Table 1.1: Characteristics of muscle and fat tissues at different frequencies [9].....	6
Table 1.2: Examples of textile and flexible materials used in wearable antenna design.	10
Table 1.3: Potential frequency bands for wearable and implantable devices [7], [45].....	11
Table 2.1: Performance summary of monopole placed at different locations on the AMC.	26
Table 2.2: Performance summary of studied scenarios.	26
Table 2.3: Dimension details of crumpled monopole antenna.....	31
Table 2.4: Performance summary at 2.45 GHz of crumpled monopole antenna.	34
Table 2.5: Dimension details of crumpled AMC antenna.	36
Table 2.6: Radiation characteristics summary for AMC antenna crumpling in E-plane.	39
Table 2.7: Zero reflection frequency point of crumpled AMC structure.....	40
Table 2.8: Electrical properties of the body tissues at 2.45 GHz [55].	41
Table 2.9: Radiation characteristics for wearable antennas on human models at 2.45 GHz.	44
Table 2.10: SAR analysis summary of wearable antennas at 2.45 GHz.....	46
Table 3.1: Radiation characteristics summary of AMC antenna at 5.8 GHz.	61
Table 3.2: Radiation characteristics summary for flat antennas at 5.8 GHz.....	66
Table 3.3: Radiation characteristics summary for bent antennas at 5.8 GHz.	69
Table 3.4: SAR analysis summary of antennas at 5.8 GHz.	71
Table 3.5: Examples of MD materials reported in literature [68] - [69].....	75
Table 3.6: Performance summary of proposed microstrip antenna configurations [73].	76
Table 3.7: Performance summary of proposed antenna array system [74].....	77
Table 3.8: Performance comparison of studied antennas at 2.45 GHz.	78
Table 3.9: Performance summary of antennas (E-plane bending).....	82

Table 3.10: Performance summary of antennas (H-plane bending).	82
Table 3.11: Radiation characteristics summary at 2.45 GHz.....	83
Table 3.12: Performance comparison of studied antennas at resonance frequency.....	85
Table 4.1: Summary of the realized gain of the capsule antenna.....	96
Table 5.1: FOM for three studied antennas.....	115
Table 5.2: Information summary of 10 subjects.	121
Table 5.3: Evaluation of respiratory rate measurements for 10 subjects.	121
Table 5.4: Simulated antenna 1 phase for scenarios 1 and 2.	134
Table 6.1: Comparison of the proposed wearable antenna with reported work in literature.	137
Table 6.2: Comparison of the proposed wearable antenna with reported work in literature.	139
Table 6.3: Comparison of the proposed implantable antenna with reported work in literature.	141

ABBREVIATIONS

EEG	Electroencephalogram
WBAN	Wireless Body Area Network
BSN	Body Sensor Network
UWB	Ultra Wide Band
RFID	Radio Frequency Identification
3D	Three Dimensional
MRI	Magnetic Resonance Imaging
SAR	Specific Absorption Rate
MICS	Medical Implanted Communication Service
MEDRadio	Medical Device Radiocommunications
WMTS	Wireless Medical Telemetry Service
ISM	Industrial Scientific and Medical
AMC	Artificial Magnetic Conductor
CPW	Coplanar Waveguide
MD	Magneto-Dielectric
PDMS	Polydimethylsiloxane
PMC	Perfect Magnetic Conductor
FBR	Front to Back Ratio
PBC	Periodic Boundary Condition
CW	Continuous-Wave
FMCW	Frequency-Modulated Continuous-Wave
SFCW	Stepped Frequency-Modulated Continuous-Wave
PC	Personal Computer
SNR	Signal to Noise Ratio
MRM RET	Monostatic Radar Module Reconfiguration and Evaluation Tool
API	Application Programming Interface
PII	Pulse Integration Index
FFT	Fast Fourier Transform
FOM	Figure-Of-Merit
GPS	Global Positioning System
FIT	Finite Integration Technique
FEM	Finite Element Method

ACKNOWLEDGMENTS

First and foremost, I express my deepest gratitude to my academic and research advisor Dr. Sima Noghianian for her guidance and help throughout my research and for gladly offering her knowledge and experience when needed. I particularly admire her scientific way of thinking and providing new ideas and her extraordinary human qualities. Thanks for making me feel at ND, USA like at my second home. Her trust and support was extremely encouraging and helpful. I would also like to express my special thanks and highest appreciation to my PhD committee; Dr. Reza Fazel-Rezai, Dr. Kouhyar Tavakolian, Dr. Colin Combs, and Dr. Surjoit Gupta for their support and help. My sincere thanks go to Dr. Mahyar Modaresi from Lunantech institution and Dr. Reza Fazel-Rezai from biomedical engineering research complex for very fruitful collaborations in two of the projects discussed in this dissertation.

Additionally, I would like to express my appreciation to North Dakota Experiment Program to Stimulate Competitive Research (ND NASA EPSCoR), and University of North Dakota for the financial support throughout my PhD studies. Also, I would like to thank my friends and colleagues from Applied Electromagnetic Lab and other labs for their continuous support and assistance.

Finally, I would like to thank all my family members. A special mention to my parents Ali Alemaryeen and Najah Alemaryeen and my brother Dr. Khalid Alemaryeen. Despite the distance, you have always been present to love and support me under any circumstances. Last, but not least, I wouldn't have made till here without endless care, love, and encouragement of my husband Qusay Alkaseasbeh. I am very thankful to have you in my life!

To my parents

Ali Alemaryeen and Najah Alemaryeen

and my husband

Qusay Alkaseasbeh

LIST OF PUBLICATIONS AND AWARDS

Journal Articles:

- J.1. **Alemaryeen** and S. Noghalian “On-body low-profile textile antenna with artificial magnetic conductor,” submitted to *IEEE Transaction in Antennas and Propagation*.
- J.2. **A. Alemaryeen** and S. Noghalian, “A wideband antenna for biotelemetry applications: design and transmission link evaluation,” *ACES Journal*, vol. 33, no. 10, pp. 1129–1130, October. 2018.
- J.3. **A. Alemaryeen**, S. Noghalian, and R. Fazel-Rezai “Antenna effects on respiratory rate measurement using a UWB radar system,” *IEEE Journal of Electromagnetics, RF, and Microwaves in Medicine and Biology*, vol. 2, no. 2, pp. 87–93, June. 2018.
- J.4. **A. Alemaryeen** and S. Noghalian, “Crumpling effects and specific absorption rates of flexible AMC integrated antennas,” *IET Microwaves, Antennas and Propagation*, vol. 12, no. 4, pp. 627–635, Nov. 2017.
- J.5. **A. Alemaryeen** and S. Noghalian, “AMC integrated textile monopole antenna for wearable applications,” *ACES Journal*, vol. 31, no. 6, pp. 612–618, June. 2016.

Conference Proceedings:

- C.1. **Alemaryeen** and S. Noghalian, “Application of dielectric and magnetic layered substrate in antenna gain enhancement,” submitted to *Proc. IEEE AP-S Int. Symp conference*.
- C.2. S. Noghalian, A. Alshami, **A. Alemaryeen**, A. Tesser, J. Lewis, and M. Haghshenas, “On the development of a bio-based dielectric material,” in *International Symposium on Electromagnetic Theory (EMTS) conference*, San Diego, California, USA, July, 2019.
- C.3. **A. Alemaryeen**, M. Modaresi, and S. Noghalian, “Phase analysis of a semi-passive RFID indoor localization system,” in *18th International Symposium on Antenna Technology and Applied Electromagnetics (ANTEM) conference*, Waterloo, ON, Canada, August. 2018.
- C.4. **A. Alemaryeen**, M. Modaresi, and S. Noghalian, “Study of an accurate phase-based localization method for semi-passive RFID tags,” in *Proc. IEEE AP-S Int. Symp conference*, Boston, Massachusetts, USA, July, 2018.
- C.5. **A. Alemaryeen** and S. Noghalian, “A wideband antenna for biotelemetry applications: design and transmission link evaluation,” in *Applied Computational Electromagnetics Society (ACES) Conference*, Denver, Colorado, March. 2018.
- C.6. **A. Alemaryeen** and S. Noghalian, “Applications of magneto-dielectric materials in wearable antenna design,” in *Proc. IEEE AP-S Int. Symp*, San Diego, California, USA, July, 2017, pp. 515-516.

- C.7. **A. Alemaryeen** and S. Noghalian, “Performance analysis of textile AMC antenna on body model,” in *Proc. IEEE AP-S Int. Symp*, San Diego, California, USA, July, 2017, pp. 41-42.
- C.8. **A. Alemaryeen**, S. Noghalian, and R. Fazel-Rezai, “Respiratory rate measurements via doppler radar for health monitoring applications,” in *39th International Conference of the IEEE Engineering in Medicine and Biology Society*, Jeju Island, Korea, July, 2017, pp. 829-832.
- C.9. **A. Alemaryeen**, S. Noghalian, and R. Fazel-Rezai, “EBG integrated textile monopole antenna for space health monitoring application,” in *Proc. IEEE AP-S Int. Symp*, Vancouver, BC, Canada, July. 2015, pp. 1209-1210.
- C.10. **A. Alemaryeen**, S. Noghalian, and R. Fazel-Rezai, “Evaluation of SAR for integrated EBG textile monopole antenna for space health monitoring application,” in *2015 USNC-URSI Radio Science Meeting (Joint with AP-S Symposium)*, Vancouver, BC, Canada, July. 2015, pp. 359-359.
- C.11. **A. Alemaryeen** and S. Noghalian, “Simulation of crumpling in integrated AMC textile CPW fed monopole antenna,” in *Applied Computational Electromagnetics Society (ACES) Conference*, Williamsburg, VA, March. 2015, pp. 1-2.

Awards:

1. **CST University Publication Award (December 2018):** The CST University Publication Award is an annual grant to university institutes and researchers for their work in the application of 3D EM field simulation. The winners are awarded with extensions to their CST Studio Suite installations.
2. **Barkeshli EM Prize (July 2018):** The award is designed for the most accurate EM simulation and the best application developed by a student based on Lunantech's hardware platform.
3. **Doctoral Dissertation Assistantship (DDA) (June 2018):** EPSCoR’s DDA program is a one year NSF sponsored scholarship designed to increase the completion rate of Ph.D. students enrolled in the STEM (science, technology, engineering, and mathematics) disciplines at North Dakota’s two research-intensive universities; and to increase the number of competitive proposals submitted to the National Science Foundation.

ABSTRACT

Recently, fabrication of miniature electronic devices that can be used for wireless connectivity becomes of great interest in many applications. This has resulted in many small and compact wireless devices that are either implantable or wearable. As these devices are small, the space for the antenna is limited. An antenna is the part of the wireless device that receives and transmits a wireless signal. Implantable and wearable antennas are very susceptible to harmful performance degradation caused by the human body and very difficult to integrate, if not designed properly. A designer need to minimize unwanted radiation absorption by the human body to avoid potential health issues. Moreover, a wearable antenna will be inevitably exposed to user movements and has to deal with influences such as crumpling and bending. These deformations can cause degraded performance or a shifted frequency response, which might render the antenna less effective. The existing wearable and implantable antennas' topologies and designs under discussion still suffer from many challenges such as unstable antenna behavior, low bandwidth, considerable power generation, less biocompatibility, and comparatively bigger size. The work presented in this thesis focused on two main aspects. Part one of the work presents the design, realization, and performance evaluation of two wearable antennas based on flexible and textile materials. In order to achieve high body-antenna isolation, hence, minimal coupling between human body and antenna and to achieve performance enhancement artificial magnetic conductor is integrated with the antenna. The proposed wearable antennas feature a small footprint and low profile characteristics and achieved a wider -10 dB input impedance bandwidth compared to wearable antennas reported in literature. In addition, using new materials in wearable antenna

design such as flexible magneto-dielectric and dielectric/magnetic layered substrates is investigated. Effectiveness of using such materials revealed to achieve further improvements in antenna radiation characteristics and bandwidth and to stabilize antenna performance under bending and on body conditions compared to artificial magnetic conductor based antenna. The design of a wideband biocompatible implantable antenna is presented. The antenna features small size (*i.e.*, the antenna size in planar form is 2.52 mm^3), wide -10 dB input impedance bandwidth of 7.31 GHz, and low coupling to human tissues.

In part two, an overview of investigations done for two wireless body area network applications is presented. The applications are: (a) respiratory rate measurement using ultra-wide band radar system and (b) an accurate phase-based localization method of radio frequency identification tag. The ultimate goal is to study how the antenna design can affect the overall system performance and define its limitations and capabilities. In the first studied application, results indicate that the proposed sensing system is less affected and shows less error when an antenna with directive radiation pattern, low cross-polarization, and stable phase center is used. In the second studied application, results indicate that effects of mutual coupling between the array elements on the phase values are negligible. Thus, the phase of the reflected waves from the tag is mainly determined by the distance between the tag and each antenna element, and is not affected by the induced currents on the other elements.

CHAPTER 1

INTRODUCTION

1.1 Research Motivation and Objectives

Advancement in technology has made the wireless electronic devices play an essential role in many applications such as the modern health monitoring systems. These systems can be either wearable (non-invasive) or implantable (invasive) where the former includes all the devices located outside the human body whereas the latter must include at least one in-body or implanted device [1]. As shown in Fig. 1.1, smart shirt and headband to track blood oxygen levels, blood pressure, skin temperature, activity level, heart rate and respiratory rate [2], health patches for temperature measurements [3], electroencephalogram (EEG) tattoo sensor [4] and motion sensor [5] are examples of non-invasive wearable devices. As shown in Fig. 1.2, deep brain neurostimulators, gastric stimulators, foot drop implants, cochlear implants, pacemakers, and insulin pumps are examples of implantable devices [6]. These devices can collect the health parameters and may send them to a central unit that is located either on- or off- the body. The central unit may then send these data to the doctor's computer using Wi-Fi or Bluetooth. Using the above technique will save the medical specialist and patients a lot of time, will make the life of patients comfortable by increasing their mobility, will reduce the cost associated with healthcare and will improve the quality of healthcare provided.

Such network of the communicating wireless devices, shown in Fig. 1.3, that are implantable and wearable is called wireless body area network (WBAN). Some other terms which are commonly used for the WBAN are body sensor network (BSN) or body-centric wireless communication [7].



Smart shirt and band [2]

Thermometer patch [3]

EEG Tattoo sensor [4]

Motion sensor [5]

Fig. 1.1: Examples of non-invasive wearable devices [2]-[5].

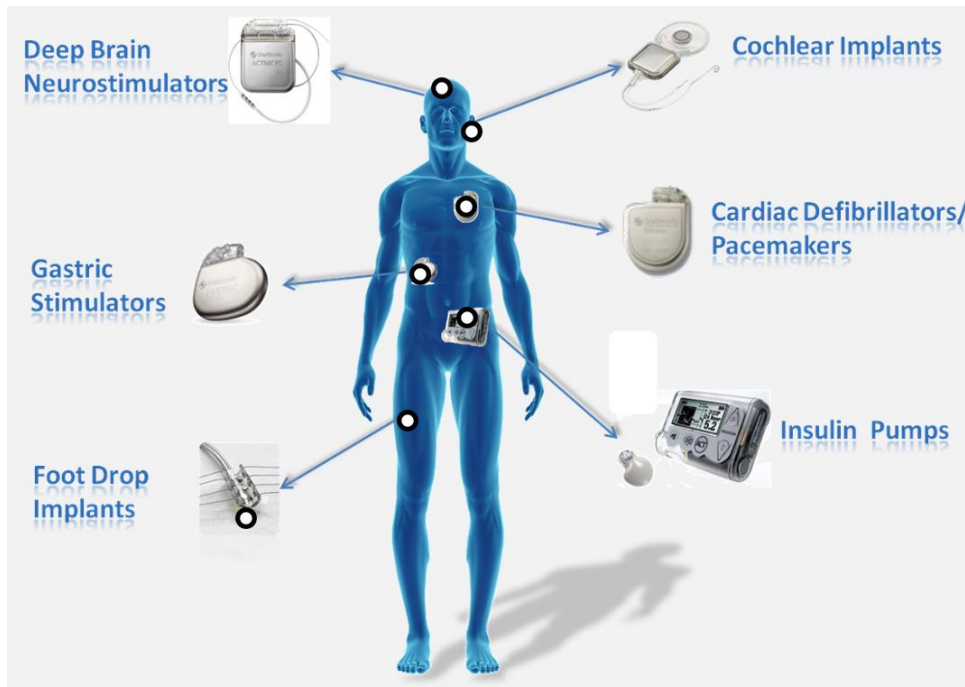


Fig. 1.2: Examples of invasive implantable devices [6].

As a critical component in wearable and implantable devices, an antenna plays a key role for the wireless communication between the devices in the WBAN. The communication takes place either through the body or over the body as in the implantable and wearable devices, respectively. This is different from the communication between a mobile phone and a base station where the communication channel is mostly through the air. Human body is considered as a hostile environment for radio due to its high tissue parameters (*i.e.*, permittivity and conductivity) at

microwave frequencies [1]. The signal loss is much higher than through the air. The reason for this is that the tissues of the human body can absorb and attenuate the signal radiated by antennas. Hence, a reliable wireless link between wearable and implantable devices in the WBAN can be designed by having knowledge of the signal loss in the communication channel (*i.e.*, human body), and the use of a proper antenna. The existing implantable and wearable antennas' topologies and designs under discussion still suffer from many challenges such as unstable antenna behavior, low bandwidth, considerable power generation, less biocompatibility, and comparatively bigger size.

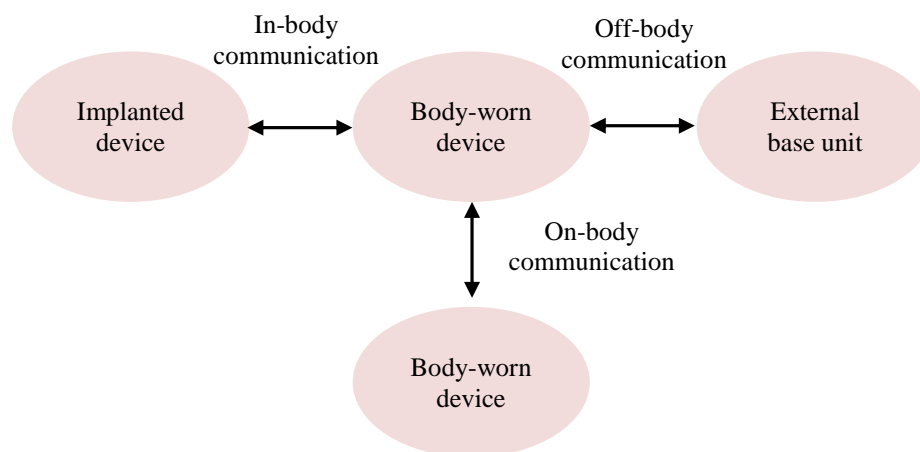


Fig. 1.3: Classifications of wireless body area communication.

This research has two main parts and will focus on two main objectives:

- Part I: to design, implement, and characterize antennas of improved characteristics for wearable and implantable devices intended for biomedical applications. The wearable/implantable antennas design constraints, requirements and challenges will be discussed in section 1.2.
- Part II: to introduce experimental and numerical investigations on the antenna effect on the system performance in two different applications. First, antenna selection criteria for the use in a non-contact respiratory rate measurement system based on ultra-wide band (UWB) radar

technology. The ultimate goal of studying this system is to address the limitations and capabilities of using it as a non-contact respiration-rate measurement device from antenna and propagation point of view. Second, antenna topology (*i.e.*, single antenna element and antenna array) effects on the phase measurement of a backscattered signal from a semi-passive radio frequency identification (RFID) tag. The phase information is then used for three dimensional (3D) localization purposes. The ultimate goal of studying this system is to address the limitations and capabilities of using it as a wearable 3D human localization device.

1.2 Design Constraints, Requirements, and Challenges

In order to perform the design of an antenna for implantable and wearable systems, several requirements in terms of physical and electromagnetic constraints summarized in Fig. 1.4, must be taken into account. A brief discussion is drawn as follows:



Fig. 1.4: Constraints and requirements of wearable and implantable antennas design.

Body phantom: usually it is not possible to initially test wearable and implantable antennas on/in an actual human due to ethical and safety issues. However, unlike free-space, the human body is lossy and frequency dependent as the electrical properties of the tissues have a large dynamic in the microwave frequency range. As an example, Table 1.1 shows the electrical properties in terms of the relative permittivity (ϵ_r) and conductivity (σ) of muscle and fat tissues at different frequencies, large variations can be observed as the frequency changes. Thus, the surrounding body tissues can strongly affect the antenna performance. They can modify the electrical size of an antenna. Given fixed dimensions, a lower resonant frequency (f_r) can be obtained, if compared to the free-space case, according to the following relation [8]:

$$f_r = \frac{f_0}{\sqrt{\epsilon_r}} \quad (1.1)$$

where f_0 is the resonance frequency in free-space. Moreover, the attenuation of the electromagnetic wave (EM) when traveling through the tissues also changes accordingly. The attenuation α_{attn} in Neper/m (1 Neper = 8.686 dB) of the EM waves in a lossy medium is given by [7]:

$$\alpha_{attn} = \omega \sqrt{\frac{\mu\epsilon_0\epsilon_r}{2} \left(\sqrt{1 + \left(\frac{\sigma}{\omega\epsilon_0\epsilon_r} \right)^2} - 1 \right)} \quad (1.2)$$

where $\mu = \mu_0 = 4\pi \times 10^{-7}$ H/m is the permeability of the free-space as the human tissues are non-magnetic, $\epsilon_0 = 8.85 \times 10^{-12}$ F/m is the permittivity of the free-space, ϵ_r is the relative permittivity of the tissue, σ is the conductivity in S/m, and $\omega = 2\pi f$ with f being the frequency in free-space. The attenuation in dB/m for fat and muscle tissues at different frequencies is shown in Table 1.1.

Human body phantom is used which can be a numerical model of actual human at the design and optimization stage of the antenna in simulation software for more realistic scenario or a physical phantom mimicking the characteristics of the biological tissues at the verification stage

of the antenna performance. The choice of the numerical body phantom affects both the design and performance of implanted and wearable antennas, as it is almost impossible to separate the performance of these antennas from the investigated body phantom.

Table 1.1: Characteristics of muscle and fat tissues at different frequencies [9].

<i>Frequency</i>	<i>Tissue</i>	<i>Relative permittivity (ϵ_r)</i>	<i>Conductivity (σ), S/m</i>	<i>Attenuation (α_{att}), dB/m</i>
915 MHz	Fat	5.459	0.051	35.565
	Muscle	54.99	0.948	206.30
2.45 GHz	Fat	5.280	0.104	75.391
	Muscle	52.72	1.738	388.84
5.8 GHz	Fat	4.954	0.293	214.44
	Muscle	48.48	4.960	1151.9

A simulated biological body could be a simple homogeneous model having the average electrical properties of the different tissues, or a more complex and anatomically phantom having almost all different tissues of a human body. The simplified body models describe the human body with different accuracies in terms of geometry, composition, and dimensions. Canonical geometries, as shown in Fig. 1.5, such as rectangular [10], cylindrical [11], and spherical [12] shapes can be used. On the other hand, muscle [13], averaged arm properties [11], and multilayered phantoms [14] are examples of different body phantom compositions. Dimensions of the body models adopted by researchers can vary in a wide range from a minimum of 8.5 mm to a maximum of 1000 mm [15].

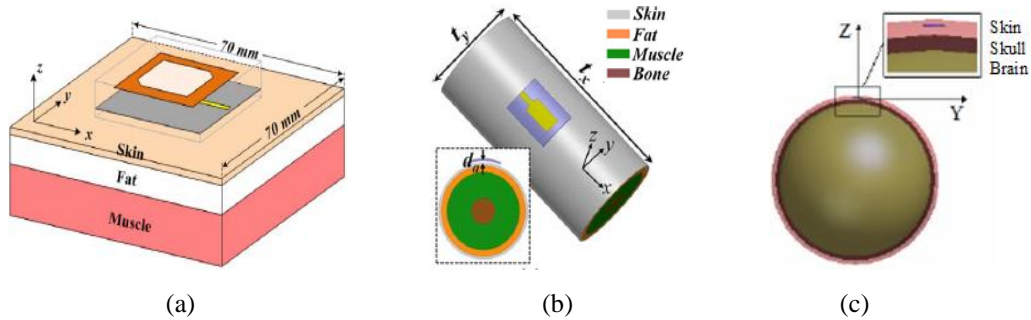


Fig. 1.5: (a) Rectangular [16], (b) cylindrical [17], and (c) spherical [18] body models.

The highest inhomogeneity in terms of the aforementioned body model parameters is provided by Virtual family phantoms with more than 84 different tissues obtained from the high resolution magnetic resonance imaging (MRI) of real human beings. They are provided by ITIS foundation [19]. The virtual family phantoms consist of four phantoms, a male phantom named Duke of age 34 year, a female phantom named Ella of age 26 year, a phantom of a girl named Billie of age 11 year, and a boy phantom named Thelonious who is 6 years old. The body model of Ella is illustrated in Fig. 1.6. It is worth mentioning that one of the limitations of using whole body phantoms with different tissues is a long simulation time due to large number of meshing cells in simulations. Hence, in order to accelerate the overall antenna design process, the phantom can be truncated to include the area of interest in the simulation domain. For example in [20], only the arm has been used for on body antenna performance evaluation.

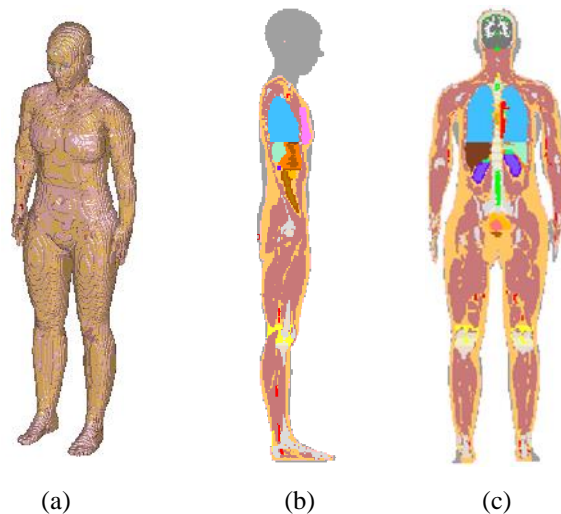


Fig. 1.6: Human body model of Ella; (a) 3D, (b) side, and (c) front views [19].

While the numerical analysis is extremely rich of body phantoms, more limitations appear when realizing a human body model to test the antenna. Physical phantoms are intended to make the evaluation of antenna performance in a controlled laboratory environment. They can be classified on the basis of the tissue types they represent. They can represent low-water content

tissue, such as bones and fats, having low permittivity and low loss. They can also represent high-water content tissues such as brain, skin and muscles, which have higher permittivity and loss [1]. Physical phantoms can be classified based on their final state as solid (dry) [21], semisolid (gel) [22] and liquid [23] phantoms. Fig. 1.7 shows different types of the skin tissue phantom.

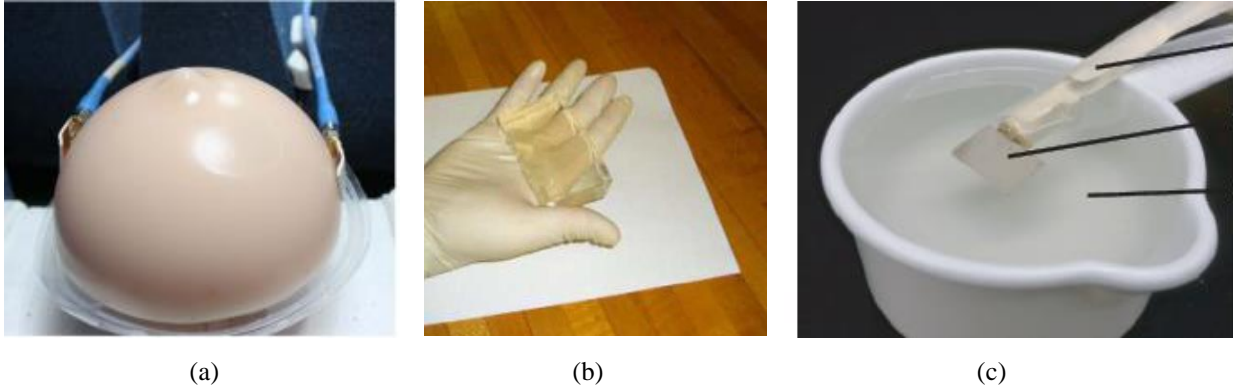


Fig. 1.7: Physical skin phantoms; (a) solid [21], (b) semisolid [22], and (c) liquid [23].

Safety regulations: due to the fact that the propagation of the electromagnetic field will be through/on the human body, electromagnetic power absorbed by the human body may pose potential health risks in case of long-term irradiation of the human body causing tissue damage. Hence, in order for the wearable/implantable antenna to adhere the health and safety requirements, the radiation from the antenna should present the least power absorbed per unit mass that is quantified by specific absorption rate (SAR). The amount of power absorbed by the human body can be expressed as [24]:

$$\frac{P}{\rho} = \frac{\sigma E^2}{2\rho} = \frac{J^2}{2\rho\sigma} \quad (1.3)$$

where, P is the power loss density (W/m^3), E is the electric field strength (V/m), J is the current density (A/m^2), ρ is the mass density (Kg/m^3) and σ is the conductivity (S/m). SAR levels should be controlled to be at the safety levels of the electromagnetic fields defined by the commonly used

SAR standards. For IEEE C95.1-2005 standard, a maximum value of 2 W/kg for the 10-g averaged SAR is stipulated [25]. On the other hand, IEEE C95.1-1999 standard restricts the 1-g averaged SAR to be less than 1.6 W/kg, the specification of which is more stringent [26].

Biocompatibility and material selection: biocompatibility implies that an antenna operating inside/on the body won't react with the surrounding tissues in order to preserve patient safety and, in case of implantable antenna, to prevent rejection of the implant. Furthermore, human tissues are conductive, and would short circuit the antenna if they were allowed to be in direct contact with its metallization. Biocompatibility and prevention of undesirable short-circuits are especially crucial in the case of antennas that are intended for long-term implantation [27]-[28]. For implantable antennas, different techniques have been explored in literature to achieve biocompatibility, including use of biocompatible materials [29], coating with thin biocompatible polymers [30], and addition of superstrates to cover the exposed metal parts [31]. The effect of the biocompatible encapsulation layer on the impedance matching and gain of the antenna is significant, therefore it should be taken into consideration when designing implantable and antenna [32].

In addition, in case of wearable antenna, to maintain easy wearing and less discomfort when antenna is mounted onto the human body, the antenna has the requirement of being reasonably flexible, low profile, and conformal to the human body. In addition, the robustness of the wearable antenna performance against various types of structural deformations such as bending and crumpling conditions should be guaranteed. Therefore, flexible and textile materials have been widely adopted in the wearable antenna design. Examples of used materials in literature are listed in Table 1.2.

Table 1.2: Examples of textile and flexible materials used in wearable antenna design.

<i>Ref.</i>	<i>Material (dielectric/conductive)</i>
[33]	Textile: wood felt/nylon
[34]	Textile: felt/shieldit Super
[35]	Textile: cotton/ NA
[36]	Textile: leather/conductive threads
[37]	Textile: jeans/NA
[38]	Textile: felt/zelt
[39]	Flexible: polyimideKapton and vinyl/NA
[40]	Flexible: jeans/flexible copper sheets
[41]	Flexible: RO3003/copper
[42]	Flexible: commercial papers/copper sheet
[43]	Flexible: latex/silver Nano-particle ink
[44]	Flexible: polydimethylsiloxane (PDMS)/silver Nano-wires

Frequency band: the operational frequency band for implantable and wearable antennas should be chosen properly taking into the account several factors such as the desirable application, antenna size, and signal attenuation through the biological tissues. In general, selection of the operation frequency involves several trade-offs. Specifically, low frequencies tend to be more attractive as they are associated with low signal attenuation (see Table 1.1), but at the same time will result in a relatively large antenna size. Moreover, the available bandwidth is low which limits the communication speed. A choice of high frequency band will result in small antenna size and high bandwidth but on the downside, it will have high attenuation (see Table 1.1). So at low frequencies the antenna becomes an inefficient radiator, and at high frequency tissue absorption losses dominate. Table 1.3 shows the characteristics of the frequency bands that could potentially be used for wearable and implantable antenna designs [7].

Table 1.3: Potential frequency bands for wearable and implantable devices [7], [45].

<i>Freq. (MHz)</i>	<i>Acronym</i>	<i>Merits</i>	<i>Demerits</i>
402 – 405	MICS ^a	Good propagation characteristics	Wearable applications not Allowed, large antenna size, limited bandwidth
401 – 406 413 – 419 426 – 432 438 – 444 451 – 457	MedRadio ^b	Worldwide availability, good propagation characteristics, quiet channel, medical only	Large antenna size, limited bandwidth
433.05 – 434.79	General telemetry	Good propagation characteristics	Crowded spectrum, large antenna, limited bandwidth
608 – 614 1395 – 1400 1427 – 1432	WMTS ^c	Good propagation characteristics, medical only	Limited spectrum, heavily used
868 – 870	General telemetry	Good propagation characteristics	EU only, limited spectrum, heavily used
902 – 928	ISM ^d	Good propagation characteristics	US/Canada only, crowded spectrum
2400 – 2500	ISM	Worldwide availability, small antenna, large bandwidth	Crowded spectrum, many standards and technologies
5725 – 5850	ISM	Worldwide availability, small antenna, large bandwidth	Existing standards and technologies, severe attenuation
3100 – 10600	UWB ^e	Worldwide availability, short range, low power, huge bandwidth	Coexistence with high data rate multimedia applications, severe attenuation

^a. Medical Implanted Communication Service (MICS), ^b. Medical Device Radiocommunications (MEDRadio), ^c. Wireless Medical Telemetry Service (WMTS), ^d. Industrial, Scientific, and Medical (ISM), and ^e. Ultra-WideBand (UWB).

Size restriction: as implantable and wearable devices are intended to be either worn on- or implanted inside the human body, respectively, the overall size of the device including the size of the antenna should be small. Several antenna miniaturization techniques proposed in the literature include the use of high-permittivity dielectric (substrate/superstrate) materials [12] such as ceramic alumina and Roger 3210, lengthening of the current-flow path in the radiating surface [46] such as meandered, spiral, waffle-type shaped radiating patch, inserting a shorting pin between the ground and patch planes to increase the effective size of the antenna, and, in turn, reduces the required physical dimensions [47], and using stacked structures [8]. It is worth mentioning that the actual process of antenna manufacturing has to be taken into account in order

to avoid extremely tight tolerances and to maximize the repeatability of the construction process itself.

Bandwidth: identifies the frequency spectrum where the antenna is matched and the provided power is radiated. In general, the reflection coefficient (S_{11}) describes the impedance mismatch between the feed line and the antenna feed point. It can be defined as the ratio of the power reflected back from the antenna at the feed point to the power fed to the antenna. If the power is completely reflected back at the feed point, S_{11} will equal to 1 or 0 dB. On the other hand, if the power is completely delivered to the antenna, the value will equal to 0 or $-\infty$ dB. -10 dB input impedance bandwidth (*i.e.*, used in this dissertation) refers to the range of frequencies in which a certain level of S_{11} can be maintained. Usually it is determined as the frequency range of -10 dB level of S_{11} , which is defined by the lower f_l and the upper frequency f_h band limits.

The surrounding environment for wearable and implantable antennas changes significantly from person to person. Therefore, the antenna should have a wide bandwidth to withstand the frequency detuning due to the human body loading. This is illustrated by the case of a wearable antenna in [11] which is simulated when it is surrounded by its body phantom and free-space. Simulated S_{11} results are reported in Fig. 1.8. A 700 MHz downward frequency shift occurs when the dielectric constant of the surrounding medium changes from 1 to 21.2, with respect to the free-space case. The selected dielectric value is used to mimic the averaged arm tissue at 5.8 GHz.

Based on the aforementioned discussion, the antenna design requirements can't be separated and the selection of one affects the others. **Therefore, the design of miniaturized efficient antenna working in/on the human body for wearable and implantable applications becomes one of the greatest challenges.** Other challenges are associated with the characteristics measurement setups of the wearable/implantable antennas in the laboratory (*i.e.*, more details will

be provided in the following chapters). Open research issues related to wearable/implantable antennas design and characterizations leave much to be desired.

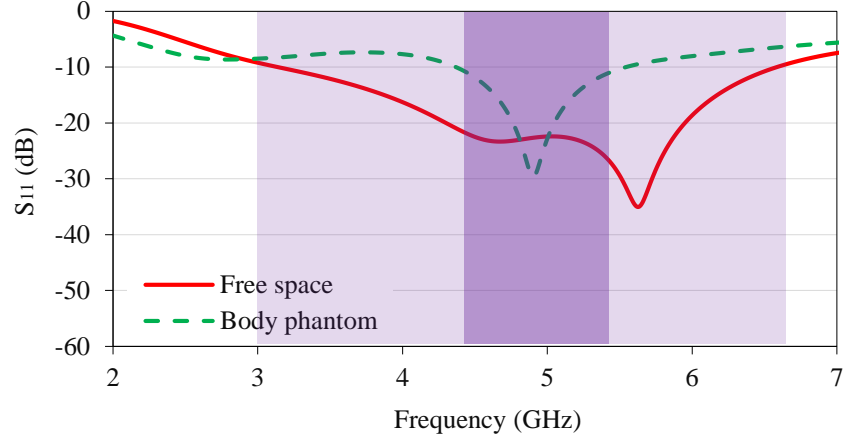


Fig. 1.8: Simulated S_{11} of wearable antenna in free-space and on body phantom.

1.3 Overview of the Thesis

Wearable antenna design (CHAPTER 2 and CHAPTER 3): artificial magnetic conductor (AMC) structures are used in the antenna design, acting as a ground plane, due to several advantages. First, AMC structures can improve the antenna radiation characteristics, such as the antenna gain, due to their in-phase reflection property while maintain small antenna volume. Second, they can isolate the antenna from the human body. Hence, the effect of the high loss tissues on the antenna performance and the EM coupling to the human body can be minimized. The targeted frequency bands are 2.45 GHz and 5.8 GHz ISM bands to achieve antenna miniaturization. Flexible material such as dielectric RO3003 and textile materials such as dielectric Pellon and conductive Shieldit Super and Pure Copper Taffeta materials are used in the antenna design to achieve the flexibility, low profile, and conformity requirements of the wearable antenna. Assessments of the proposed wearable flexible and textile antennas are carried out in free-space and on body conditions for antennas in flat form and under deformation effects such as bending

and crumpling. SAR evaluations are carried out for different scenarios to account for the safety regulations. Finally, investigations on proposing new materials such as flexible magneto-dielectric (MD) materials and dielectric and magnetic layered substrate in wearable antenna design are presented.

Implantable antenna design (CHAPTER 4): the design of antenna for implantable device of a capsule shape is of our interest due to the easy packaging process. As the antenna can be printed on the outer wall of the capsule, the inner volume can be used for the other electronic components. Biocompatible materials are used for the antenna and capsule designs. To achieve antenna miniaturization, meandered antenna shape is adopted. Wide band implantable antenna that is working within different frequency bands to consider different implanting scenarios is achieved.

Investigated wireless body area network (WBAN) applications (CHAPTER 5): (1) Respiratory rate measurement using UWB radar system: the process of measuring respiratory rate should be simple, reliable, and comfortable for patients. The use of UWB radar as a mechanism to measure respiration is useful due to its non-contact form of use. To evaluate a radar-based sensing system using different antenna types for respiratory-rate measurement, antenna type selection is done by testing the performance of three types of antennas attached to a TimeDomain PulseOn® 410 UWB [48] radar system, measuring the movement rate of controlled movable device. Experiments are designed in order to assess the tradeoffs between antenna selection and the proposed sensing system's accuracy. Results indicate that the proposed sensing system is less affected and shows less error when an antenna with directive radiation pattern, low cross-polarization and stable phase center was used. Due to its good radiation characteristics and small form-factor this antenna is then selected to study the respiratory rates of ten test subjects to investigate whether it is possible to measure the respiratory-rate using this system. Reference

measurements are performed and the accurate values of the respiratory-rates of the test subjects are collected and compared with the radar setup results. (2) An accurate phase-based localization method of RFID tag: real-time indoor localization has recently received intensive interests for a large variety of applications. A simulation study of indoor localization method of a semi-passive RFID tag is presented. The localization method is based on the phase information of the backscattered signal from a semi-passive RFID tag. Simulations and measurements of the backscattered phase for different cases are studied and compared in this chapter. The phase information is then will be used for 3D tracking purposes.

Conclusions, contributions, and future work (CHAPTER 6): this chapter will summarize the use of the research achievements/novelties and draw the main conclusions of this thesis. In addition, recommendations for future work will be included.

CHAPTER 2

DESIGN OF FLEXIBLE WEARABLE ANTENNA

2.1 Introduction

The main goals of this chapter are:

- To present the design cycle of a wearable textile-based monopole antenna integrated with a flexible artificial magnetic conductor (AMC) structure. The proposed design covers the ISM 2.45 GHz band. An AMC reflector is utilized to isolate the human body from undesired electromagnetic radiation and to improve the antenna radiation characteristics. Modeling and numerical analysis were carried out using full-wave electromagnetic simulation software, CST Microwave Studio (MWS) [49];
- To realize and characterize the proposed wearable antennas, *i.e.*, textile coplanar-waveguide (CPW) fed monopole antenna and flexible AMC antenna, in flat form and free-space conditions;
- To perform flexibility tests on the proposed wearable antennas, based on numerical analysis and prototypes measurements, in order to study effects of structural deformation, *i.e.*, different crumpling conditions, on the input impedance matching and radiation characteristics of the proposed wearable antennas;
- To study effects of structural deformation, *i.e.*, crumpling conditions, on the in-phase reflection characteristics of the AMC reflector;
- To perform numerical analysis of the proposed antennas mounted on different body models in order to discuss effects of human body loading in terms of frequency detuning and variations

of antenna radiation characteristics. A three-layered planer human body model was first considered, then a voxel body model was presented;

- To evaluate effects of antenna-body separation distance, using the simplified layered body model, on the stability of the proposed antennas' input matching characteristics;
- To consider the safety concerns and limits imposed by the standards such as IEEE C95.1-1999 [26] and the IEEE C95.1-2005 standards [25], when the proposed antennas are close to the human body. SAR assessments were carried out for the proposed wearable antennas in flat and crumpled forms.

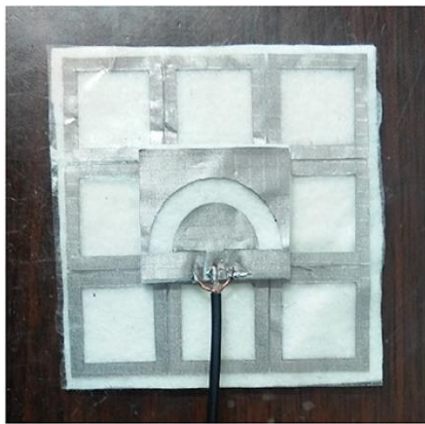
In order to reach these goals, this chapter is organized as follows:

Section 2.2 presents a literature survey on different textile/flexible wearable antennas that were integrated with AMC reflectors. These antennas are operating within ISM 2.45 GHz band (2.4 GHz – 2.5 GHz). The design details and prototypes realization of the textile monopole antenna and flexible AMC reflector are presented in Section 2.3. Section 2.4 presents performance evaluation, based on numerical and measurement analysis, of monopole and AMC antennas in terms of reflection coefficient and radiation characteristics. Challenges during the simulation and measurement phases of the design are discussed in this section. Evaluation of the proposed antennas in free-space is carried out in flat form and under different crumpling conditions. Section 2.5 presents a discussion on the performance evaluation of the proposed wearable antennas in the presence of different human body models.

2.2 Background

The use of AMC in different textile/flexible wearable antennas has been investigated and presented in the literature. In [33], a circular ring slot antenna was integrated with a 3×3 rectangular ring-shaped AMC array as shown in Fig. 2.1(a). The integrated antenna measures $81 \times 81 \times 4 \text{ mm}^3$ and implemented using dielectric wood felt and nylon conducive textile materials. The measured antenna gain and -10 dB input impedance bandwidth at 2.45 GHz are 7.3 dBi and 14.7%, respectively. The maximum averaged 1 g SAR value with the AMC layer was 95.9% lower than that obtained using the stand-alone circular ring slot antenna. However, variations in the matching properties in terms of frequency detuning and a reduction in S_{11} levels were observed when the integrated AMC antenna was mounted on different parts of the human body such as leg, arm and stomach.

In [39], a flexible polyimide Kapton and vinyl materials were utilized to design the M-shaped monopole antenna and slotted Jerusalem Cross (JC) AMC structure, respectively, as depicted in Fig. 2.1(b). The AMC antenna has 18% -10 dB input impedance bandwidth, 3.7 dB increase in the antenna gain, and 64% reduction in SAR at 2.45 GHz. The total size of the antenna is $65.5 \times 65.5 \times 3.2 \text{ mm}^3$.



(a)



(b)

Fig. 2.1: AMC antennas based on (a) textile [33] and (b) flexible materials [39].

In [41], a folded slot antenna was integrated with a 3×3 rectangular shaped AMC unit cells, as depicted in Fig. 2.2(a). Both antenna and AMC were fabricated, using an etching process, on Rogers RO3003 flexible substrate. The antenna was placed, approximately $\lambda/20$ (at 2.4 GHz), above the AMC surface, and a flexible foam material was used to fill the space between the radiating element and the AMC surface as shown in Fig. 2.2(b). Hence, the antenna design resulted in a relatively large size of $88 \times 83 \times 9 \text{ mm}^3$. In addition, the -10 dB input impedance bandwidth of 4% at 2.45 was relatively low for the ISM 2.45 GHz band. A significant reduction in the S_{11} level was observed when the antenna was mounted and tested on a human leg.

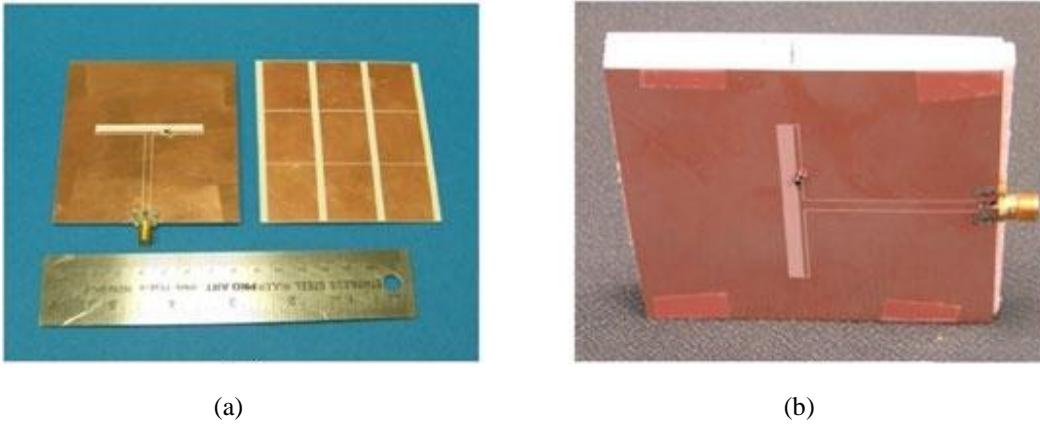


Fig. 2.2: Fabricated prototypes; (a) folded antenna and AMC and (b) AMC antenna [41].

In [42], microstrip monopole antenna with single-ring resonators was inkjet-printed on the commercially available 0.23 mm-thick photo paper using conductive Nano-silver ink, as shown in Fig. 2.3. A 2.54 mm-thick spacer made of Styrofoam was inserted as between the AMC array and a copper sheet which was used as a metallic reflector, as shown in Fig. 2.3(c). The antenna measures $150 \times 130 \times 2.87 \text{ mm}^3$. It is worth mentioning that, while the antenna with the AMC reflector was well matched within the ISM 2.45 GHz band with -10 dB input impedance bandwidth of 10%, in the absence of the AMC array, the antenna did not resonate. The antenna gain of a conventional microstrip monopole on chest human phantom was as low as -9 dBi. On the other

hand, the gain of the proposed AMC backed monopole, measured on a human phantom was 0.95 dBi.

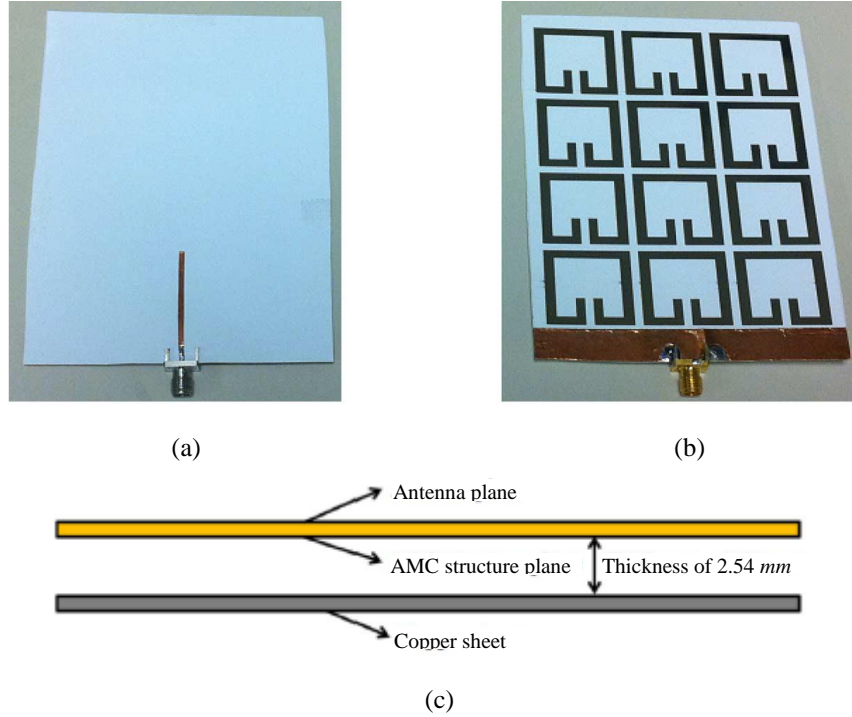


Fig. 2.3: Fabricated prototype; (a) front view, (b) rear view and (c) entire antenna [42].

A dual band fractal based monopole patch was fabricated using dielectric jeans fabric and flexible copper sheets, as shown in Fig. 2.4(a) [40]. The integrated AMC antenna measures $150 \times 150 \times 3 \text{ mm}^3$ with -10 dB input impedance bandwidth of 5.08% at 2.45 GHz. Due to the presence of AMC reflector, the back lobe of the antenna was reduced by 15.64 dB at 2.45 GHz. The antenna was evaluated under different bending and crumpling conditions to test the flexibility of the proposed design. In general, a frequency detuning effect was observed under these conditions.

In another design, Yagi-Uda antenna over an AMC reflector was printed on a flexible latex substrate using silver Nano-particle ink [43]. The antenna was separated from the upper AMC surface using flexible Styrofoam of thickness $0.044\lambda_0$ at 2.4 GHz. The resultant antenna size is $50 \times 50 \times 9.5 \text{ mm}^3$. The antenna suffered from a very narrow -10 dB input impedance bandwidth of

1.8% at 2.4 GHz. Antenna gain of 0.12 dBi in the end-fire direction was obtained when antenna was mounted on human chest. A photograph depicting the antenna on human chest is shown in Fig. 2.5. Performance sensitivity to bending conditions was observed in terms frequency detuning and radiation patterns widening.

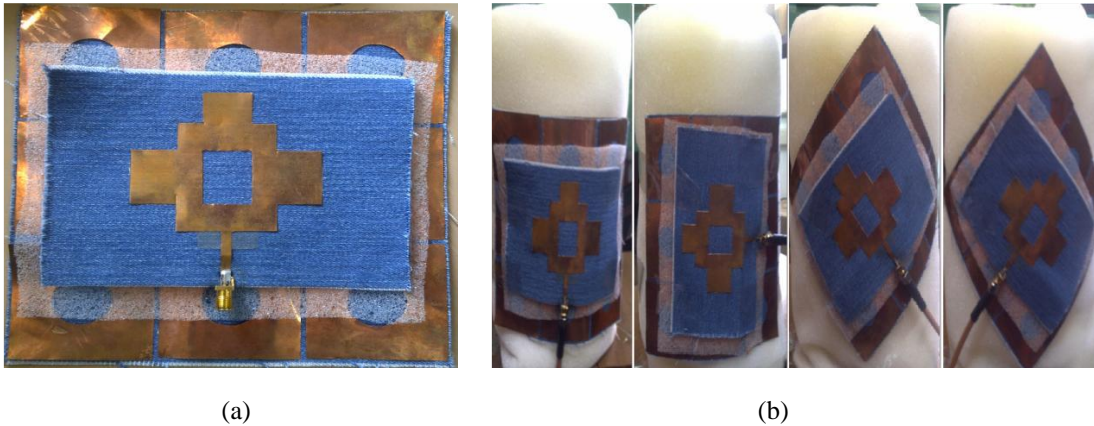


Fig. 2.4: (a) Fabricated prototype and (b) antenna under bending conditions [40].



Fig. 2.5: Flexible antenna mounted on the human chest [43].

In [44], authors are presenting an antenna utilizing a low-loss composite polydimethylsiloxane (PDMS) and silver Nano-wires, used as the dielectric and conductive materials, respectively, of a flexible ring monopole antenna integrated with AMC reflector. The antenna topology is shown in Fig. 2.6. A foam spacer was used between the antenna and the AMC structure resulting in a $50 \times 50 \times 5.5 \text{ mm}^3$ antenna size. The integrated antenna features antenna

input impedance bandwidth and gain of 11.3% and 5.2 dBi at 2.44 GHz, respectively. Robustness of the antenna was evaluated under different bending conditions and on body scenarios.

In the last example we present here the AMC unit element was designed based on the rectangular patch structure, which was then integrated using slots and slits for bandwidth broadening [34]. Meanwhile, the combination of the slits and L-shaped parasitic elements applied at four edges of the rectangular antenna structure enabled unidirectional radiation outwards from the body. The antenna shown in Fig. 2.7 measures $100 \times 100 \times 6 \text{ mm}^3$ and was fabricated using dielectric felt and conductive Shieldit Super textile materials. Although the antenna features light weight and small size properties, the antenna has a low gain and -10 dB input impedance bandwidth of 2.42 dBi and 9.85% at 2.45 GHz, respectively.

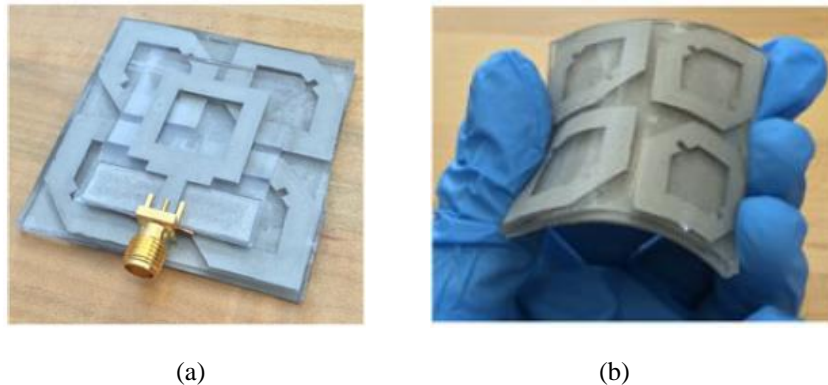


Fig. 2.6: (a) Fabricated AMC antenna and (b) flexibility test [44].

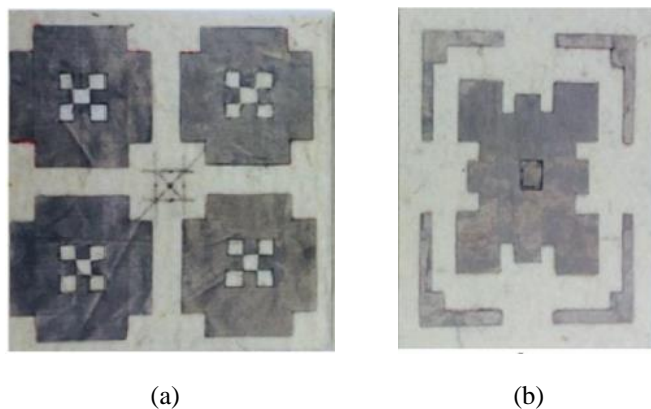


Fig. 2.7: (a) AMC structure and (b) proposed antenna [34].

2.3 Antenna Topology and Materials

The monopole antenna configuration was designed based on the proposed design in [50] and was optimized to operate in the ISM 2.45 GHz band. The radiating element and the CPW feeding line were located on the same side of a Pellon fabric substrate with a thickness of 3.6 mm , relative permittivity (ϵ_r) of 1.08, and loss tangent ($\tan\delta_e$) of 0.008. Fig. 2.8 depicts the dimension details of the monopole antenna. It is worth noting that the separation between the two arms (W_3) in addition to the slot width (W_l) were selected to achieve the minimum reflection coefficient ($S_{11} < -10\text{ dB}$). Pellon fabric was chosen as the antenna's substrate since it exhibits a low profile and flexible characteristics, which enable stacking multiple layers to control the thickness of the substrate while the antenna is conformal to the user's body [51]. A 0.17 mm -thick electro-textile, Shieldit Super from LessEMF [52], was used to fabricate the conductive layers.

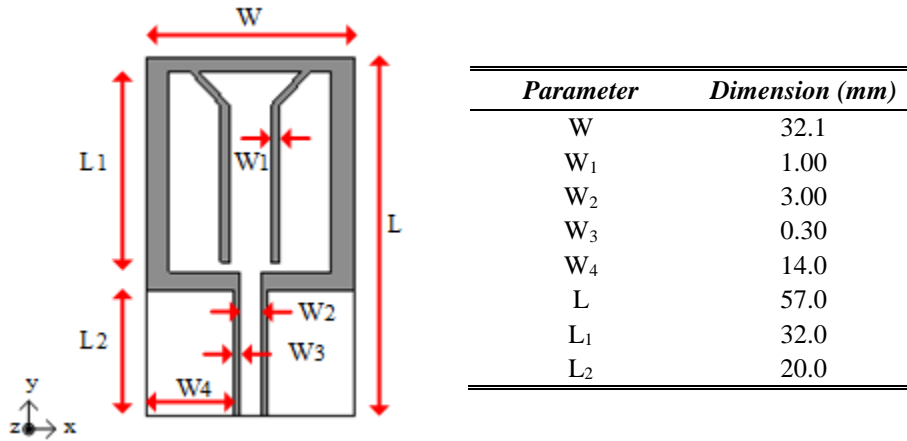


Fig. 2.8: Configuration of CPW-fed monopole antenna (right) and dimension details (left).

The AMC reflector was designed by reflection phase characterization. AMC acts as a perfect magnetic conductor (PMC) in a specific frequency band in which it provides in-phase reflection characteristics. The proposed monopole antenna was placed on a symmetric 4×4 AMC array, measuring $124\text{ mm} \times 124\text{ mm}$. The AMC unit cell has a size of $31\text{ mm} \times 31\text{ mm}$, and it was

printed on a 1.52 mm thick RO3003 flexible material with $\epsilon_r = 3$ and $\tan\delta_e = 0.0013$. Fig. 2.9 shows the configuration along with the dimension details of the proposed AMC unit cell. Fabrication of the textile antenna process was performed using Silhouette®, and CNC machine was used for the flexible printed circuit board (PCB) materials. Prototypes of the fabricated monopole antenna and AMC reflector are shown in Fig. 2.10.

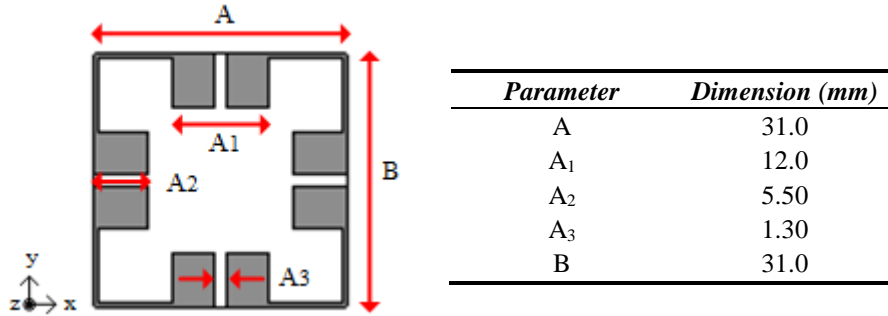


Fig. 2.9: Configuration of AMC unit cell (right) and dimension details (left).

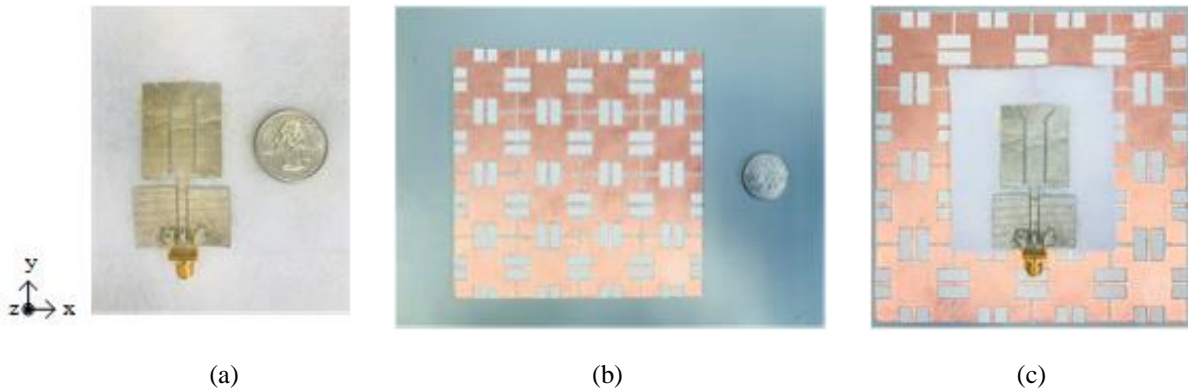


Fig. 2.10: Photograph of fabricated (a) monopole, (b) AMC reflector, and (c) AMC antenna.

For the AMC reflection phase characterization procedure we followed the same methodology applied in [53]. In order to find the AMC in-phase band (*i.e.*, within $\pm 90^\circ$ phase values), a single cell with periodic boundary conditions (PBC) in the x - and y -directions was simulated in CST MWS. For the proposed cell, as shown in Fig. 2.11, the exact point of zero reflection phase is located at 2.45 GHz with a bandwidth of 138 MHz (2.34 GHz to 2.48 GHz) within $\pm 90^\circ$ phase values.

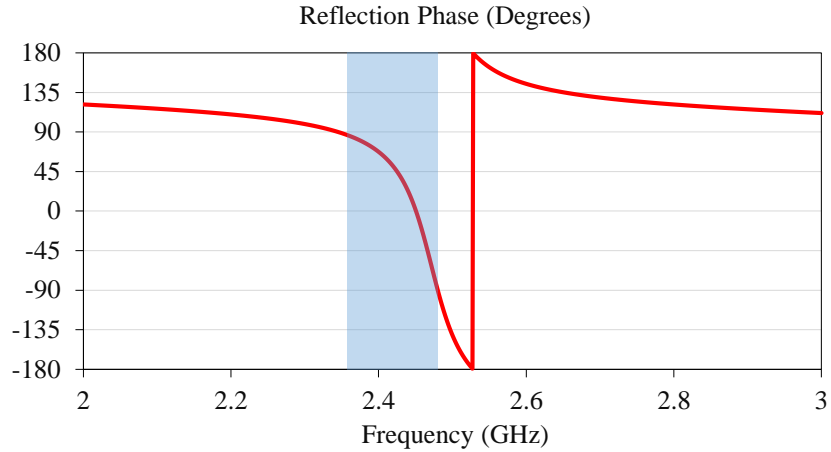


Fig. 2.11: Reflection phase diagram of AMC unit cell.

2.4 Performance of Wearable Antennas in Free-space

2.4.1 Performance of Wearable Antennas in Planar Configuration

In order to decide on the alignment of the monopole antenna on the AMC reflector, a comparison of two cases, one when the monopole antenna was placed at the center and the second one when it was at the edge of the AMC structure, was carried out. The comparison was based on simulations of the antenna on a flat plane. Results are summarized in Table 2.1. Although the AMC reflector was designed to have the in-phase reflection property at 2.45 GHz, it can be seen that if the monopole antenna was placed at the edge of the AMC structure, the 2.45 GHz frequency point did not show much improvement in the performance. On the other hand, when antenna was placed at the center of AMC structure, a higher gain value was achieved at 2.45 GHz.

Furthermore, a study on the advantage of using the AMC structure in improving the antenna performance at a relatively small size was carried out. Four different cases were studied for comparison purposes and results are shown in Table 2.2.

Table 2.1: Performance summary of monopole placed at different locations on the AMC.

<i>Parameter</i>	<i>Monopole placed at the edge</i>	<i>Monopole placed at the center</i>
Resonance frequency (f_r), GHz	2.42	2.46
S_{11} at f_r , dB	-21.79	-23.63
Gain at f_r , dBi	4.65	8.55
Front-to-back ratio (FBR) at f_r , dB	13.95	16.16
S_{11} at 2.45 GHz, dB	-2.56	-11.87
Gain at 2.45 GHz, dBi	2.54	8.41
FBR at 2.45 GHz, dB	22.14	22.16

Table 2.2: Performance summary of studied scenarios.

<i>Parameter</i>	<i>Case1</i>	<i>Case2</i>	<i>Case3</i>	<i>Case4</i>
Resonance frequency (f_r), GHz	2.16	NA ^a	1.91	2.46
Input impedance bandwidth, GHz	2.58	NA	3.40	0.047
Lower frequency (f_l), GHz	1.75	NA	1.66	2.43
Upper frequency (f_h), GHz	4.33	NA	5.06	2.48
S_{11} at f_r , dB	-16.92	NA	-17.77	-23.63
Gain at f_r , dBi	2.23	NA	7.43	8.55
Front-to-back ratio (FBR) at f_r , dB	0.008	NA	15.73	16.16
S_{11} at 2.45 GHz, dB	-15.81	-1.19	-11.62	-11.87
Gain at 2.45 GHz, dBi	2.45	1.39	7.91	8.41
FBR at 2.45 GHz, dB	0.009	23	15.13	22.16

^a. Antenna does not show a -10 dB S_{11} value.

Where the wavelength (λ) is calculated at 2.45 GHz, these cases were defined as follows:

1. Case 1: Monopole antenna without ground plane or AMC layer,
2. Case 2: Monopole antenna with ground plane at zero distance,
3. Case 3: Monopole antenna with ground plane at $\lambda/4$ distance,
4. Case 4: Monopole antenna with the proposed AMC structure.

As expected, the addition of ground plane at $\lambda/4$ (30.6 mm at 2.45 GHz) distance away from the monopole antenna has improved the antenna gain and front-to-back-ratio (FBR) compared to the stand-alone antenna case, due to constructive effect of antenna's image. However, placing the ground plane at zero distance away from the antenna resulted in a non-resonating radiator due the destructive image. Also as expected, AMC reflector of 3.6 mm thickness at zero

distance away from the antenna showed a significant improvement in antenna gain and FBR. In case of using a ground plane, the separation distance between antenna and ground plane is important to get the constructive addition of image, which can be achieved when the ground plane is approximately at $\lambda/4$ distance away from the antenna. However, this can result in a large antenna size, which is not feasible in case of wearable antennas. On the other hand, the antenna operating frequency should be within the $\pm 90^\circ$ reflection phase bandwidth of the AMC reflector in order to get the constructive effect, with the best performance can be achieved at 0° phase point.

Reflection coefficient (S_{11}) was simulated and measured with and without the AMC reflector as shown in Fig. 2.12. Measurements were conducted using Keysight E5071C vector network analyzer with (300 kHz – 20 GHz) frequency operating range. Discrepancies between first set of simulations (simulation 1) and measurements were observed that might be attributed due to errors during simulation, fabrication, and measurement phases of the study. Despite the fact that the measured results confirmed our design approach for the wearable antennas operating within ISM 2.45 GHz band, the proposed wearable antennas did not provide the expected performance in terms of matching characteristics, therefore we started looking for the error sources in our investigation. The most significant potential source of error we found was the error in the assumption of material properties used during the simulation phase. In the first set of simulations (simulation 1), for simplicity we used copper with the conductivity of 5.8×10^7 S/m as the conductive material in monopole antenna simulation. However, the conductivity of the electro-textile materials is different from that of a good conductor such as copper. To validate this conclusion, a parametric study on the conductivity of the electro-textile material was carried out based on simulations. Good agreement with the measurement results was obtained with the assumption of 500 S/m as the conductivity of electro-textile material (see simulation 2).

Simulation 2 of monopole antenna yields a wide -10 dB input impedance bandwidth of 4.88 GHz (1.32 GHz – 6.20 GHz) with a good impedance matching at 2.45 GHz ($S_{11} = -12.82$ dB). Measurement result showed a good agreement with the simulation 2 result within the ISM 2.45 GHz band showing -10 dB input impedance bandwidth of 1.40 GHz (2.3 GHz – 3.7 GHz). On the other hand, measurement result of AMC antenna showed a wider -10 dB input impedance bandwidth of 400 MHz (2.2 GHz – 2.6 GHz) compared to simulation 2 results (2.38 GHz – 2.48 GHz). It is worth mentioning that the reported simulation results of the rest of simulations in this chapter are based on assumption of a conductive material of 5.8×10^7 S/m conductivity.

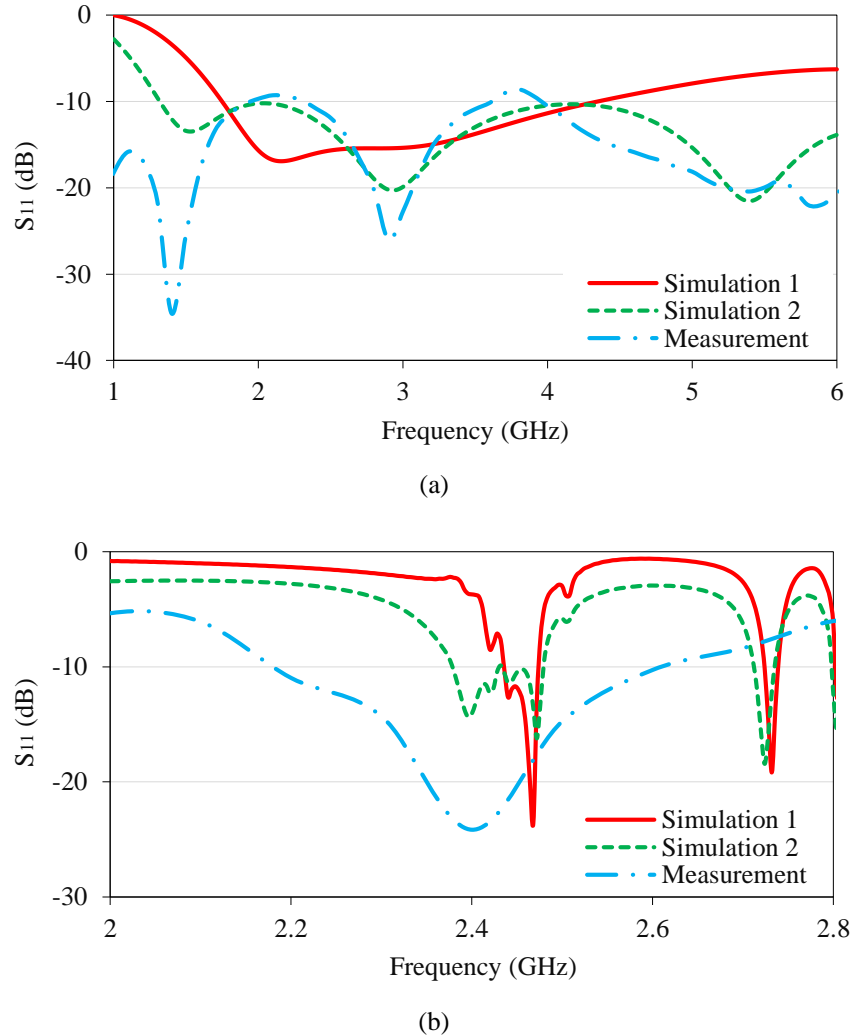


Fig. 2.12: Simulated and measured S_{11} of (a) monopole and (b) AMC antennas in free-space.

Many challenges were faced during the measurement phase due to the stiffness of the vector network analyzer cables and SMA connectors and the flexibility of the textile material. We could not firmly fix the antenna and we noticed a large variation in the resonances and S_{11} level when we changed the position of the antenna and the cables during the setup of the test. Also, a large variation in S_{11} with the pressure on the antenna connector while moving the cable was confirmed. Some problems in terms of misalignment of the monopole antenna on the AMC structure and air gap between monopole antenna and AMC structure were also faced. The impact of a thin air layer in the proposed AMC antenna, representing a layer between textile antenna and AMC structure, was studied via electromagnetic simulation. Results showed a degradation in the return loss of the antenna, and variations of the resonance frequency (f_r) and -10 dB input impedance bandwidth.

The effectiveness and usefulness of the AMC reflector can be assessed by comparing antenna radiation characteristics in presence and absence of an AMC reflector. The normalized far-field radiation patterns of the principal planes, E-plane (yz -plane) and H-plane (xz -plane), were measured inside the University of North Dakota anechoic chamber with an automated antenna movement platform. Radiation patterns of monopole and AMC antennas at 2.45 GHz are depicted in Fig. 2.13 and Fig. 2.14, respectively. The three-dimensional radiation pattern is quasi-hemispherical when the AMC reflector was integrated, while the original pattern is close to omnidirectional radiation. This shows an increase in the FBR and antenna directivity, achieved by the in-phase reflection of the AMC reflector. The measured antenna gain was improved from 2.6 dBi for monopole antenna to 4.6 dBi for monopole on AMC reflector.

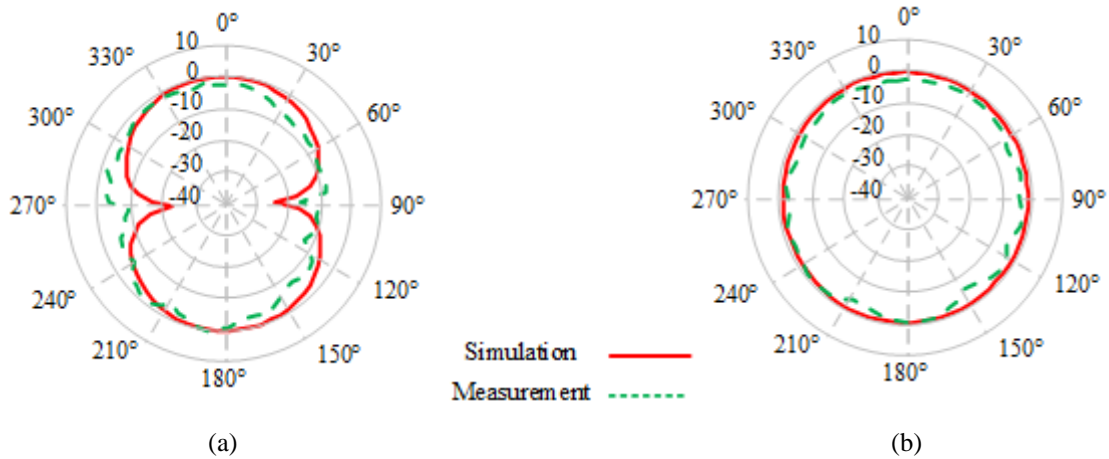


Fig. 2.13: Co-pol radiation of monopole antenna at 2.45 GHz in (a) E-plane and (b) H-plane.

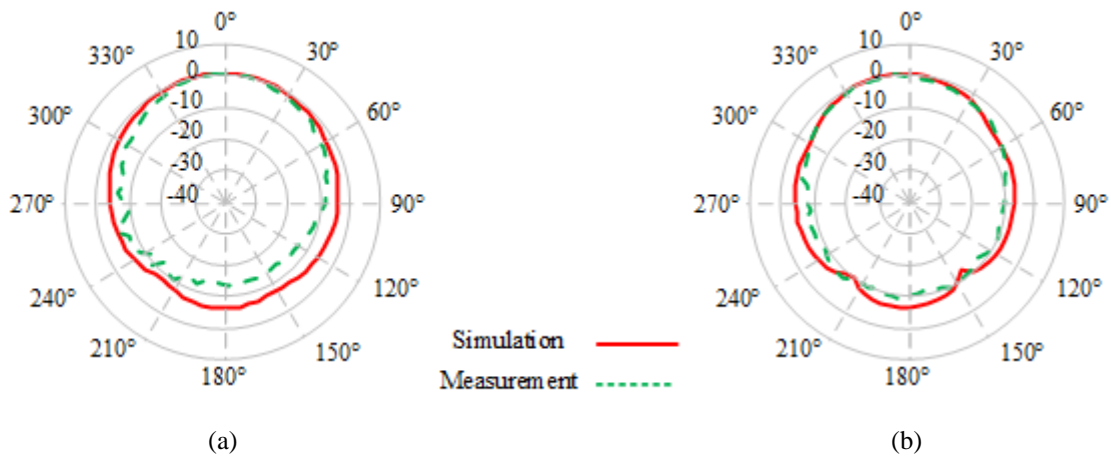



Fig. 2.14: Co-pol radiation of AMC antenna at 2.45 GHz in (a) E-plane and (b) H-plane.

2.4.2 Performance of Wearable Antennas under Crumpling Effects

In wearable applications, many types of crumpling may take place. Four typical forms of crumpling were selected as the main investigation targets in two perpendicular planes of the antenna, namely the E-plane (yz -plane) and H-plane (xz -plane). Dimensions of the antenna in each crumpling case are described in Table 2.3 for antenna crumpling in E- and H-plane directions. On the human body, cases 1 and 2 are typical for general clothing distortion most likely to appear when the antenna is placed on the chest or the back of the wearer. Crumpling in cases 3 and 4 is

likely to be observed near the knee or the elbow. Crumpling profile is defined by crumple depth (N) and crumple period (M). A central part of the antenna (0.5 mm) was kept flat for the feeding requirements imposed by the simulation program when antenna crumpled in E-plane direction. On the other hand, antenna crumpling in H-plane started from the center of the feeding line.

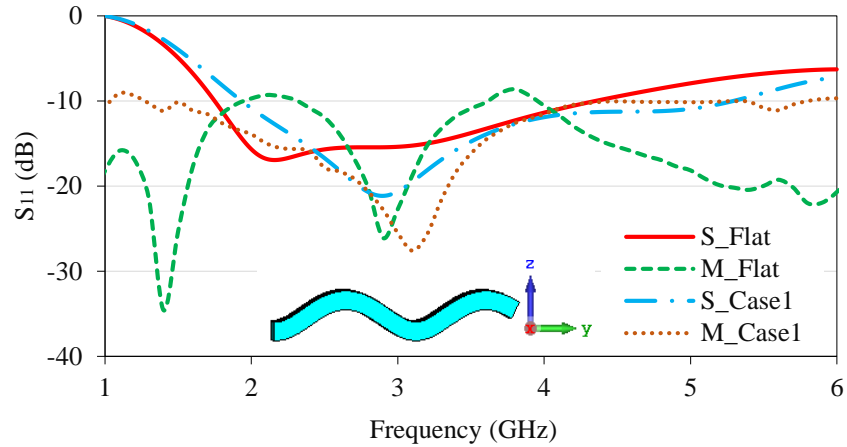
Table 2.3: Dimension details of crumpled monopole antenna.

		<i>Antenna width(mm)</i>	<i>Antenna length(mm)</i>	<i>N(mm)</i>	<i>M(mm)</i>	<i>Crumpling profile</i>
	Flat	32.10	57.00	-	-	
E-plane bending	Case1	-	54.37	6.00	31.00	
	Case2	-	50.25	6.00	24.00	
	Case3	-	44.92	11.00	31.00	
	Case4	-	40.40	35.00	60.00	
H-plane bending	Case1	30.00	-	6.00	31.00	
	Case2	31.00	-	6.00	24.00	
	Case3	27.13	-	11.00	31.00	
	Case4	25.70	-	35.00	60.00	

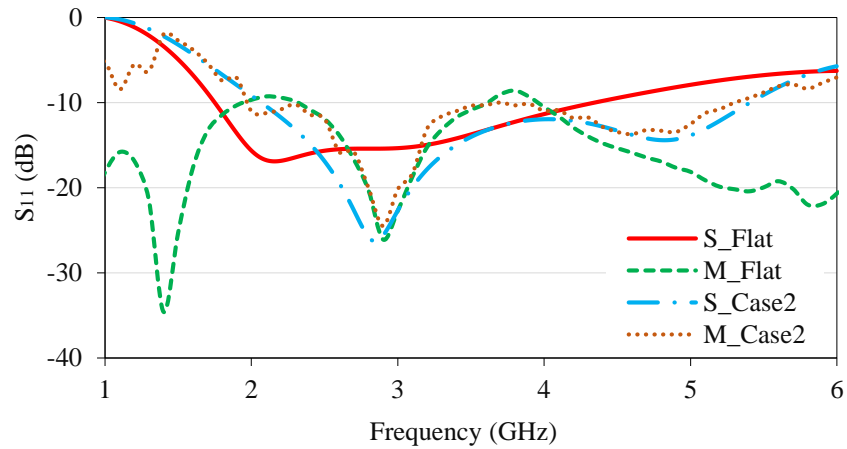
Reflection coefficients were measured for crumpling cases 1 and 2 in E- and H- plane crumpling directions, as shown in Fig. 2.15 and Fig. 2.16, respectively. In general, a good agreement between simulated and measured S_{11} of crumpled monopole antenna was achieved. A summary of performance of all studied crumpling cases, based on simulations, is given in Table 2. In case of E-plane crumpling, stable input impedance matching within the ISM 2.45 GHz band and a slight upwards shift in f_r were observed under different crumpling conditions.

It is worth mentioning that although the antenna was bent almost 90° in case 4, which is the most severe crumpling scenario, the -10 dB input impedance bandwidth was slightly reduced compared to that obtained when the antenna was flat, with f_r shifted upward by 58 MHz. Significant changes in S_{11} were observed due to antenna crumpling in H-plane. The -10 dB input impedance bandwidth was increased due to crumpling in cases 1, 2, and 3, with the maximum bandwidth obtained in case 2 (1.67 GHz – 5.65 GHz) as compared to the flat antenna (1.76 GHz

– 4.35 GHz). In contrast, the -10 dB input impedance bandwidth was halved due to crumpling in case 4. All crumpling cases studied in E- and H- planes successfully yield a wide -10 dB input impedance bandwidth that covers the ISM 2.45 GHz band of interest.



(a)

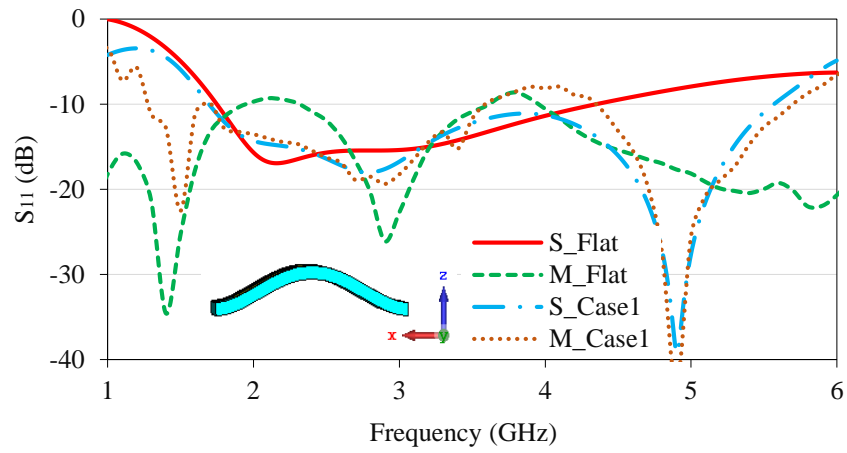


(b)

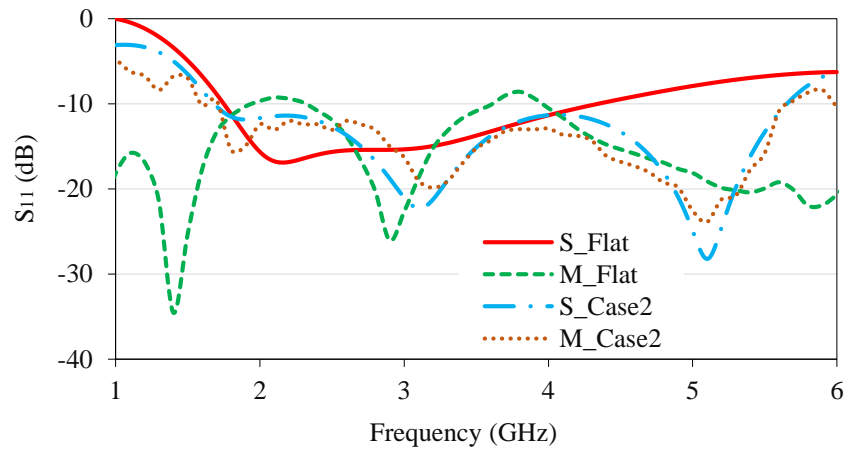
Fig. 2.15: S_{11} of crumpled monopole antenna based on simulation (S) and measurement (M) results in E-plane; (a) case1 and (b) case2.

Antenna radiation characteristics in free-space at 2.45 GHz under crumpling conditions in the E- and H-planes are summarized in Table 2.4 based on simulation results. Antenna crumpling in the E-plane caused less distortion in radiation characteristics compared to crumpling in the H-plane. The most significant degradation in antenna gain and total efficiency was observed in the

crumpling of case 4 along the H-plane. Crumpling in case 4 in H-plane direction showed the highest amount of ground plane excitation, as shown in Fig. 2.17. Radiation patterns measurement of crumpled monopole antenna at 2.45 GHz were conducted for crumpling cases 1 and 2 in the E- and H-planes as shown in Fig. 2.18 and Fig. 2.19, respectively. A good agreement between simulation and measurement results was observed.



(a)



(b)

Fig. 2.16: S_{11} of crumpled monopole antenna based on simulation (S) and measurement (M) results in H-plane; (a) case1 and (b) case2.

Table 2.4: Performance summary at 2.45 GHz of crumpled monopole antenna.

	<i>Parameter</i>	<i>Flat</i>	<i>Case1</i>	<i>Case2</i>	<i>Case3</i>	<i>Case4</i>
E-plane crumpling	f_l^a (GHz)	1.75	1.92	2.08	2.32	1.91
	f_h^b (GHz)	4.33	4.08	5.04	5.54	3.83
	S_{11} (dB)	-16.92	-16.06	-15.83	-11.42	-16.58
	Gain (dBi)	2.45	2.45	2.32	2.21	2.32
	Directivity (dBi)	2.67	2.66	2.50	2.58	2.50
	Efficiency (%)	95	95	95	92	95
H-plane crumpling	f_l (GHz)	1.75	1.94	1.69	1.15	2.04
	f_h (GHz)	4.33	5.27	5.65	3.50	3.06
	S_{11} (dB)	-16.92	-16.03	-12.30	-13.86	-17.68
	Gain (dBi)	2.45	2.53	2.62	2.00	0.69
	Directivity (dBi)	2.67	2.85	2.85	2.86	2.86
	Efficiency (%)	95	93	95	82	61

^a f_l represents the lower -10 dB frequency band limit and ^b f_h represents the higher -10 dB frequency band limit.

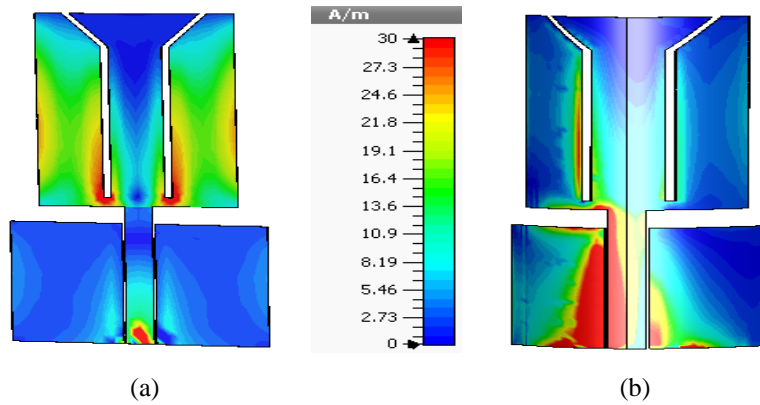


Fig. 2.17: Monopole current distribution; (a) flat form, and (b) crumpling case 4 in H-plane.

Because of the limitations imposed by the simulation program to build a crumpled AMC antenna structure due to the total thickness of the structure and the feeding requirements to keep enough distance between the crumpling point and feeding line, performance of AMC antenna under crumpling conditions was studied only in the E-plane direction. Crumpling profile is defined in the same manner as for monopole antenna crumpling, where (M) is the crumpling periodic length and (N) is the crumpling depth. The effects of change in crumpling profile parameters on the performance of AMC antenna was studied. AMC antenna crumpling was investigated for two

series. Series 1 had three crumpling cases where M was 30 mm and N was 5 mm , 6 mm , and 7 mm . In series 2, M was 31 mm while N had the same values as in series 1. Dimensions of the AMC antennas for these crumpling series are shown in Table 2.5. The AMC antenna aperture was reduced due to crumpling from $124\text{ mm} \times 124\text{ mm}$ (flat) to a minimum value of $111.60\text{ mm} \times 124\text{ mm}$ obtained when $M = 30\text{ mm}$ and $N = 7\text{ mm}$.

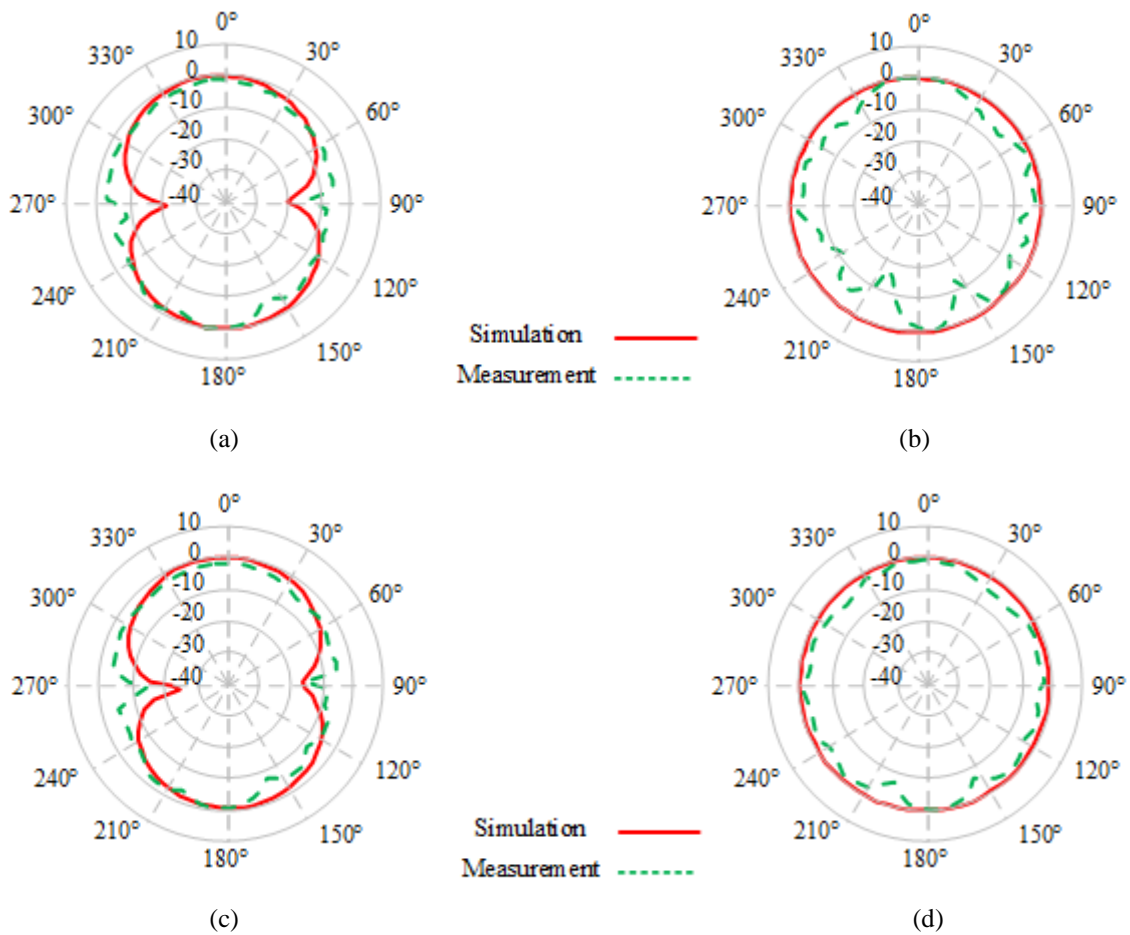


Fig. 2.18: Co-pol radiation at 2.45 GHz of monopole antenna crumpled in E-plane; (a) case1_E-plane, (b) case1_H-plane, (c) case2_E-plane, (d) case2_H-plane.

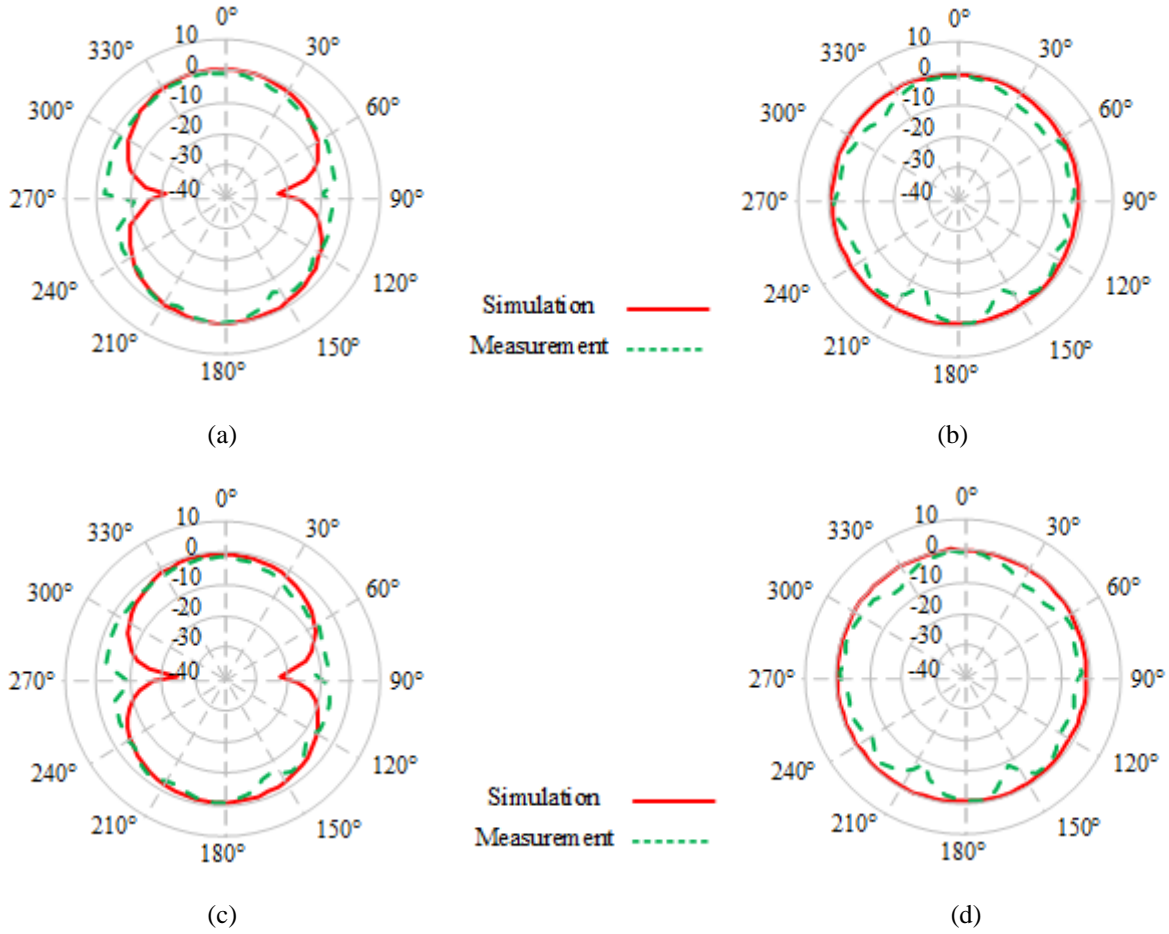


Fig. 2.19: Co-pol radiation at 2.45 GHz of monopole antenna crumpled in H-plane; (a) case1_E-plane, (b) case1_H-plane, (c) case2_E-plane, (d) case2_H-plane.

Table 2.5: Dimension details of crumpled AMC antenna.

		<i>Antenna length(mm)</i>	<i>N(mm)</i>	<i>M(mm)</i>	<i>Crumpling profile</i>
	Flat	124.00	-	-	
Series1	Case1	116.78	5	30	
	Case2	114.25	6	30	
	Case3	111.60	7	30	
Series2	Case1	117.48	5	31	
	Case2	114.97	6	31	
	Case3	111.89	7	31	

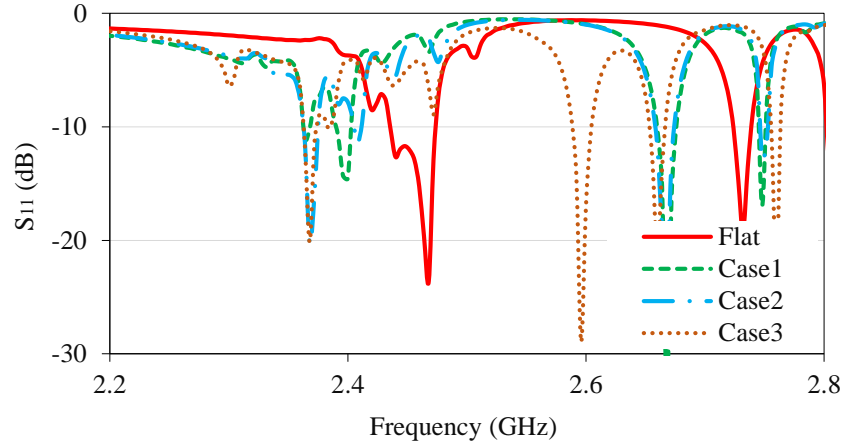
Reflection coefficients of AMC antenna due to crumpling in series 1 and series 2 are depicted in Fig. 2.21. In general, due to crumpling the AMC antenna, a shift in f_r and a reduction

in the -10 dB input impedance bandwidth were observed. The effect of changing M value from 30 mm to 31 mm can be seen as a shift in f_r toward higher values. On the other hand, it can be concluded that changing N value had less impact on AMC antenna performance. Crumpling in series 2 showed better matching within the frequency range of interest, S_{11} being less than -10 dB, as compared with crumpling in series 1.

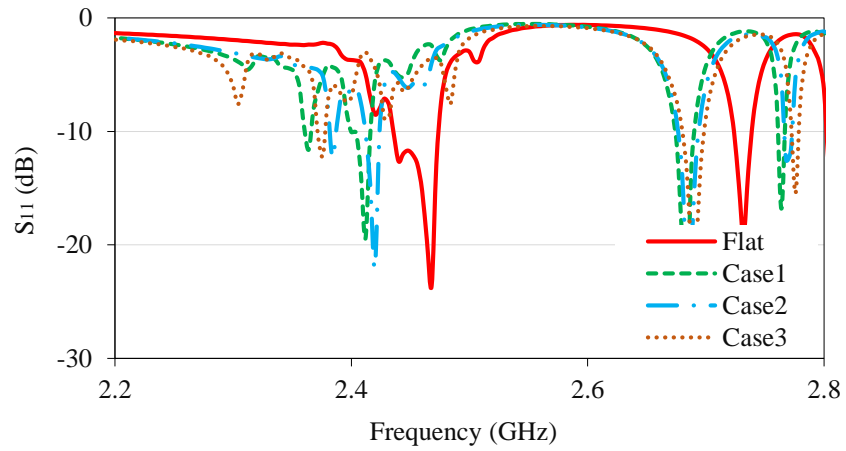
S_{11} was measured for crumpled AMC antenna for case 2 of series 2. It is worth mentioning that despite our best efforts to fix the monopole antenna on the surface of crumpled AMC structure, we noticed an air gap layer that might have caused discrepancies in the obtained results. In addition, S_{11} for crumpled AMC antenna in H-plane was measured for the same selected crumpling case, *i.e.*, case 2 of series 2. Reflection coefficient results, as shown in Fig. 2.21, showed that there was no significant changes compared to the case of E-plane crumpling.

Radiation characteristics of AMC antenna at f_r and 2.45 GHz frequencies for crumpling conditions in series 1 and series 2 are summarized in Table 2.6. For the cases in which the AMC antenna experiences a multi-resonance behavior, f_r that was chosen for investigation was the closest one to the ISM 2.45 GHz band. Radiation characteristics of the AMC antenna for crumpling cases 1 and 2 in both series at f_r were in comparison to those obtained when the antenna was flat, while a degradation in the antenna performance was noticed due to crumpling in case 3 with the f_r being shifted out of the ISM 2.45 GHz band.

The most noticeable crumpling effect at 2.45 GHz was a significant reduction in the antenna gain and efficiency of 6.69 dB and 41%, respectively, due to crumpling in case 1 in series 1. Please note that in this case the resonance frequency is no longer at 2.45 GHz. Crumpling in case 2 in series 2, which represents the typical crumpling case that may take place in reality, showed acceptable performance when compared to the antenna in flat form.



(a)



(b)

Fig. 2.20: Simulated S_{11} of crumpled AMC antenna (a) series 1 and (b) series 2.

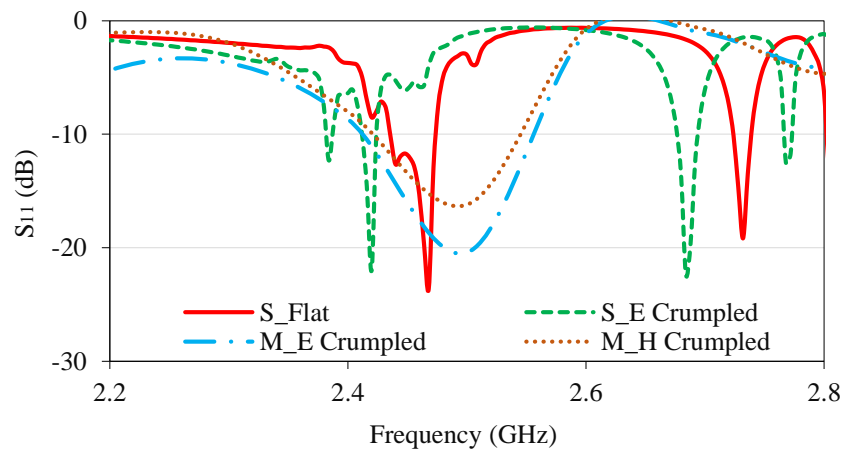


Fig. 2.21: Simulation (S) and measurement (M) results of crumpled AMC antenna of (E) E-plane crumpling and measurement results of (H) H-plane crumpling in case 2 from series 2.

Table 2.6: Radiation characteristics summary for AMC antenna crumpling in E-plane.

	<i>Parameter</i>	<i>Flat</i>	<i>Case1</i>	<i>Case2</i>	<i>Case3</i>
Series1	f_r (GHz)	2.46	2.40	2.41	2.36
	Gain at f_r (dBi)	8.55	7.27	7.46	2.01
	Directivity (dBi)	10.17	9.43	9.60	6.07
	Efficiency (%)	70	61	61	40
	FBR (dB)	12.50	15.88	20.27	6.85
	Gain at 2.45 GHz (dBi)	8.41	1.72	3.50	6.23
	Directivity (dBi)	9.86	7.34	8.35	8.86
	Efficiency (%)	71	30	33	55
	FBR (dB)	8.50	9.81	10.08	18.00
	Series2	f_r (GHz)	2.46	2.41	2.41
Gain at f_r (dBi)		8.55	7.29	7.41	5.33
Directivity (dBi)		10.17	9.57	9.28	6.61
Efficiency (%)		70	59	65	74
FBR (dB)		12.50	19.91	16.75	15.10
Gain at 2.45 GHz (dBi)		8.41	3.75	6.80	5.64
Directivity (dBi)		9.86	7.49	9.15	8.16
Efficiency (%)		71	42	58	56
FBR (dB)		8.50	14.82	14.58	13.00

In order to explain changes in AMC antenna radiation characteristics and input impedance matching due to crumpling conditions, the effect of AMC reflector crumpling on $\pm 90^\circ$ reflection phase bandwidth was simulated and results are summarized in Table 2.7. It can be concluded that crumpling the AMC reflector shifts the point of zero phase reflection that represents the maximum constructive effect of antenna's image that can be achieved using AMC reflector, which is not at the resonance frequency of the crumpled AMC antennas nor at 2.45 GHz frequency point. One may expect that a significant improvement in antenna performance should still be achieved since these frequency points are within $\pm 90^\circ$ reflection phase bandwidth for most of the studied crumpled AMC antennas. However, the achieved performance of crumpled AMC antenna was not as good as that obtained when AMC antenna is in flat form.

Table 2.7: Zero reflection frequency point of crumpled AMC structure.

		f_l^a (GHz)	Zero reflection point (GHz)	f_h^b (GHz)
Series1	Case1	2.302	2.435	2.443
	Case2	2.404	2.452	2.531
	Case3	2.325	2.486	2.523
Series2	Case1	2.365	2.456	2.514
	Case2	2.406	2.477	2.480
	Case3	2.406	2.500	2.701

^{a.} f_l represents $+90^\circ$ phase point and ^{b.} f_h represents -90° phase point

2.5 Performance of Wearable Antennas on Human Body Models

Two scenarios were considered for antenna performance assessment on human body, that were based on simulations using CST MWS. Antennas were initially placed on a simplified three-layered planar rectangular human tissue model, in order to minimize the computational costs and simulation times. It was assumed that the curvature of the body could be neglected for physically small antennas. The simplified human body model consisted of three tissue layers: skin, fat, and muscle, with an overall surface size of $200\text{ mm} \times 200\text{ mm}$, which was more than 3 times the surface area of the designed antenna. This layered body model represented most of body regions quite well. Since fat tissue has similar properties to bone tissue and the electrical parameters of muscle tissue and many inner organs are similar [54]. Thickness and dielectric properties of the layers considered in the body model [55] are tabulated in Table 2.8. Antennas were subsequently simulated considering Ella model which represents a 26 year old female with a height of 1.36 m and weight of 57.3 kg. Ella belongs to the Virtual Family [19]. A layer of Pellon fabric ($\epsilon_r = 1.08$, $\tan\delta_e = 0.008$) of 3.6 mm thickness was placed between the antennas and the presenting body models during simulation in order to account for clothing.

Analysis of frequency detuning, antenna radiation characteristics, and SAR values were performed and results are summarized in the following subsections. Moreover, the effect of the

antenna-body separation was studied to find its effects on the antennas' matching and performance.

Table 2.8: Electrical properties of the body tissues at 2.45 GHz [55].

<i>Layer</i>	<i>Thickness (mm)</i>	<i>Relative permittivity (F/m)</i>	<i>Conductivity (S/m)</i>
Skin	3	38.01	1.46400
Fat	7	5.28	0.10452
Muscle	60	52.73	1.73880

2.5.1 Frequency Detuning

Reflection coefficients of monopole and AMC antennas for free-space, layered body model, and Ella body model conditions are shown in Fig. 2.22. In general, the high permittivity and losses of human tissue affects the matching properties of the monopole antenna, causing both attenuation and frequency detuning. A reduction of 79% and 75% in the -10 dB input impedance bandwidth, in addition to the antenna not resonating within ISM 2.45 GHz band, were observed when the conventional monopole antenna was placed close to the layered and Ella body models, respectively. On the other hand, the AMC antenna retained its impedance matching for both scenarios. A small shift to lower frequency of 2.464 GHz was observed for the AMC antenna when placed close to human body models, as compared to its resonance in free-space at 2.468 GHz. This shows that AMC antenna is nearly 100% tolerant to the positioning on lossy material, such as the human body. Moreover, these performances confirm the validity of the choice and the effectiveness of the simplified layered body model.

In order to consider the applicability of the AMC reflector on different wearable antenna operational scenarios, a parametric study on antenna-body separation distance (d), using the simplified layered body model, was performed to examine the stability of the antenna's matching properties. The distance between antenna and tissue model (d) varied from 2 mm to 20 mm. As shown in Fig. 2.23, monopole antenna resonance frequency was shifted when antenna was placed

closer to the surface of the tissue model. In addition, poor impedance matching within ISM 2.45 GHz band was observed. On the other hand, AMC antenna showed steady impedance matching similar its operation in free-space.

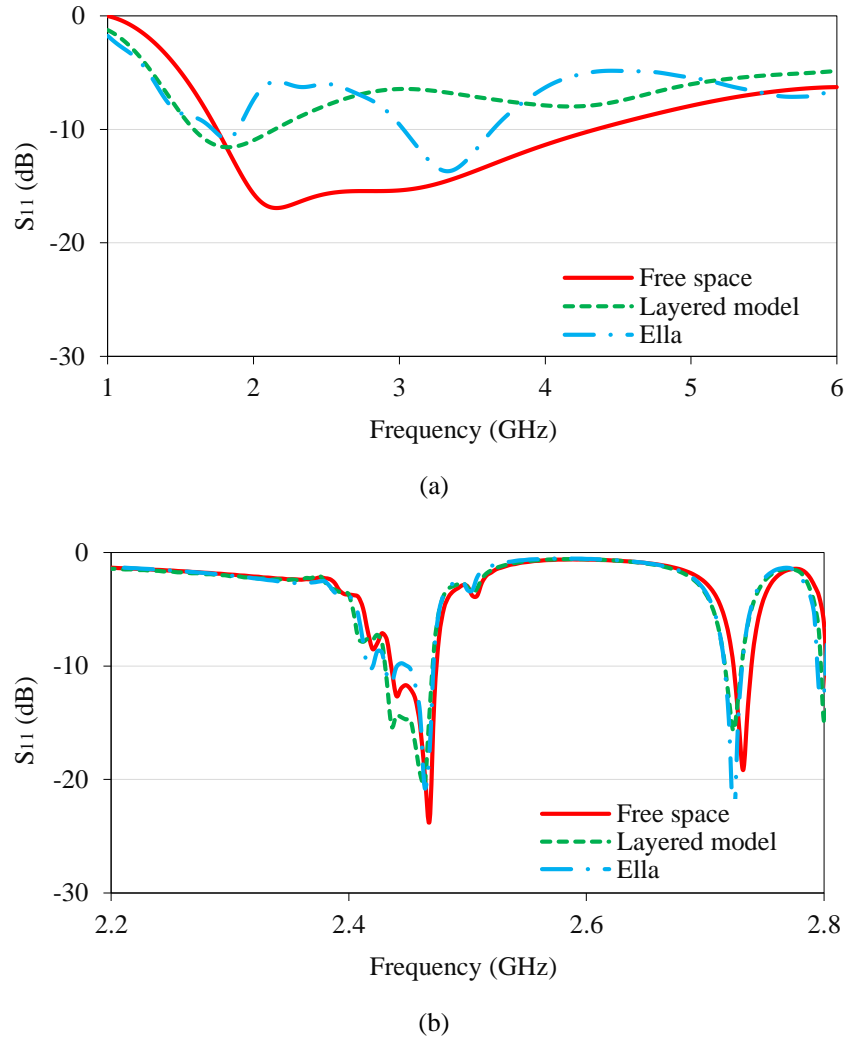


Fig. 2.22: S_{11} of (a) monopole and (b) AMC antennas on different body models.

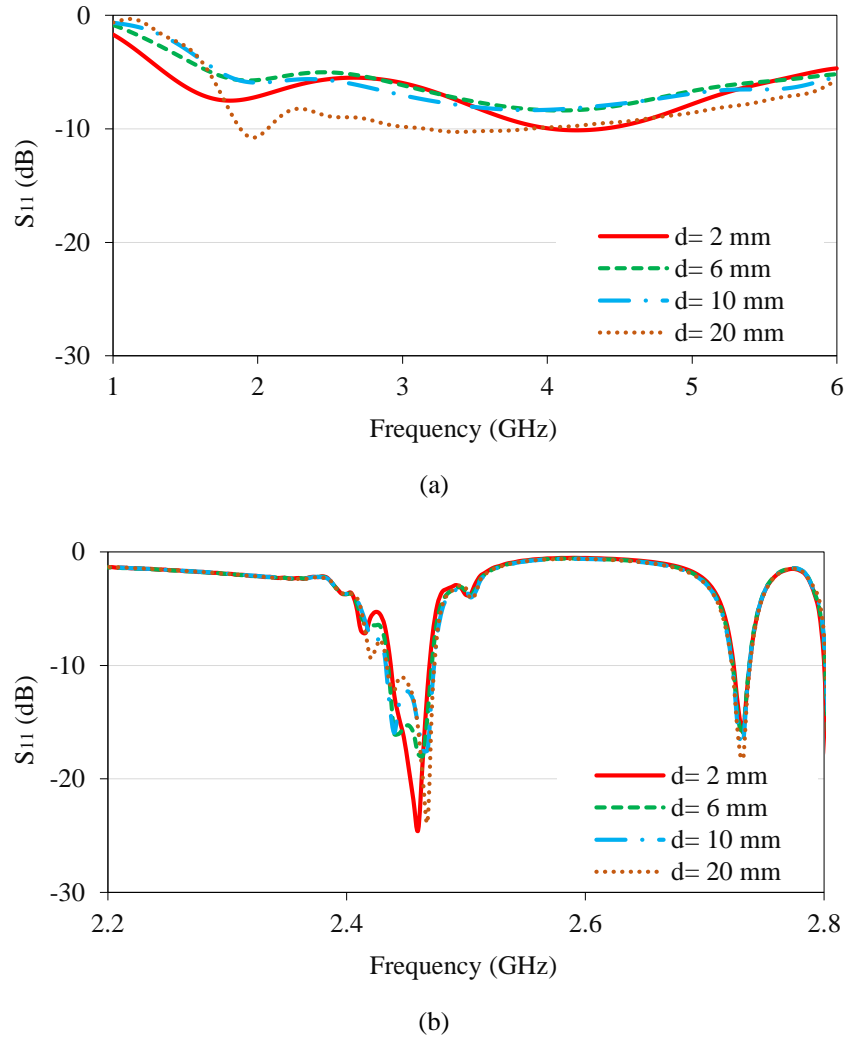


Fig. 2.23: S_{11} (a) monopole and (b) AMC antennas at different separation distances.

2.5.2 Radiation Characteristics

Table 2.9 summarizes the radiation properties of monopole and AMC antennas evaluated when placed on human body models and when it was left in free-space. Important observations can be made from the presented results. The first is that the presence of the human body deteriorates the gain and efficiency of the antenna when the AMC reflector is not present. The second observation is that AMC reflector effectively isolates the human body from the radiating antenna since the radiation characteristics in terms of gain and efficiency remained comparable in

the presence and the absence of the human body. Results of S_{11} in combination with the radiation characteristics of studied antennas demonstrated the necessity of the AMC reflector in order for the antenna to be effectively and efficiently used for wearable applications, since it reduces the effect of human body on the antenna's performance. Moreover, despite larger discrepancies found when focusing on antennas radiation performances considering the simplified layered and Ella body models in comparison with matching properties, the simplified layered body model is a satisfactory representation of the human body.

Table 2.9: Radiation characteristics for wearable antennas on human models at 2.45 GHz.

	<i>Scenario</i>	<i>Gain (dBi)</i>	<i>Efficiency (%)</i>
Monopole Antenna	Free-space	2.45	95
	Layered model	-1.69	10
	Ella model	0.35	21
AMC Antenna	Free-space	8.41	71
	Layered model	8.40	66
	Ella model	9.08	68

2.5.3 Analysis of Specific Absorption Rate (SAR)

SAR analysis is essential to evaluate the performance of the antenna when it is close to the human body and to consider the safety concerns and limits imposed by the standards. The maximum SAR limit is 1.6W/kg for any 1 g tissue by IEEE C95.1-1999 [26] or 2W/kg for any 10 g tissue by the IEEE C95.1-2005 standards [25]. SAR is a measure of the rate at which energy is absorbed by the human body when exposed to an electromagnetic field. Mass averaged SAR method (typically 1g and 10g), using the simplified layered body model, is used in the simulation for 1 Watt delivered power.

SAR analysis was carried out for monopole and AMC antennas in flat form and under crumpling condition of $N = 6 \text{ mm}$ and $M = 31 \text{ mm}$. This crumpling case was chosen for SAR

analysis since it is the common crumpling case among aforementioned crumpling cases of monopole and AMC antennas, which makes it easy for SAR comparison. Simulated averaged SAR values are summarized in Table 2.10, where “crumpled monopole 1” and “crumpled monopole 2” are monopole antennas crumpled in E- and H-planes, respectively, and “crumpled AMC” is AMC antenna crumpled in E-plane. Fig. 2.24 shows the simulated averaged SAR for flat antennas.

The mass-averaged method depends on the surface area of the human body model chosen for investigation; however, this method is still valid to show the benefit of using AMC reflectors in wearable antenna design. Maximum point SAR analysis was performed, and results are shown in Table 2.10. In addition, half power beam width (HPBW) and FBR values are summarised and listed in Table 2.10 in order to study effects of variations in the radiation characteristics on the obtained SAR.

For the considered input power, a significant reduction in SAR at 2.45 GHz was achieved using an AMC reflector for the antenna in flat form and under crumpling conditions. The obtained SAR levels of AMC antenna were within the specified limits allowed by the aforementioned standards, which gives a reliable indication of the benefits of AMC being used as an antenna ground plane. In addition, antennas crumpling showed variations in the obtained SAR compared to the flat form. Crumpling antennas in E-plane resulted in a lower SAR values compared to SAR values of antennas in flat form. On the other hand, monopole crumpling in H-plane resulted in a higher SAR levels compared to SAR levels of the flat antenna.

Table 2.10: SAR analysis summary of wearable antennas at 2.45 GHz.

	<i>1 g Tissue (W/Kg)</i>	<i>10 g Tissue (W/Kg)</i>	<i>Point SAR (W)</i>	<i>HPBW in E- plane (degrees)</i>	<i>HPBW in H- plane (degrees)</i>	<i>FBR (dB)</i>
Flat Monopole	16.46	9.390	56.62	61.5	81.2	25.52
Crumpled Monopole 1	11.71	6.704	40.49	57.5	80.3	30.61
Crumpled Monopole 2	17.50	9.825	61.13	58.6	80.9	28.66
Flat AMC	0.33	0.166	2.14	66.9	45.5	32.33
Crumpled AMC	0.19	0.098	0.75	60.6	40.3	35.18

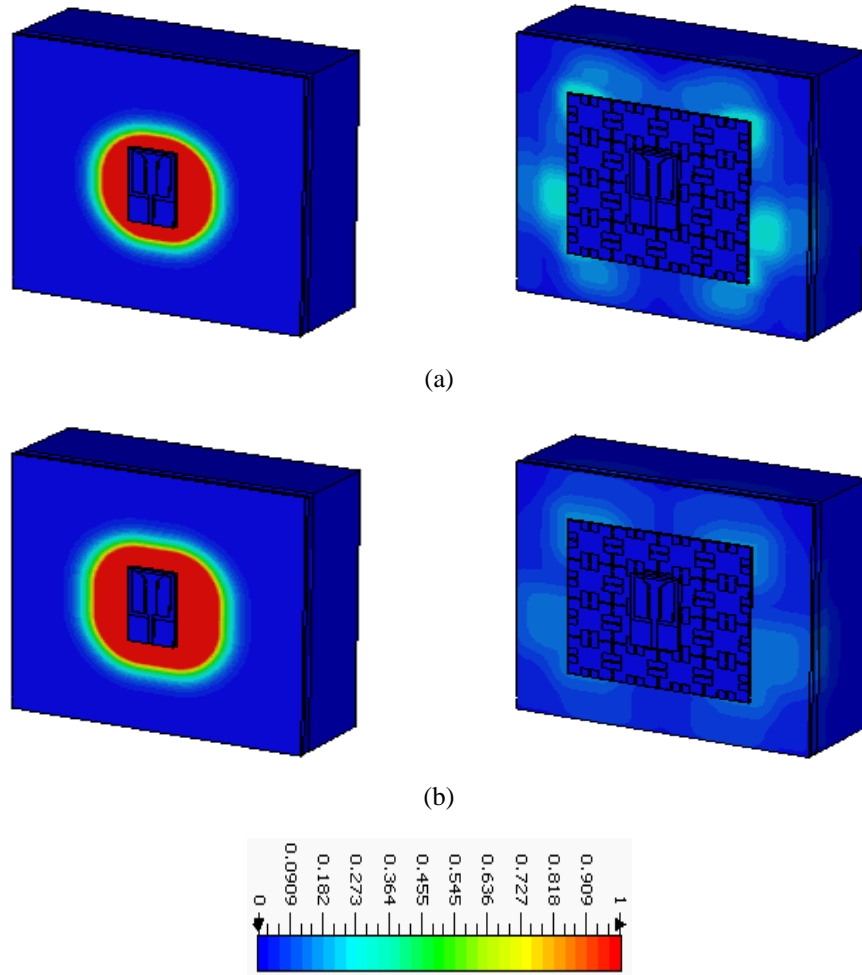


Fig. 2.24: Simulated averaged SAR (W/Kg) at 2.45 GHz for monopole antenna (left) and AMC antenna (right); (a) 1 g, and (b) 10 g.

2.6 Summary

In this chapter, the design, realization and characterization of a wearable textile-based monopole antenna integrated with a flexible AMC structure was presented. The proposed design covers the ISM 2.45 GHz band. An AMC reflector was utilized to isolate the human body from undesired electromagnetic radiation and to improve the antenna radiation characteristics. A monopole antenna was backed with an AMC reflector and tested in free-space and on human body models. The in-phase reflection characteristic of the AMC structure significantly enhanced the FBR ratio and antenna gain in free-space. On the human body models, the AMC antenna provided stable performance compared to the conventional monopole antenna. The calculated SAR values for the AMC-based antenna were very low, with a reduction of more than 90% compared to the SAR values of the same antenna without an AMC reflector. Moreover, performance of the antenna with and without AMC reflector under different crumpling conditions was studied and presented. The effect of crumpling on reflection phase characteristics of the AMC reflector was analyzed as well.

CHAPTER 3

DESIGN OF TEXTILE WEARABLE ANTENNA

3.1 Introduction

The main goals of this chapter are:

- To present the design cycle of low profile, small size and fully textile based wearable monopole antenna integrated with artificial magnetic conductor (AMC) structure. The proposed design covers the ISM 5.8 GHz band. Modelling and numerical analysis of the entire work were done using full-wave electromagnetic simulation software, CST Microwave Studio (MWS) [49];
- To discuss challenges of realization and characterization processes of the proposed textile wearable antennas, *i.e.*, CPW fed monopole and AMC antennas;
- To perform flexibility tests on the proposed textile wearable AMC antenna, based on numerical analysis and prototypes measurements, in order to study effects of antenna bending on the input matching and radiation characteristics of the proposed AMC antenna. Antenna bending was investigated for two bending directions: bending in E- and H- principle planes of the antenna;
- To perform flexibility tests on the proposed textile wearable AMC antenna, based on numerical analysis and prototypes measurements, in order to study effects of antenna crumpling on the input matching and radiation characteristics of the proposed AMC antenna;
- To perform numerical analysis of the proposed wearable antennas in flat form and under different bending conditions when mounted on different body models in order to discuss effects of human body loading in terms of frequency detuning and variations of antenna radiation characteristics. In addition, to give a close study on the accuracy of on body evaluation for

wearable antenna using different human body models of different compositions, geometries, and homogeneity properties;

- To present the *in-vitro* test results and a simple method in the lab to measure the robustness of the textile antennas performance in a scenario of realistic operation, the fabricated antennas were placed on the top of muscle tissue phantom;
- To consider the safety concerns and limits imposed by the standards such as IEEE C95.1-1999 [26] and the IEEE C95.1-2005 standards [25], when the proposed antennas are close to the human body. SAR assessments were carried out for the proposed wearable antennas in flat and bent forms;
- To investigate the advantages of using flexible magneto-dielectric (MD) materials and dielectric and magnetic layered substrate in wearable antenna design.

In order to reach these goals, this chapter is organized as follows:

A survey on the proposed textile antennas, in literature, integrating AMC structures is discussed in section 3.2. These textile antennas are operating within the ISM 5.8 GHz band (5.725 GHz – 5.875 GHz). Section 3.3 presents the design details and prototypes realization of the textile monopole and AMC antennas. Section 3.4 presents performance evaluation in free-space, based on numerical and measurement analysis, of monopole and AMC antennas in flat form and under structural deformation effects. Challenges during the simulation and measurement phases of the design are discussed in this section. Section 3.5 presents a discussion on the performance evaluation of the proposed wearable antennas in the presence of different human body models in flat and bent forms. Also, it discusses the results of experimental study of antennas on muscle phantom. The use of flexible MD material and dielectric and magnetic layered substrate in wearable antenna design is introduced in Section 3.6.

3.2 Background

The following is a literature survey on different textile wearable antennas that are integrating AMC reflectors. In [56], as shown in Fig. 3.1(a), the radiating element of a U-shaped wearable antenna integrating AMC structure, fabricated using stretch conductive textile, is presented. The conductive parts of the antenna and AMC were printed on a felt and denim textile materials, respectively. The -10 dB input impedance bandwidth of the integrated antenna was 13% at 5.4 GHz with an overall antenna size of $8.5 \times 8.5 \times 3.6 \text{ mm}^3$. In [57], a dual band textile antenna was designed using felt and Shieldit Super materials for the dielectric and conductive parts of the design, respectively. The AMC inclusion resulted in $90 \times 90 \times 6.51 \text{ mm}^3$, 5.12 dBi and 12% as the antenna size, gain and -10 dB input impedance bandwidth, respectively, at 5.8 GHz.

The antenna presented in [35], although possessed a light weight property, as it was implemented using dielectric cotton material, the gain of a conventional microstrip antenna at 5.4 GHz was only improved from 6.17 dBi (without AMC) to 7.25 dBi (with AMC). In addition, the design resulted in a big size of $147 \times 147 \times 6 \text{ mm}^3$. In [50], a textile hexagonal AMC shown in Fig. 3.1(b) was integrated with a CPW fed monopole antenna. The design was implemented using dielectric felt and conductive Shieldit Super textile materials with an overall size of $87 \times 77 \times 8 \text{ mm}^3$. The AMC antenna showed -10 dB input impedance bandwidth and gain of 18.1% and 5 dBi, respectively, at 5.5 GHz. It is worth mentioning that the proposed designs in [50], [56], and [35] were not evaluated in the presence of the human body or under deformation effects, which are the key issues that should be considered in wearable antenna context.

The proposed textile circular patch antenna shown in Fig. 3.2 was designed using Shieldit Super conductive sewing threads and leather material for the conductive and dielectric parts of the design, respectively [36]. Antenna miniaturization was achieved at 5.8 GHz by integrating AMC

structure. The antenna diameter/thickness was reduced from 160/7 mm without AMC to 100/3 mm with AMC. The overall size of the AMC antenna is $\pi \times (50^2)$ [area] $\times 3 \text{ mm}^3$ with input impedance bandwidth of 8.1% at 5.8 GHz. However, antenna gain at 5.8 GHz was reduced from 3.83 dBi in free-space to -0.55 dBi in the presence of a fabricated two-third muscle-equivalent phantom.

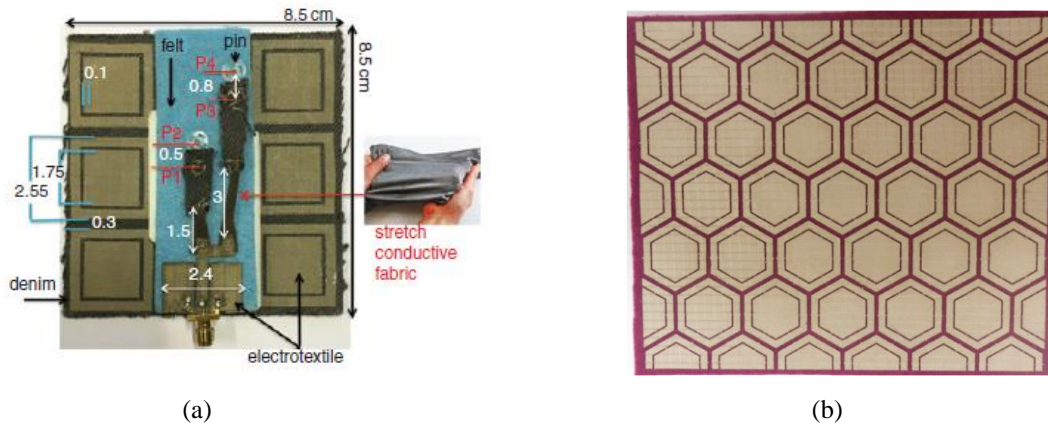


Fig. 3.1: Textile (a) stretch AMC antenna [56] and (b) hexagonal AMC structure [50].

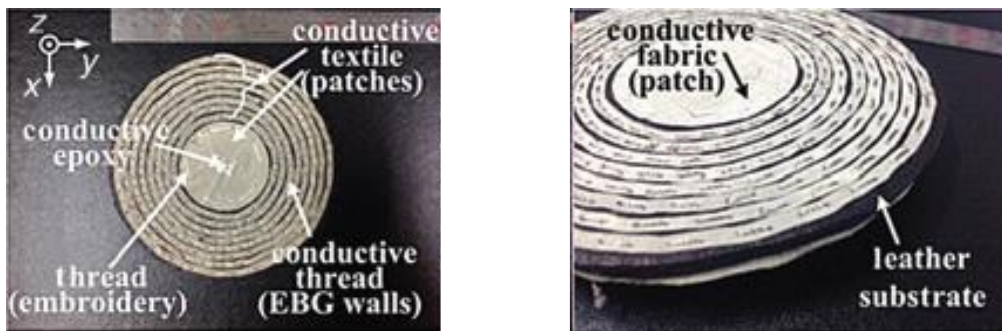


Fig. 3.2: Photograph of circular AMC textile antenna [36].

A dual band textile antenna was implemented using dielectric felt and conductive Shieldt Super materials as shown in Fig. 3.3 [58]. The inclusion of AMC reflector resulted in a low value of 10g averaged SAR of 0.03 W/kg at 5.8 GHz. The antenna measures $100 \times 100 \times 3 \text{ mm}^3$, working at 5.8 GHz with 15.4% -10 dB input impedance bandwidth and 4 dBi gain. A shift in the resonance frequency and degradation in the reflection coefficient (S_{11}) level were observed due to antenna bending in free-space. SAR levels of the proposed AMC antenna in [38] were reduced by 96.5%

for 1 g tissues and 97.3% for 10 g tissues compared to the conventional coplanar patch antenna. The antenna, as shown in Fig. 3.4(a), was realized using felt and zelt textile materials for the dielectric and conductive parts of the design, respectively. It measures $120 \times 120 \times 4.3 \text{ mm}^3$, working at 5.8 GHz. In addition, the AMC layer reduced the radiation into the body by over 10 dB and improved the antenna gain by 3 dB compared to the conventional coplanar patch antenna. However, a reduction in the antenna resonance frequency by 2% was observed due to antenna bending in E-plane direction. Similar antenna configuration was designed using conductive plate stitched on a jeans substrate, as shown in Fig. 3.4(b) [37]. The antenna working at 5.5 GHz is smaller in size measures $110 \times 110 \times 3.3 \text{ mm}^3$. However, at 5.5 GHz the antenna -10 dB input impedance bandwidth was low and of 6% value.

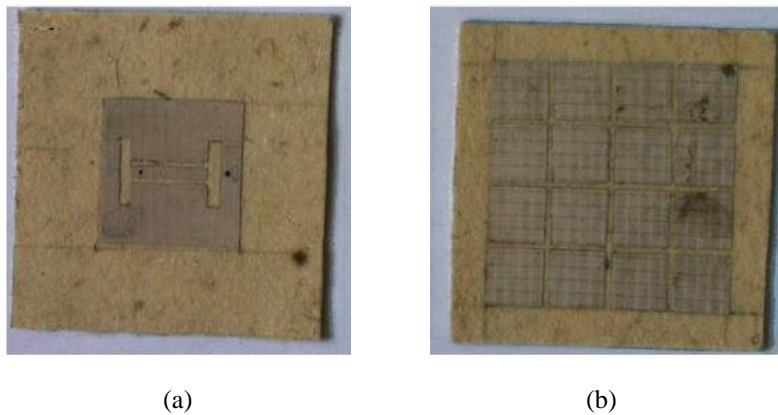


Fig. 3.3: (a) A textile slot antenna integrating (b) a square patch AMC structure [58].

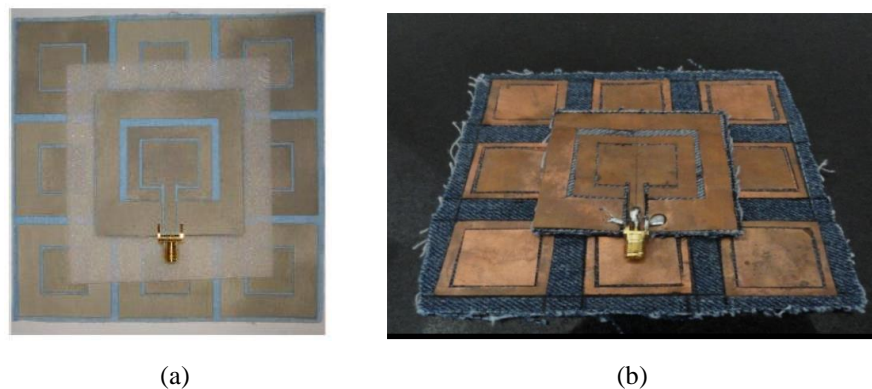


Fig. 3.4: AMC antenna using (a) felt/zelt [38] and (b) jeans/conductive plates [37].

3.3 Antenna Topology and Materials

The proposed antenna consists of a CPW fed monopole antenna with dimensions of $27 \times 34 \text{ mm}^2$. The monopole antenna was placed on an AMC layer of 4×6 units, with overall dimensions of $102 \times 68 \text{ mm}^2$. These structures were designed on a 1.8 mm -thick Pellon fabric substrate, with a relative permittivity (ϵ_r) and loss tangent ($\tan\delta_e$) of 1.08 and 0.008, respectively. A 0.08 mm -thick electro-textile, Pure Copper Taffeta from LessEMF [52] was used to fabricate the conductive layers. Its estimated conductivity (σ) is $2.5 \times 10^5 \text{ S/m}$. Geometries of the monopole antenna and AMC unit cell are based on the proposed designs in [59] and [60], respectively. By tuning the geometrical dimensions of both monopole antenna and AMC unit cell, the desired impedance matching and radiation properties of the AMC antenna were achieved in the operation ISM 5.8 GHz band.

It is worth mentioning that in order to determine the size of AMC reflector, the AMC array was increased by one row and one column at a time during the simulation phase of the antenna design. This increment was stopped until a satisfactory performance in terms of high gain, high FBR, and good impedance matching was achieved within ISM 5.8 GHz frequency band. However, a relatively small antenna size is maintained. The optimized dimensions of monopole antenna and AMC unit cell are presented in Fig. 3.5 and Fig. 3.6, respectively.

Fabrication process was performed using Silhouette® cutting machine and simple dimensioning tools. Prototypes of fabricated monopole antenna and AMC reflector are shown in Fig. 3.7. Reflection phase characterization method was used to analyze the AMC structure. In the proposed AMC unit cell, as shown in Fig. 3.8, the exact zero-reflection phase point is at 5.8 GHz. Moreover, a bandwidth of 390 MHz (5.61 GHz – 6.00 GHz) was achieved within $\pm 90^\circ$ phase values.

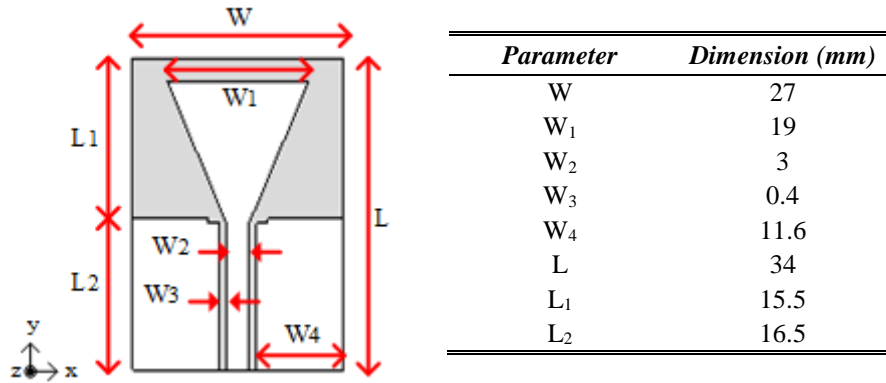


Fig. 3.5: Configuration of CPW-fed monopole antenna (right) and dimension details (left).

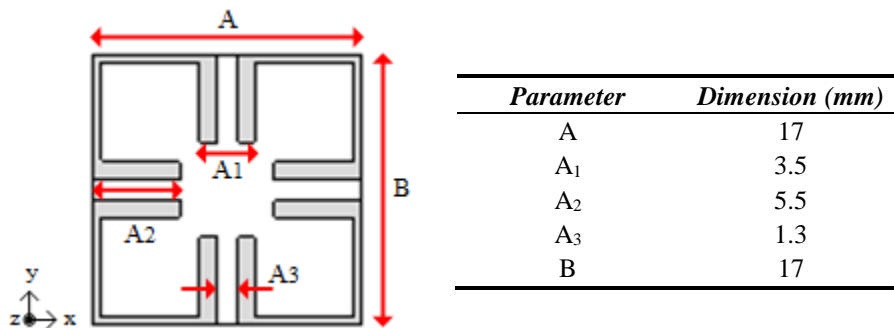


Fig. 3.6: Configuration of AMC unit cell (right) and dimension details (left).

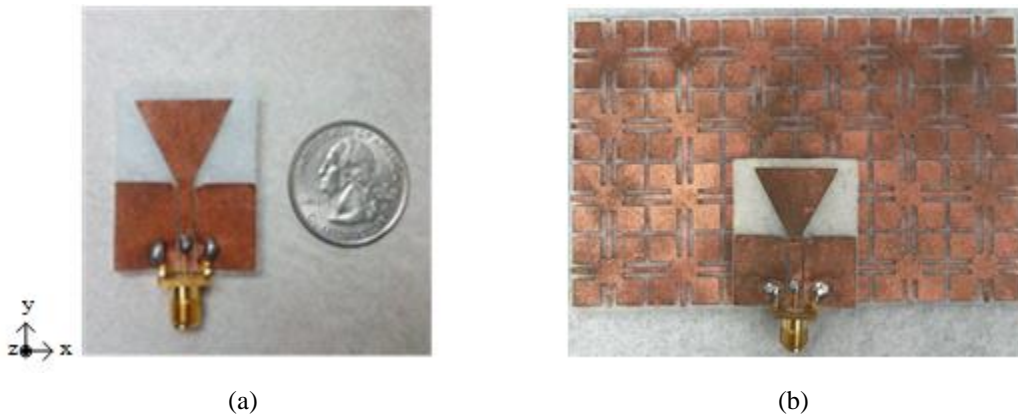


Fig. 3.7: Photograph of the fabricated (a) monopole and (b) AMC antennas.

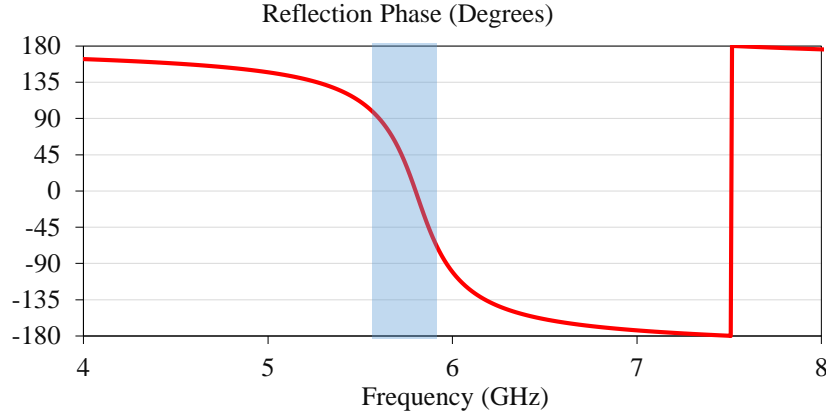


Fig. 3.8: Reflection phase diagram of AMC unit cell.

3.4 Performance of Wearable Antennas in Free-space

3.4.1 Performance of Wearable Antennas in Planar Configuration

It is worth mentioning that during the initial work on this design there was a main concern regarding discrepancies between S_{11} simulation and measurement results. Measurements showed that monopole and AMC antennas were resonating at 4.8 GHz while simulations showed 5.8 GHz, although 5.8 GHz was still within input impedance band of both antennas. After consulting with the technical support of CST Microwave Studio we found out that we did not have the right values of some of the parameters in simulations. A detailed discussion on the studied investigations can be found in Appendix A. Results shown in this chapter are based on the new corrected simulations.

S_{11} of the proposed antenna measured in free-space, without, and with AMC reflector, named as “*monopole*” and “*AMC*” antennas, respectively, as depicted in Fig. 3.9. S_{11} measurements were carried out using Keysight E5071C vector network analyzer with (300 kHz – 20 GHz) frequency operating range. The inclusion of the AMC reflector resulted in a shift in the resonance frequency (f_r) from 4.8 GHz (monopole antenna) to 4.7 GHz (AMC antenna) with a 14.47 dB decrease in the S_{11} level. On the other hand, a robust -10 dB input impedance bandwidth (4.3 GHz – 5.9 GHz) was achieved in both cases.

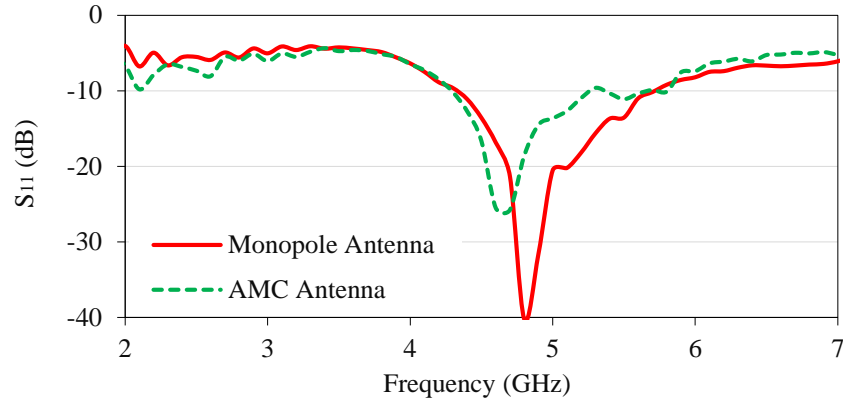


Fig. 3.9: Measured S_{11} of monopole and AMC antennas in free-space.

As shown in Fig. 3.10, simulated and measured S_{11} are compared for both antennas. In case of monopole antenna, simulated -10 dB input impedance bandwidth of (3.60 GHz – 5.95 GHz) was found to be wider than the measured bandwidth of (4.3 GHz – 5.9 GHz). On the other hand, compared to simulation results, a shift in the measured operating -10 dB input impedance bandwidth of 200 MHz toward lower frequencies was observed in case of AMC antenna. However, both antennas cover the entire ISM 5.8 GHz band (5.725 GHz – 5.875 GHz).

It's worth mentioning that difficulties were encountered during the fabrication and testing processes of textile antennas. Elastic properties of textile materials, where the variation of dimensions due to stretching and compression are typical for fabrics, can be a major source of inaccuracies. This dimension changes could lead to changes in the resonant length of the antenna and detune its frequency band. For example, the dielectric substrate height for monopole antenna was considered to be 1.8 mm in the simulation. However, when fabricated, the Pellon fabric did not give the constant thickness. The thickness of the fabric may change at different parts. In addition, during fabrication, when the electro-textile material was cut into the shape of the patch, a simple cutting machine and scissor were used. The manual cutting does not provide very clean straight edges and some threads might be fringed. Keep the constant spacing between patch surface

and the AMC layer, and cutting the precise and straight edges of the conductive elements were very challenging when fabricating the textile antenna manually. For a better result a laser cutting method can be utilized.

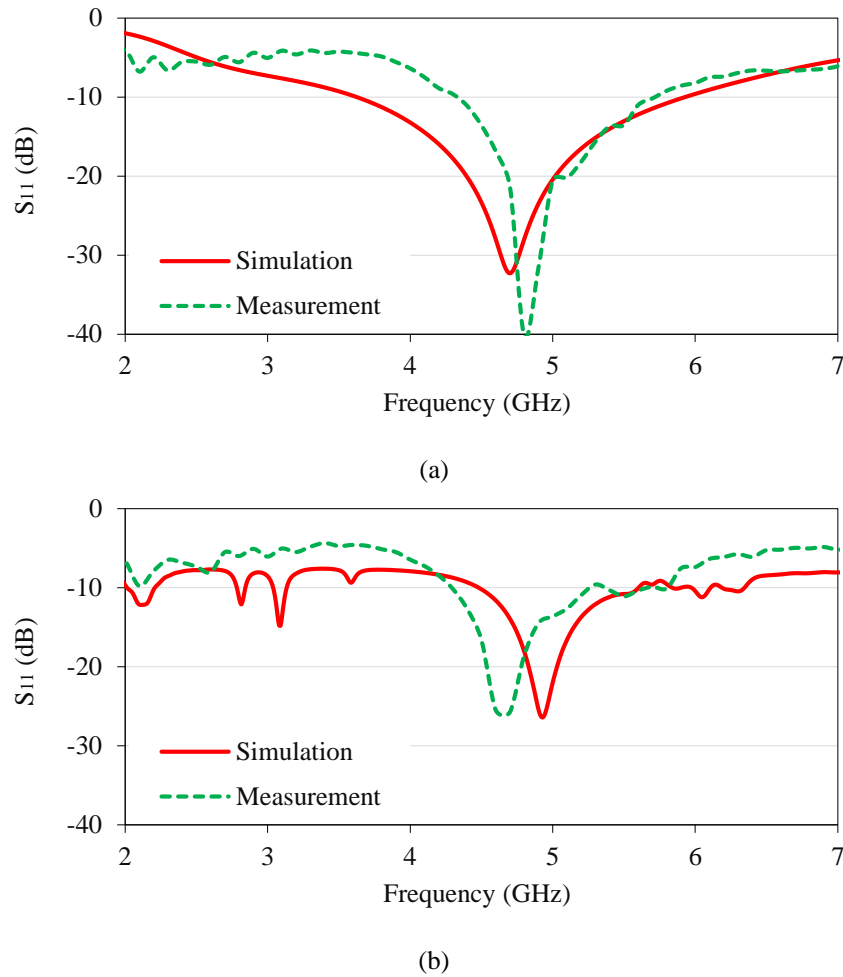


Fig. 3.10: Simulated and measured S_{11} of (a) monopole and (b) AMC antennas in free-space.

The normalized far-field radiation patterns of the principal planes, E-plane (yz -plane) and H-plane (xz -plane), were measured inside the University of North Dakota anechoic chamber with an automated antenna movement platform. Radiation patterns of monopole and AMC antennas at 5.8 GHz are depicted in Fig. 3.11 and Fig. 3.12, respectively. The measured radiation patterns in both planes as well as gain values agreed well with the simulated results, for both antennas. The monopole antenna retains a dipole like pattern in its E-plane and an omni-directional pattern in its

H-plane. In both planes, measured and simulated cross-polarization radiation levels are below -20 dB. Addition of the AMC resulted in a quasi-hemispherical radiation patterns and increase in the FBR achieved by the in-phase reflection property of the AMC structure. The measured gain for the proposed AMC antenna is 6.12 dBi compared to 2.65 dBi for the monopole antenna. The simulated gains are 3.18 dBi and 7.34 dBi for the monopole and AMC antennas, respectively.

3.4.2 Performance of AMC Antenna under Structural Deformation Effects

In a practical on-body application, the textile antenna may change its shape and dimensions due to conformability with the surface of the human body. Therefore, it is essential to study the performance of the antenna under structural deformation conditions such as bending and crumpling. In such conditions, f_r and S_{11} need to be evaluated since they are prone to change due to impedance mismatch and change in the effective electrical length of the radiating element [39]. For bending analysis, the AMC antenna was placed on a foam cylinder with a radius of 50 mm. This radius was carefully chosen to emulate the antenna conformed on an average human arm. AMC antenna bending was studied for two bending configurations, *i.e.*, antenna bending in the E-plane (around y -axis) and the H-plane (around x -axis), as shown in Fig. 3.13(a). The flexibility test setup where the bent AMC antenna was connected to the Keysight E5071C network analyzer for S_{11} measurements is shown in Fig. 3.13(b).

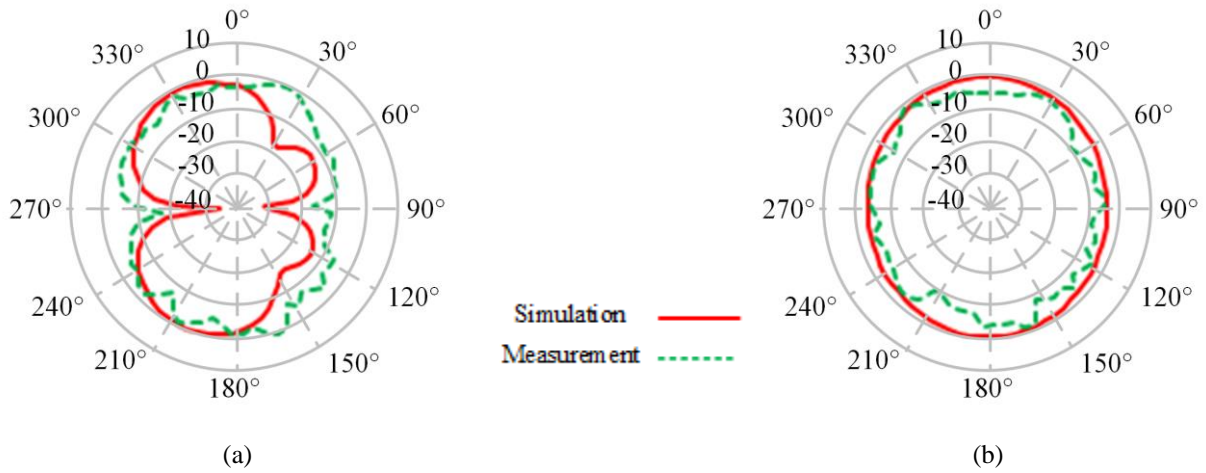


Fig. 3.11: Co-pol radiation of monopole antenna at 5.8 GHz in (a) E-plane and (b) H-plane.

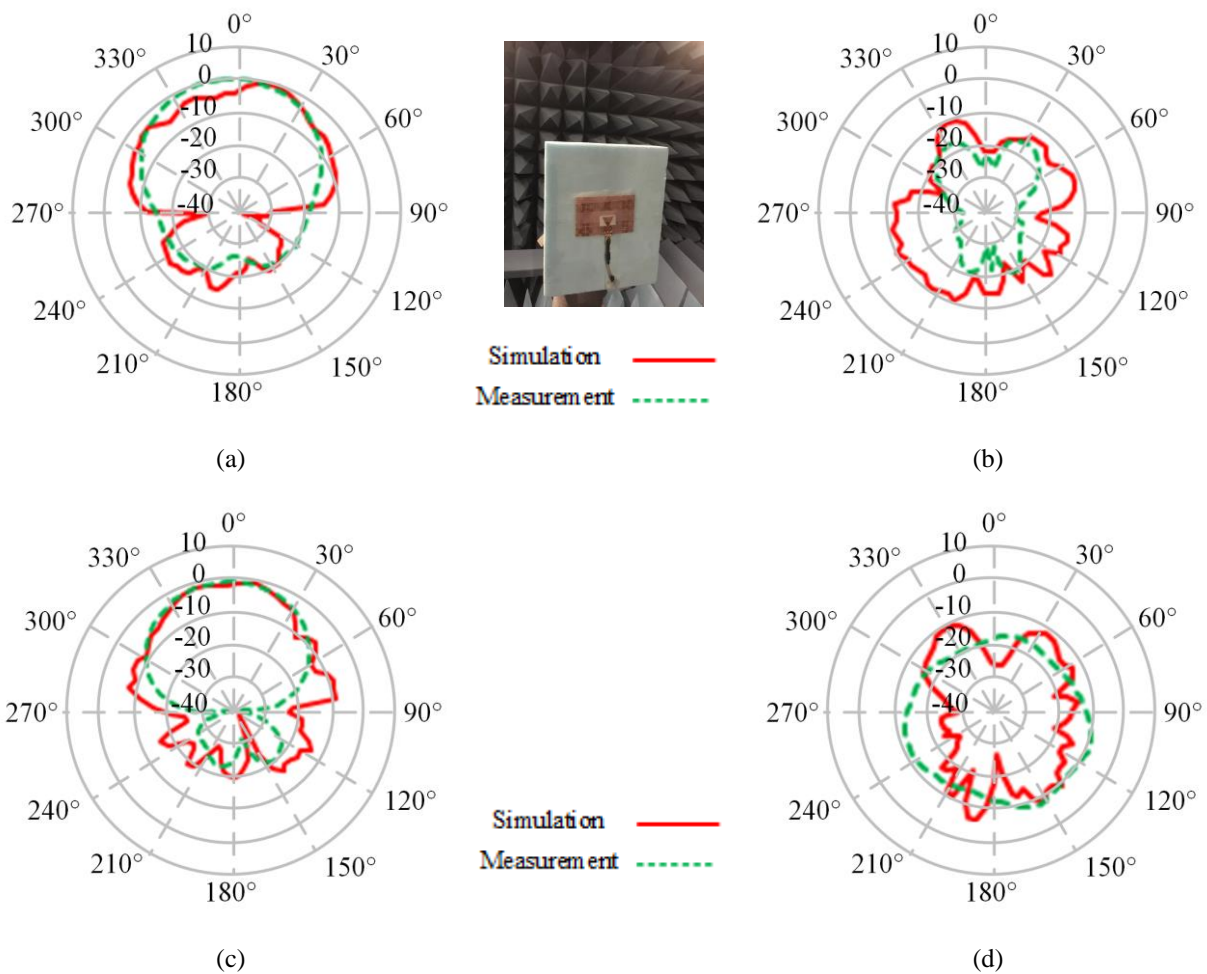


Fig. 3.12: (a) co-pol radiation in E-plane, (b) cross-pol radiation in E-plane, (c) co-pol radiation in H-plane, and (d) cross-pol radiation in H-plane of AMC antenna at 5.8 GHz.

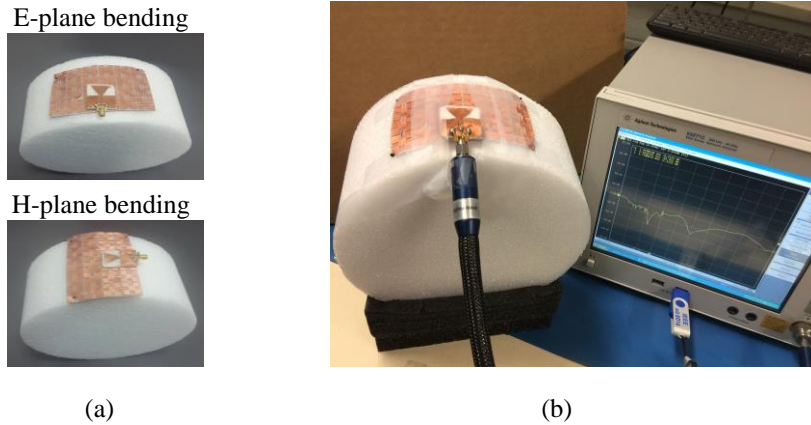


Fig. 3.13: Photograph depicting (a) bending configurations and (b) S_{11} measurement setup.

Fig. 3.14 shows S_{11} results in both bending directions. Despite our best effort, some discrepancies between simulations and measurements, particularly in case of E-plane bending, exist. This may be due to fabrication inaccuracy discussed earlier, as well as the antenna misalignments, which are unavoidable, since it is impossible to reach an ideal uniformity of the bending radius across the antenna structure as accurate as in simulations [61]. Bending AMC antenna in E-plane direction caused a slight f_r shift, of order of 10 MHz, to a lower frequency, within frequency band of interest. On the other hand, more stable f_r was observed in case of E-plane bending. Both bent antennas retained their -10 dB input impedance bandwidth as achieved in the flat AMC antenna. Variations in the radiation characteristics of the AMC antenna due to bending conditions at 5.8 GHz are summarized in Table 3.1. These results are based on simulation, and they show that antenna's radiation characteristics are sensitive to both E- and H-plane bending, causing a reduction in the antenna gain and FBR. In addition, due to bending conditions, changes in the radiation patterns were observed.

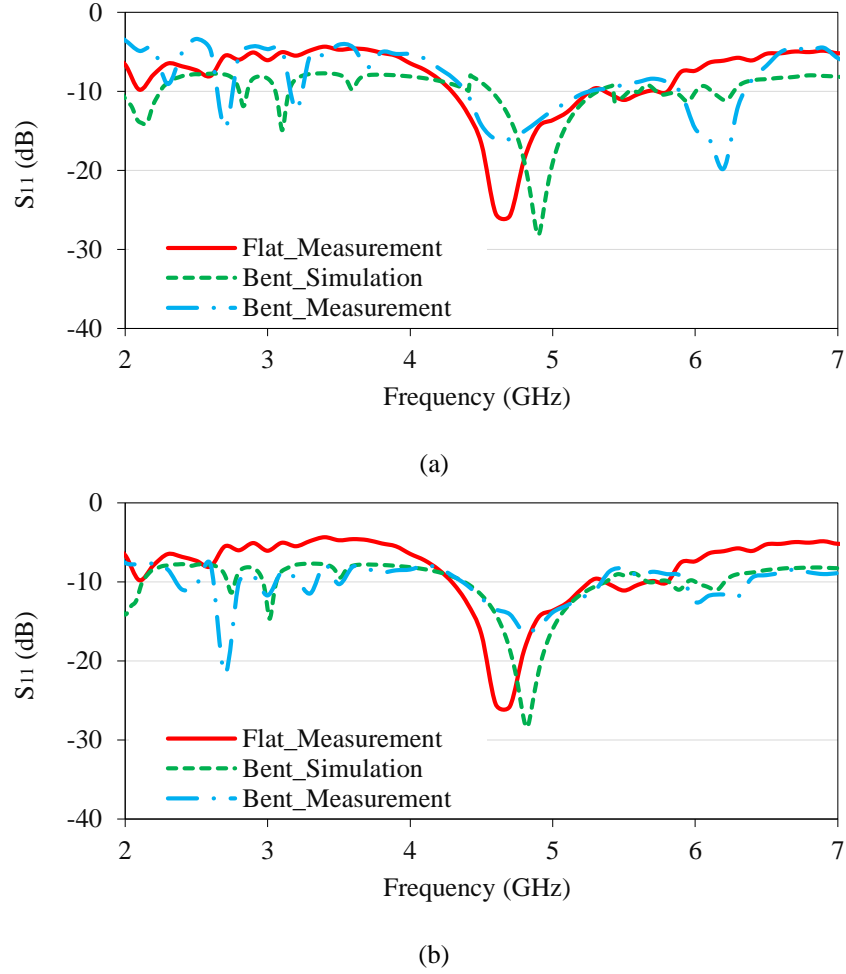


Fig. 3.14: S_{11} results of bent AMC antenna in (a) E-plane and (b) H-plane directions.

Table 3.1: Radiation characteristics summary of AMC antenna at 5.8 GHz.

<i>Scenario</i>	<i>Gain (dBi)</i>	<i>HPBW^a: E-plane</i>	<i>HPBW: H-plane</i>	<i>FBR (dB)</i>
Flat	7.53	46.70	26.70	27.75
E-plane bending	4.18	44.30	39.50	17.87
H-plane bending	6.36	54.90	29.10	17.04

^aHPBW given in degrees.

For crumpling analysis, the crumpling profile was defined by the crumple depth (N) and the peak distance between the two troughs (M). In this study, N is chosen to be 6 mm and M is chosen 31 mm and 24 mm, for crumpling cases 1 and 2, respectively, as shown in Fig. 3.15(a). The crumpling profiles were manufactured using foam material. In measurements, the AMC antenna

was crumpled in the H-plane direction (along x -axis). As depicted in Fig. 3.15(b), a shift in f_r and a wider -10 dB input impedance bandwidth were observed with a good impedance matching within frequency band of interest.

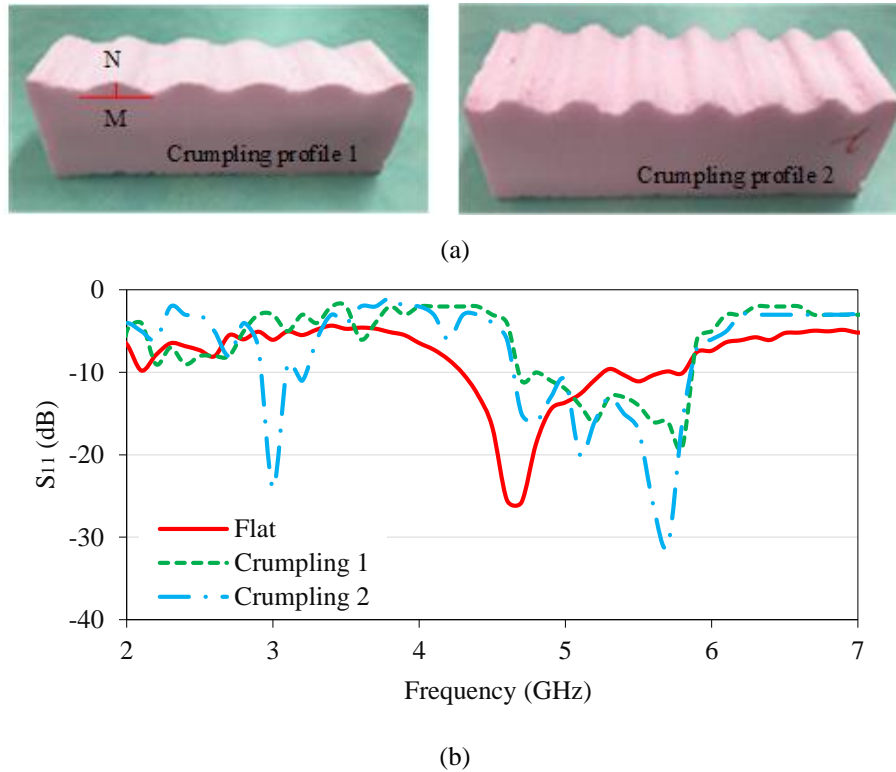


Fig. 3.15: (a) Crumpling profiles and (b) S_{11} measurement results of crumpled AMC antenna.

3.5 Performance of Wearable Antennas on Human Body Models

To validate the on-body performance and investigate effects of human body loading on the proposed antennas, we performed full-wave simulations using monopole and AMC antennas in the vicinity of three different human body models. First, we used a body model of averaged human arm phantom properties of $\epsilon_r = 21.2$ and $\sigma = 3.38$ S/m, at 5.8 GHz [62]. Second, a multilayer human tissue model was employed to mimic the human arm. This model consists of four layers representing skin, fat, muscle, and bone. Properties of dispersive tissue layers were obtained from the material library in CST MWS. Finally, the proposed antennas placed on the arm of Ella voxel

model. These body models are named “*BM_equivalent*”, “*BM_layered*”, and “*Ella*”, respectively. Since the antennas may be bent and worn on the user’s arm, their performance on the proposed human body models was studied under two bending configurations in addition to the flat one: bending in the E- and H-planes.

For this purpose, we designed *BM_equivalent* and *BM_layered* body models in cubic and cylindrical forms, respectively. The total size of the cubic tissue body model is $177.2 \times 177.2 \times 50$ mm^3 (length \times width \times depth), which is equivalent in volume to the cylindrical tissue body model that has 200 mm height and 50 mm radius. The numerical setups for the different human body models are shown in Fig. 3.16. The same cylindrical topology was used when antennas bent around *Ella*’s arm, as shown in Fig. 3.16(e). To reduce the simulation time, a reasonably sized portion of *Ella*’s arm (sectional area of about the same size as other models) was selected for simulation, instead of simulating the antenna on the entire numerical body model. In all studied scenarios, antennas were separated from the skin layer by an additional layer of Pellon fabric of 1.8 mm thickness to account for clothing.

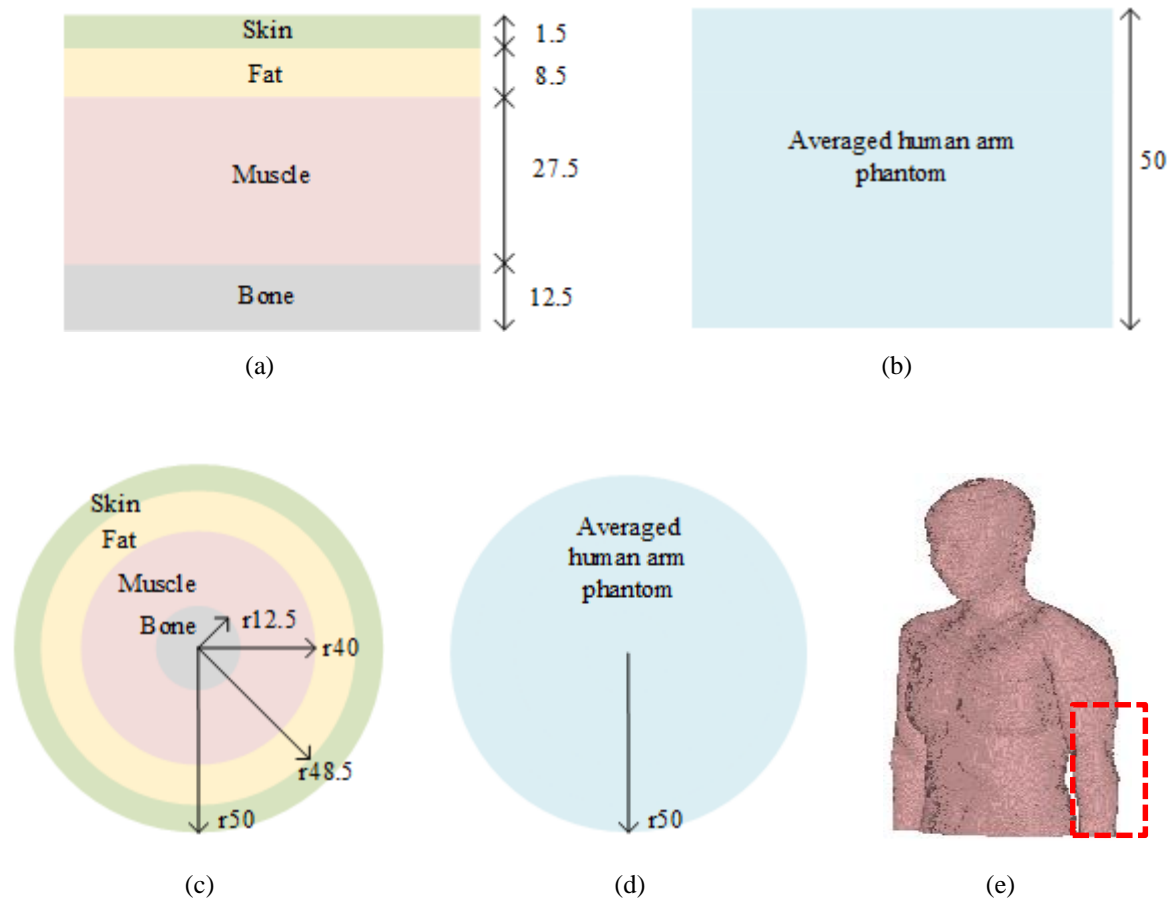
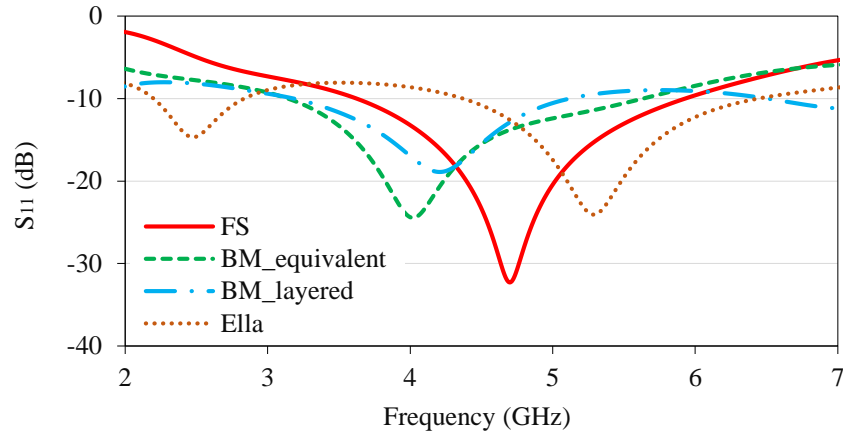


Fig. 3.16: Cross sections (a) Cubic BM_layered, (b) Cylindrical BM_layered, (c) Cubic BM_equivalent, (d) Cylindrical BM_equivalent, and (e) Ella; dimensions are in *mm*.

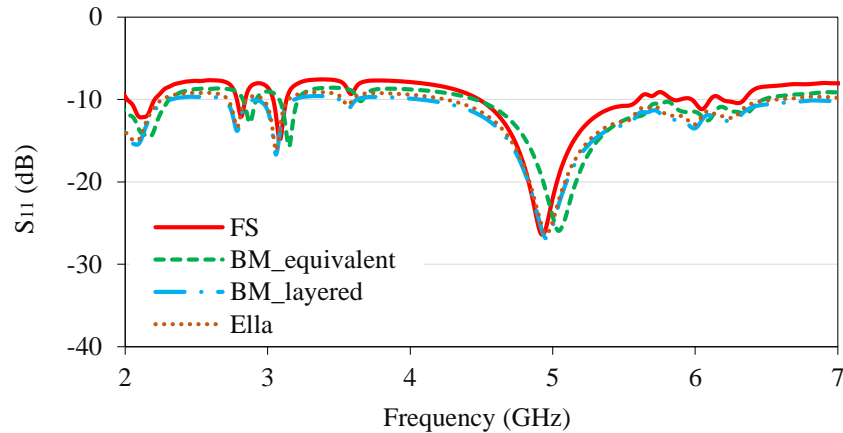
3.5.1 Performance of Wearable Antennas in Planar Configuration

A comparison between antennas' performances, *i.e.*, monopole and AMC antennas, in free-space and on the body models, while antennas are in flat form, is presented in this subsection. Simulation results for S_{11} are shown in Fig. 3.17. In the case of monopole antenna, similar loading effects due to different human body models were observed. These effects are frequency detuning toward lower frequencies, and a reduction in the -10 dB input impedance bandwidth, compared to the free-space case. The detuning of frequency is due to the high dielectric constant values of various tissues that are considered in the human body models. The maximum shift in the resonant frequency was observed in the case of BM_equivalent body model, from 4.70 GHz (in free-space)

to 4.10 GHz (on body). While the maximum bandwidth reduction was observed in the case of BM_layered body model from the bandwidth of 3.60 GHz – 5.95 GHz (in free-space), to the bandwidth of 3.18 GHz – 5.10 GHz (on body).



(a)



(b)

Fig. 3.17: Simulated S_{11} of flat (a) monopole and (b) AMC antennas.

On the other hand, as shown in Fig. 3.17(b), AMC antenna showed a robust impedance matching characteristics, compared to monopole antenna. However, a slight bandwidth broadening within frequency band of interest was observed, when it was placed on the Ella body model. Radiation characteristics summary, *i.e.*, antenna gain, HPBW, and FBR are given in Table 3.2 at 5.8 GHz. For monopole antenna, placing antenna on different human body models caused an

improvement in the antenna gain and FBR, and a reduction in the HPBW. In contrast, with the presence of AMC structure stable results and improvement in the FBR were observed.

Table 3.2: Radiation characteristics summary for flat antennas at 5.8 GHz.

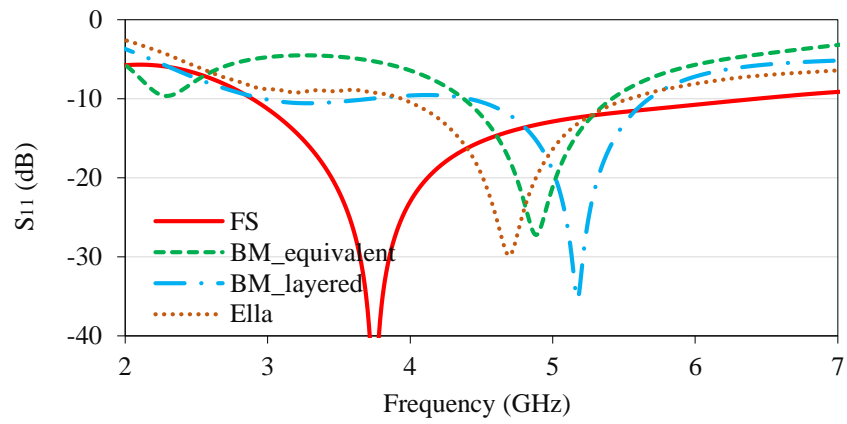
<i>Scenario</i>	<i>Gain (dBi)</i>	<i>HPBW^a: E-plane</i>	<i>HPBW: H-plane</i>	<i>FBR (dB)</i>
<i>Monopole Antenna</i>				
FS ^b	3.18	54.10	165.60	12.70
BM_equivalent ^c	5.00	44.00	89.30	29.05
BM_layered ^d	5.85	42.40	71.50	36.94
Ella	6.05	50.20	85.50	33.53
<i>AMC Antenna</i>				
FS	7.34	48.50	28.60	27.57
BM_equivalent	8.29	45.90	25.30	44.88
BM_layered	8.15	45.30	24.70	41.39
Ella	7.89	44.78	23.65	26.86

^aHPBW given in degrees, ^bFree-space (FS), ^cEquivalent human body model (BM_equivalent), and ^dLayered human body model (BM_layered).

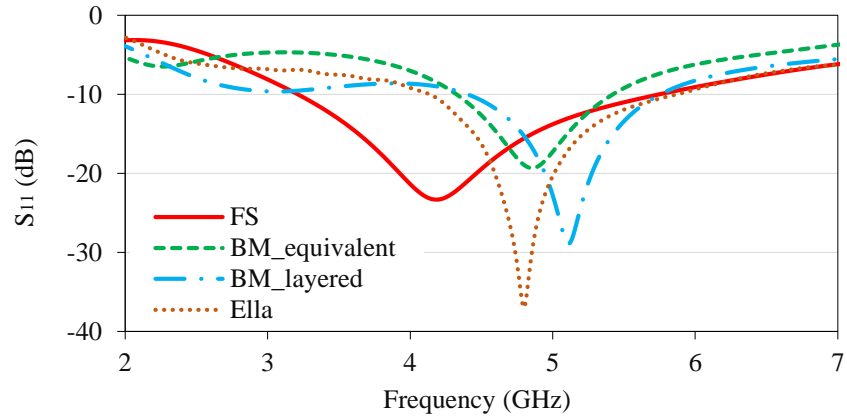
3.5.2 Performance of Wearable Antennas in Bending Configuration

For comparison purposes, results of antennas bending in free-space condition are presented to examine the impact of human body loading on the bent antennas. S_{11} results are shown in Fig. 3.18 and Fig. 3.19 for monopole and AMC antennas, respectively. In general, the impact of human body loading on the bent monopole antenna, in both directions, was similar. A shift in the resonant frequency toward higher values, as well as a reduction in the impedance bandwidth were observed. The monopole antenna was prone to bending. On the contrary, with the presence of AMC structure, the antenna retained its impedance matching properties with a slight detuning of the resonant frequency. Therefore, AMC provides a good insulation layer. Radiation characteristics of monopole and AMC antenna for all the studied bending configurations are summarized in Table 3.3 at 5.8 GHz. In the case of monopole antenna, the presence of different body models resulted in improvement in the antenna gain and FBR and reduction in the HPBW. On the other hand,

stable results with improvement in the FBR were observed in case of AMC antenna.

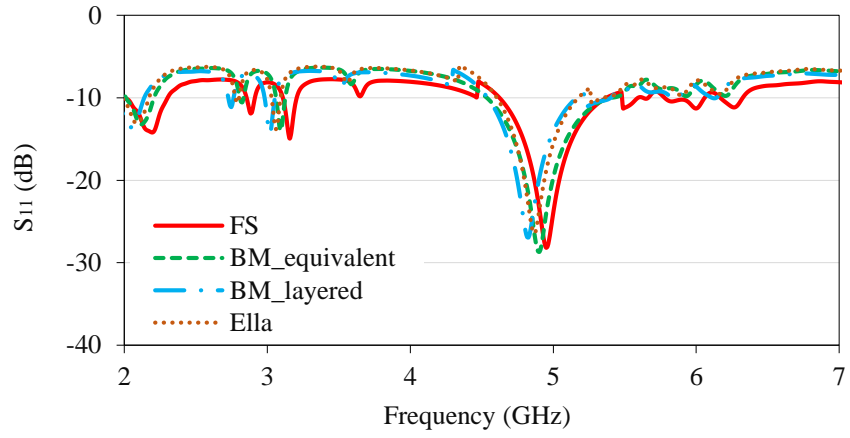


(a)

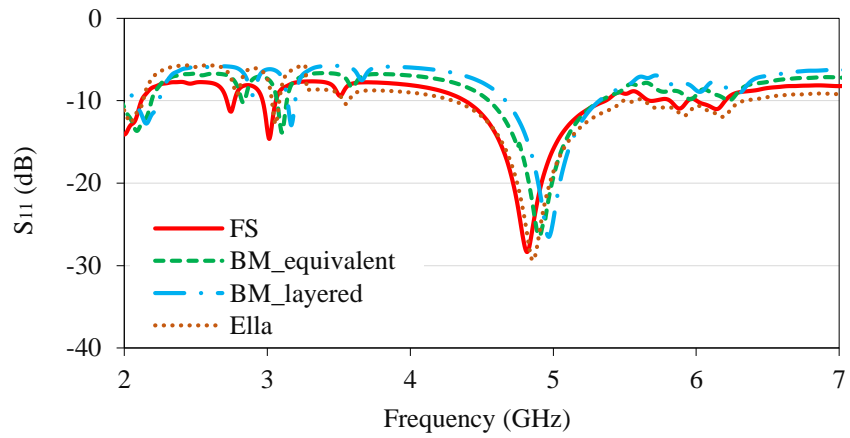


(b)

Fig. 3.18: Simulated S_{11} of bent monopole antenna in (a) E-plane and (b) H-plane directions.



(a)



(b)

Fig. 3.19: Simulated S_{11} of bent AMC antenna in (a) E-plane and (b) H-plane directions.

Table 3.3: Radiation characteristics summary for bent antennas at 5.8 GHz.

<i>Scenario</i>	<i>Gain (dBi)</i>	<i>HPBW^a: E-plane</i>	<i>HPBW: H-plane</i>	<i>FBR (dB)</i>
<i>Monopole Bending in E-plane</i>				
FS ^b	2.98	55.50	146.4	5.66
BM_equivalent ^c	3.81	45.20	108.20	26.13
BM_layered ^d	4.69	43.40	91.00	37.26
Ella	3.98	40.32	96.36	29.68
<i>Monopole Bending in H-plane</i>				
FS	3.90	53.20	134.6	5.81
BM_equivalent	4.33	44.30	82.30	35.66
BM_layered	4.90	48.50	83.80	22.16
Ella	4.89	43.36	93.96	10.46
<i>AMC Bending in E-plane</i>				
FS	4.05	45.10	40.30	19.40
BM_equivalent	4.39	48.00	40.40	21.68
BM_layered	4.22	43.50	40.50	21.66
Ella	4.36	30.96	39.90	20.36
<i>AMC Bending in H-plane</i>				
FS	5.40	56.60	31.00	18.83
BM_equivalent	5.29	52.00	29.70	33.82
BM_layered	6.29	53.50	29.70	25.20
Ella	5.96	53.97	28.64	17.68

^aHPBW given in degrees, ^bFree-space (FS), ^cEquivalent human body model (BM_equivalent), and ^dLayered human body model (BM_layered).

3.5.3 SAR Validation

The SAR level of wearable antenna must be validated in the antenna design stage to ensure conformance to safety regulations. Moreover, SAR was utilized in order to address the health risks imposed by wearable antennas to the human body. Hence, the radiofrequency energy absorbed by human tissues should not exceed critical values of 1.6W/kg for any 1 g tissue or 2W/kg for any 10 g tissue according to the guidelines of the IEEE C95.1-1999 [26] and the IEEE C95.1-2005 standards [25], respectively. SAR was calculated based on the root mean square (rms) of the electric field strength inside the human body and the human body tissue properties such as conductivity and mass density [63]. Researchers have been using the numerical evaluation of SAR

as the mean of design validation due to the equipment scarcity and costs involved in experimentally evaluated SAR. In the area of textile antennas, such simulations have been shown to agree well with measurements [64].

A series of numerical SAR investigations based on mass-averaged method were performed using IEEE C95.1 standard provided in the CST MWS software. The input power to the antennas for SAR calculations was set at 1 W (rms). The calculated SAR results are summarized in Table 3.4 for monopole and AMC antennas located on different body models in flat form and under different bending conditions. For 10 g SAR analysis, despite the use of three different body models of different tissue composition, the obtained SAR values of the proposed antennas (individually) in flat form and under bending effects were comparable. This suggests that for the proposed antennas; 10 g SAR analysis was less sensitive to antenna deformation and shape and body tissue composition. Same discussion can be applied to 1 g SAR analysis of monopole antenna.

On the other hand, in case of AMC antenna, 1 g SAR values showed sensitivity to bending conditions. The minimum 1 g SAR value of 0.37 W/Kg was achieved due to AMC antenna E-plane bending on Ella model and the maximum value was observed due to AMC antenna H-plane bending on Ella model. It is worth mentioning that the body models surface area was larger than that for the monopole antenna. For example, the surface area of the BM_layered body model in a cubic form was about 51 times the surface area of the monopole antenna. Most importantly, all evaluated SAR values for the AMC antenna were far below the regulated SAR thresholds, while this was not true for the monopole antenna. The reason could be in the fact that monopole antenna provides an omnidirectional pattern while the AMC antenna has a directive radiation characteristic. SAR analysis demonstrated the superiority of the AMC antenna for operation in close proximity to the human body. Thus, it can be concluded that maintaining the SAR values within the regulated

levels will not be an issue for future applications of the proposed AMC antenna.

Table 3.4: SAR analysis summary of antennas at 5.8 GHz.

<i>Scenario</i>	<i>1 g Tissue (W/Kg)</i>	<i>10 g Tissue (W/Kg)</i>
<i>Flat Monopole Antenna</i>		
BM_equivalent ^a	47.26	12.59
BM_layered ^b	48.59	11.90
Ella	45.97	13.19
<i>Monopole Antenna Bent in E-plane</i>		
BM_equivalent ^a	49.05	11.32
BM_layered ^b	48.61	10.56
Ella	46.23	12.35
<i>Monopole Antenna Bent in H-plane</i>		
BM_equivalent ^a	45.42	14.17
BM_layered ^b	47.88	11.60
Ella	48.32	11.89
<i>Flat AMC Antenna</i>		
BM_equivalent ^a	0.60	1.18
BM_layered ^b	0.61	1.49
Ella	0.56	1.18
<i>AMC Antenna Bent in E-plane</i>		
BM_equivalent ^a	0.59	1.64
BM_layered ^b	0.37	1.76
Ella	0.53	1.54
<i>AMC Antenna Bent in H-plane</i>		
BM_equivalent ^a	0.93	1.77
BM_layered ^b	0.88	1.40
Ella	0.97	1.32

^aEquivalent human body model (BM_equivalent), and ^bLayered human body model (BM_layered).

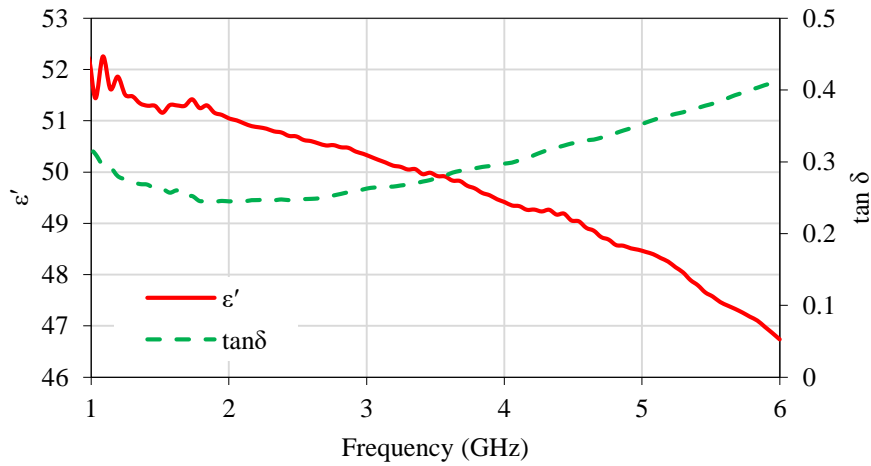
3.5.4 Experimental Analysis of Antennas Performance on Body Phantom

In order to get an initial insight into the human body loading effects in a scenario of realistic operation, the fabricated antennas were placed on the top of muscle tissue phantom. A cylindrical container of 45 mm radius and 25 mm length was filled with the muscle tissue phantom as shown in Fig. 3.20(a). The details of phantom preparation can be found in [65]. The dielectric constant and loss tangent of muscle tissue phantom were measured using Keysight 85070E high-

performance dielectric probe, for frequency range of 1 GHz – 6 GHz. Results are shown in Fig. 3.20(b), where $\epsilon' = \epsilon_r \epsilon_0$.



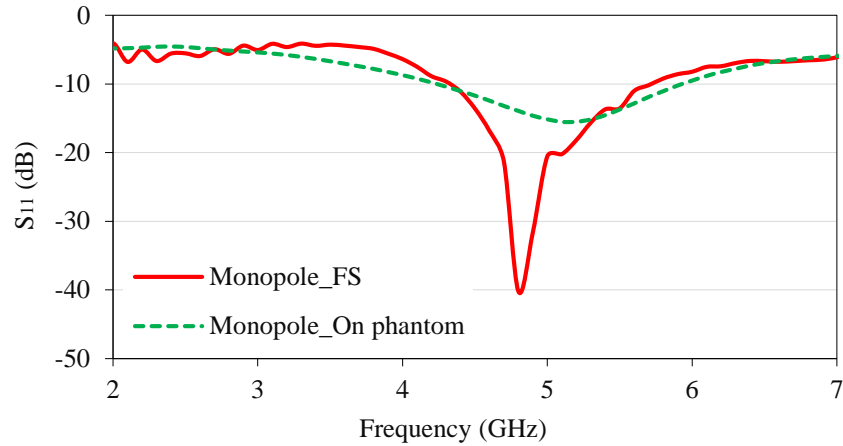
(a)



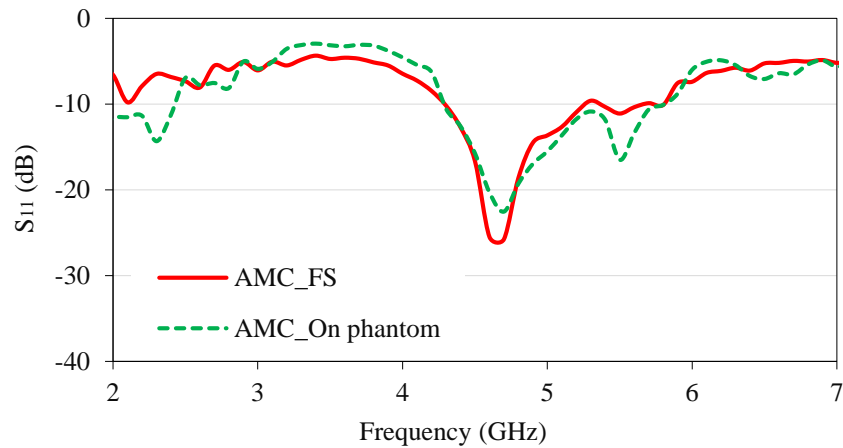
(b)

Fig. 3.20: Muscle phantom dielectric property measurements; (a) setup and (b) results.

As can be seen in Fig. 3.21(a), the presence of muscle phantom caused a 400 MHz shift in the resonant frequency toward a higher value, in addition to about 25 dB increase in the S_{11} level, for the monopole antenna. On the other hand, in the presence of the AMC reflector, the antenna was able to maintain a good impedance matching when positioned on muscle tissue phantom as shown in Fig. 3.21(b).



(a)



(b)

Fig. 3.21: Measured S_{11} of flat (a) monopole and (b) AMC antennas on body phantom.

3.6 Application of Magneto-Dielectric Material in Wearable Antenna Design

3.6.1 Background

The knowledge of the electric and magnetic properties of materials over a broadband frequency range is an essential requirement for accurate modeling and design in several engineering applications. Such applications span printed circuit board design, electromagnetic shielding, biomedical research and determination of EM radiation hazards [66]. The electric and magnetic properties of materials usually depend on several factors: frequency, temperature,

linearity, isotropy, homogeneity, and so on. In particular, the antenna response is affected by the frequency dependent permittivity and permeability of the material. The dispersive behavior exhibited by these materials can be represented by a complex permittivity and magnetic permeability which depend on frequency as [67]:

$$\begin{aligned}\varepsilon(\omega) &= \varepsilon'(\omega) - j\varepsilon''(\omega) \\ \mu(\omega) &= \mu'(\omega) - j\mu''(\omega)\end{aligned}\tag{3.1}$$

being ω the angular frequency, ε' and μ' are the real parts, and ε'' and μ'' are the imaginary parts of the complex electric permittivity and magnetic permeability, respectively. The real part takes the ability of the medium to store electrical (or magnetic) energy into account, the imaginary part describes the dielectric (or magnetic) energy losses. The complex permittivity is used to describe the interaction of a material in the presence of an external electric field, such material is called dielectric material, *i.e.*, glass. On the other hand, the complex permeability is used to characterize the interaction of a material in the presence of an external magnetic field, such material is called magnetic material, *i.e.*, nickel. Another way to construct permittivity and permeability of a given material is in terms of the electric and magnetic loss tangents given as [67]:

$$\begin{aligned}\tan \delta_e &= \frac{\varepsilon''}{\varepsilon'} \quad , \quad \varepsilon = \varepsilon_r \varepsilon_0 (1 - j \tan \delta_e) \\ \tan \delta_m &= \frac{\mu''}{\mu'} \quad , \quad \mu = \mu_r \mu_0 (1 - j \tan \delta_m)\end{aligned}\tag{3.2}$$

where ε_r and μ_r are relative permittivity and permeability of the medium, respectively, ε_0 and μ_0 are free-space permittivity and permeability, respectively, and $\tan \delta_e$ and $\tan \delta_m$ are electric and magnetic loss tangents of the medium, respectively.

Magneto-dielectric (MD) materials are another type of materials that exhibit both magnetic as well as dielectric properties at the same time. Such materials are not available readily in nature and need to be realized through material synthesis. Examples of MD materials in microwave

frequencies reported by literature are listed in Table 3.5 along with their properties. Details on material preparation and methods of measurement can be found in the mentioned references.

Table 3.5: Examples of MD materials reported in literature [68] - [69].

<i>Ref.</i>	<i>Dielectric Properties</i>	<i>Magnetic Properties</i>	<i>Frequency</i>
[68]	$\epsilon_r = 4, \tan \delta_e = 0.02$	$\mu_r = 3.5, \tan \delta_m = 0.04$	(300 - 700) MHz
[70]	$\epsilon_r = 3.5, \tan \delta_e = 0.001$	$\mu_r = 5.5, \tan \delta_m = 0.01$	(400 - 1000) MHz
[71]	$\epsilon = 4.81 - j0.06$	$\mu = 4.88 - j0.18$	400 MHz
[71]	$\epsilon = 6.51 - j0.9$	$\mu = 2.8 - j0.16$	400 MHz
[69]	$\epsilon = 3.5 - j0.15$	$\mu = 4 - j0.2$	(100 - 700) MHz
[72]	$\epsilon = 7.678 - j0.000689$	$\epsilon = 1.1634 - j0.065$	Complex permittivity at 10 GHz Complex permeability at 9.86 GHz

Considerable efforts have been devoted toward development of MD materials in antenna design. MD material has been used for microstrip antenna miniaturization [73]. As shown in Fig. 3.22, initially a conventional microstrip antenna with the high-permittivity dielectric superstrate was designed. Then, using a periodic structure of metallic patches, acting as an AMC, the antenna size was reduced. Furthermore, another size reduction method was achieved using MD material. MD material both relative permeability and permittivity are assumed to be $\mu_r = \epsilon_r = 10$. A performance summary of the proposed microstrip antenna configurations is listed in Table 3.6.

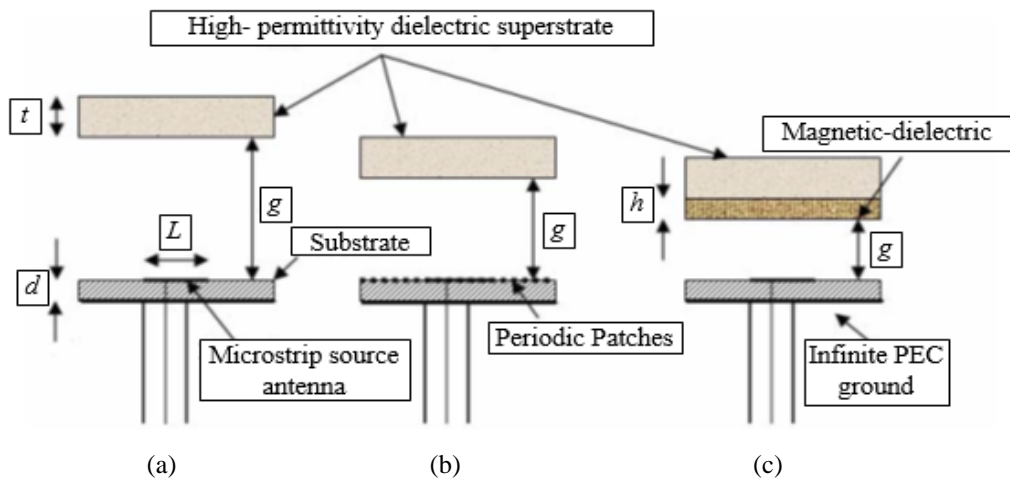


Fig. 3.22: Microstrip antenna with (a) superstrate, (b) AMC ground, and (c) MD material [73].

Table 3.6: Performance summary of proposed microstrip antenna configurations [73].

<i>Scenario</i>	<i>Air-gap height (g) (mm)</i>	<i>f_r^a (GHz)</i>	<i>Antenna gain (dBi)</i>
Antenna with superstrate	18.9	7.280	15.15
Antenna with AMC ground plane	12.5	7.275	14.64
Antenna with MD material	8.9	7.240	14.15

^aResonance frequency.

Another example is presented in [74], where MD material was used for enhancing the isolation performance, thus, reducing the mutual coupling of a folded monopole antenna array for multiple-input, multiple-output (MIMO) applications. As shown in Fig. 3.23, the single antenna occupies a compact volume of $7.5 \times 18.5 \times 3.4 \text{ mm}^3$ was integrated with the main antenna substrate made of FR-4 material and a supporter made of MD material. The parameters of the MD material were $\epsilon' - j\epsilon'' = 3.29 - j0.09$ and $\mu' - j\mu'' = 2.01 - j0.38$ at 780 MHz. A performance summary of the proposed antenna system is listed in Table 3.7 for the cases antennas with/without MD supporter. A good impedance matching was achieved and the isolation performance between two antennas was improved by adding MD material.

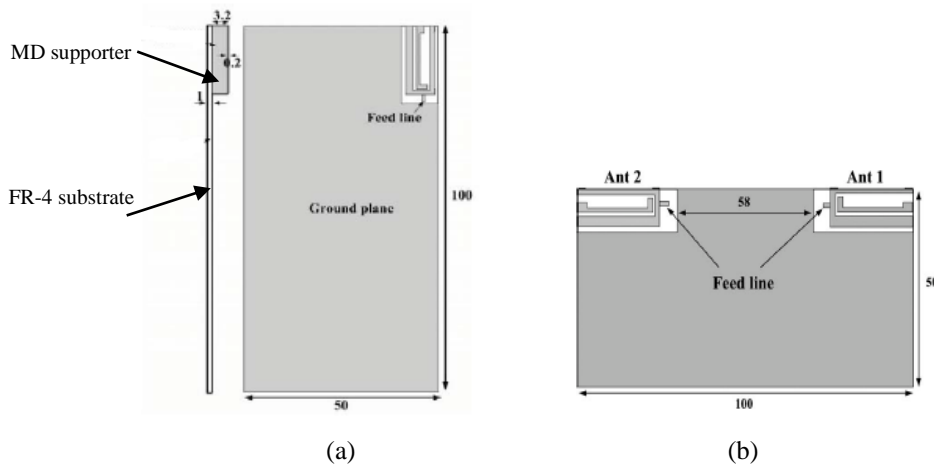


Fig. 3.23: (a) Side and top views of single antenna and (b) antenna array [74].

Table 3.7: Performance summary of proposed antenna array system [74].

<i>Scenario</i>	<i>Bandwidth (MHz)</i>	<i>Mutual coupling^a (dB)</i>	<i>Radiation efficiency^a (%)</i>
Antennas with MD	18.9	7.280	15.15
Antennas without MD	8.9	7.240	14.15

^aMeasured at 790 MHz.

New materials always raise the hope that the fundamental limitations, *i.e.*, human body loading and structural deformation effects on wearable antennas might be abrogated. However, the current state of the art in wearable antenna design leaves much to be desired. In this section, the design of a wearable monopole antenna using flexible MD material is presented.

3.6.2 Antenna Topology and Materials

Different monopole antenna configurations were studied. First, the monopole antenna discussed in Section 2.3 was designed using dielectric substrate made of Pellon fabric with a thickness of 3.6 mm, $\epsilon_r = 1.08$, and $\tan\delta_e = 0.008$. Second, the antenna was then backed with AMC structure discussed in Section 2.3 acting as a ground plane printed on 1.52 mm thick RO3003 flexible material with $\epsilon_r = 3$ and $\tan\delta_e = 0.0013$. Third, the dielectric material was replaced by MD material with a thickness of 3.6 mm, $\epsilon_r = \mu_r = 4$, and $\tan\delta_e = \tan\delta_m = 0.008$.

3.6.3 Performance of Antennas in Planar Configuration

Performances of the studied antennas were evaluated at 2.45 GHz as summarized in Table 3.8 and Fig. 3.24. It can be observed that using MD material in the antenna design did not improve the antenna gain that much. In addition, it resulted in a reduction in the antenna -10 dB input impedance bandwidth compared to the antenna on a dielectric layer. However, the integration of a ground plane (GP) of copper material at a distance of 4 mm away from antenna, which was designed using MD substrate, showed an improvement in the antenna gain comparable to that obtained using AMC structure. Moreover, a higher -10 dB input impedance bandwidth value was

achieved compared to the antenna integrated AMC structure. In order to verify that the addition of the GP has in fact superior effects when the antenna design was based on MD material, another scenario was studied while integrating the GP with the antenna on a dielectric layer. Results demonstrated that the antenna gain did not improve as much as antenna on MD layer. In addition, the -10 dB input impedance bandwidth shifted out of band of interest.

Table 3.8: Performance comparison of studied antennas at 2.45 GHz.

<i>Antenna Topology</i>	<i>Size (mm²)</i>	<i>Gain (dB)</i>	<i>B.W.^a</i>
Monopole, Dielectric	32×57	2.447	2.59 GHz
AMC Antenna	124×124	8.410	40 MHz
Monopole, MD ^b	32×57	2.487	1.05 GHz
Monopole, MD, GP ^c	84×107	8.120	350 MHz
Monopole, Dielectric, GP	84×107	3.671	NA ^d

^a Bandwidth (B.W.), ^b Magneto-Dielectric (MD), ^c Ground Plane (GP), and ^d Antenna does not show a -10 dB S_{11} value.

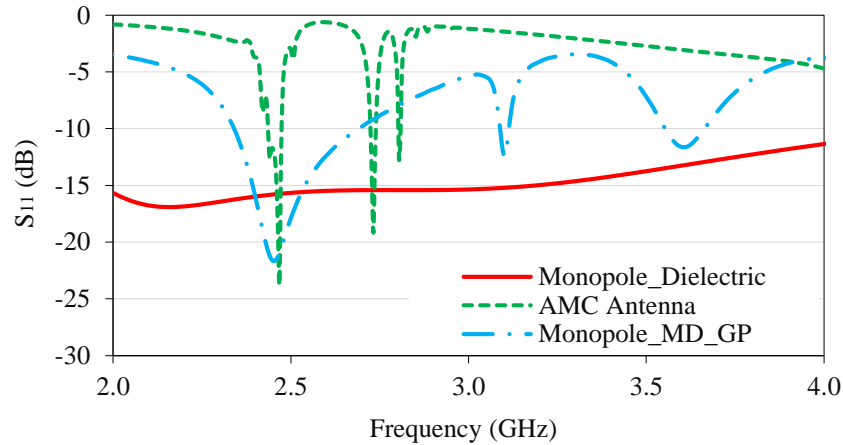


Fig. 3.24: Simulated S_{11} of antennas in free-space.

3.6.4 Structural Deformation Effects

Investigation of the antenna performance on the dynamic body environment such as under bending conditions is one of the important factors to be considered. Bending radii (R) chosen in our investigation were: 40 mm, 100 mm and 140 mm to approximate a human adult's arm, leg and

thigh. Moreover, investigations of antenna performance were executed for two bending directions: E- and H-planes, as shown in Fig. 3.25 and Fig. 3.26, respectively. It is worth mentioning that monopole 1 and monopole 2 refer to the monopole antenna designed using dielectric and MD materials, respectively. In case of monopole2, the antenna was backed with a GP at 4 mm as described earlier in this section. S_{11} for E- and H-planes bending conditions of studied antennas are shown in Fig. 3.27 and Fig. 3.28, respectively. Radiation performance summary within ISM 2.45 band of studied monopole antenna configurations are summarized in Table 3.9 and Table 3.10 for E- and H-planes bending conditions, respectively. The advantage of using MD material in realizing wearable antennas can be seen through the performance stabilization when the antenna was subject to different bending conditions. The MD material utilization helped to achieve the desired antenna functionality over the frequency range of interest.

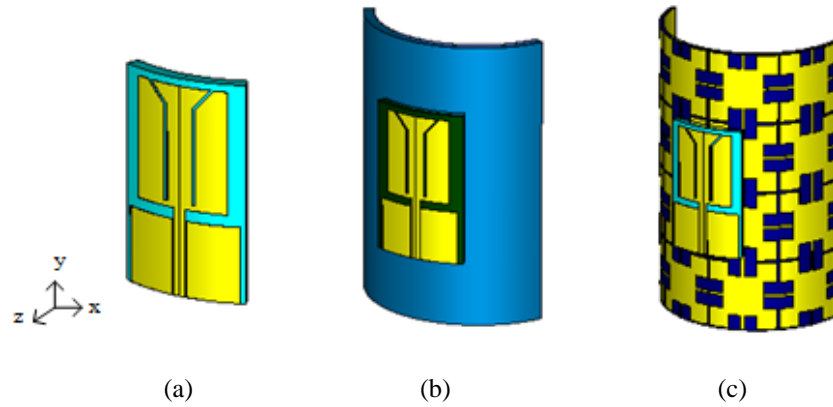


Fig. 3.25: (a) Monopole1, (b) monopole2, and (c) AMC antennas bent in E-plane.

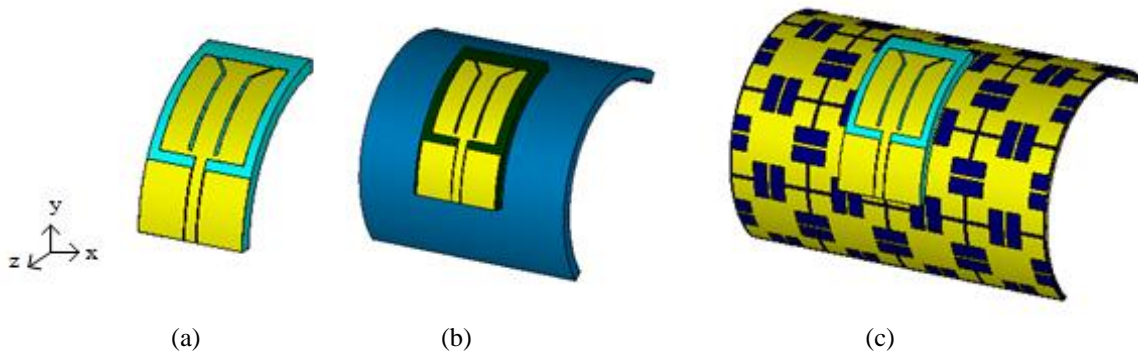
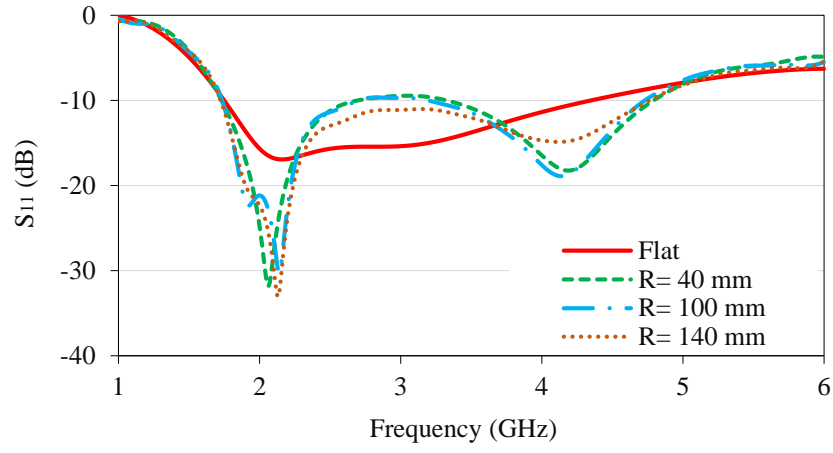
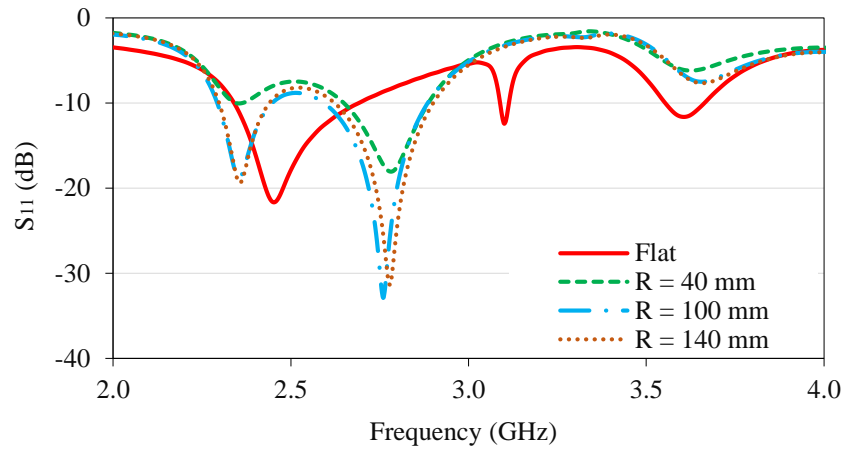


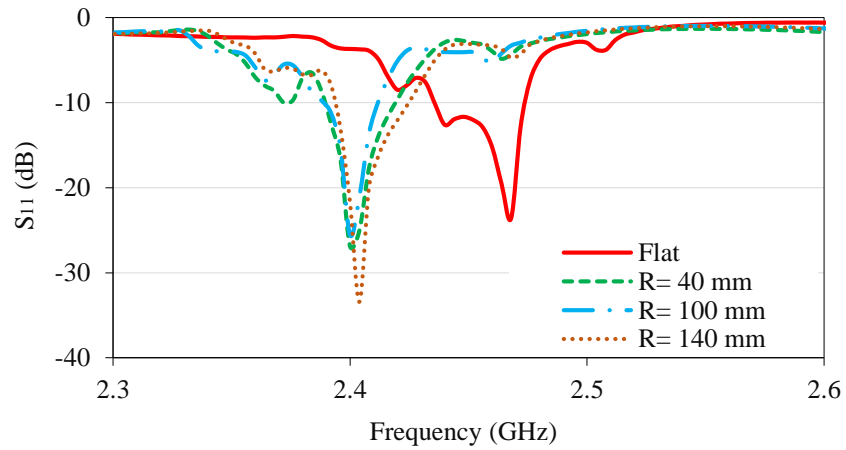
Fig. 3.26: (a) Monopole1, (b) monopole2, and (c) AMC antennas bent in H-plane.



(a)

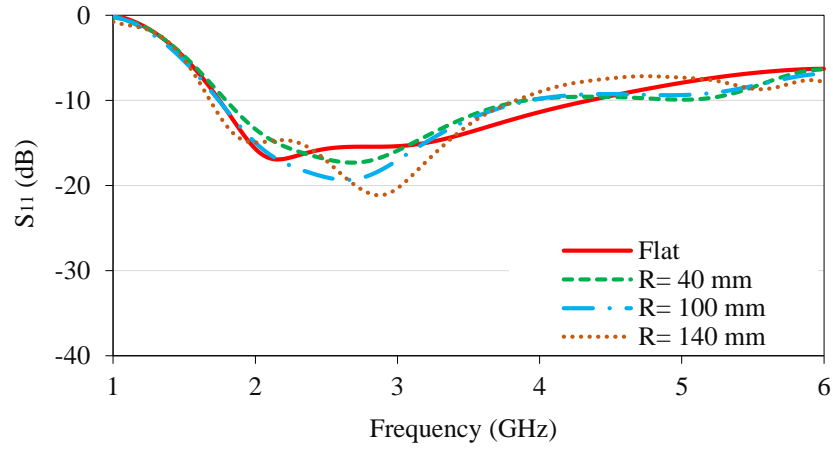


(b)

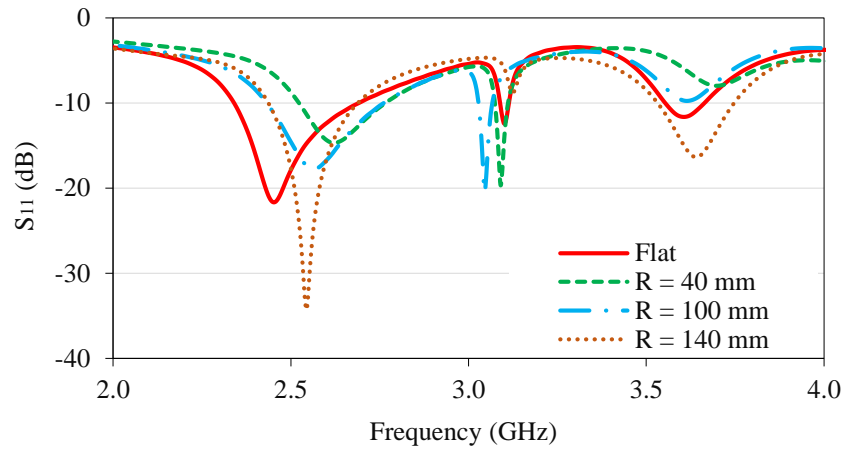


(c)

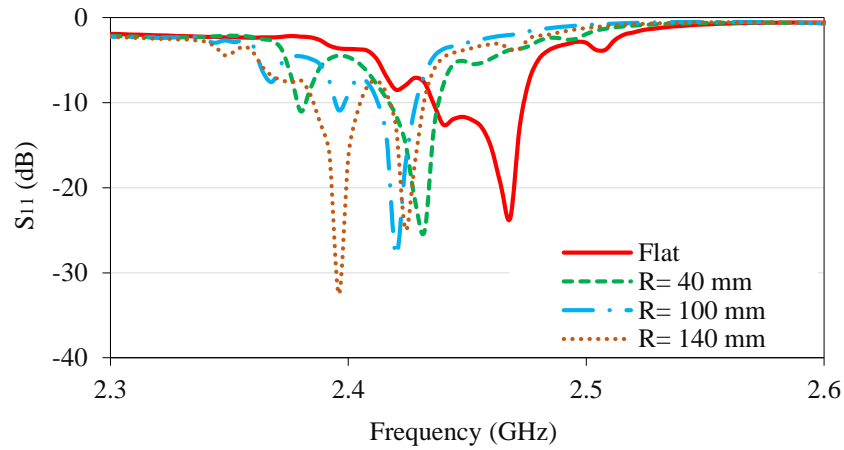
Fig. 3.27: S_{11} of bent (a) monopole1, (b) monopole2, and (c) AMC antennas in E-plane.



(a)



(b)



(c)

Fig. 3.28: S_{11} of bent (a) monopole1, (b) monopole2, and (c) AMC antennas in H-plane.

Table 3.9: Performance summary of antennas (E-plane bending).

	2.4 GHz		2.45 GHz		2.5 GHz	
	<i>Gain (dBi)</i>	<i>FBR^a</i>	<i>Gain (dBi)</i>	<i>FBR</i>	<i>Gain (dBi)</i>	<i>FBR</i>
Monopole Antenna, Dielectric Material						
Flat	2.413	0.0089	2.447	0.0096	2.482	0.0108
R= 40 mm	2.547	0.7162	2.580	0.7401	2.603	0.7680
R= 100 mm	2.414	0.5940	2.403	0.6304	2.370	0.7836
R= 140 mm	2.546	0.5598	2.539	0.6330	2.519	0.6960
Monopole Antenna, Magneto-Dielectric Material						
Flat	7.610	9.4041	8.115	9.7870	8.152	10.265
R= 40 mm	6.975	9.7563	6.930	9.7342	6.786	9.7723
R= 100 mm	7.578	9.6801	7.640	9.8234	7.565	10.052
R= 140 mm	7.544	9.6354	7.606	9.8247	7.524	10.102
AMC Antenna						
Flat	1.937	10.882	8.410	22.4247	0.7752	8.4247
R= 40 mm	6.475	12.086	-0.1179	8.05620	0.1721	7.5251
R= 100 mm	8.802	17.224	2.6300	8.6005	1.2300	18.616
R= 140 mm	9.470	19.264	0.4224	8.2606	2.2060	21.753

Table 3.10: Performance summary of antennas (H-plane bending).

	2.4 GHz		2.45 GHz		2.5 GHz	
	<i>Gain (dBi)</i>	<i>FBR^a</i>	<i>Gain (dBi)</i>	<i>FBR</i>	<i>Gain (dBi)</i>	<i>FBR</i>
Monopole Antenna, Dielectric Material						
Flat	2.413	0.0089	2.447	0.0096	2.482	0.0108
R= 40 mm	2.459	0.6097	2.526	0.6507	2.589	0.6987
R= 100 mm	2.640	0.6152	2.706	0.6570	2.768	0.6945
R= 140 mm	2.646	0.4014	2.697	0.4542	2.747	0.5162
Monopole Antenna, Magneto-Dielectric Material						
Flat	7.610	9.4041	8.115	9.7870	8.152	10.265
R= 40 mm	4.622	9.4182	5.002	8.0643	5.137	6.9332
R= 100 mm	6.554	10.292	7.137	9.9807	7.318	9.9007
R= 140 mm	6.580	10.192	7.349	10.044	7.664	10.088
AMC Antenna						
Flat	1.937	10.882	8.410	22.424	0.7752	8.4247
R= 40 mm	1.266	5.4520	0.500	2.6120	2.7130	20.890
R= 100 mm	2.189	11.116	2.664	22.505	-0.8567	18.928
R= 140 mm	4.352	24.404	2.791	17.242	0.3762	9.4850

3.6.5 Human Body Effects

To validate the on-body performance, simulations of the proposed MD based antenna on body models, *i.e.*, layered and Ella body models, were carried out. Details of these body models are discussed in Section 2.5. As shown in Fig. 3.29, stable S_{11} results were observed in the presence of different body models compared to the free-space case. In addition, radiation characteristics comparison in terms of the antenna gain and FBR with monopole based dielectric and AMC antennas is summarized in Table 3.11. A robust antenna performance was achieved.

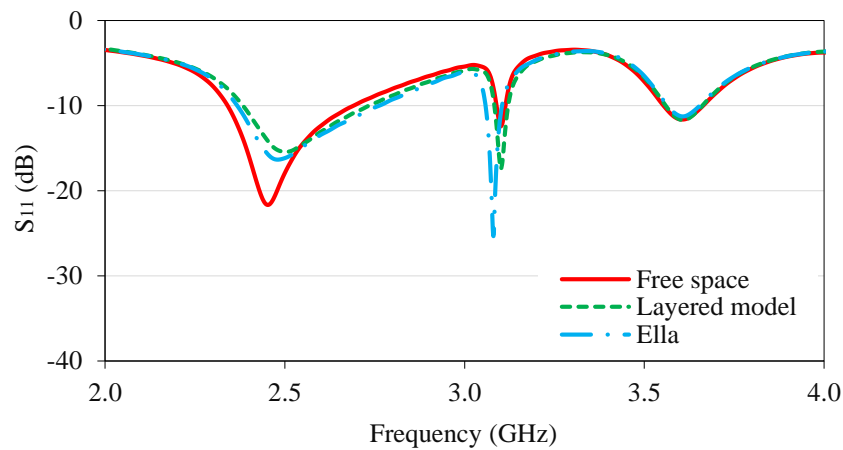


Fig. 3.29: S_{11} of monopole_MD_GP.

Table 3.11: Radiation characteristics summary at 2.45 GHz.

<i>Antenna</i>	<i>Environment</i>	<i>Gain (dBi)</i>	<i>FBR (dB)</i>
Monopole, dielectric	Free-space	2.45	00.01
	Layered body model	-1.69	25.51
	Ella model	0.35	17.88
Monopole, MD, GP	Free-space	8.14	10.27
	Layered body model	7.82	18.30
	Ella model	7.72	16.58
AMC	Free-space	8.41	8.42
	Layered body model	8.40	23.33
	Ella model	8.06	27.33

3.7 Application of Layered Substrate in Wearable Antenna Design

As mentioned earlier, the process of engineering artificial MD materials using standard manufacturing methods and traditional solid MD materials is complex and very challenging. On the other hand, composites made using bulk Nano-ferrite inclusion in polymers can result in natural MD materials. Although, these materials are simple to synthesize, mostly cannot be used for high frequencies as the material losses become more pronounced with frequency [4]. In addition, material flexibility and comfortable embedding into the system are not guaranteed. In this section, we introduce investigations carried out on the use of thin layers of magnetic and dielectric materials, alternating in a sequence with horizontal or vertical arrangements to be utilized as the antenna substrate and in place of MD or dielectric substrate. This method offers less complexity and easier fabrication than AMC and MD methods with similar effect on antenna radiation characteristics.

3.7.1 Antenna Topology and Materials

Different Monopole Antenna (MA) configurations are studied and their performances are evaluated at their resonance frequency using CST Microwave Studio (MWS) [49]. The results are summarized in Table 3.12. Initially, the monopole antenna discussed in Section 2.3 was designed using dielectric textile material (*i.e.*, Pellon fabric) with a thickness of 3.6 mm , ϵ_r of 1.08, and $\tan\delta_e$ of 0.008. The first case we use as a reference for comparison is placed on GP made of copper material at a quarter wavelength distance (*i.e.*, 34.7 mm at 2.16 GHz). The GP size is $84 \times 107\text{ mm}^2$ (width \times length). In the next case the dielectric material is replaced by MD material with the same thickness with properties of $\epsilon_r = \mu_r = 4$ and $\tan\delta_e = \tan\delta_m = 0.008$. The GP in this case is placed at a distance of 4 mm away from antenna.

Table 3.12: Performance comparison of studied antennas at resonance frequency.

<i>Antenna Topology</i>	f_r^a (GHz)	Size (mm ²)	Gain (dB)	B.W. ^b
MA, Dielectric	2.16	32×57	2.23	2.59 GHz
MA, Dielectric, GP ^c	1.91	84×107	6.73	3.43 GHz
MA, MD, GP ^d	2.46	84×107	8.17	350 MHz
MA, VS, GP ^d	3.19	84×107	9.63	433 MHz
MA, HS, GP ^d	3.01	84×107	9.38	620 MHz

^a Resonance frequency (f_r), ^b Bandwidth (B.W.), ^c Ground Plane (GP) 34.7 mm, and ^d Ground Plane (GP) 4 mm.

The dielectric layer has $\epsilon_r = 4$ and $\tan\delta_e = 0.008$, and the magnetic layer has $\mu_r = 4$ and $\tan\delta_m = 0.008$. Two cases include the monopole antenna (MA) on vertical layers (MA, VS, GP) and MA on horizontal layers (MA, HS, GP). It is worth mentioning that, for proof of concept, in addition to dielectric and magnetic material properties, the total thickness of the substrate of 3.6 mm was kept the same as MD antenna configuration for easy of comparison. However, these values can be adjusted to meet the requirements of the targeted operating frequency band and antenna performance. As shown in Fig. 3.30, in the first sequence, 6 layers each of 0.6 mm thickness were arranged vertically along the z -axis to form the antenna substrate (MA, VS, GP). The layers divided equally as 3 layers of dielectric and 3 layers of magnetic materials. In the second sequence, 57 layers each of 1 mm thickness were arranged horizontally along the y -axis (MA, HS, GP). The sequence consists of 28 layers of dielectric and 29 layers of magnetic materials.

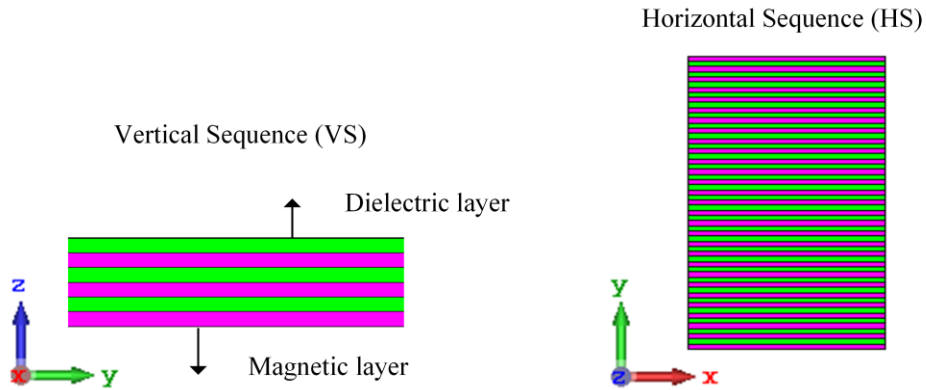


Fig. 3.30: Studied layered substrate sequences.

3.7.2 Results and Discussion

Summary of results of the studied antenna configurations is provided in Table 3.12. In addition, variations in S_{11} along with the radiation patterns in the principle planes (*i.e.*, E- and H-planes) of the antennas at their resonance frequencies are shown in Fig. 3.31 and Fig. 3.32, respectively. As expected, the integration of a GP at quarter wavelength distance (*i.e.*, 34.7 mm at 2.16 GHz) away from the MA improved the antenna gain compared to the stand-alone antenna. However, this resulted in a large antenna size. On the other hand, a superior performance was achieved when the GP is placed at only 4 mm distance away from the antenna. In addition, by using layered substrates, further improvements in the antenna radiation characteristics and bandwidth were achieved compared to MD based antenna with the advantage of ease of fabrication.

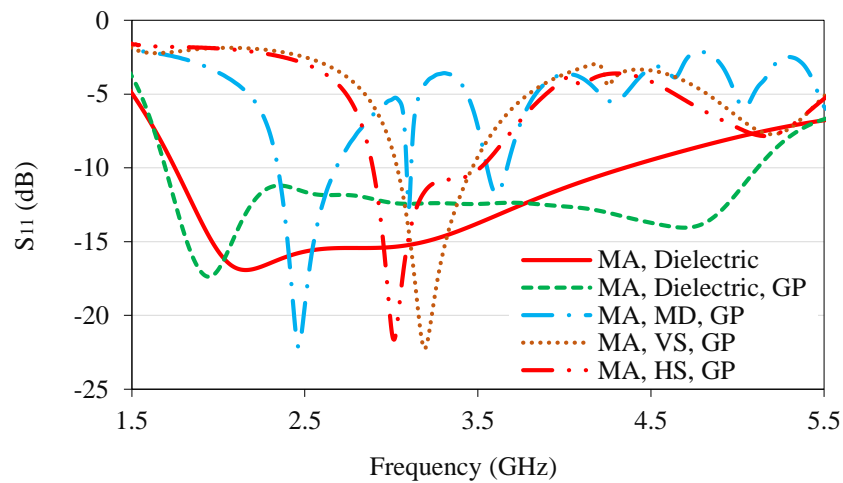


Fig. 3.31: S_{11} of studied monopole antenna configurations.

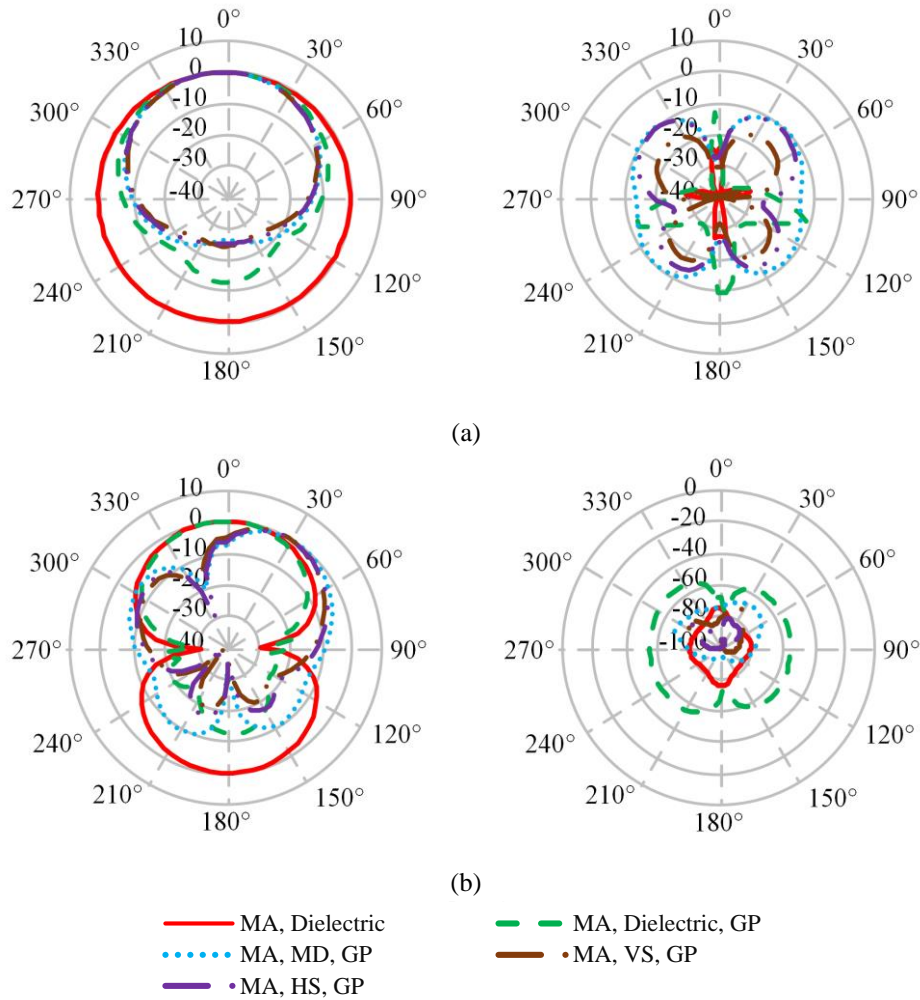


Fig. 3.32: Simulated co-pol (left) and cross-pol (right) radiations of MA configurations in (a) E-plane and (b) H-plane at f_r .

3.8 Summary

In this chapter, the design, realization and characterization of a wearable textile antenna were presented. The antenna is a combination of monopole with AMC structure as a ground plane. The AMC antenna was fully fabricated using textile layers and working within ISM 5.8 GHz band. The AMC antenna features low profile and small footprint characteristics, with dimensions of $102 \times 68 \times 3.6 \text{ mm}^3$. In order to verify the simulation results, prototypes of the antennas were fabricated

and measured in different conditions. In free-space, the realized AMC antenna showed -10 dB input impedance bandwidth of 34% (4.30 GHz – 5.90 GHz), with a gain value of 6.12 dBi. Numerical simulations and experimental measurements further revealed that the proposed AMC antenna is robust in respect to impedance resonance frequency, showing minimal changes due to structural deformation such as bending and crumpling, as well as loading effects of human body. In addition, the inclusion of the AMC reflector considerably reduced the SAR values and the back radiation, making the AMC antenna far superior to a single monopole antenna. Finally, realizing antennas using flexible MD materials for wearable applications was proposed through numerical analysis. Effectiveness of using flexible MD materials in wearable antenna design was evaluated under bending conditions and on body scenarios. Stable antenna performance was achieved under the aforementioned conditions. Finally, the potential of using layers of magnetic materials in a sequence combined with dielectric layers was investigated. Improvements in the antenna radiation characteristics and bandwidth was observed.

CHAPTER 4

DESIGN OF IMPLANTABLE ANTENNA

4.1 Introduction

The main goals of this chapter are:

- To present the configuration of the proposed flexible biocompatible implantable antenna. Modelling and numerical analysis of the entire work was carried out using full-wave electromagnetic simulation software, CST Microwave Studio (MWS) [49];
- To investigate the effect of different body tissue models such as simplified layered body model and voxel body model on the proposed antenna performance;
- To investigate the effect of internal capsule components integration such as the battery on the proposed antenna performance;
- To discuss results of accurate assessment study of the antenna performance for near/far-field communication in biotelemetry applications.

In order to reach these goals, this chapter is organized as follows:

Section 4.2 presents a literature survey on antennas with similar antenna topology, which has a capsule shape design. The design details of the proposed implantable antenna is discussed in Section 4.3. In addition, the considered scenarios for antenna performance evaluation are presented in this section. Section 4.4 presents a discussion on the obtained results of the carried studies in terms of the antenna reflection coefficient and gain. Performance evaluation of the proposed antenna for near/far-field communication is presented in Section 4.5.

4.2 Background

A flexible dual band implantable antenna, working within MICS 403 MHz and ISM 2.45 GHz frequency bands, was printed on the inner wall of a capsule [32], as shown in Fig. 4.1(a). The capsule was made of biocompatible parylene-C material with a size of $10.2 \text{ mm} \times 25.2 \text{ mm}$, *i.e.*, (diameter \times length). The antenna was implanted at 3 mm depth in skin tissue cube of $100 \times 100 \times 100 \text{ mm}^3$ size. The implantable antenna size had a volume of 186.3 mm^3 . The obtained antenna -10 dB input impedance bandwidths were (321MHz – 532 MHz), and (2.15 GHz – 2.74 GHz), within the MICS and ISM frequency bands, respectively. In addition, the antenna gains were -30.5 dBi and -22.2 dBi within MICS and ISM frequency bands, respectively. *In vitro* measurements were performed using minced pork, as shown in Fig. 4.1(b), and frequency detuning effects were observed.

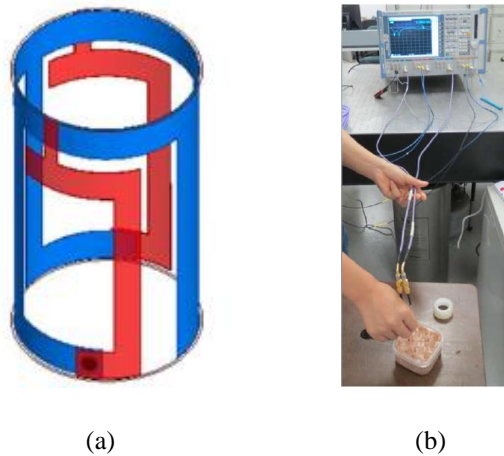


Fig. 4.1: (a) Geometry of implanted antenna and (b) *In vitro* measurement setup [32].

The capsule antenna shown in Fig. 4.2(a) was implanted at 3 mm in skin tissue model of $180 \times 180 \times 180 \text{ mm}^3$ size [75]. A 0.15 mm-thick flexible and biocompatible polyimide material was used to implement the capsule of $11 \text{ mm} \times 24 \text{ mm}$, *i.e.*, (diameter \times length) size. The antenna bandwidth was (358 MHz – 516 MHz), and its gain at 402 MHz was -37 dBi. Furthermore, when

the delivered power was assumed to be 1 W, the maximum SAR value was 485 W/kg at 402MHz. Therefore, the delivered power had to be decreased to 3.3 mW to meet the SAR standards. The fabricated antenna, shown in Fig. 4.2(b), was tested inside a skin mimicking gel to validate its performance. The followed recipe of skin gel consisted of 56.18% sugar, 2.33% salt, and 41.49% deionized water.

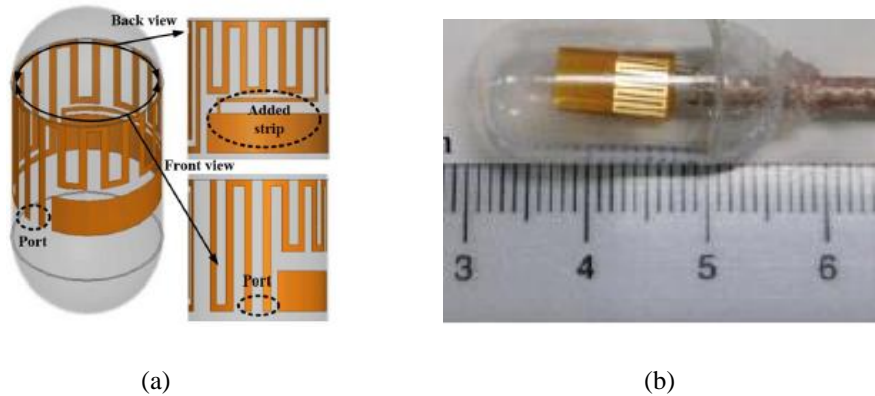


Fig. 4.2: (a) Geometry of implanted antenna and (b) fabricated prototype [75].

Meander lines and inverse T matching branch were loaded to achieve antenna miniaturization and better impedance matching within the ISM 2.45 GHz band, as shown Fig. 4.3(a) [13]. The antenna was implanted at 50 mm depth inside a muscle tissue cube of $100 \times 100 \times 100 \text{ mm}^3$ size. The antenna bandwidth was shifted from (2.38 GHz – 2.5 GHz) to (2.36 GHz – 2.44 GHz), when measured for antenna implanted inside minced pork. Effects of different antenna orientations on the antenna performance were evaluated for different scenarios.

A conformal capsule antenna of 66.7 mm^3 volume was implanted inside a muscle tissue cube of $100 \times 100 \times 100 \text{ mm}^3$ size at 50 mm depth and proposed for working within the ISM 915 MHz band [76]. The antenna topology is shown Fig. 4.3(b). The antenna of helical shape was printed on the outer wall of a capsule to achieve circular polarization property. The capsule was made of biocompatible polyethylene material with the dimensions of $10.2 \text{ mm} \times 25.2 \text{ mm}$, *i.e.*,

(diameter \times length). The antenna showed 185 MHz (780 MHz – 965 MHz), and 222 MHz (900 MHz – 1122 MHz) as the antenna input impedance bandwidth, and 3 dB axial ratio (AR) bandwidth, respectively.

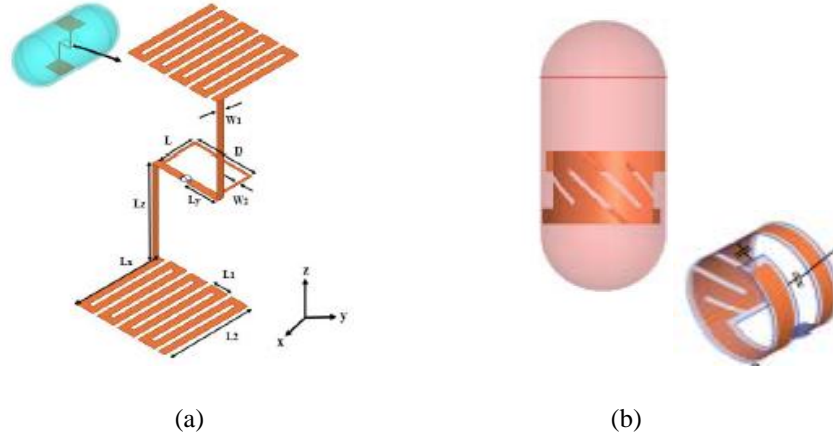


Fig. 4.3: Geometry of implanted antenna proposed in (a) [13] and (b) [76].

4.3 Implantable Antenna Design and Simulation Setups

The configuration of the proposed implantable antenna is shown in Fig. 4.4(a). The antenna is a conformal meandered antenna. To achieve miniaturization antenna was designed on the outer wall surface of a capsule, with a diameter of 11 mm and length of 24 mm. It was assumed that the capsule’s inner volume will be utilized for the necessary electronic circuits and sensors. A flexible biocompatible material, ultem of 0.5 mm thickness with ϵ_r and $\tan\delta_e$ of 3.15 and 0.0013 S/m, respectively, was considered to be covering the outer layer of the capsule and was used as the substrate of the antenna. This material was chosen because it has stable properties not affected by the variations of different parameters, such as temperature and frequency.

For easy optimization of the antenna, the antenna was first embedded in a three-layer body model *i.e.*, named as Layered_Model, as shown in Fig. 4.4(b). This model consisted of skin, fat and muscle body tissues of 2 mm, 8 mm, and 80 mm thicknesses, respectively. The volume of the

body model was $100 \times 100 \times 90 \text{ mm}^3$, and the depth of embedding the capsule was 40 mm . Properties of dispersive tissue layers were obtained from the material library in CST Microwave Studio software. The antenna in planar form has the volume of $12 \times 6 \times 0.035 \text{ mm}^3$. The geometrical parameters of the antenna are shown in Fig. 4.5.

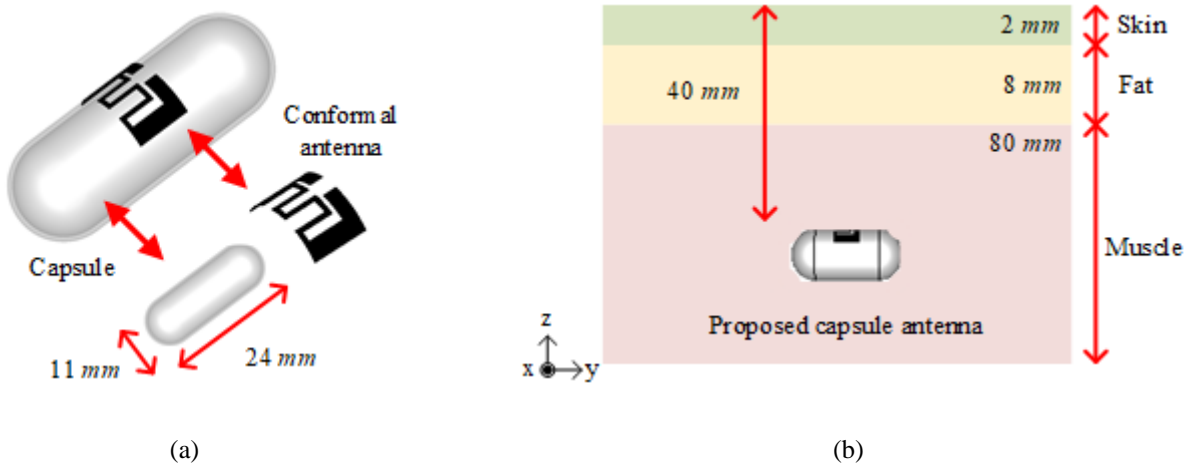


Fig. 4.4: Proposed antenna; (a) conformal form and (b) implanted in layered body model.

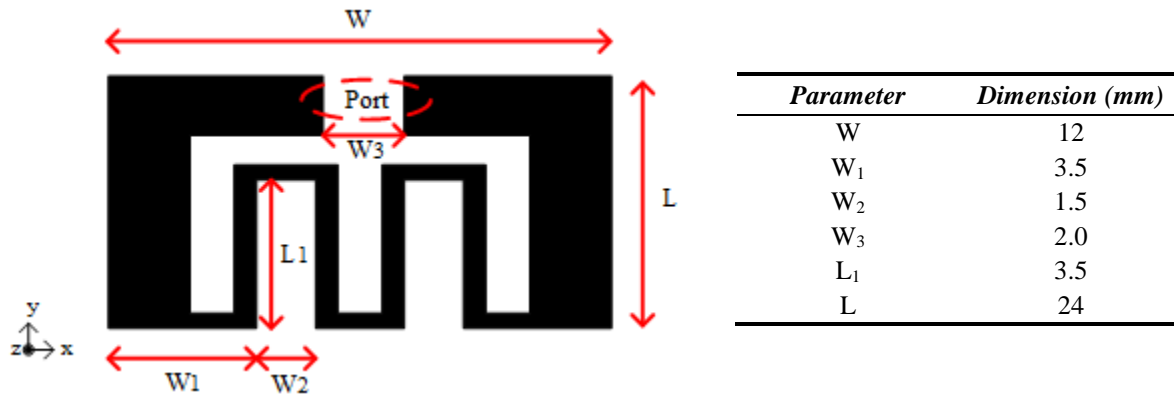


Fig. 4.5: Configuration of the proposed capsule antenna in planar form.

When considering influence of the electrical components of the implantable system on the antennas, batteries are expected to have the most significant effects because of their size. In our simulations, batteries were simply represented as a perfect electric conductor (PEC) cylinder with a length of 8 mm and diameter of 10 mm inside the capsule, as shown in Fig. 4.6(a). The antenna

was implanted inside the layered body model and this configuration was named as Layered_battery. Moreover, the proposed capsule antenna was analyzed in the anatomical Ella voxel model (without the battery) at two different locations: chest and shoulder, named as Ella_shoulder and Ella_chest, respectively, as shown in Fig. 4.6(b). For the chest implanting, the proposed antenna was envisioned as a pacemaker antenna, and for the shoulder implanting the application was for patients suffering from osteoarthritis [32]. In order to reduce the simulation time, we only imported the upper part of the human body torso, excluding the head, into our simulation model.

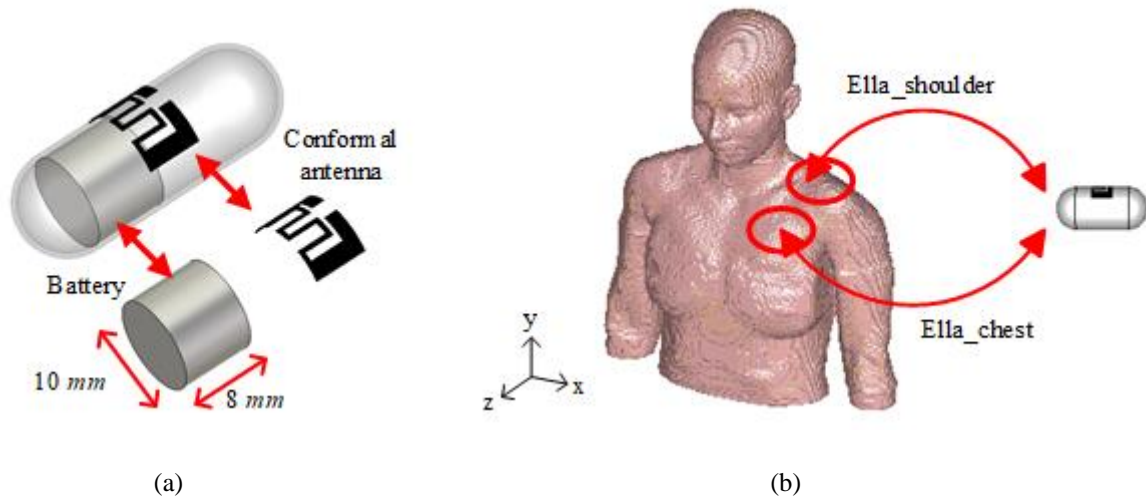
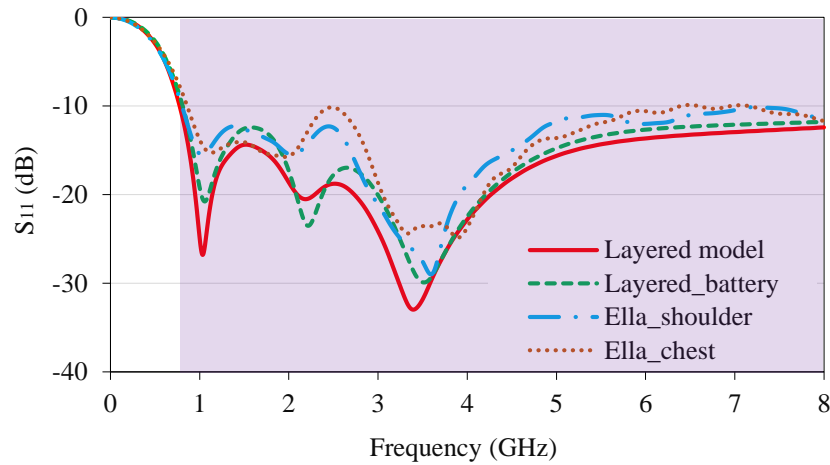


Fig. 4.6: Capsule antenna; (a) considering the battery and (b) inside Ella model.

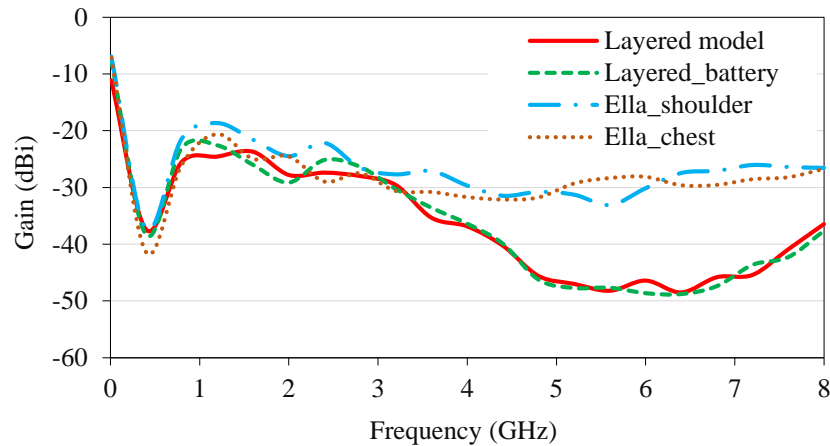
4.4 Results and Discussion

In order to test the robustness of the proposed antenna, S_{11} for the aforementioned simulation setups are compared in Fig. 4.7(a). The antenna input impedance bandwidth of the layered model implantation case was about 7.31 GHz (0.78 GHz – 8 GHz). Integrating the battery caused a slight shift in the resonance frequencies. The implanted antennas in Ella’s shoulder or chest also showed a reduction in the S_{11} level and a detuning effect. The most noticeable reduction

in the obtained bandwidth, which was about 800 MHz, was observed in the case of implanting antenna in the Ella's chest. However, since the antenna is a wideband, these detuning effects did not cause a significant effect on the bandwidth variation. Antenna gain over its entire operating frequency band is shown in Fig. 4.7(b). Antenna gain at the center frequencies of the 902.8 MHz – 928.0 MHz, and 2.40 GHz – 2.50 GHz ISM bands are summarized in Table 4.1. These frequency bands were selected as they are commonly used for biotelemetry applications [76]. From Table 4.1, it is clear that the antenna gain was higher within ISM 915 MHz for all the studied cases.



(a)



(b)

Fig. 4.7: (a) S_{11} and (b) gain of capsule antenna for different configurations.

Table 4.1: Summary of the realized gain of the capsule antenna.

<i>Scenario</i>	<i>915 MHz</i>	<i>2.45 GHz</i>
Layered model	-25.23 dBi	-27.51 dBi
Layered_battery	-23.31 dBi	-25.32 dBi
Ella_shoulder	-21.77 dBi	-22.20 dBi
Ella_chest	-25.86 dBi	-28.78 dBi

4.5 Transmission Link Evaluation

For accurate assessment of the antenna performance for near/far-field communication in biotelemetry applications, where the near-field boundary is approximated at $\lambda/2\pi$ [77], the coupling strength (S_{12}) between an external half-wavelength dipole and the proposed capsule antenna implanted in the layered body model was evaluated for two scenarios. First, the free-space distance (s) of the external dipole was changed in the range of $10\text{ mm} - 70\text{ mm}$, while the implanting depth (d) is 40 mm . Second, distance d was changed in a range of $10\text{ mm} - 70\text{ mm}$, while s is 10 mm . The simulation setup is shown in Fig. 4.8. For each of the studied frequency bands, a different dipole was adopted. As shown in Fig. 4.9 and Fig. 4.10, the coupling strength at 915 MHz was higher than that at 2.45 GHz for both studied cases due to the larger obtained gain values at 915 MHz , with changing d and s .

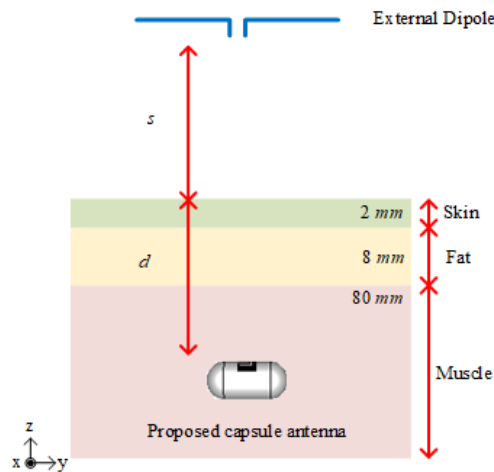
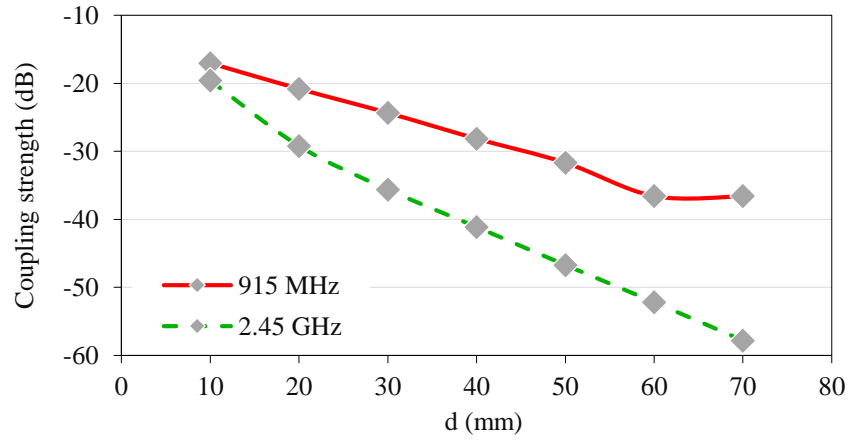
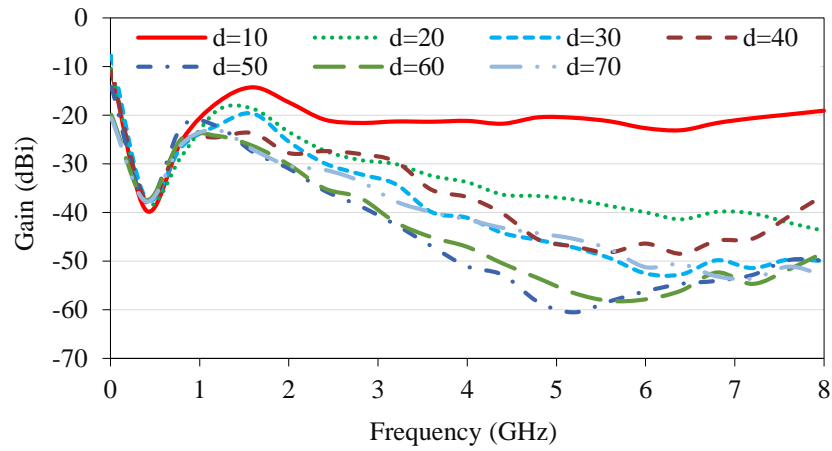


Fig. 4.8: Simulation setup of coupling strength for external half wavelength dipole.



(a)



(b)

Fig. 4.9: Different implanting depths (d); (a) coupling strength and (b) realized gain.

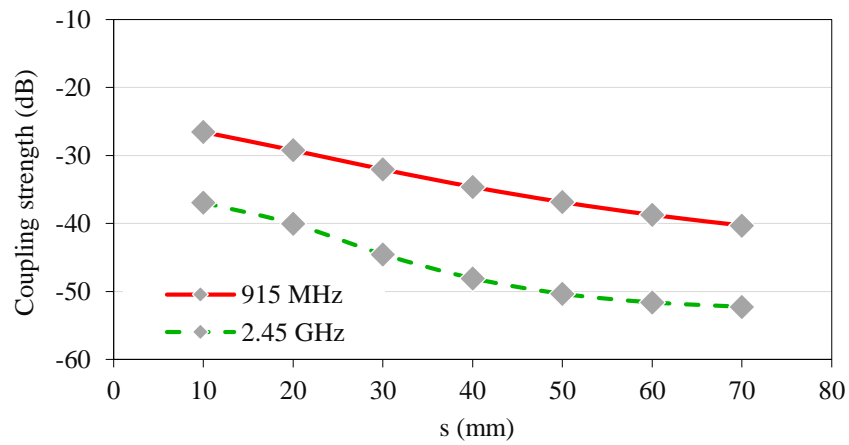


Fig. 4.10: Coupling strength results for different free-space distances (s).

4.6 Summary

In this chapter, the design and performance evaluation of a miniaturized wideband implantable capsule antenna was presented. The advantage of the wideband property of the proposed antenna was demonstrated through the performance evaluation of this antenna when it was implanted in a simplified layered body model and an anatomical realistic body model, as well as when it was integrated with a battery. Also, the near/far-field communication analysis was carried out at 915 MHz and 2.45 GHz for different free-space distances of the receiver and different implant depths parameters.

CHAPTER 5

INVESTIGATED WIRELESS BODY AREA NETWORK APPLICATIONS

5.1 Introduction

This chapter provides an overview of investigations done for various wireless body area network (WBAN) applications during the course of this thesis. The applications are: (a) Respiratory rate measurement using ultra-wide band (UWB) radar system and (b) An accurate phase-based localization method of radio frequency identification (RFID) tag. Although none of these studies used wearable and implanted antennas, they were chosen to show the importance of antennas in these applications and how the antenna design can affect the overall system performance.

In Section 5.2, effects of antenna characteristics on ultra-wide band (UWB) radar-based respiratory rate measurement system for telehealth-monitoring applications were investigated. The performances of three types of antenna for a UWB radar respiratory rate measurement system were studied in this work. In this context, the proposed system was comprehensively evaluated using two experimental sets. First, a mechanical setup was used to provide a series of controlled frequency and distance motions to mimic the human chest movements while breathing for measurement test. Second, the reliability test of the UWB radar system was evaluated through respiration-rate measurements of ten test subjects. Measurement results were then compared to a reference measurements using a BIOPAC biological data acquisition [78] to confirm the study findings. In Section 5.3, a full electromagnetic simulation model, using CST Microwave Studio [49] software, is presented for indoor localization system of a semi-passive radio frequency identification (RFID) tag demonstrated in [105]. The method is based on the phase measurements of the backscattered wave collected by transceiver antenna(s) attached to the RFID reader.

5.2 Respiratory Rate Measurement using UWB Radar System

5.2.1 Background

Respiratory rate is one of the most crucial vital signs used to assess human body functions and physiological stability. In fact, respiratory rate is helpful in predicting potential clinical events. For example, a sudden change in respiratory rate is considered a marker for cardiac arrest [79] and one of the strongest predictors of mortality [80]. Furthermore, respiratory rate is helpful in monitoring patient illness progression to determine the effective treatments that should be received [81]. The research community in the healthcare field has investigated different methods for respiratory rate measurement. Generally, existing work can be classified into two categories. The first category requires a physical contact with the patient while conducting the measurement. The operating principles of contact devices include the measurement of respiration air flow [82], sound [83], electrocardiogram signals [84], abdomen/chest movements [85], and photoplethysmography using oximetry-based probe [86]. As these techniques require direct contact with the patient during the entire measurement period, they can be inconvenient or even impractical in many situations; for instance, in long term sleep monitoring and respiration monitoring of patients with dermatological conditions or burn patients. Moreover, most of the aforementioned methods are affected by the changes in environmental factors such as ambient temperature and light interference, which may cause insufficient accuracy in respiration measurement [87]–[88].

To overcome these shortcomings, a second category of measurements using non-contact methods are proposed. Researchers have demonstrated the feasibility of radar-based sensing systems for detecting or monitoring human respiratory rate in many applications such as diagnostic tools in the biomedical field [89]–[90], rescue tools for finding survivors buried under snow cover

[91], and security devices [92]. Several radar systems have been proposed in the literature for detecting vital signs, *e.g.*, continuous-wave (CW) [93] and ultra-wide band (UWB) [94] radars. CW radar falls into three basic subcategories: single-tone [95], frequency-modulated continuous-wave (FMCW) [96], and stepped frequency-modulated continuous-wave (SFCW) [97].

Single tone continuous-wave (CW) radars have a simple system architecture considering high-level chip integration, which transmits a single-tone frequency of narrow bandwidth. They have been widely used because of their high precision in displacement measurement. However, they can hardly detect range information. Hence, the vital sign detection becomes a challenging process, especially in the presence of high interference and rich multipath levels. In addition, the phase difference between transmitted and received waveforms is directly proportional to the target's motion. Unlike single tone CW radar, FMCW radar is capable of providing range information. However, it still requires calibration, to compensate for the nonlinearities in frequency sweeping. SFCW radar combines the advantages of single tone CW and FMCW radars with the resolution being highly dependent on the transmission bandwidth. This often favors the systems that are working at high frequencies. Therefore, the SFCW radars require high costs, hardware complexity, and have to deal with high losses.

UWB radar can overcome the aforementioned drawbacks. This method is based on the transmission of a very short duration pulse, which produces high bandwidth signals. Thus, it provides distance, and Doppler information measurements of the target with high accuracy. In addition, spreading of the transmitted signal across a large spectrum, is necessary to obtain a low transmit power density [98]-[99]. It is worth mentioning that, depending on the specific application, any of these radar systems may provide non-contact vital sign detection.

5.2.2 *Experimental Setups*

Experimental set was designed to validate the performance of the proposed radar-based sensing system for respiratory rate measurement. First, we developed a mechanical setup of real-time performance supported by Quarc [100] to provide a series of controlled frequency and displacement motions for measurement test. The mechanical setup consisted of SRV02 movable unit measuring $15 \times 15 \times 18 \text{ cm}^3$, Q2-USB data acquisition device, and a voltage-controlled amplifier. The moving plate was made of paper and cardboard materials. To mimic the chest wall movement (*i.e.*, by imitating the respiration of human), the mechanical setup was programmed to perform a simple back-and-forth motion toward the fixed position radar. At this stage the main goal was to compare and quantify the antenna performance and its effect on the system accuracy. The controlled moving unit was placed in front of the antennas attached to the radar. Therefore, we attributed any performance improvements and issues to the antenna effects, rather than the positioning of the moving unit. Three parameters were studied: frequency (f) and displacement (s) of the moving unit that simulated the chest movements, and distance (d) between the radar antenna and moving unit, as shown in Fig. 5.1. MATLAB® and Simulink® programs were used for data acquisition and signal processing.

After selecting the best antenna among the three choices, a pilot study was conducted on ten human subjects. Volunteers were recruited and each of them were asked to sit on a chair, facing towards the radar, as shown in Fig. 5.2. The distance between the subject chest and the radar antennas was set to 1 m in all the measurements presented in this experiment. Subjects were asked to breathe normally, stay still and reduce their movements as much as possible, during the measurement. Simultaneously, BIOPAC biological data acquisition system [78] was used to obtain direct reading of the respiratory-rates of the test subjects. Pneumographs were obtained using

respiratory transducer (SS5L) attached around the test subject's chest. All signals were recorded with commercial data acquisition hardware (MP35) and a personal computer (PC) software (BIOPAC BSL 4.0) at a sampling rate of 1000 samples/second [95].

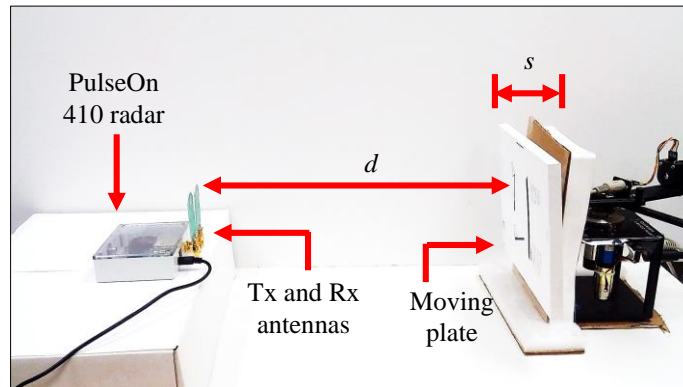


Fig. 5.1: Experimental setup for measuring the movement of a controlled moving unit.

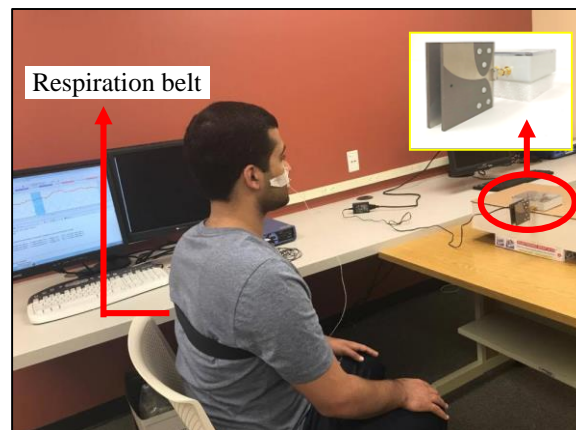


Fig. 5.2: The UWB radar is measuring respiratory rate from one subject.

5.2.3 UWB Radar Configuration

A commercially available UWB radar module that comprises one TimeDomain PulseOn ® 410 transceiver was used [48]. The functional block diagram of PulsON ® P410 transceiver is shown in Fig. 5.3. As can be seen, a transfer switch, *i.e.*, T/R switch, was used to allow user to configure antennas as one of the four available configurations:

- 1) Transmit/Receive on Port A; Monostatic radar configuration
- 2) Transmit/Receive on Port B; Monostatic radar configuration
- 3) Transmit on A, Receive on B; Bistatic radar configuration
- 4) Transmit on B, Receive on A; Bistatic radar configuration

The configuration that was used in the conducted experiments was Transmit on A, Receive on B; bistatic radar configuration. The module had a spectrum bandwidth of 3.1 GHz – 5.3 GHz, and a center frequency of approximately 4 GHz. The waveforms generated by the transceiver were in the form of Gaussian modulated sinusoidal pulse as shown in Fig. 5.4. TimeDomain PulseOn® UWB radar relies on low duty cycle transmissions, with coherent signal processing. Because the transmissions are coherent, the signal energy can be spread over multiple pulses, thereby, increasing the energy per bit and consequently the signal to noise ratio (SNR). The typical pulse repetition rate was 10 MHz, corresponding to a duty cycle of approximately 1%.

Radar configuration parameters were adjusted using monostatic radar module reconfiguration and evaluation tool (MRM RET) [101]. MRM RET is a graphical user interface program that operates on a PC or microprocessor and exercises all of the radar application programming interface (API) commands. It provides a real-time display of the raw radar returns, filtered data, and detections within the scan range, and it can also log the radar data into a file for post-processing. Each scan of the target conducted by the radar system requires a certain amount of time to complete, including radio wave transmission and reflected wave reception. The step size defines the total number of the data points in each scan. Scan time is a function of pulse integration index (PII) and size of the scan window settings.

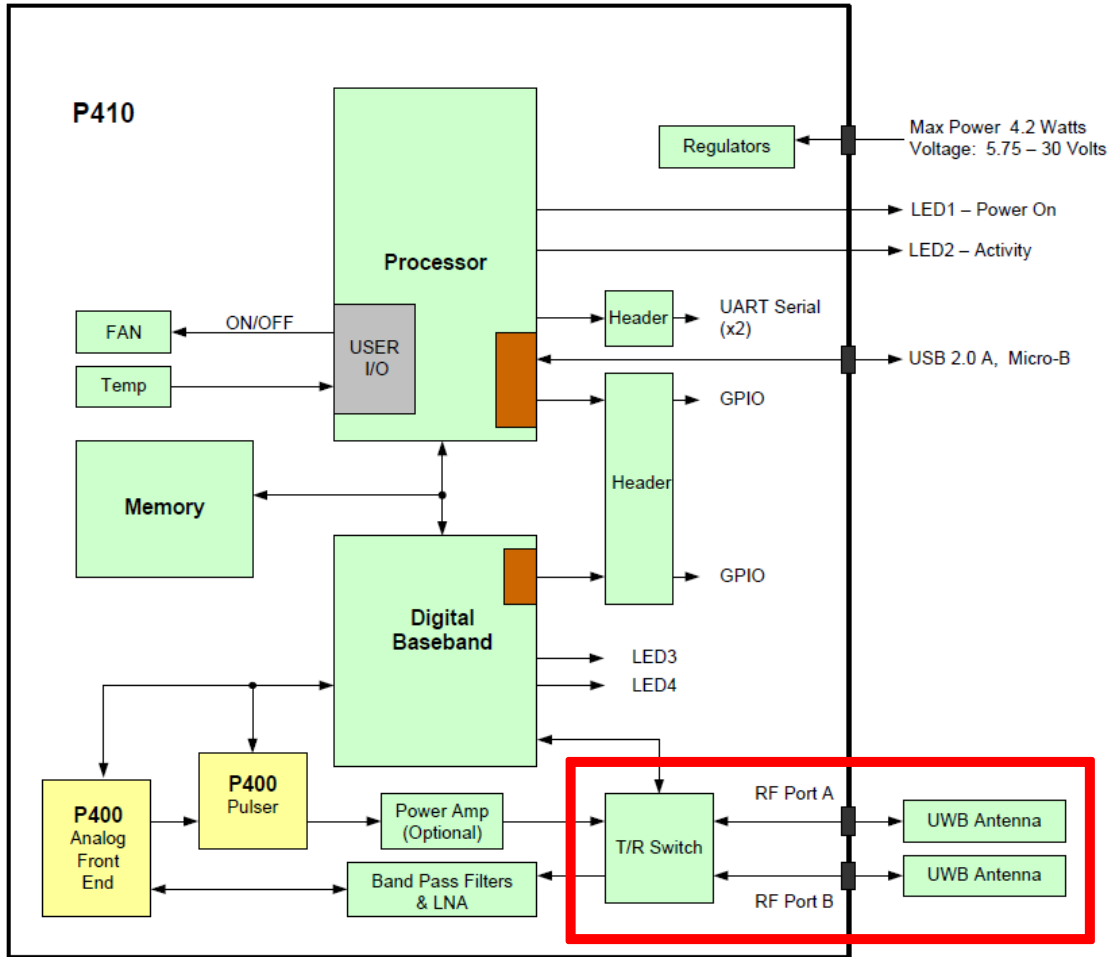


Fig. 5.3: PulseON @ 410 hardware functional block diagram [48].

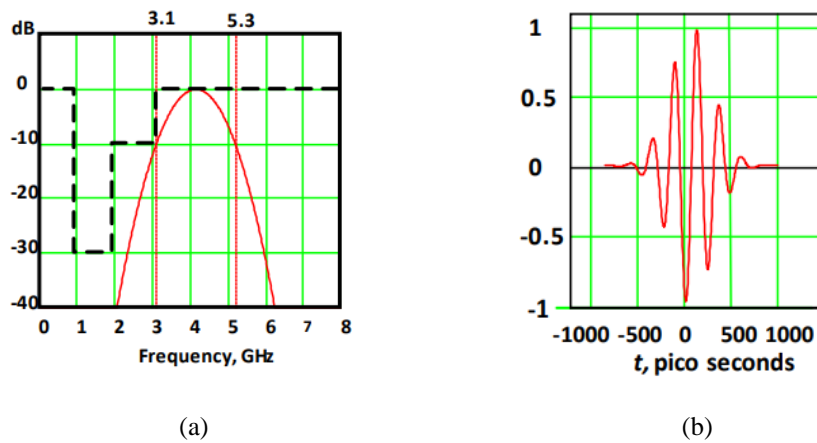


Fig. 5.4: PulseON @ 410 generated waveform in (a) frequency and (b) time domains [48].

These parameters are defined as [101]: Pulse Integration Index (PII): Since the MRM has been designed for coherent operation, it is possible to integrate multiple scans and thereby improve the received SNR. Each time the integration is doubled, the SNR of the received signal will improve by 3dB. Consequently, doubling the integration also doubles the amount of time it takes to produce a scan. Scan Start: This is the starting time in picoseconds of the first data point in the scan. Scan Stop: This is the ending time in picoseconds of the last data point in the scan. Scan Window: This is the difference between the Scan Start and Scan Stop times. The radar scan data will be reported from the MRM to the MRM RET Host PC as a serial data stream. The update rate of the radar system measures how fast the system is, or alternatively, it defines the total number of the scans that the radar can achieve during the time of the experiment.

PulseON ® 410 transceiver provides a software controlled adjustable, variable gain attenuator (*i.e.*, transmit gain). This allows the user to reduce the transmit power of the PulseON ® 410 unit (*i.e.*, by as much as 30 dB below the regulatory limit) by setting the value of a register to number between 0 and 63. The relationship between the value selected for transmit gain and transmit power delivered to the antenna port is shown in Fig. 5.5. When transmit gain set to zero, the PulseON ® 410 unit will transmit at the minimum power supported by the PulseON ® 410 transmitter. Setting the transmit gain to a value of 63 will set the PulseON ® 410 unit to maximum transmit power. The default setting is 44, which yields a transmit power of -14.78 dBm. In our experiments, the default setting of the transmit gain of 44; hence a transmit power of – 14.78 dBm, was used with all antenna types. Thus, a fair comparison on the impact of different antenna radiation characteristics on the obtained measurement accuracy was carried out.

The PulseON ® 410 transceiver applies bandpass filtering with characteristics shown in Fig. 5.6. Different other filtering types can be applied through the radar software such as motion

and detection data filters. It should be noted that these filters are very general in nature as they are built-in options provided by the software. It is worth mentioning that all the parameter settings associated with PulseOn ® 410 radar were kept the same in all experiments in order to study only antenna selection effects on the measurements. The detailed description of the TimeDomain PulseOn ® 410 transceiver and its parameters settings can be found in [48] and [101].

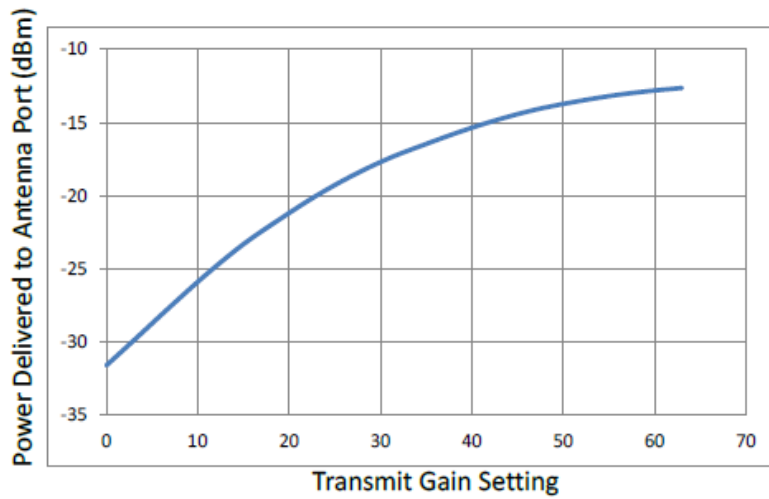


Fig. 5.5: PulseON ® 410 transmit gain setting vs. transmit power [101].

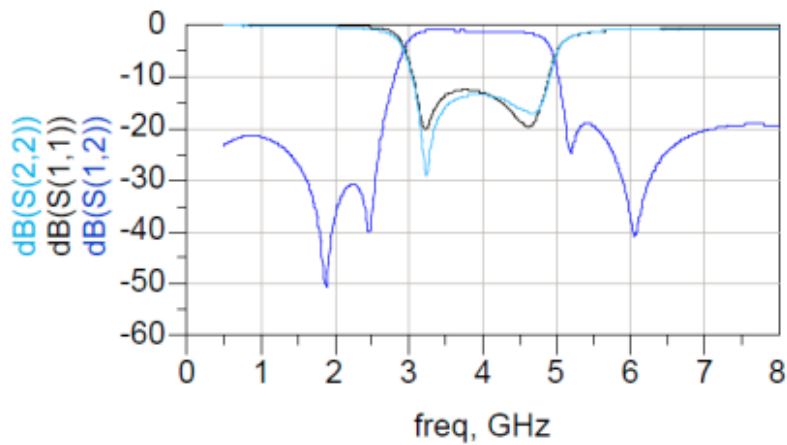


Fig. 5.6: Characteristics of bandpass filter applied by PulseON ® 410 transceiver [101].

5.2.4 Antenna Selection

Antennas such as single patch [87], Yagi [102], patch array [91], and horn antennas [95] have been widely used for several non-contact radar-based sensing systems of vital signs. In order to assess the tradeoffs between antenna characteristics and performance of the proposed radar sensing system for respiratory-rate measurements, three different antenna types were considered: 1) Broadspec UWB antenna [103], 2) A-info JXTXLB-20180 double ridged horn antenna [104], and 3) a double layered Vivaldi antenna proposed in [105]. These antennas were named antenna 1, antenna 2, and antenna 3, respectively, and shown in Fig. 5.7. Two identical antennas were used for transmitting and receiving in a bistatic setting. In order to compare and quantify effects and performance of different antenna types on respiration-rate measurement, each antenna was characterized and then used in the proposed non-contact radar sensing system.

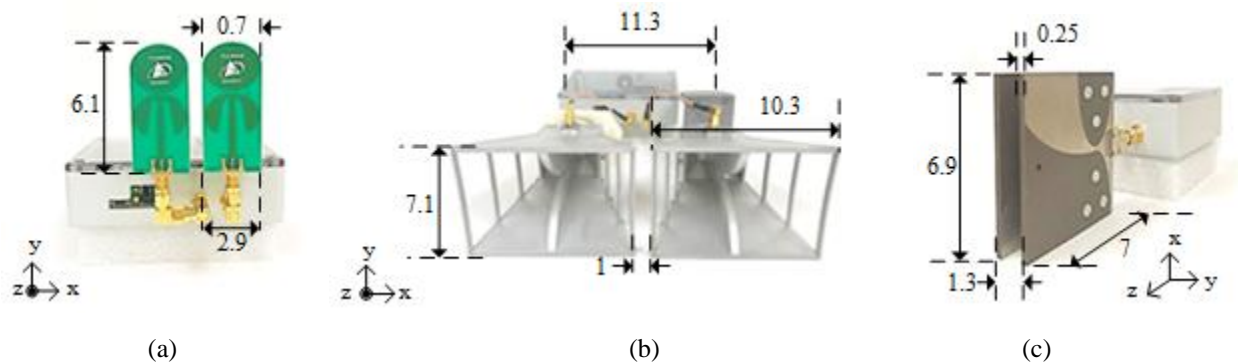


Fig. 5.7: Dimension details of (a) antenna 1, (b) antenna 3, and (c) antenna 2 given in *cm*.

5.2.5 Evaluation of the Proposed Radar System in a Controlled Environment

Experimental sets were designed using a mechanical setup to evaluate the accuracy of the radar sensing system. In the controlled environment experiment, three sets of experiments were conducted:

- 1) The movement frequency varied in range of 0.2 to 0.7 Hz, where s and d were 3 *cm* and 1 *m*, respectively. We chose to study this frequency range as it is close to the reported typical respiratory rates [106]. Frequencies of 0.2 Hz and 0.7 Hz are corresponding to 12 and 42 breaths per minutes, respectively.
- 2) The unit displacement (s) varied in range of 1 to 5 *cm*, while f was kept at 0.3 Hz (18 breaths per minutes) and d was 1 *m*.
- 3) The measurement distance (d) varied in range of 1 to 3 *m*, while f was kept at 0.3 Hz and s was 3 *cm*.

We chose to study this range of displacement and frequency based on the reported studies in the literature [87], [93]. In [87], a Doppler radar sensing system was used to sense the movement of an actuator mimicking the chest wall movements while breathing. The displacement was set from 0.1 *cm* to 4 *cm*, and the movement frequency was changed from 0.2 Hz to 2 Hz. In [93], a similar study was conducted using bistatic radar system where the displacement and the frequency were set at 2 *cm* and 0.2 Hz, respectively.

The signal processing technique used for respiratory-rate extraction from radar received signal was based on the proposed an algorithm presented in [107]. The radar received signal was represented by a matrix. Each row of the matrix represents a sample of a complete radar scan. The first step in the signal processing was to remove the target movement effect. The time-domain autocorrelation of each radar scan was first calculated, followed by shifting the radar scan data to the point where they had the maximum correlation. In order to remove the background clutter, the mean of each column was subtracted from each scan data sample. Finally, by applying fast fourier transform (FFT) to the column of the maximum variance and using frequency domain peak detection, the respiration frequency was detected. Fig. 5.8 shows a sample of processing result of

the SRVD2 unit moved at s of 2 *cm* and f of 0.3 Hz. The measured frequency at 1 *m* distance was 0.3 Hz.

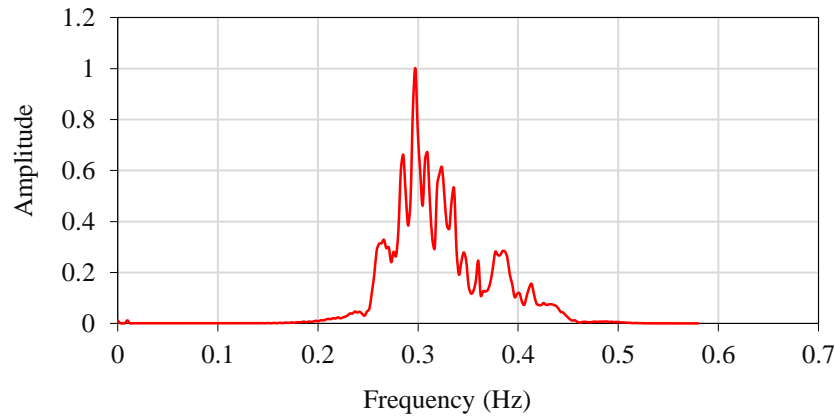
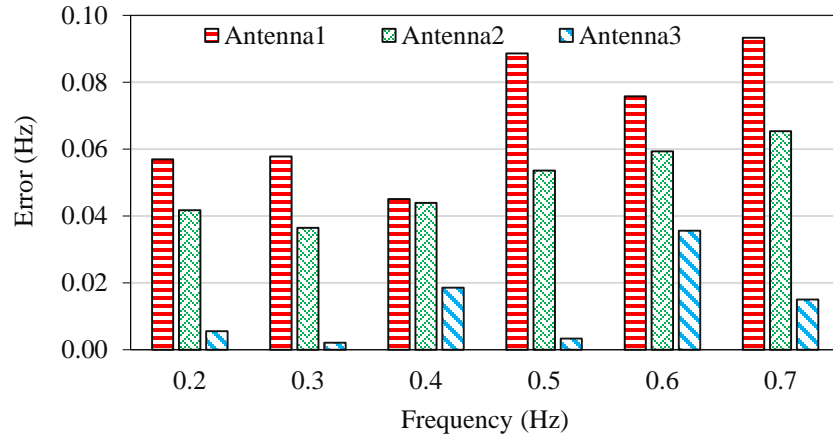
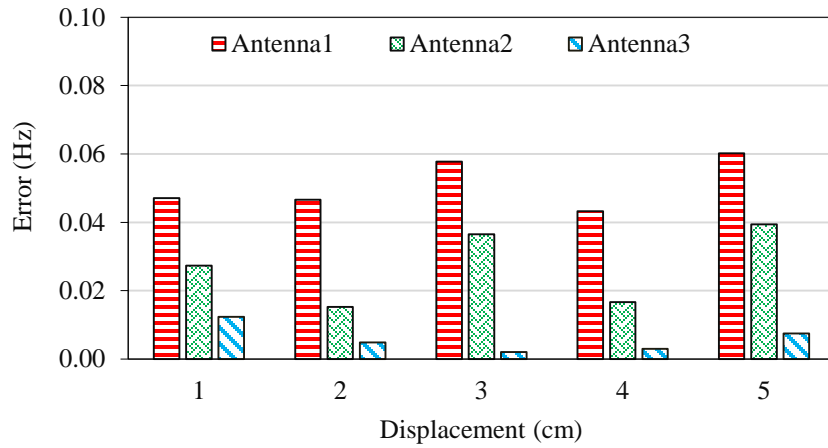


Fig. 5.8: Result of frequency analysis of data received by the radar sensing system.

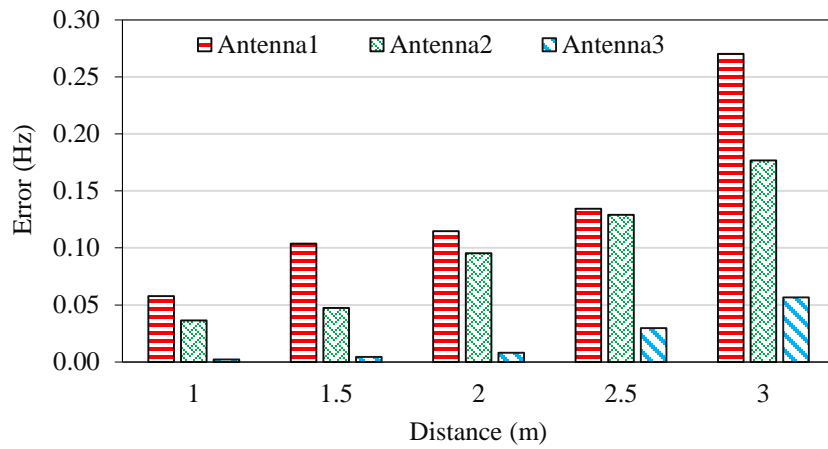
Error in frequency measurements, when three different antennas were used, was calculated and is shown in Fig. 5.9. Measurement error is represented by the absolute difference between the average of five measurement trials using the radar system, for each of 10 seconds duration, and system reference frequency. In general, results demonstrate that the capability of the proposed sensing system depends on the antenna type. The error caused by antennas may be attributed to four possible reasons: (1) bandwidth, (2) cross-polarization, (3) directivity and gain, (4) phase center. The -10 dB input impedance bandwidth of the antennas was measured and results are shown in Fig. 5.10. Bandwidths of the studied antennas are 3.4 GHz – 10.4 GHz (101%), 2 GHz – 18 GHz (160%), and 3.3 GHz – 10 GHz (100%), for antennas 1, 2, and 3, respectively. Antenna bandwidths of these three antennas are sufficient to cover the PulseON® 410 transceiver spectrum 3.1 GHz – 5.3 GHz. Hence, the other three factors were studied.



(a)

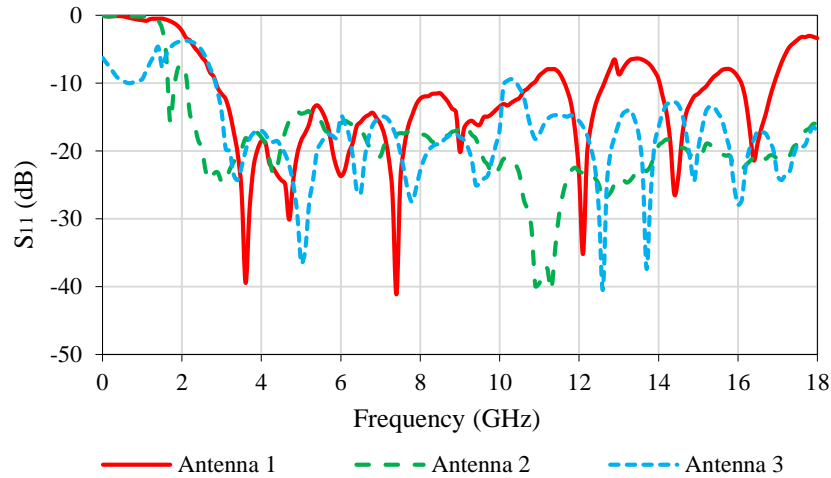


(b)

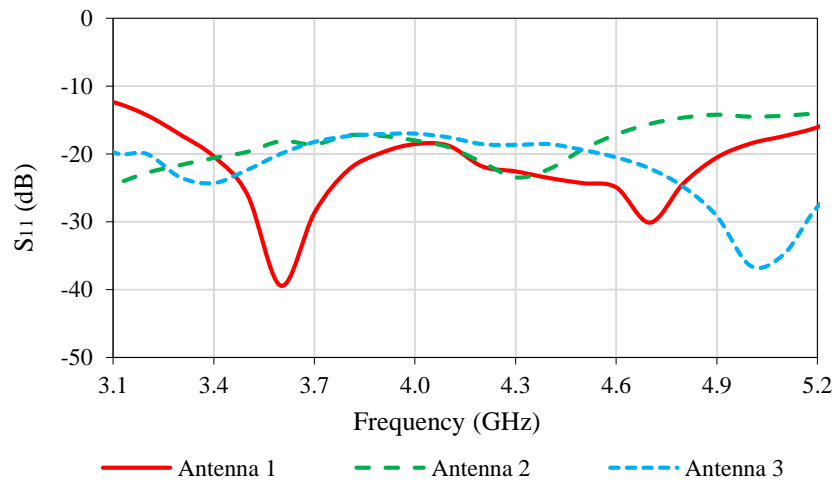


(c)

Fig. 5.9: Absolute error values of radar-based measurement results using three different antennas for different (a) frequencies, (b) displacements, and (c) measurement distances.



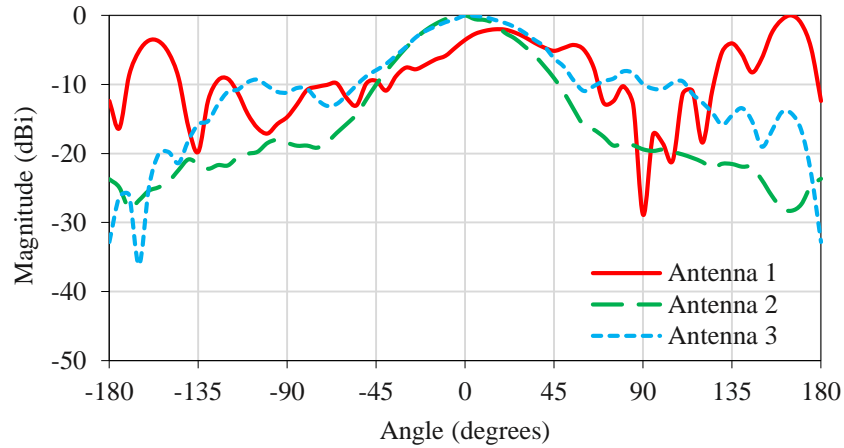
(a)



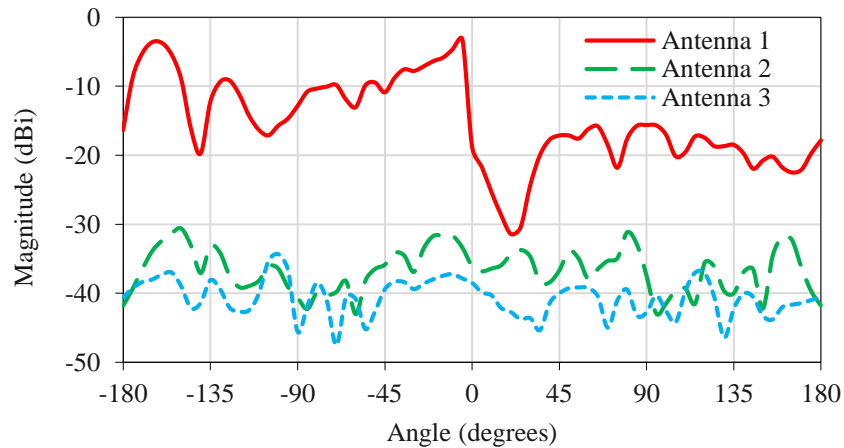
(b)

Fig. 5.10: S_{11} of antennas; (a) [0-18] GHz and (b) [3.1-5.2] GHz frequency band.

Radiation characteristics of the antennas were measured in anechoic chamber, for two principle planes, E-plane (yz -plane) and H-plane (xz -plane), at 4 GHz. Results are shown in Fig. 5.11 and Fig. 5.12, respectively. This frequency was chosen to represent the operating frequency of these antennas that was compatible with the proposed PulseOn[®] 410 UWB radar. Also antennas' gain was measured over the frequency range of 2 GHz – 5.5 GHz and results are shown in Fig. 5.13.



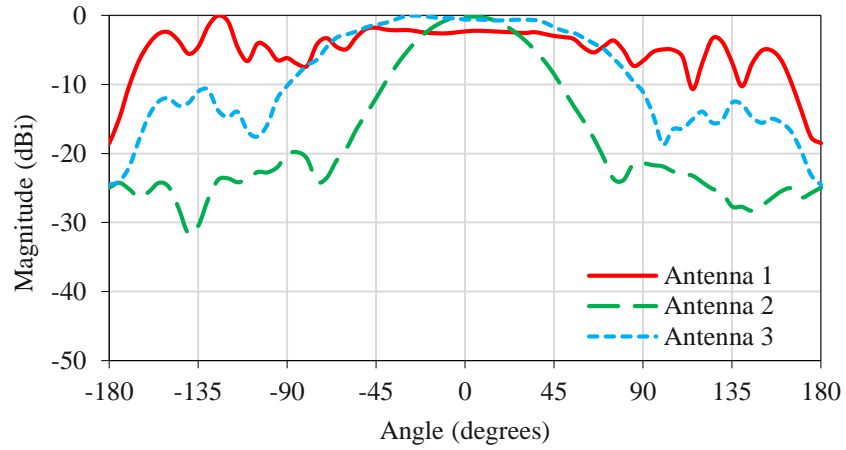
(a)



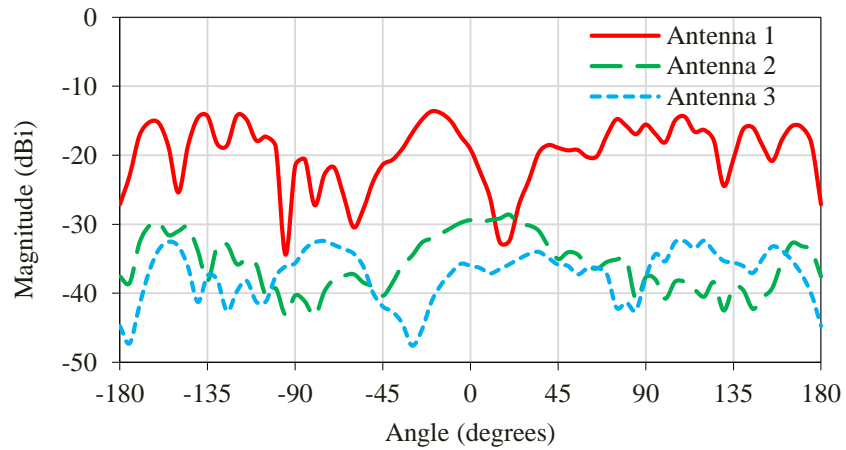
(b)

Fig. 5.11: (a) Co- and (b) cross-polarization of antennas' E-plane.

The highest error levels occurred when antenna 1 was used. Antenna 1 has an omnidirectional radiation characteristic, which means that the antenna is radiating equally in all directions, resulting in transmitting power to the unwanted direction and receiving unwanted reflections from these angles. This antenna also has the highest cross-polarization level among three antennas; hence, it suffers from higher polarization losses compared to other antenna types. Antennas 2 and 3 are both directive. Antenna 3 has a medium gain and directivity and shows the least amount of cross-polarization level. Antenna 2 has the highest gain.



(a)



(b)

Fig. 5.12: (a) Co- and (b) cross-polarization of antennas' H-plane.

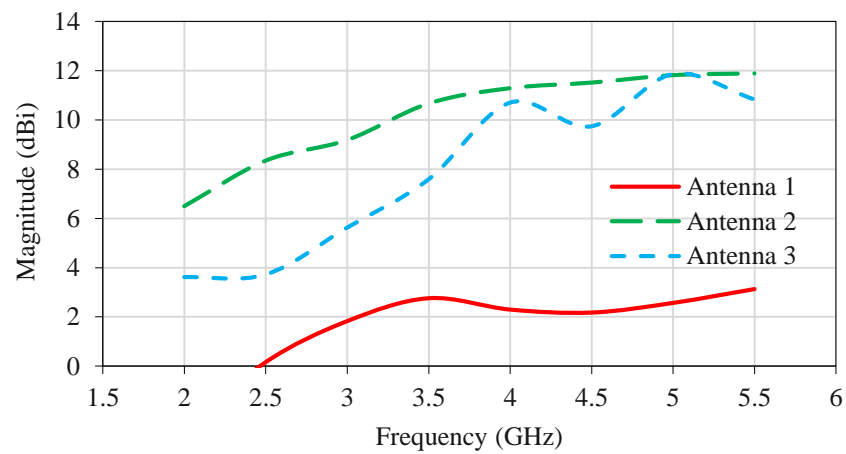


Fig. 5.13: Antenna gains versus frequency.

To compare the three antennas a figure-of-merit (FOM) was defined as follow:

$$FOM = w_1 \times G + w_2 \times BW + w_3 \times PR_E + w_4 \times PR_H \quad (5.1)$$

where G represents the average of antennas' linear gain, shown in Fig. 5.13, BW represents the bandwidth percentage, PR_E and PR_H represent the ratio of antenna co-polarization over cross-polarization field values (in linear scale) in E- and H- planes, respectively, measured along z -axis, where the antenna was pointing toward the target and at the center frequency of 4 GHz. Coefficients w_1 , w_2 , w_3 , and w_4 are weight factors that were set at 0.7, 1, 0.06, and 0.07, respectively. These values were chosen to use antenna 1 as a reference and have each term of Antenna 1 around 1, and the FOM for antenna 1 would be close to 4. The values of these parameters along with calculated FOM are summarized in Table 5.1. The result showed that antenna 3 has the highest FOM. This is in agreement with the respiratory rate results.

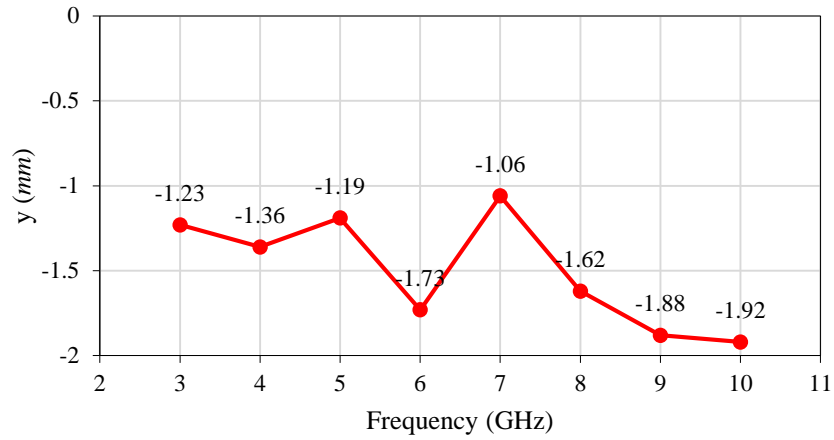
Table 5.1: FOM for three studied antennas.

	<i>Antenna1</i>	<i>Antenna2</i>	<i>Antenna3</i>
G	1.525	11.195	7.835
BW	1.014	1.600	1.008
PR_E	17.783	1148.154	5382.698
PR_H	14.028	724.436	2728.978
FOM	4.131	129.036	520.482

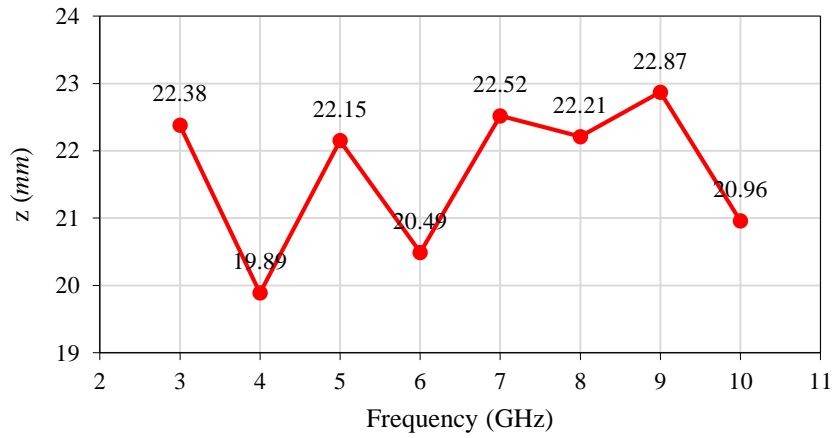
Phase center is another important factor. UWB antennas are dispersive by nature and they usually radiate different frequency components from different parts of the antenna [108]. Dispersive behavior of such antenna type can cause ambiguity in measuring the distance and movement, and therefore, respiratory-rate. Phase center stability is often studied to show the accuracy of radar measurement when various UWB antenna types are used. The antenna phase center is the antenna vocal point from which the electromagnetic radiation spreads spherically

outwards [109]. The movement of the phase center, at different frequencies, will cause signal distortion when antenna is used for pulse transmission/reception. Consequently, it can cause error in distance measurements when they are used as a part of a radar system with UWB signals. An accurate knowledge of the phase center location is essential to the operation of UWB antennas, especially when they are used in radar systems. Numerical investigations of the phase center variations of antenna 3 was carried out using CST MWS [49]. Antenna dimensions along x -, y -, and z -axes are 6.9 cm, 0.25 cm, and 7 cm, respectively (see Fig. 5.7(c)). Results showed no variations along the x -axis. As shown in Fig. 5.14, the maximum observed variations along y - and z -axes were in range of 0.086 cm and 0.298 cm, respectively. In addition, the maximum standard deviation (σ) of the calculations of the phase center location are shown in Fig. 5.15. Small σ indicates that the phase is pretty much identical on all points of the considered calculation area. In simulations, both E- and H- planes of the antenna were considered in the calculations of the phase center location. Since antennas 1 and 2 are commercial antennas, we decided to compare antenna 3 phase center variation with the phase center of similar antenna topologies as those we used, *i.e.*, UWB monopole [110] and a horn antenna [49]. Large phase center movements at different frequencies of operation for these antennas were observed.

Increasing measurement distance between the moving unit and radar increased the error levels, as shown in Fig. 5.9(c). This was more pronounced for antenna 1. As the distance was increased, although, in ideal situation it should not affect the phase measurement, there are more possibility of picking up the multi-path. Therefore, antenna 1 that has omnidirectional pattern showed more increase in error. It is worth mentioning that the physical separation between the two ports of Tx/Rx antennas in the PulseOn® 410 UWB radar is 1.3 cm. Antenna 3 has an end-fire radiation pattern that helps reduce the distance between the Tx and Rx antennas (Fig. 5.7(c)).



(a)



(b)

Fig. 5.14: Phase center variations vs. frequency of antenna 3 along (a) *y*-axis and (b) *z*-axis.

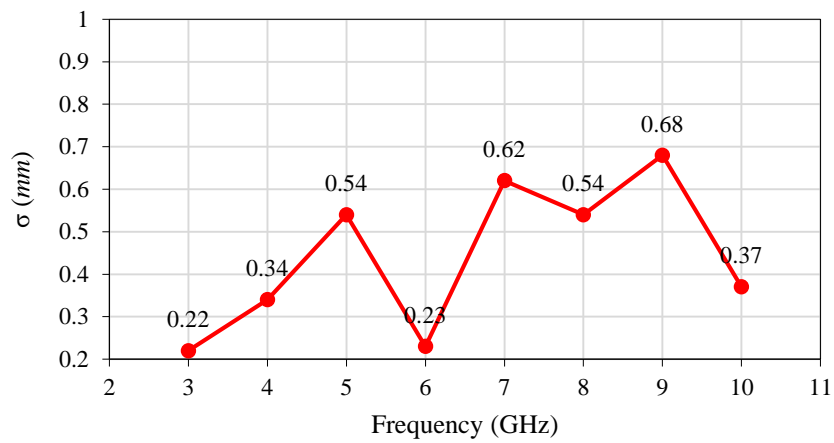


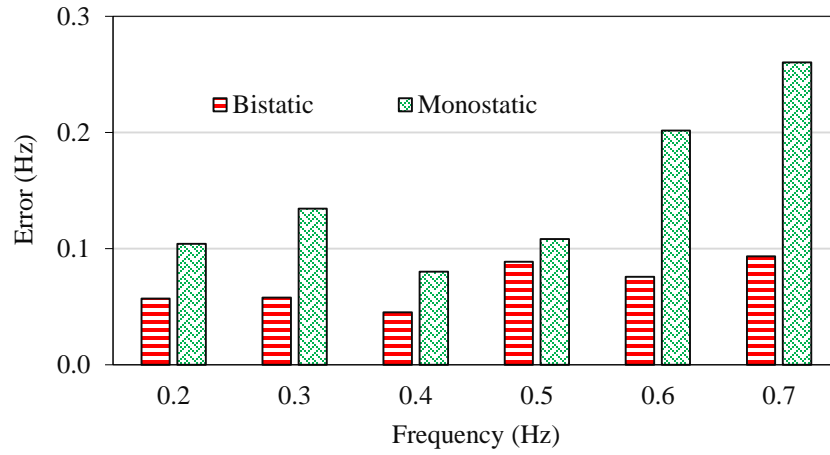
Fig. 5.15: Maximum standard deviation of calculations of the phase center location.

this close proximity is important to ensure the object is in the main beam of end-fire radiation of both antennas.

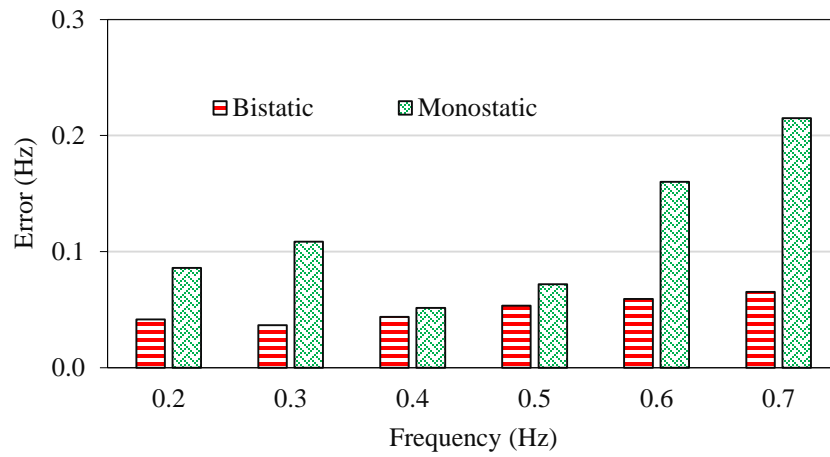
It is worth mentioning that, for comparison purposes, two more studies were conducted. First, a monostatic radar (*i.e.*, single antenna for Tx and Rx) setting was used to do experiment 1 (*i.e.*, measurements of the movement frequency of the mechanical setup). The movement frequency varied in range of 0.2 Hz to 0.5 Hz, where the displacement and separation distance were 3 cm and 1 m, respectively. Error analysis showed that for all three antennas the bistatic setup provided less error compared to monostatic setup, as shown in Fig. 5.16. However, antenna 3 still outperformed the other two antennas, even in monostatic setup. Second, the impact of using metallic target, instead of cardboard plate, on the obtained measurement accuracy, was evaluated for experiment 1. Results using both targets were comparable for frequency ranges (0.2 Hz - 0.5 Hz) using three antenna types, as shown in Fig. 5.17. However, at higher frequencies, the obtained error values using metallic target were higher than those obtained when using cardboard target. Overall, antenna 3 showed the least error in all conducted studies, therefore, it was chosen for the rest of the studies and experiments carried out on human subjects' respiratory-rate measurements.

5.2.6 Respiratory Rate Measurement with Human Subjects

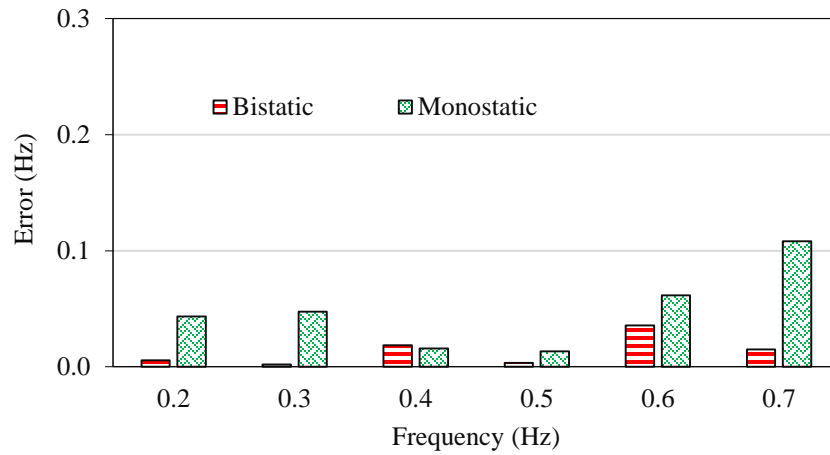
In an effort to evaluate the reliability of the proposed radar sensing system, respiratory-rates of ten test subjects were measured. The participants for the study were recruited via an oral and email advertisements on Electrical Engineering department at University of North Dakota (UND) campus. The approval for experimentation was obtained from the Institutional Review Board (IRB) and Research Development and Compliance (RD&C), which approved the experimental protocols as a minimum risk protocol (*i.e.*, IRB number is IRB-201708-030).



(a)

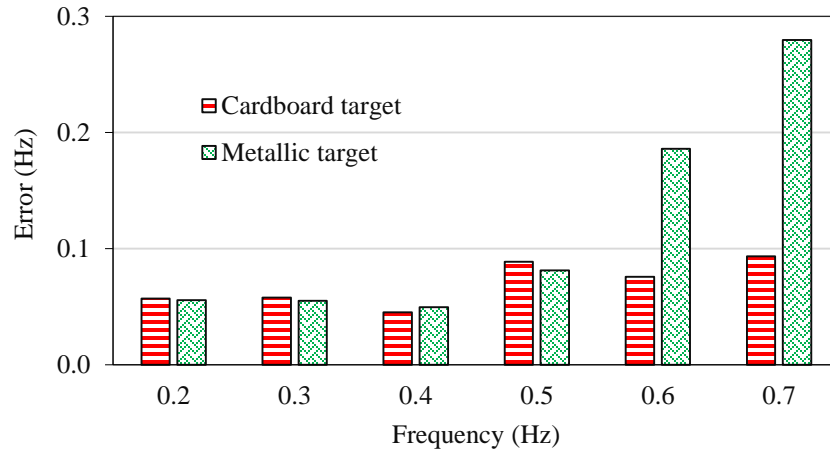


(b)

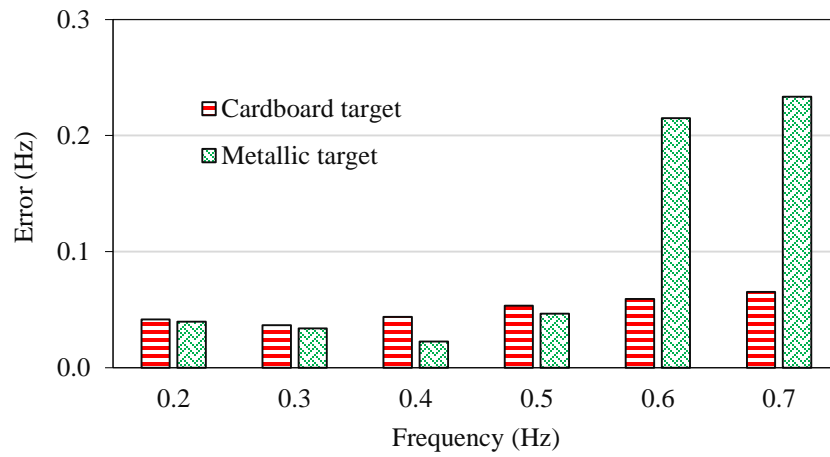


(c)

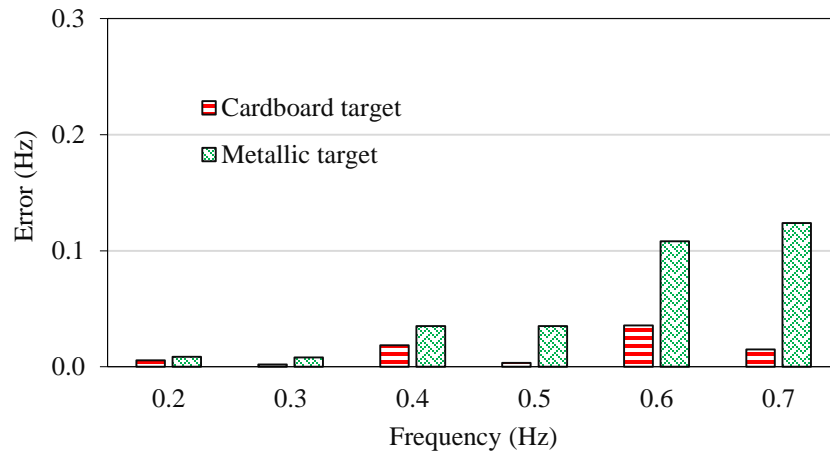
Fig. 5.16: Comparison of monostatic and bistatic radars using antennas (a) 1, (b) 2, and (c) 3.



(a)



(b)



(c)

Fig. 5.17: Results of cardboard and metallic targets using antennas (a) 1, (b) 2, and (c) 3.

Measurements were performed using antenna 3. Each subject was tested 5 times with a total measurement duration of 50 s. The average of these measurements was then compared to a reference respiratory rate measurement to verify the obtained results. Reference measurements were conducted using respiratory belt transducer (SS5L). The detailed characteristics of the ten subjects and the respiratory-rate measurement values are summarized in Table 5.2 and Table 5.3, respectively. Respiration-rates determined by the proposed radar sensor had a generally high correlation with the reference rates measured by SS5L transducer over all subjects. The average of the obtained measurement error values on these subjects was calculated to be less than 0.03 Hz with statistical standard deviation of 0.03 Hz. Fig. 5.18 shows a sample of processing result of respiratory-rate measurements using radar system and SS5L respiratory belt transducer.

Table 5.2: Information summary of 10 subjects.

<i>Subject</i>	<i>Sex (M/F)</i>	<i>Age</i>	<i>Weight (kg)</i>	<i>Height (cm)</i>	<i>Chest Circumference (cm)</i>
S1	F	21	46	102	81
S2	M	21	63	178	85
S3	M	23	85	176	105
S4	M	32	100	173	109
S5	F	27	77	165	97
S6	F	26	53	162	34
S7	M	26	81	172	102
S8	F	27	68	162	93
S9	M	28	56	181	81
S10	F	31	83	180	110

Table 5.3: Evaluation of respiratory rate measurements for 10 subjects.

<i>Subject</i>	<i>f_{reference} (Hz)</i>	<i>f_{radar} (Hz)</i>	<i>Error (%)</i>	<i>Reference value (breaths/min)</i>	<i>Radar value (breaths/min)</i>
S1	0.49	0.5	1.14	29	30
S2	0.24	0.2	18.08	14	12
S3	0.34	0.3	2.07	20	18
S4	0.21	0.2	2.45	12	12
S5	0.18	0.2	4.02	10	12
S6	0.24	0.2	2.89	14	12
S7	0.40	0.4	4.58	24	24
S8	0.27	0.3	1.78	16	18
S9	0.35	0.3	1.71	21	18
S10	0.32	0.3	1.16	19	18

In addition, a study on the effect of different measurement times (*i.e.*, 10, 20, and 30 seconds) on the measurement accuracy was conducted for two test subjects using PulseON® 410 radar system. Results were compared to the reference measurements using a BIOPAC biological data acquisition system. As can be seen in Fig. 5.19, results obtained using PulseON® 410 radar system with scanning times of 10, 20, and 30 seconds were comparable and close to the reference values. It is worth mentioning that for each scanning time, the reported results using PulseON® 410 radar system were the average of five measurements. Hence, we chose to have the measurement time set at 10 seconds in the previous reported studies (*i.e.*, in this case the total time of measurement duration is 50 seconds) to avoid long time of measurement, which could cause subject discomfort. In addition, it was easier to have a constant and controlled experimental conditions spatially the surrounding environment within 10 seconds.

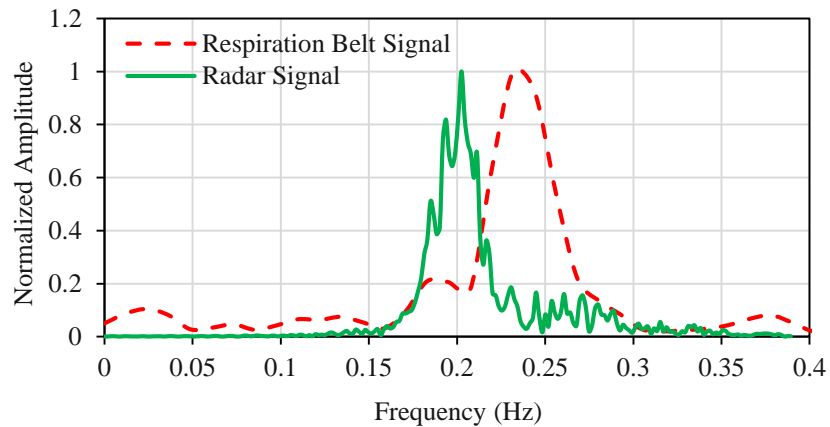


Fig. 5.18: Example result of respiratory rate measurement of test subject (S6).

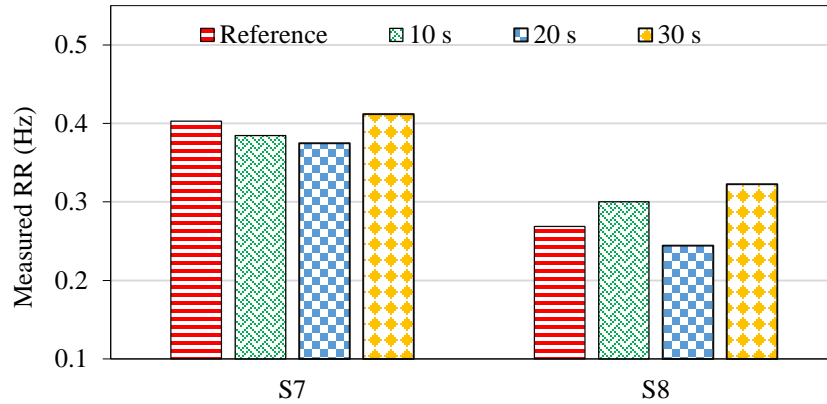


Fig. 5.19: Respiration-rates of two test subjects for four different scanning times.

5.3 An Accurate Phase-Based Localization Method of RFID Tag

5.3.1 Background

Positioning is the process of determining positions of people, equipment, and other objects. It has recently been an active research area in which much of the research focuses on utilizing existing technologies to address the problem of positions' determination. Positioning can be classified, according to the environment where the positioning is conducted, into two types: outdoor positioning and indoor positioning. Whereas outdoor positioning is performed outside buildings, indoor positioning is performed inside buildings (*i.e.*, houses, hospitals, and malls). Location detection and tracking functions have been very successfully implemented at outdoor environments using global positioning system (GPS) technology. The GPS has made a tremendous impact on our everyday lives by supporting a wealth of applications in guidance, mapping, and so forth. Nevertheless, in indoor environments, GPS or equivalent satellite-based location systems perform poorly in accuracy and precision, due to the lack of line of sight and attenuation of GPS signals as they cross through walls [111]-[112].

In recent years we have witnessed a major interest and research efforts in developing an accurate RF-based indoor localization and tracking systems in a diverse range of applications involving telemedicine [102]. Currently, indoor positioning is central in the deployment of seamless emergency response services such as E911 in the U.S. For instance, the possibility to track patients while they are inside a hospital and especially in first aid area is becoming increasingly important. In these areas emergencies frequently occur and this causes a constant flow of doctors and nurses from one room to another. For example, specific mental disease such as Alzheimer disease, often leads to lost or forgotten patients around the hospital. Hence, knowing the right position of a person inside a medical facility at any time is a need that presents a problem within indoor localization research field. Unfortunately, application of such a service is hindered by the lack of common benchmarks and platforms. The medical scenario is a particularly hostile context for indoor localization because the transmitters and receivers usually adopted to locate objects have to deal with medical devices; indeed, these machineries often come with some limitation on the allowed radiofrequency range to be used near them. This has recently pushed different research entities worldwide to propose advanced and beyond state-of-the-art solutions in this domain. For example, in [113], indoor localization system based on RFID technology was proposed in a hospital environment. The infrastructure was deployed and evaluated in the emergency unit of a large Italian hospital (*i.e.*, 48 rooms covering about 4000 m^2) to detect the room where lost or forgotten patients lie. Extensive experiments showed the potential of such technology for indoor localization applications in terms of accuracy, precision, complexity, robustness and scalability. In 98% of cases the system localized the correct room (83%) or one of its adjacency (15%). In [114], investigations in indoor scenarios on UWB for human body localization were performed via numerical and analytical methods by placing wearable compact

sensors on the upper part of the body. This work succeeded in performing 3D localization using such sensors with localization accuracy of 2 *cm* to 3 *cm*.

Accuracy, reliability, and estimation speed, are the key parameters for indoor localization and tracking system. In 2016, Alarifi *et al.*, classified indoor positioning technologies according to the infrastructure of the system that uses them, as shown in Fig. 5.20. Indoor positioning technologies are classified into two main classes; building dependent and building independent. Building dependent indoor positioning technologies refer to technologies that depend either on an existing technology in the building or on the map and structure of the building. On the other hand, the building independent technologies do not require any special hardware in a building. Building dependent indoor positioning technologies can be further divided into two major classes: indoor positioning technologies that require dedicated infrastructure and indoor positioning technologies that utilize the building's infrastructure. For example, most buildings contain WIFI while almost none contains radio frequency identification. Indoor positioning technologies that require dedicated infrastructure are radio frequency, that is either RFID [115] or UWB [116], infrared [117], ultrasonic [118], and Zigbee [119]. Indoor positioning technologies that utilize the building's infrastructure are WIFI [120], cellular based [121], and Bluetooth [122]. On the other hand, the building independent technologies are dead reckoning [123] and image based technologies [124]. In dead reckoning, an object can determine its current position by knowing its past position, its speed and the direction in which it is moving. Image based technologies mainly rely on a camera (*i.e.*, sensor and image processing) [111].

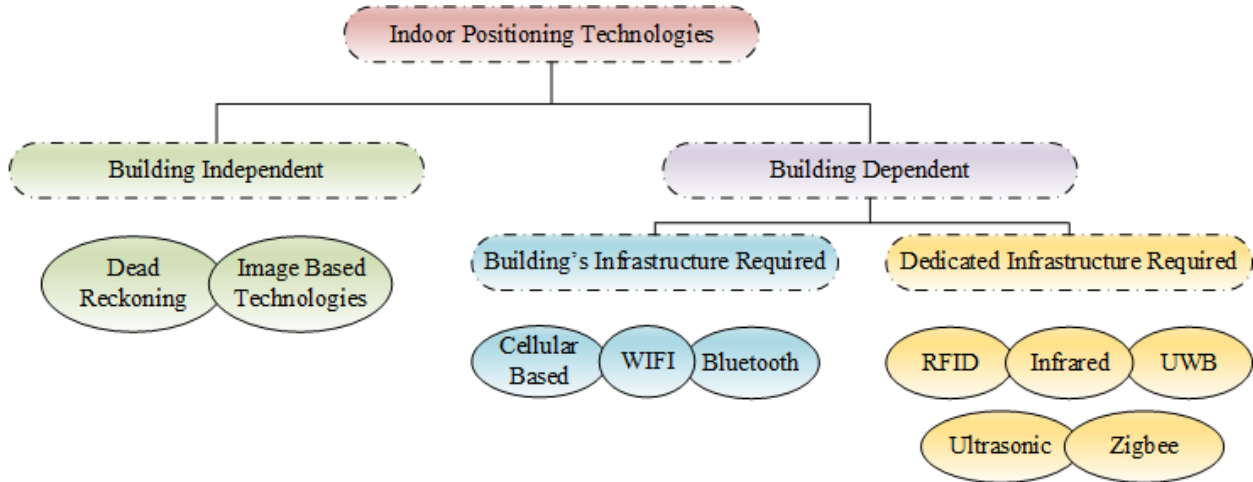


Fig. 5.20: Classification of indoor positioning technologies.

The appropriate indoor positioning technology should be selected carefully in order to make the right balance between the complexity and the performance of the indoor localization system. Among the proposed localization and tracking technologies, RFID technology provides an accurate tool for indoor localization with advantages of high resolution of position estimation, flexibility, and low-cost of system installation. RFID is a technology that uses radio waves to make a specialized circuit produce a response containing a unique identifier; as the circuit could be attached to people, animals, or objects, it provides a method for identifying and tracking them [112]. It is based on exchanging different frequencies of radio signals between two main components: readers and tags. Tags emit radio signals that are received by readers and vice versa. Both tags and readers use predefined radio frequencies and protocols to send and receive data between them. There are two types of tags; active tags and passive tags [111]. Passive RFID tags operate without a battery. They are mainly used to replace the traditional barcode technology and are much lighter, smaller in volume, and less expensive than active tags [125]. On the other hand, an RFID reader consists of different components; including an antenna, transceiver, power supply, processor, and interface, in order to connect to a server [111].

5.3.2 System Overview

A commercially off-the-shelf 3D positioning RFID-based system from Lunantech Inc. [126] was used. This system operates within the industrial, scientific, and medical ISM 2.45 GHz band and capable to find the (x, y, z) coordinates of a semi-passive RFID tag with a precision of 0.1 mm and under 10 ms response time. Two studies were performed to compare the theoretical, measured and simulated phase of the backscattered signal from the RFID tag. First, for simplicity, the module was used to evaluate the phase data of a single transceiver antenna. Second, antenna array of four elements was used for enhanced system performance. The two measurement setups are shown in Fig. 5.21 and Fig. 5.22 for a single antenna and antenna array transceivers, respectively. Antennas connected to the RFID reader were inset fed patch antennas with $48 \text{ mm} \times 48 \text{ mm}$ (length \times width) dimensions and placed at a distance along the z -axis from the RFID tag. They were made of a 1.6 mm-thick FR4 substrate, with ϵ_r and $\tan\delta_e$ of 4.14 and 0.025, respectively. The tag antenna had similar specifications. It is worth mentioning that antennas in the array were numbered as shown in Fig. 5.22. The antenna on the right was antenna 1 and the rest are numbered counter-clockwise. The tag antenna was numbered as antenna 5. Antennas 1 and 3 were horizontally polarized, while antennas 2 and 4 were vertically polarized. The tag antenna was dual polarized.

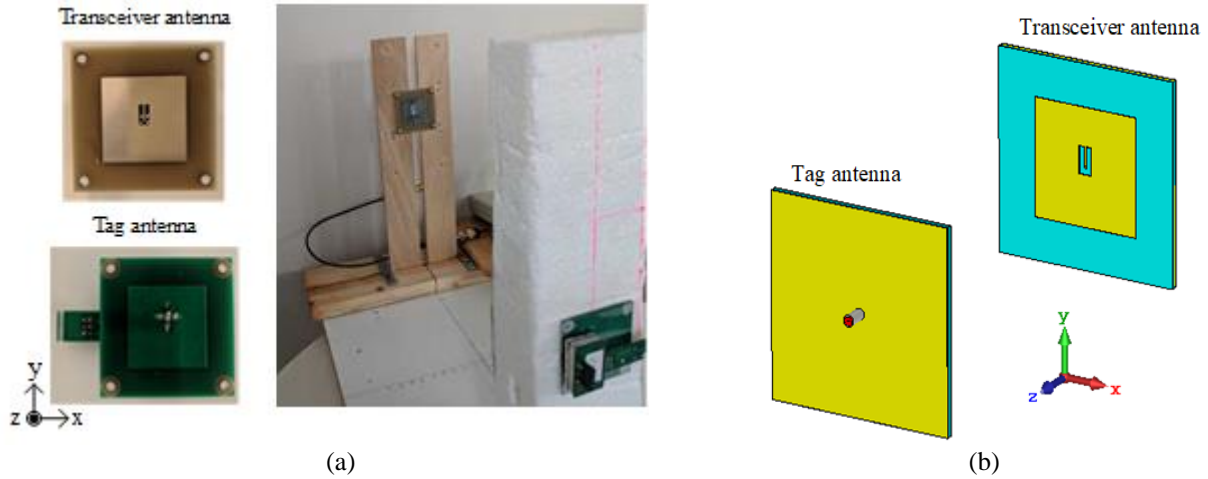


Fig. 5.21: Localization using single antenna; (a) measurement and (b) simulation setups.

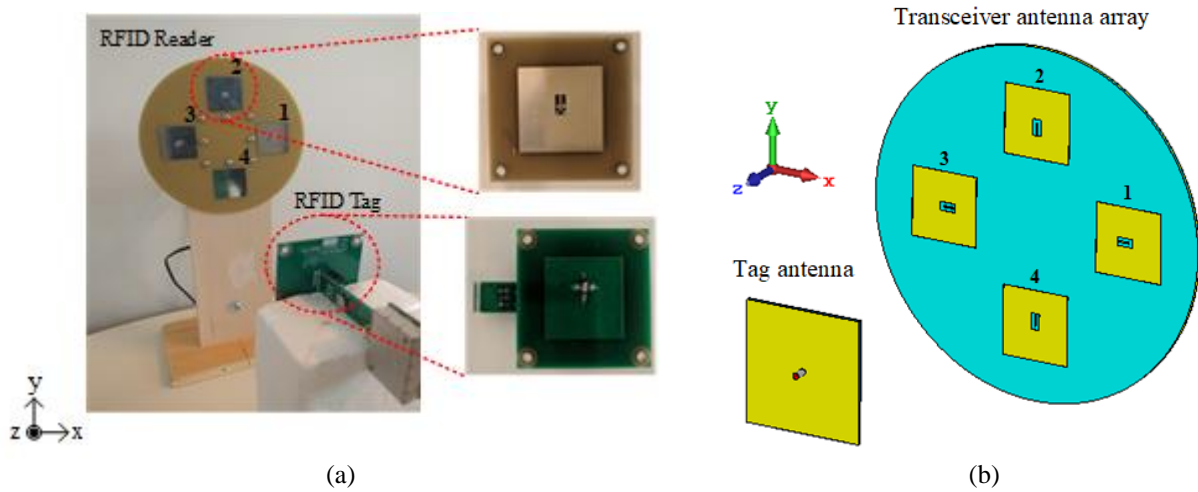


Fig. 5.22: Localization using antenna array; (a) measurement and (b) simulation setups.

The RFID tag backscattered and encoded the waves transmitted by the transceiver antenna(s) (*i.e.*, a single antenna in case of the first setup and four elements antenna array in case of the second setup) using a battery-operated encoder. The transceiver calculated the phase of the backscattered wave from the tag with respect to the transceiver antenna(s). The phase of the backscattered changed based on the distance of the tag from the transceiver antenna(s). This property was used to find the tag location by having the phase data from the transceiver antenna(s)

[126]. In order to distinguish the backscattered tag wave from the rest of the waves received by the transceiver antenna(s), the tag impedance was encoded with a unique pseudo noise code (PN). The transceiver was factory calibrated to provide zero phase value when the tag is located at $x = 0, y = 0, z = 15 \text{ cm}$. This distance represents the minimum distance of the tag to the RFID reader to achieve the normal operation of the system. The detailed description of the system as well as the theory of operation can be found in [126]. In simulations, antennas attached to the RFID reader in both setups and the tag antenna were modeled with the same specifications as those used in the measurement setup.

5.3.3 Results and Discussion

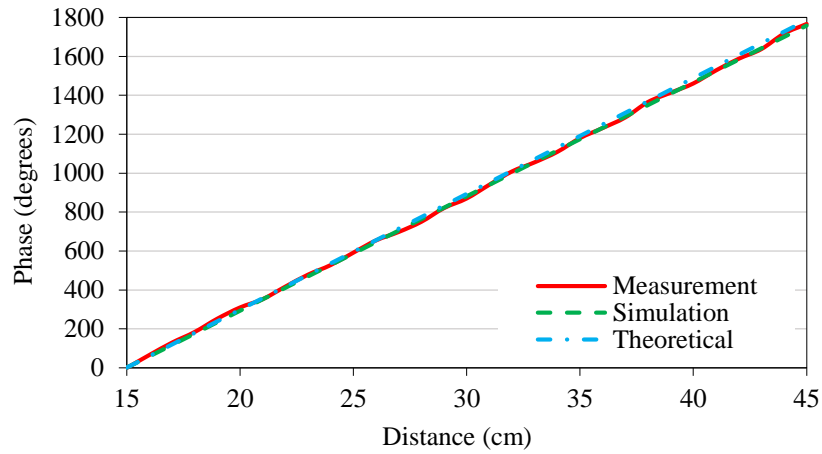
Using setup 1 (Fig. 5.21), the phase of the backscattered signal from the tag antenna was recorded for three different scenarios based on simulations and measurements. In the first scenario the separation distance between the transceiver antenna and tag antennas in z -direction (*i.e.*, perpendicular to transmitter antenna) was changed from 15 cm to 45 cm with increments of 1 cm . In the second scenario the distance in z -direction was kept at 15 cm while the tag antenna was moved in x -direction (*i.e.*, horizontal to transceiver antenna) between -15 cm to 15 cm , with increments of 1 cm . Finally, in the last scenario, the distance in z -direction was kept at 30 cm while the tag antenna was moved in x -direction between -15 cm to 15 cm with increments, of 1 cm . These scenarios were named as case 1, case 2, and case 3, respectively. In addition, the expected values of the phase (*i.e.*, theoretical) were calculated using (6.1) and results are shown in Fig. 5.23:

$$d = \frac{\lambda}{2} \left(\frac{\varphi}{2\pi} + n \right) \quad (6.1)$$

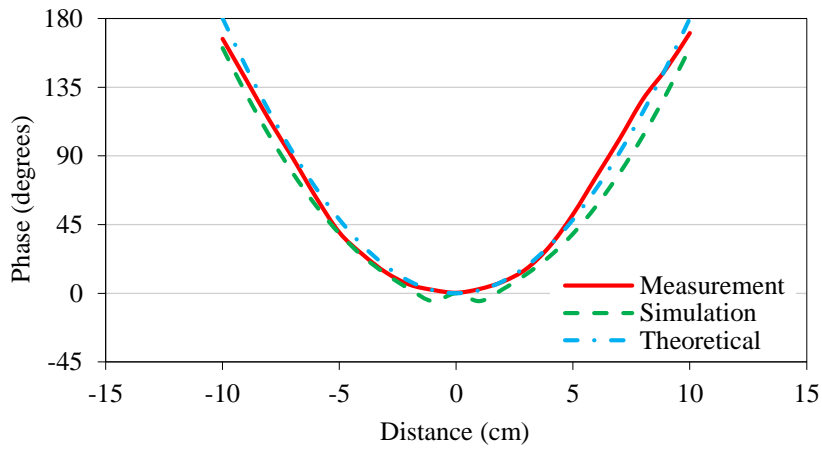
where d is the distance between transmitter and tag antennas, λ is the wavelength, φ is the received phase, and n is an integer number due to the periodic change in the phase.

Using setup 2 (Fig. 5.22), the phase of the backscattered signal from the tag antenna was recorded for two different scenarios, using the antenna array, based on simulations and measurements. In the first scenario the separation distance between the transceiver array and tag antennas in z -direction (*i.e.*, perpendicular to transmitter antenna) was changed from 15 *cm* to 25 *cm* with increments of 1 *cm*. In the second scenario the distance in x -direction (*i.e.*, horizontal to transceiver antenna) was kept at 4 *cm* while the tag antenna was moved in z -direction between 15 *cm* to 25 *cm*, with increments of 1 *cm*. These scenarios were named as case 4 and case 5, respectively. Results of backscattered phases recorded using the four antennas in the array are shown in Fig. 5.24 and Fig. 5.25 for cases 4 and 5, respectively.

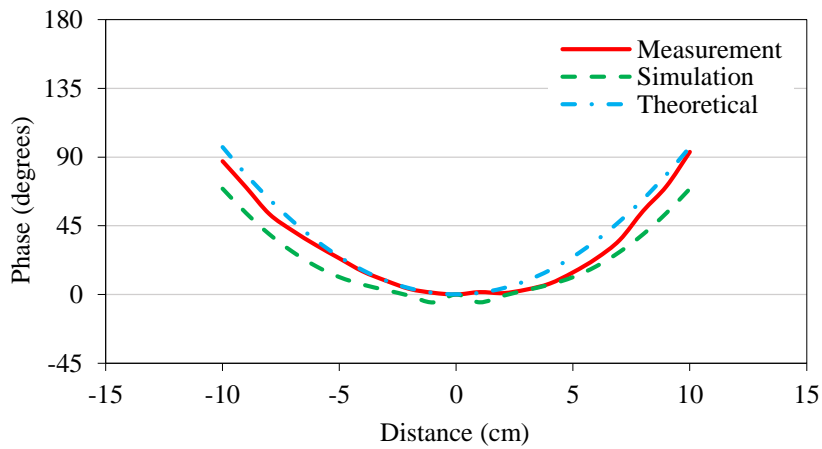
A good agreement between theoretical, simulation, and measurement values of the backscattered phase was achieved using both setups. The slight disagreement between actual phase and simulation results can be attributed to the error in the tag placement or the reflections by the nearby objects around the transceiver antenna(s).



(a)

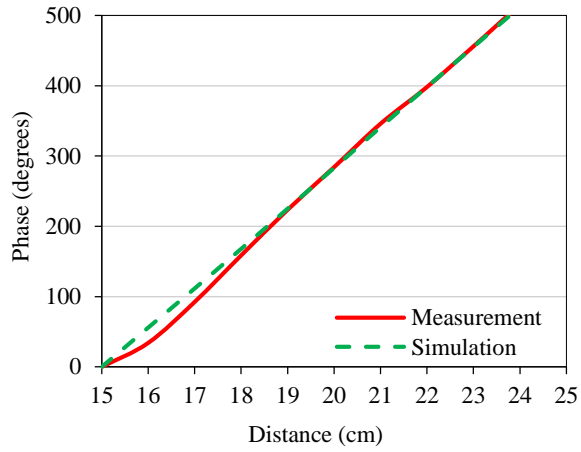


(b)

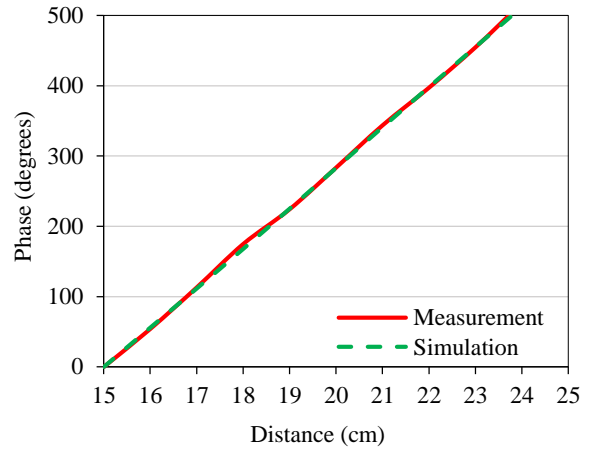


(c)

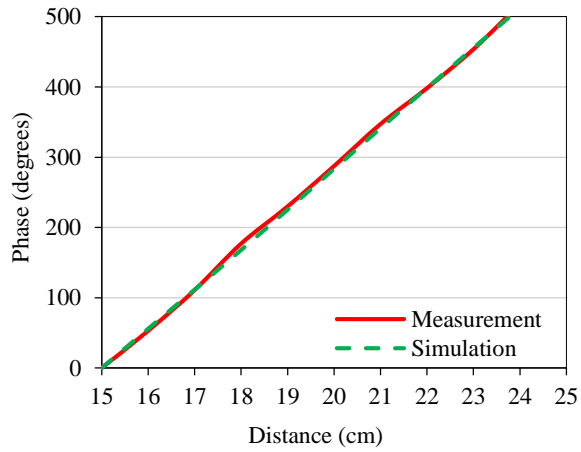
Fig. 5.23: Phase results of (a) case 1, (b) case 2, and (c) case 3.



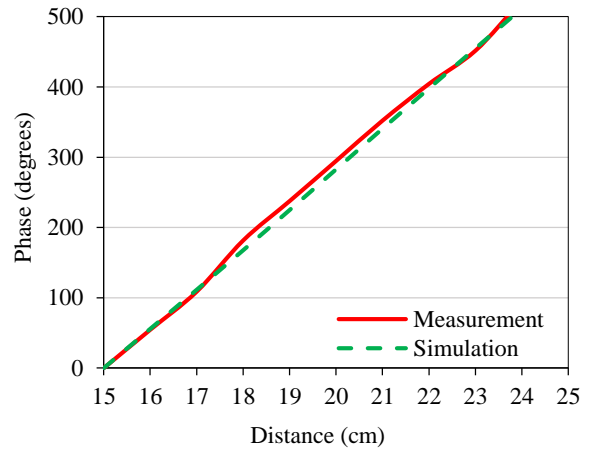
(a)



(b)



(c)



(d)

Fig. 5.24: Phase results of case 4; (a) antenna1, (b) antenna2, (c) antenna3, and (d) antenna4.

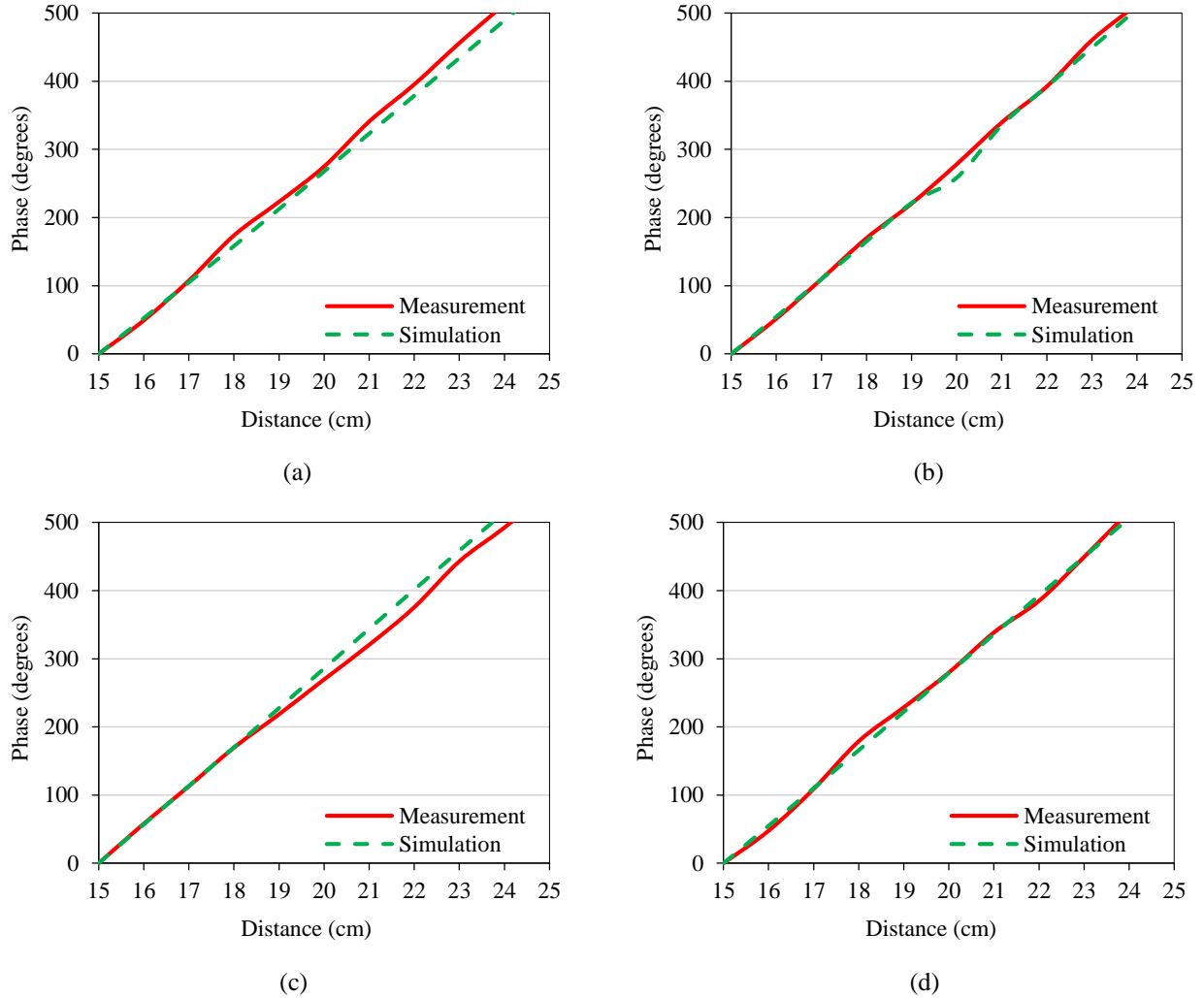


Fig. 5.25: Phase results of case 5; (a) antenna1, (b) antenna2, (c) antenna3, and (d) antenna4.

In addition, based on simulations, a study on the effects of mutual coupling between the array elements in the second setup on the phase measurements was carried out and results are shown in Table 5.4. The backscattered signal phase was recorded by antenna 1 in presence of the other array elements (*i.e.* scenario 1) and the absence of the other array elements (*i.e.* scenario 2). The slight differences in the phase values were observed due to the coupling effects. Fig. 5.26 shows the transmission coefficient when the tag was placed at $x = 4 \text{ cm}$, $y = 0$, $z = 15 \text{ cm}$, over the frequency range of 2 GHz to 3 GHz.

Table 5.4: Simulated antenna 1 phase for scenarios 1 and 2.

<i>Distance (cm)</i>	<i>Scenario1 (degrees)^a</i>	<i>Scenario2 (degrees)^b</i>
15	0.0000	0.000
16	52.463	52.905
17	105.003	103.803
18	158.168	155.218
19	-147.636	-151.308
20	-92.447	-96.706
21	-36.876	-41.142
22	18.523	13.873
23	73.730	68.378
24	128.986	122.921
25	-175.201	-181.845

^aScenario1: antenna array and ^b Scenario2: single antenna.

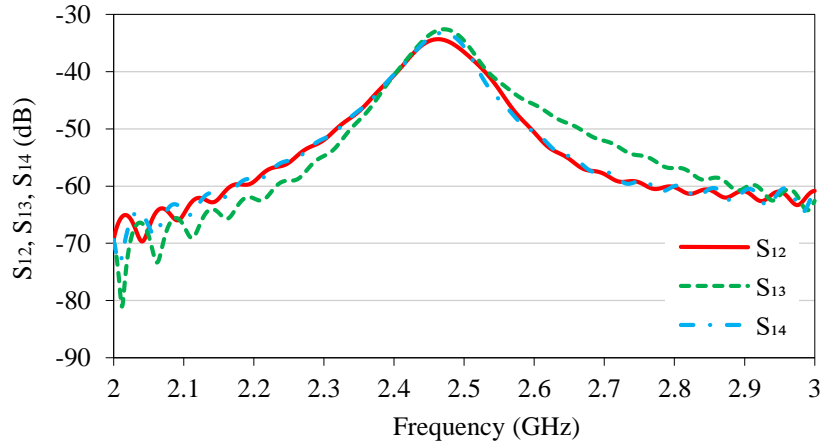


Fig. 5.26: Simulated transmission coefficients of antenna array elements.

5.4 Summary

First, to evaluate a radar-based sensing system using different antenna types for respiratory-rate measurement, antenna type selection was done by testing the performance of three types of antennas attached to a TimeDomain PulseOn ® 410 UWB radar system, measuring the movement rate of controlled movable device. Experiments were designed in order to assess the tradeoffs between antenna selection and the proposed sensing system's accuracy. Error analysis for various parameters associated with pulmonary activities, such as breathing frequency and chest

displacement and measurement distance, was performed. Different system scenarios were considered for evaluation such as monostatic vs. bistatic radar configurations, cardboard target vs. metallic target, and different scanning time windows. Results indicated that the proposed sensing system is less affected and shows less error when an antenna with directive radiation pattern, low cross-polarization and stable phase center is used. Due to its good radiation characteristics and small form-factor this antenna was then selected to study the respiratory rates of ten test subjects to investigate whether it is possible to measure the respiratory-rate using this system. Reference measurements were performed and the accurate values of the respiratory-rates of the test subjects were collected and compared with the radar setup results. The mean error value of the respiratory rate measurements was 0.03 Hz with a statistical standard deviation of 0.03 Hz.

Second, an accurate electromagnetic model of indoor localization system of a semi-passive RFID tag was presented. Simulation and measurement results of the backscattered wave phase demonstrated the capability of the proposed simulation model to provide an accurate estimation of the phase measurements in a realistic scenario. Moreover, it was found that the effects of mutual coupling between the array elements on the phase values were negligible. Thus, the phase of the reflected waves from the tag was mainly determined by the distance between the tag and each antenna element, and was not affected by the induced currents on the other elements.

CHAPTER 6

CONCLUSIONS, CONTRIBUTIONS, AND FUTURE WORK

This chapter presents an overview of the research conclusions, challenges, and contributions to the research fields discussed in the previous chapters. In addition, a general discussion on thoughts for the future work are presented.

6.1 Research Conclusions and Challenges

6.1.1 *Wearable Antenna Design*

The design, realization, and characterization of flexible and textile wearable antennas were presented. The proposed wearable antennas consisted of monopole antennas integrated with AMC structures, acting as a ground plane. The main conclusions and achievements of the flexible wearable antenna design, working within ISM 2.45 GHz band, are explained as follows:

- The proposed AMC antenna featured a small footprint, with dimensions of $124 \times 124 \times 3.6 \text{ mm}^3$, and provided -10 dB input impedance bandwidth of 16% (2.2 GHz – 2.6 GHz).
- The in-phase reflection characteristic of the AMC structure enhanced the radiation characteristics of the antenna in terms of antenna gain and FBR. The achieved AMC antenna gain and FBR were 4.6 dBi and 22.16 dB, respectively. On the other hand, the monopole antenna had a 2.6 dBi antenna gain and 0.009 dB FBR values.
- A robust matching properties of the proposed AMC antenna were observed compared to the stand-alone monopole antenna in the presence of different human body models such as the simplified layered and voxel body models. AMC antenna showed steady impedance matching similar to when it functioned in free-space for different studied scenarios.

- The calculated SAR values for flat and crumpled AMC antenna were very low, with a reduction of more than 90% compared to the SAR values of the stand-alone flat and crumpled monopole antenna. The obtained SAR levels of AMC antenna were within the specified limits allowed by SAR standards, which give a reliable indication of the benefits of AMC being used as an antenna ground plane.

However, although the proposed flexible antenna showed performance superiority in terms of the wide -10 dB input impedance bandwidth compared to some of the reported wearable antennas in literature, as shown in Table 6.1, flexibility tests in terms of monopole and AMC antennas' performance under crumpling conditions showed that AMC antenna was more susceptible to crumpling conditions. Also, the chosen substrate flexible material (*i.e.*, flexible RO3003) was adding more limitations to the overall antenna flexibility. As the ultimate goal is to design miniaturized efficient wearable antenna, but at the same time to achieve flexibility, low profile, and conformity requirements of the wearable antenna. Hence, the research was directed toward entire textile based wearable antenna design.

Table 6.1: Comparison of the proposed wearable antenna with reported work in literature.

<i>Ref.</i>	<i>Year</i>	<i>Freq. (GHz)</i>	<i>Volume (mm³)</i>	<i>B.W.^a (GHz)</i>	<i>B.W. (%)</i>	<i>Gain (dBi)</i>	<i>Material (dielectric/conductive)</i>
[44]	2017	2.44	50×50×5.5	2.37 – 2.64	11.3	5.20	PDMS/Silver Nano-wires
[41]	2017	2.45	88×83×9	2.40 – 2.50	4.00	6.40	RO3003/Copper
[34]	2016	2.45	100×100×6	NA	9.85	2.42	Felt/ShieldIt Super
[43]	2016	2.4	50×50×9.5	2.42 – 2.47	1.80	4.12	Latex/Silver ink
[39]	2013	2.45	65.5×65.5×3.2	NA	18.0	4.00	PolyimideKapton and vinyl/NA
[40]	2013	2.48	150×150×3	2.38 – 2.50	5.08	NA	Jeans/Flexible copper sheets
[42]	2012	2.45	150×130×2.87	2.36 – 2.61	10.0	NA	Commercial papers/Copper
Proposed	2016	2.40	124×124×5.12	2.20 – 2.60	16.0	4.60	Pellon and RO3003/ShieldIt Super

^a Bandwidth (B.W.).

The main conclusions and achievements of the textile wearable antenna design, working within ISM 5.8 GHz band, are explained as follows:

- The proposed compact low-profile AMC antenna featured a small footprint, with dimensions of $102 \times 68 \times 3.6 \text{ mm}^3$, and achieved -10 dB input impedance bandwidth of 34% (4.30 GHz – 5.90 GHz), with a gain value of 6.12 dBi.
- For on body performance, different numerical body models of different compositions, geometries and homogeneity properties were proposed in order to give a close study on the accuracy of the numerical on body evaluation of wearable antennas. Results demonstrated that when focusing on the matching performances of the antennas, different body models can be satisfactory representations. The presence of different tissues is instead of crucial importance for a precise assessment of the radiation performances of the antennas. Hence, antenna simulation requires a realistic model (or at least of a portion of it).
- Numerical simulations and experimental measurements revealed that the proposed textile AMC antenna was robust in respect to impedance resonance frequency, showing minimal changes due to structural deformation such as bending, as well as loading effects of human body.
- Comprehensive SAR analysis was carried out for monopole and AMC antennas in flat and bent forms using different body models. The inclusion of AMC reflector considerably reduced the SAR values and the back radiation compared to stand-alone monopole antenna for all studied scenarios.
- In vitro test was carried out in the laboratory. Antennas were placed on top of a semisolid muscle tissue phantom contained in a cylindrical container. The measured dielectric properties of the prepared muscle phantom at 5.8 GHz were $\epsilon_r = 45.41$ and $\tan\delta_e = 0.48$. Measurements

showed that AMC antenna was able to maintain a good impedance matching while more variations were observed in case of monopole antenna.

Table 6.2 compares the proposed textile antenna with antennas reported in literature in terms of the resonance frequency, volume, antenna bandwidth, gain, and material type. These antennas are working within the ISM 5.8 GHz band. It is evident that the proposed textile antenna provides the largest antenna bandwidth to account for the frequency detuning that might take place due to human body loading and/or structural deformation effects. In addition, it has small occupied volume and high antenna gain.

Table 6.2: Comparison of the proposed wearable antenna with reported work in literature.

<i>Ref.</i>	<i>Year</i>	<i>Freq. (GHz)</i>	<i>Volume (mm³)</i>	<i>B.W.^a (GHz)</i>	<i>B.W. (%)</i>	<i>Gain (dBi)</i>	<i>Material (dielectric/conductive)</i>
[127]	2017	5.8	147×147×8	5.62 – 5.90	4.83	6.08	PDMS/NA
[56]	2016	5.4	8.5×8.5×3.6	5.15 – 5.87	13.0	NA	Felt/NA
[57]	2016	5.8	90×90×6.51	5.46 – 6.18	12.0	5.26	Felt/Shieldit Super
[35]	2016	5.4	147×147×6	NA	6.70	7.25	Cotton/ NA
[36]	2015	5.8	$\pi \times (50)^2$ [area]×3	5.56 – 6.03	8.10	3.83	Leather/Conductive threads
[58]	2014	5.8	100×100×3	5.04 – 5.94	15.4	4.00	Felt/Shieldit Super
[128]	2013	5.5	40×50×2.1	5.00 – 6.00	18.0	6.20	Photo paper/Silver ink
[50]	2012	5.5	87×77×8	5.04 – 6.04	18.1	5.00	Felt/Shieldit Super
[37]	2012	5.5	110×110×3.3	NA	6.00	9.80	Jeans/ NA
[129]	2010	5.5	102×102×7	NA	12.4	5.20	Polyethylene foam/Zelt
[38]	2009	5.8	120×120×4.3	5.40 – 6.15	12.0	5.20	Felt/Zelt
Proposed	2018	4.8	102×68×3.6	5.30 – 5.90	34.0	6.12	Pellon/Pure Copper Taffeta

^a. Bandwidth (B.W.).

Many challenges were faced during the measurement phase of the proposed AMC based wearable antennas as discussed in Sections 2.4.1 and 3.4.1. Hence, the potential of using new materials such as flexible MD material and dielectric and magnetic layered substrate in wearable antenna design were investigated.

Different monopole antenna configurations were studied and their performances evaluated at 2.45 GHz based on numerical analysis. Monopole based MD antenna integrated a ground plane

at a distance of 4 *mm* away from the antenna showed a comparable performance to the monopole integrated flexible AMC structure and a superior performance compared to the monopole based dielectric antenna. Effectiveness of using MD materials in wearable antenna design is revealed to stabilize antenna performance under bending and on body conditions. In addition, by using layered substrates, further improvements in the antenna radiation characteristics and bandwidth are achieved compared to MD based antenna with the advantage of ease of fabrication.

6.1.2 Implantable Antenna Design

The design and characterization of a wideband biocompatible small capsule antenna was presented. The main conclusions and achievements are explained as follows:

- The proposed antenna featured small size (*i.e.*, the antenna size in planar form is 2.52 *mm*³), wide impedance bandwidth of 7.31 GHz (*i.e.*, 0.78 GHz – 8 GHz, for -10dB reflection coefficient), and low coupling to human tissues.
- The near/far-field communication analysis was carried out at 915 MHz and 2.45 GHz for different free-space distances of the receiver and different implant depths. Findings of this study suggested that the proposed capsule antenna support the functionality of wireless data transmission and wake-up receiver signal within 902.8 MHz – 928.0 MHz and 2.40 GHz – 2.50 GHz ISM bands, respectively. The wake-up receiver signal is necessary to save power by transmitting data only when is needed.

Table 6.3 compares the proposed implantable antenna with antennas reported in literature of similar topology (*i.e.*, capsule antenna). Among the mentioned antennas, the proposed antenna provides the largest antenna bandwidth of 7.31 GHz and the least occupied volume of 2.5 *mm*³. In

terms of antenna gain the proposed antenna provides a comparable antenna gain with that obtained using bigger size antennas.

Table 6.3: Comparison of the proposed implantable antenna with reported work in literature.

<i>Ref.</i>	<i>Implantation tissue</i>	<i>Depth (mm)</i>	<i>B.W.^a</i>	<i>Vol. (mm³)</i>	<i>Gain (dBi)</i>
[32]	Skin	3	MICS: (321–532) MHz ISM: (2.15–2.74) GHz	186.3	MICS: -30.5 ISM: -22.2
[75]	Skin	3	MICS: (358–516) MHz	N/A	MICS: -37.0
[13]	Muscle	50	ISM: (2.38 – 2.5) GHz	N/A	ISM: -32.4
[76]	Muscle	50	ISM: (780–965 MHz)	66.7	ISM: -19.4
Proposed	Layered	40	(0.78– 8) GHz	2.5	ISM 9.15: -25.2 ISM 2.45: -27.5

^a Bandwidth (B.W.).

6.1.3 Investigated Wireless Body Area Network Applications

Antenna Effects on Respiratory Rate Measurement System: Experiments were designed in order to assess the tradeoffs between antenna selection and the proposed radar based sensing system’s accuracy as a non-contact respiration-rate measurement tool. Three antennas of different antenna characteristics such as bandwidth, cross-polarization, and antenna gain and directivity were used. The sensing system was first evaluated using a controlled movable device when changing the movement frequency and displacement and the measurement distance parameters using the three antennas. The obtained results suggest that better system’s performance can be provided using an antenna with high polarization purity, small physical separation between Rx and Tx, and stable phase center.

The system was then evaluated, using the antenna that provided the least error values, through a pilot study on respiration-rate measurements of ten subjects. Reference measurements are performed and the accurate values of the respiratory-rates of the test subjects were collected

and compared with the radar setup results. The mean error value of the respiratory rate measurements was 0.03 Hz with a statistical standard deviation of 0.03 Hz.

The main challenge of the used radar system was the sensitivity of the received radar waveform to the surrounding environment, specially the moving objects, in terms of changing the signal strength and SNR value calculated by the software.

An Accurate Phase-Based Localization Method of RFID Tag: An accurate electromagnetic model of indoor localization system of a semi-passive RFID tag was presented. Results demonstrated that the proposed simulation model comparatively provided an accurate estimation as well as assessment tool of phase measurements for indoor localization application. In addition, effects of the mutual coupling of the transceiver antenna array elements on the phase measurements found to be negligible due to the robustness of the proposed system.

6.2 Future Work

Wearable antenna based on flexible MD material: the development of MD materials is a study in mechanical and chemical engineering fields, as one must attempt to satisfy multiple of antenna goals that focus on minimizing material losses and designing materials for low cost production. Realizing flexible MD materials is challenging using the standard manufacturing methods and traditional solid MD materials. Future research will continue investigating the possibility of fabricating flexible MD materials. Afterward, antenna testing under different deformation effects and on body performance evaluations will be considered.

Implantable antenna design: preliminary investigations on the design of a wideband implantable antenna stated the formulation of an efficient implantable antenna design strategy. Several steps need to be taken for a complete design and assessment phases of the antenna, discussed as follows:

- In order to reduce the coupling between the EM field and the surrounding biological tissues, antenna biocompatibility should be satisfied. The current state of the proposed capsule antenna design involves a biocompatible capsule with the antenna of copper material in a direct contact with the body tissues. Coating the antenna with thin biocompatible polymers technique will be adopted to achieve entire antenna biocompatibility. Effects of the insulating layers on the antenna performance will be investigated. In addition, new materials such as biodegradable materials are of our interest. The main attraction of a biodegradable antenna, to both surgeons and patients, is that it harmlessly degrades over time. This means that there is no need for an additional removal operation.
- SAR assessment is of great importance to consider the human body safety. Future research will continue to carry out SAR analysis in order to define the maximum allowed antenna input power levels that meet the safety regulations.
- Performance evaluation of the implanted antenna under different operation scenarios include different positions and orientations inside the human body is of interest. The objective of the study is to propose recommendations on the optimum position of implantation and antenna orientations from antenna and propagation point of view. The optimum selection criteria are defined by the largest antenna gain and bandwidth and smallest SAR levels.
- Antenna miniaturization is an endless need for implantable antenna design. More research efforts will be dedicated to achieve further antenna miniaturization.
- Antenna fabrication and performance evaluation based on *in-vitro* measurements are necessary to validate the proposed numerical studies. Solutions to the well-known

problems of measuring electrically small antennas including the interaction between a feeding cable (*i.e.*, used for testing purposes) and the body phantom should be investigated.

- Wireless power transfer is always of interest to save the pain and cost of replacing or charging the implant battery. Hence, in order to extend the life time of an implant and reduce its volume, wireless data transmission can include, or work side by side with, power transfer. This capability calls for the design of antenna that share different working functionalities or coexist with different EM systems. Future research will continue to address the capability of the current antenna design to support or coexist with wireless power transfer system.

An Accurate Phase-Based Localization Method of RFID Tag: further investigations will be carried out in terms of using antenna of different types and topologies and to evaluate the system performance to address the antenna selection criteria. Possibility of using the proposed system (*i.e.*, measurement setup and simulation model) for human localization is of our interest as well.

REFERENCES

- [1] M. Rizwan, “Study of on-body antennas and channel properties for short-range communications in the context of Wireless Body Area Sensor Networks (WBASN),” Université de Bretagne Occidentale, 2016.
- [2] Tecnoneo Technologies: Smart Shirt. [Online]. Available: <http://www.tecnoneo.com/2016/11/carre-technologies-desarrolla-astroskin.html>. [Accessed: 20-Aug-2018].
- [3] Baby Tech Showcase: Thermometer Patch. [Online]. Available: <http://awardsarchive.babytechsummit.com/bestof2018/temptraq/>. [Accessed: 20-Aug-2018].
- [4] Health Professions Education Center: EEG Tattoo Sensor. [Online]. Available: <https://hpectechtrends.wordpress.com/2015/03/24/two-week-temporary-tattoo-like-sensor-opens-the-door-for-brain-computer-interfacing/>. [Accessed: 20-Aug-2018].
- [5] Blog Modern Mom: Motion Sensor. [Online]. Available: <http://www.blogmamasmodernas.com/nueva-generacion-de-monitor-de-bebe/>. [Accessed: 20-Aug-2018].
- [6] Wireless Implantable Medical Devices. [Online]. Available: <https://www.thinglink.com/scene/763443028189773826>. [Accessed: 20-Aug-2018].
- [7] R. Chandra, “Antennas, Wave Propagation, and Localization in Wireless Body Area Networks,” Lund University, 2014.
- [8] J. Kim and Y. Rahmat-Samii, “Implanted antennas inside a human body: Simulations, designs, and characterizations,” *IEEE Trans. Microw. Theory Tech.*, vol. 52, no. 8 II, pp. 1934–1943, 2004.
- [9] Institute of Applied Physics. [Online]. Available: <http://www.ifac.cnr.it/>. [Accessed: 20-Aug-2018].
- [10] A. Alemaryeen and S. Noghianian, “A Wideband Antenna for Biotelemetry Applications: Design and Transmission Link Evaluation,” in *Applied Computational Electromagnetics Society (ACES) Conference*, 2018.
- [11] A. Alemaryeen and S. Noghianian, “Performance analysis of textile AMC antenna on body model,” in *Proc. IEEE AP-S Int. Symp*, 2017, pp. 41–42.
- [12] A. Kiourti and K. S. Nikita, “Miniature scalp-implantable antennas for telemetry in the MICS and ISM bands: Design, safety considerations and link budget analysis,” *IEEE Trans. Antennas Propag.*, vol. 60, no. 8, pp. 3568–3575, 2012.
- [13] L. Yan, “Orientation Insensitive Antenna With Polarization Diversity for Wireless Capsule Endoscope System,” *IEEE Trans. Antennas Propag.*, vol. 65, no. 7, pp. 3738–3743, 2017.
- [14] A. Alemaryeen and S. Noghianian, “AMC integrated textile monopole antenna for wearable applications,” *ACES J.*, vol. 31, no. 6, pp. 612–618.
- [15] F. Merli, “Implantable antennas for biomedical applications,” EPFL University, 2011.
- [16] X. Zhu, Y. Guo, and W. Wu, “Miniaturized dual band and dual-polarized antenna for

- MBAN applications,” *IEEE Trans. Antennas Propag.*, vol. 62, no. 7, pp. 2805–2817, 2016.
- [17] Z. H. Jiang, D. E. Brocker, P. E. Sieber, and D. H. Werner, “A compact, low-profile metasurface-enabled antenna for wearable medical body-area network devices,” *IEEE Trans. Antennas Propag.*, vol. 62, no. 8, pp. 4021–4030, 2014.
- [18] A. Kiourti, M. Christopoulou, S. Koulouridis, and K. S. Nikita, “Design of a novel miniaturized implantable PIFA for biomedical telemetry,” in *Lecture Notes of the Institute for Computer Sciences, Social-Informatics and Telecommunications Engineering*, 2011, vol. 55 LNICST, pp. 127–134.
- [19] M.-C. Gosselin *et al.*, “Development of a new generation of high-resolution anatomical models for medical device evaluation: the Virtual Population 3.0.,” *Phys. Med. Biol.*, vol. 59, no. 18, pp. 5287–5303, 2014.
- [20] A. Alemaryeen and S. Noghianian, “On-Body Low-Profile Textile Antenna with Artificial Magnetic Conductor,” *IEEE Antennas Propagation Trans.*
- [21] A. Rahman, M. T. Islam, M. J. Singh, S. Kibria, and M. Akhtaruzzaman, “Electromagnetic Performances Analysis of an Ultra-wideband and Flexible Material Antenna in Microwave Breast Imaging: To Implement A Wearable Medical Bra,” *Sci. Rep.*, vol. 6, 2016.
- [22] T. Karacolak, A. Z. Hood, and E. Topsakal, “Design of a dual-band implantable antenna and development of skin mimicking gels for continuous glucose monitoring,” *IEEE Trans. Microw. Theory Tech.*, vol. 56, no. 4, pp. 1001–1008, 2008.
- [23] J. Ung and K. Tutku, “A Dual-Band Meandered Dipole Antenna for Medical Telemetry Applications,” *Prog. Electromagn. Res.*, vol. 63, pp. 85–94, 2016.
- [24] K. M. Jones, J. A. Mechling, J. W. Strohbehn, and B. S. Trembly, “Theoretical and Experimental SAR Distributions for Interstitial Dipole Antenna Arrays Used in Hyperthermia,” *IEEE Trans. Microw. Theory Tech.*, vol. 37, no. 8, pp. 1200–1209, 1989.
- [25] Commission of European Communities: Council recommendation on limits for exposure of the federal public to electromagnetic fields: 0Hz-300 GHz. June 1998.
- [26] IEEE Std C95.3-2002: IEEE recommended practice for measurements and computations of radio frequency electromagnetic fields with respect to human exposure to such fields 100 kHz–300 GHz. 2002.
- [27] A. Kiourti and K. S. Nikita, “A review of in-body biotelemetry devices: Implantables, ingestibles, and injectables,” *IEEE Transactions on Biomedical Engineering*, vol. 64, no. 7, pp. 1422–1430, 2017.
- [28] A. Kiourti and K. S. Nikita, “A review of implantable patch antennas for biomedical telemetry: Challenges and solutions,” *IEEE Antennas and Propagation Magazine*, vol. 54, no. 3, pp. 210–228, 2012.
- [29] S. a Shabalovskaya, “Surface, corrosion and biocompatibility aspects of Nitinol as an implant material,” *Biomed. Mater. Eng.*, vol. 12, no. 1, pp. 69–109, 2002.
- [30] T. Karacolak, R. Cooper, J. Butler, S. Fisher, and E. Topsakal, “In vivo verification of implantable antennas using rats as model animals,” *IEEE Antennas Wirel. Propag. Lett.*, vol. 9, pp. 334–337, 2010.

- [31] P. Soontornpipit, "Miniaturized biocompatible microstrip antenna using genetic algorithm," *IEEE Trans. Antennas Propag.*, vol. 64, no. 240, pp. 69\|-1945, 2005.
- [32] Z. Duan, Y. X. Guo, M. Je, and D. L. Kwong, "Design and in vitro test of a differentially fed dual-band implantable antenna operating at MICS and ISM Bands," *IEEE Trans. Antennas Propag.*, vol. 62, no. 5, pp. 2430–2439, 2014.
- [33] G. P. Gao, B. Hu, S. F. Wang, and C. Yang, "Wearable Circular Ring Slot Antenna with EBG Structure for Wireless Body Area Network," *IEEE Antennas Wirel. Propag. Lett.*, vol. 17, no. 3, pp. 434–437, 2018.
- [34] H. Lago, P. J. Soh, M. F. Jamlos, N. Shohaimi, S. Yan, and G. A. E. Vandenbosch, "Textile antenna integrated with compact AMC and parasitic elements for WLAN/WBAN applications," *Appl. Phys. A* 122, no. 12, p. 1059, 2016.
- [35] A. Ahmad, F. Faisal, S. Khan, S. Ullah, and U. Ali, "Performance analysis of a wearable and dual band planar antenna using a mushroom-like electromagnetic bandgap (EBG) ground plane," in *ICOSST 2015 - 2015 International Conference on Open Source Systems and Technologies, Proceedings*, 2016, pp. 24–29.
- [36] Y. Hong, J. Choi, and J. Tak, "Textile antenna with EBG structure for body surface wave enhancement," *Electron. Lett.*, vol. 51, no. 15, pp. 1131–1132, 2015.
- [37] S. Tarigonda and B. Bharath, "Design and fabrication of dual-band coplanar antenna using EBG structures," in *Proceedings: Turing 100 - International Conference on Computing Sciences, ICCS 2012*, 2012, pp. 249–254.
- [38] S. Zhu and R. Langley, "Dual-band wearable textile antenna on an EBG substrate," *IEEE Trans. Antennas Propag.*, vol. 57, no. 4 PART. 1, pp. 926–935, 2009.
- [39] H. R. Raad, A. I. Abbosh, H. M. Al-Rizzo, and D. G. Rucker, "Flexible and compact AMC based antenna for telemedicine applications," *IEEE Trans. Antennas Propag.*, vol. 61, no. 2, pp. 524–531, 2013.
- [40] S. Velan *et al.*, "Dual-band EBG integrated monopole antenna deploying fractal geometry for wearable applications," *IEEE Antennas Wirel. Propag. Lett.*, vol. 14, pp. 249–252, 2015.
- [41] S. M. Saeed, C. A. Balanis, C. R. Birtcher, A. C. Durgun, and H. N. Shaman, "Wearable Flexible Reconfigurable Antenna Integrated with Artificial Magnetic Conductor," *IEEE Antennas Wirel. Propag. Lett.*, vol. 16, pp. 2396–2399, 2017.
- [42] S. Kim, Y. J. Ren, H. Lee, A. Rida, S. Nikolaou, and M. M. Tentzeris, "Monopole antenna with inkjet-printed EBG array on paper substrate for wearable applications," *IEEE Antennas Wirel. Propag. Lett.*, vol. 11, pp. 663–666, 2012.
- [43] K. Agarwal, Y. X. Guo, and B. Salam, "Wearable AMC Backed Near-Endfire Antenna for On-Body Communications on Latex Substrate," *IEEE Trans. Components, Packag. Manuf. Technol.*, vol. 6, no. 3, pp. 346–358, 2016.
- [44] Z. H. Jiang, Z. Cui, T. Yue, Y. Zhu, and D. H. Werner, "Compact, Highly Efficient, and Fully Flexible Circularly Polarized Antenna Enabled by Silver Nanowires for Wireless Body-Area Networks," *IEEE Trans. Biomed. Circuits Syst.*, vol. 11, no. 4, pp. 920–932, 2017.

- [45] M. Patel and J. Wang, "Applications, challenges, and prospective in emerging body area networking technologies," *IEEE Wirel. Commun.*, vol. 17, no. 1, pp. 80–88, 2010.
- [46] J. Kim and Y. Rahmat-Samii, "Planar inverted-F antennas on implantable medical devices: Meandered type versus spiral type," *Microw. Opt. Technol. Lett.*, vol. 48, no. 3, pp. 567–572, 2006.
- [47] W. C. Liu, S. H. Chen, and C. M. Wu, "Implantable broadband circular stacked pifa antenna for biotelemetry communication," *J. Electromagn. Waves Appl.*, vol. 22, no. 13, pp. 1791–1800, 2008.
- [48] Time Domain. [Online]. Available: <http://www.timedomain.com>. [Accessed: 20-Aug-2017].
- [49] CST Microwave Studio 2017 [Online]. Available: <http://www.cst.com>. [Accessed: 2016].
- [50] M. Mantash, A. C. Tarot, S. Collardey, and K. Mahdjoubi, "Investigation of flexible textile antennas and AMC reflectors," *Int. J. Antennas Propag.*, vol. 2012, 2012.
- [51] A. Alemaryeen, S. Noghianian, and R. Fazel-Rezai, "EBG integrated textile monopole antenna for space health monitoring application," in *Proc. IEEE AP-S Int. Symp.*, pp. 1209–1210.
- [52] LessEMF. [Online]. Available: <http://www.lessemf.com>. [Accessed: 20-Jun-2016].
- [53] F. Yang and Y. Rahmat-Samii, "Reflection phase characterizations of the EBG ground plane for low profile wire antenna applications," *Antennas Propagation, IEEE*, 2003.
- [54] M. Klemm and G. Troester, "EM energy absorption in the human body tissues due to UWB antennas," *Electromagnetics*, vol. 62, pp. 261–280, 2006.
- [55] J. Gemio, J. Parrón, and J. Soler, "Human Body Effects on Implantable Antennas For ISM Bands Applications: Models Comparison," *Prog. Electromagn. Res.*, vol. 110, pp. 437–452, 2010.
- [56] S. Collardey, M. Mantash, K. Mahdjoubi, and A.-C. Tarot, "Design methodology for wearable antenna on artificial magnetic conductor using stretch conductive fabric," *Electron. Lett.*, vol. 52, no. 2, pp. 95–96, 2016.
- [57] P. J. Soh, F. N. Gimán, M. F. Jamlos, H. Lago, and A. A. Al-Hadi, "A C-slotted dual band textile antenna for WBAN applications," in *2016 URSI Asia-Pacific Radio Science Conference, URSI AP-RASC 2016*, 2016, pp. 1621–1624.
- [58] S. Yan, P. J. Soh, and G. A. E. Vandenbosch, "Low-profile dual-band textile antenna with artificial magnetic conductor plane," *IEEE Trans. Antennas Propag.*, vol. 62, no. 12, pp. 6487–6490, 2014.
- [59] W. Liu and P. Kao, "CPW-fed triangular monopole antenna for ultra-wideband operation," *Microw. Opt. Technol. Lett.*, vol. 47, no. 6, pp. 580–582, 2005.
- [60] J. R. J. Sohn, H.-S. H. Tae, J.-G. J. J.-H. Lee, and J.-G. J. J.-H. Lee, "Comparative analysis of four types of high-impedance surfaces for low profile antenna applications," in *AP-S IEEE Int. Symp. (Digest) Antennas Propag. Society*, 2005, vol. 1A, pp. 758–761.
- [61] H. M. R. Nurul, P. J. Soh, M. F. A. Malek, and G. A. E. Vandenbosch, "Dual-band suspended-plate wearable textile antenna," *IEEE Antennas Wirel. Propag. Lett.*, vol. 12, pp.

- 583–586, 2013.
- [62] CTIA Certification Standard: Test Plan for Wireless Device Over-the-Air Performance, Revision 3.5.2. September 2015.
- [63] S. Yan, P. Jack Soh, and G. A. E. Vandenbosch, “Compact all-textile dual-band antenna loaded with metamaterial-inspired structure,” *IEEE Antennas Wirel. Propag. Lett.*, vol. 14, pp. 1486–1489, 2015.
- [64] P. J. Soh, G. A. E. Vandenbosch, F. H. Wee, A. Van Den Bosch, M. Martinez-Vazquez, and D. M. M. P. Schreurs, “Specific Absorption Rate (SAR) evaluation of biomedical telemetry textile antennas,” in *IEEE MTT-S International Microwave Symposium Digest*, 2013, pp. 1–3.
- [65] T. Yilmaz, R. Foster, and Y. Hao, “Broadband tissue mimicking phantoms and a patch resonator for evaluating noninvasive monitoring of blood glucose levels,” *IEEE Trans. Antennas Propag.*, vol. 62, no. 6, pp. 3064–3075, 2014.
- [66] K. Han, M. Swaminathan, R. Pulugurtha, H. Sharma, R. Tummala, and V. Nair, “Magneto-dielectric material characterization and Antenna Design for RF applications,” in *EuCAP*, 2014, no. EuCAP, pp. 381–384.
- [67] L. Sandrolini, M. Artioli, and U. Reggiani, *Electric and Magnetic Characterization of Materials*. 2011.
- [68] J. F. Pintos *et al.*, “Ultra-miniature UHF antenna using magneto-dielectric material,” in *2010 14th International Symposium on Antenna Technology and Applied Electromagnetics and the American Electromagnetics Conference, ANTEM/AMEREM 2010*, 2010.
- [69] F. Ferrero, A. Chevalier, J. M. Ribero, R. Staraj, J. L. Mattei, and Y. Queffelec, “A new magneto-dielectric material loaded, tunable UHF antenna for handheld devices,” *IEEE Antennas Wirel. Propag. Lett.*, 2011.
- [70] F. Ferrero, A. Chevalier, J. M. Ribero, R. Staraj, J. L. Mattei, and P. Queffelec, “Influence of a magneto-dielectric resonator on DVB-H antenna performances,” *Proc. 5th Eur. Conf. Antennas Propag.*, 2011.
- [71] A. Thakur, A. Chevalier, J. L. Mattei, and P. Queffelec, “Low-loss spinel nanoferrite with matching permeability and permittivity in the ultrahigh frequency range,” *J. Appl. Phys.*, 2010.
- [72] K. Borah and N. Bhattacharyya, “Magnetodielectric composite with NiFe₂O₄ inclusions as substrates for microstrip antennas,” *IEEE Trans. Dielectr. Electr. Insul.*, 2012.
- [73] A. Foroozesh and L. Shafai, “Size reduction of a microstrip antenna with dielectric superstrate using meta-materials: Artificial magnetic conductors versus magneto-dielectrics,” in *IEEE Antennas and Propagation Society, AP-S International Symposium (Digest)*, 2006.
- [74] Y. S. Shin and S. O. Park, “A monopole antenna with a magneto-dielectric material and its MIMO application for 700 MHz-LTE-band,” *Microw. Opt. Technol. Lett.*, 2010.
- [75] L. J. Xu, Y. X. Guo, and W. Wu, “Bandwidth enhancement of an implantable antenna,” *IEEE Antennas Wirel. Propag. Lett.*, vol. 14, pp. 1510–1513, 2015.

- [76] R. Das and H. Yoo, "A wideband circularly polarized conformal endoscopic antenna system for high-speed data transfer," *IEEE Trans. Antennas Propag.*, vol. 65, no. 6, pp. 2816–2826, 2017.
- [77] J. Kraus, *Antenna measurements*, 3rd ed. New York, NY, USA: McGraw-Hill, 2002.
- [78] BIOPAC Systems Inc. [Online]. Available: <https://www.biopac.com>.
- [79] M. Cretikos, J. Chen, K. Hillman, R. Bellomo, S. Finfer, and A. Flabouris, "The objective medical emergency team activation criteria: A case-control study," *Resuscitation*, vol. 73, no. 1, pp. 62–72, 2007.
- [80] T. J. Hodgetts, G. Kenward, I. G. Vlachonikolis, S. Payne, and N. Castle, "The identification of risk factors for cardiac arrest and formulation of activation criteria to alert a medical emergency team," *Resuscitation*, vol. 54, no. 2, pp. 125–131, 2002.
- [81] A. Diaz, M. G. Bourassa, M.-C. Guertin, and J.-C. Tardif, "Long-term prognostic value of resting heart rate in patients with suspected or proven coronary artery disease.," *Eur. Heart J.*, vol. 26, no. 10, pp. 967–74, 2005.
- [82] F. Q. Al-Khalidi, R. Saatchi, D. Burke, H. Elphick, and S. Tan, "Respiration rate monitoring methods: A review," *Pediatric Pulmonology*, vol. 46, no. 6, pp. 523–529, 2011.
- [83] D. Frasca, L. Geraud, J. M. Charriere, B. Debaene, and O. Mimoz, "Comparison of acoustic and impedance methods with mask capnometry to assess respiration rate in obese patients recovering from general anaesthesia," *Anaesthesia*, vol. 70, no. 1, pp. 26–31, 2015.
- [84] S. Babaeizadeh, S. H. Zhou, S. D. Pittman, and D. P. White, "Electrocardiogram-derived respiration in screening of sleep-disordered breathing," *J. Electrocardiol.*, vol. 44, no. 6, pp. 700–706, 2011.
- [85] C. L. Marcus *et al.*, "Diagnosis and management of childhood obstructive sleep apnea syndrome.," *Pediatrics*, vol. 130, no. 3, pp. 576–84, 2012.
- [86] P. Leonard, "Standard pulse oximeters can be used to monitor respiratory rate," *Emerg. Med. J.*, vol. 20, no. 6, pp. 524–525, 2003.
- [87] M. C. Huang, J. J. Liu, W. Xu, C. Gu, C. Li, and M. Sarrafzadeh, "A Self-Calibrating Radar Sensor System for Measuring Vital Signs," *IEEE Trans. Biomed. Circuits Syst.*, vol. 10, no. 2, pp. 352–363, 2016.
- [88] P. N. P. C. L. S. T. C. Yee Siong Lee, "Monitoring and Analysis of Respiratory Patterns Using Microwave Doppler Radar.," *IEEE J. Transl. Eng. Heal. Med.*, vol. 2, p. 1800912, 2014.
- [89] C. G. Caro and J. A. Bloice, "Contactless Apnoea Detector Based on Radar," *Lancet*, 1971.
- [90] A. Droitcour, T. Seto, and B. Park, "Non-contact respiratory rate measurement validation for hospitalized patients," in *Annu. IEEE Int. Eng. Med. Biol. Soc. Conf.*, 2009, pp. 4812–4815.
- [91] M. Pieraccini, G. Luzi, D. Dei, L. Pieri, and C. Atzeni, "Detection of breathing and heartbeat through snow using a microwave transceiver," *IEEE Geosci. Remote Sens. Lett.*, vol. 5, no. 1, pp. 57–59, 2008.
- [92] J. Geisheimer and E. Greneker, "A non-contact lie detector using radar vital signs monitor

- (RVSM) technology,” in *Proc. IEEE 34th Annu. 2000 Int. Carnahan Conf. Security Technology*, 2001, pp. 257–259.
- [93] M. Nosrati and N. Tavassolian, “Effects of antenna characteristics on the performance of heart rate monitoring radar systems,” *IEEE Trans. Antennas Propag.*, vol. 65, no. 6, pp. 3296–3301, 2017.
- [94] B. Schleicher, I. Nasr, A. Trasser, and H. Schumacher, “IR-UWB radar demonstrator for ultra-fine movement detection and vital-sign monitoring,” *IEEE Trans. Microw. Theory Tech.*, vol. 61, no. 5, pp. 2076–2085, 2013.
- [95] J. Kuutti, M. Paukkunen, M. Aalto, P. Eskelinen, and R. E. Sepponen, “Evaluation of a Doppler radar sensor system for vital signs detection and activity monitoring in a radio-frequency shielded room,” *Meas. J. Int. Meas. Confed.*, vol. 68, pp. 135–142, 2015.
- [96] S. Wang *et al.*, “A novel ultra-wideband 80 GHz FMCW radar system for contactless monitoring of vital signs,” in *Proceedings of the Annual International Conference of the IEEE Engineering in Medicine and Biology Society, EMBS*, 2015, vol. 2015–Novem, pp. 4978–4981.
- [97] H. Wang *et al.*, “An Elegant Solution: An Alternative Ultra-Wideband Transceiver Based on Stepped-Frequency Continuous-Wave Operation and Compressive Sensing,” *IEEE Microw. Mag.*, vol. 17, no. 7, pp. 53–63, 2016.
- [98] L. Ren, L. Kong, F. Foroughian, H. Wang, P. Theilmann, and A. E. Fathy, “Comparison Study of Noncontact Vital Signs Detection Using a Doppler Stepped-Frequency Continuous-Wave Radar and Camera-Based Imaging Photoplethysmography,” *IEEE Trans. Microw. Theory Tech.*, vol. 65, no. 9, pp. 3519–3529, 2017.
- [99] X. Hu and J. Tian, “Short-range vital signs sensing based on EEMD and CWT Using IR-UWB radar,” *Sensors*, vol. 16, no. 12, p. 2025, 2016.
- [100] Quanser Innovate Educate. [Online]. Available: <http://www.quanser.com>.
- [101] Time Domain® 2001-2014, “Monostatic radar module reconfiguration and evaluation tool (MRM RET) user’s guide.” [Online]. Available: <http://www.timedomain.com>. [Accessed: 20-Jun-2010].
- [102] H. Bo, F. Qiang, X. Lisheng, L. Fleming, and D. Yuanzhu, “Design and Implementation of a 2.45 GHz RF Sensor for Non-contacting Monitoring Vital Signs,” in *IEEE Computing in Cardiology Conference (CinC)*, 2016, pp. 1113–1116.
- [103] Time Domain® 2001-2014, ‘Broadspec UWB antenna’, March 2011. [Online]. Available: <http://www.timedomain.com>. [Accessed: October 2016].
- [104] Ainfoinc® 2011, ‘Broadband horn antenna’, March 2011. [Online]. Available: http://www.ainfoinc.com/en/p_ant_h_brd.asp. [Accessed: December 2016].
- [105] M. Ostadrahimi, S. Noghianian, L. Shafai, A. Zakaria, C. Kaye, and J. LoVetri, “Investigating a double layer Vivaldi antenna design for fixed array field measurement,” *Int. J. Ultra Wideband Commun. Syst.*, vol. 1, pp. 282–290, 2010.
- [106] K. Barrett, H. Brooks, S. Boitano, and S. Barman, *Ganong’s Review of Medical Physiology*. 2010.

- [107] M. Baboli, O. Boric-Lubecke, and V. Lubecke, "Heart and respiratory detection and simulations for tracking humans based on respiration by using pulse-based radar," in *NORCHIP*, 2012, pp. 1–4.
- [108] H. G. Schantz, "Introduction to ultra-wideband antennas," in *2003 IEEE Conference on Ultra Wideband Systems and Technologies, UWBST 2003 - Conference Proceedings*, 2003.
- [109] C. A. Balanis, "Antenna Theory: A Review," *Proc. IEEE*, 1992.
- [110] I. Hossein, *Ultra-Wide Band Planar Antennas for Microwave Imaging Applications*, M.Sc. Thesis, University of Manitoba, 2007.
- [111] A. Alarifi *et al.*, "Ultra wideband indoor positioning technologies: Analysis and recent advances," *Sensors (Switzerland)*. 2016.
- [112] R. F. Brena, J. P. García-Vázquez, C. E. Galván-Tejada, D. Muñoz-Rodríguez, C. Vargas-Rosales, and J. Fangmeyer, "Evolution of Indoor Positioning Technologies: A Survey," *Journal of Sensors*. 2017.
- [113] L. Calderoni, M. Ferrara, A. Franco, and D. Maio, "Indoor localization in a hospital environment using Random Forest classifiers," *Expert Syst. Appl.*, 2015.
- [114] A. Yassin *et al.*, "Recent Advances in Indoor Localization: A Survey on Theoretical Approaches and Applications," *IEEE Communications Surveys and Tutorials*. 2017.
- [115] M. N. Lionel, Y. Liu, Y. C. Lau, and A. P. Patil, "LANDMARC: Indoor location sensing using active RFID," in *Wireless Networks*, 2004.
- [116] P. Steggle and S. Gschwind, "The Ubisense smart space platform," *Adjun. Proc. Third Int. Conf. Pervasive Comput.*, 2005.
- [117] S. Sayeef and U. K. Madawala, "Indoor personnel tracking using infrared beam scanning," *Position Locat. ...*, 2004.
- [118] H. Schweinzer and M. Syafrudin, "LOSNU: An ultrasonic system enabling high accuracy and secure TDoA locating of numerous devices," in *2010 International Conference on Indoor Positioning and Indoor Navigation, IPIN 2010 - Conference Proceedings*, 2010.
- [119] G. Gonçalo and S. Helena, "Indoor location system using ZigBee technology," in *Proceedings - 2009 3rd International Conference on Sensor Technologies and Applications, SENSORCOMM 2009*, 2009.
- [120] A. Rai, K. K. Chintalapudi, V. N. Padmanabhan, and R. Sen, "Zee: Zero-Effort Crowdsourcing for Indoor Localization," in *Proceedings of the 18th annual international conference on Mobile computing and networking - Mobicom '12*, 2012.
- [121] R. Mautz, "Indoor Positioning Technologies," 2012.
- [122] D. Zhang, F. Xia, Z. Yang, L. Yao, and W. Zhao, "Localization technologies for indoor human tracking," in *2010 5th International Conference on Future Information Technology, FutureTech 2010 - Proceedings*, 2010.
- [123] S. Beauregard and H. Haas, "Pedestrian dead reckoning: A basis for personal positioning," *Proc. 3rd Work. Positioning, ...*, 2006.
- [124] J. G. Liu, D. M. Shi, and M. K. Leung, "Indoor navigation system based on omni-directional

- corridor guidelines,” in *Proceedings of the 7th International Conference on Machine Learning and Cybernetics, ICMLC, 2008*.
- [125] H. Liu, H. Darabi, P. Banerjee, and J. Liu, “Survey of wireless indoor positioning techniques and systems,” *IEEE Transactions on Systems, Man and Cybernetics Part C: Applications and Reviews*. 2007.
- [126] Lunantech Inc. 2017 [Online]. Available: <http://www.lunantech.com>. [Accessed: Oct. 2017].
- [127] M. N. Ramli, P. J. Soh, M. F. Jamlos, H. Lago, N. M. Aziz, and A. A. Al-Hadi, “Dual-band wearable fluidic antenna with metasurface embedded in a PDMS substrate,” *Appl. Phys. A Mater. Sci. Process.*, vol. 123, no. 2, 2017.
- [128] B. S. Cook and A. Shamim, “Utilizing wideband AMC structures for high-gain inkjet-printed antennas on lossy paper substrate,” *IEEE Antennas Wirel. Propag. Lett.*, vol. 12, pp. 76–79, 2013.
- [129] N. Chahat, M. Zhadobov, R. Sauleau, and K. Mahdjoubi, “Improvement of the on-body performance of a dual-band textile antenna using an EBG structure,” in *2010 Loughborough Antennas and Propagation Conference, LAPC 2010, 2010*, pp. 465–468.
- [130] High Frequency Electromagnetic Field Simulation (HFSS) [Online]. Available: <https://www.ansys.com/products/electronics/ansys-hfss>. [Accessed: Oct. 2017].
- [131] M. Klemm and G. Troester, “Textile UWB Antennas for Wireless Body Area Networks,” *IEEE Trans. Antennas Propag.*, vol. 54, no. 11, pp. 3192–3197, 2006.
- [132] M. A. R. Osman, M. K. A. Rahim, M. Azfar, N. A. Samsuri, F. Zubir, and K. Kamardin, “Design, Implementation and Performance of Ultra-Wideband Textile Antenna,” *Prog. Electromagn. Res. B*, vol. 27, no. December 2010, pp. 307–325, 2011.
- [133] S. J. Boyes, P. J. Soh, Y. Huang, G. A. E. Vandenbosch, and N. Khiabani, “Measurement and performance of textile antenna efficiency on a human body in a reverberation chamber,” *IEEE Trans. Antennas Propag.*, vol. 61, no. 2, pp. 871–881, 2013.
- [134] L. A. Yimdjo Poffelie, P. J. Soh, S. Yan, and A. E. G. Vandenbosch, “A High-Fidelity All-Textile UWB Antenna with Low Back Radiation for Off-Body WBAN Applications,” *IEEE Trans. Antennas Propag.*, vol. 64, no. 2, pp. 757–760, 2016.
- [135] W. El Hajj, C. Person, and J. Wiart, “A novel investigation of a broadband integrated inverted-F antenna design; Application for wearable antenna,” *IEEE Trans. Antennas Propag.*, vol. 62, no. 7, pp. 3843–3846, 2014.
- [136] I. C. O. J, and V. P, “Reducing the influence of feed cables on small antenna measurements,” *Electron. Lett.*, vol. 35, no. 15, pp. 1212–1214, 1999.

APPENDIX A

The monopole antenna was designed for 5.8 GHz. Then based on the dimensions given by the design we did the fabrication process. As mentioned earlier, the fabrication process of monopole antenna and AMC reflector was performed using Silhouette® cutting machine and simple dimensioning tools. In order to quantify the accuracy of the fabrication process, during the measurement phase of the antenna design, three different prototypes of monopole antenna were fabricated and their performances were evaluated. These antennas are named Monopole 1, Monopole 2, and Monopole 3. The measured S_{11} of these antennas along with the simulation results are compared and showed in Fig. A1. In addition, this comparison is summarized in Table A1. The three fabricated antennas were resonating around 4.8 GHz with a slight difference in the S_{11} levels and antenna bandwidths.

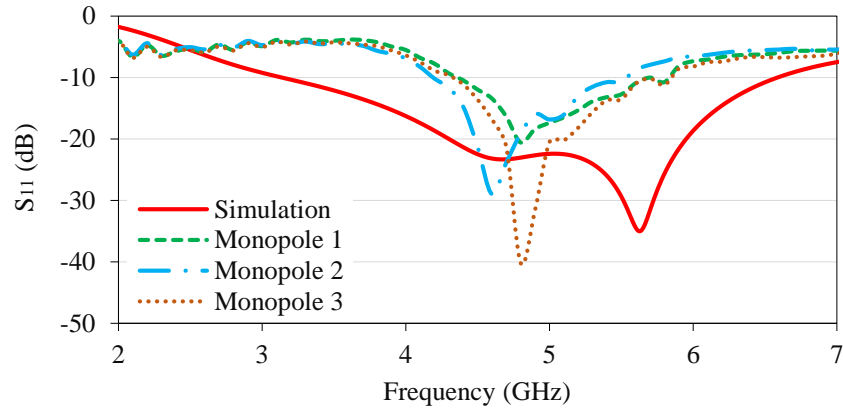


Fig. A1: S_{11} of simulation and three fabricated monopole antennas in free-space.

Table A1: Matching characteristics summary of fabricated monopole antennas.

	f_l^a (GHz)	f_h^b (GHz)	f_r^c (GHz)	S_{11} at f_r (dB)	S_{11} at 5.8 GHz (dB)
Simulation	3.06	6.62	5.63	-35.03	-25.68
Monopole 1	4.40	5.80	4.80	-20.61	-10.76
Monopole 2	4.20	5.60	4.60	-28.99	-7.37
Monopole 3	4.30	5.90	4.80	-40.22	-11.20

^a. f_l represents the lower -10 dB frequency band limit, ^b. f_h represents the higher -10 dB frequency band limit and ^c. f_r represents the resonance frequency.

For the AMC antenna, Monopole 3 was integrated with three different fabricated AMC structures. These antennas are named MA3_AMC1, MA3_AMC2, and MA3_AMC3. The measured S_{11} of these antennas along with the simulation results are compared and showed in Fig. A2. Despite the fact that the measured S_{11} results confirmed our design approach for the monopole antenna, (see results of Monopole 3), and AMC antenna, (see results of MA3_AMC1), operating within ISM 5.8 GHz band, the measured S_{11} results did not exactly agree with the simulation results.

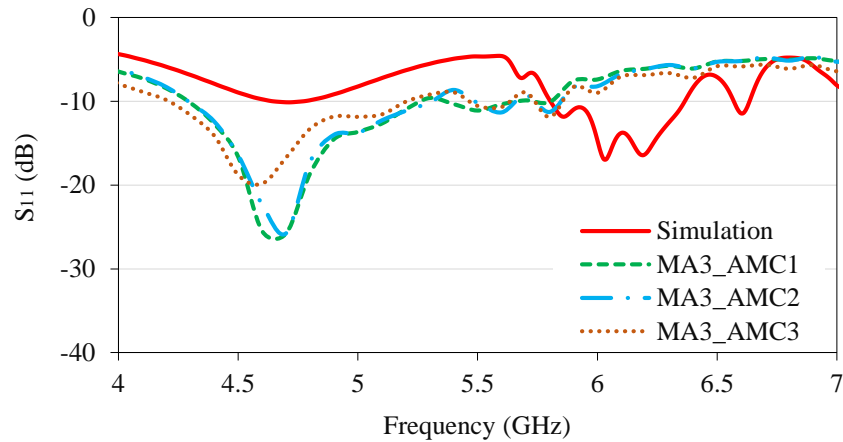
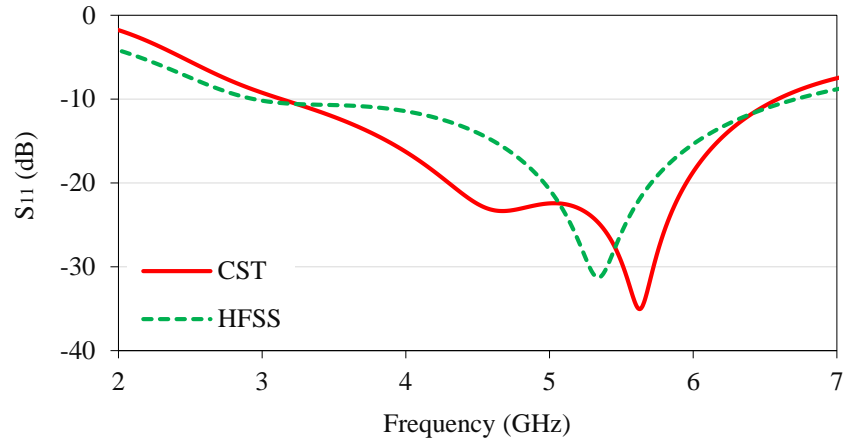
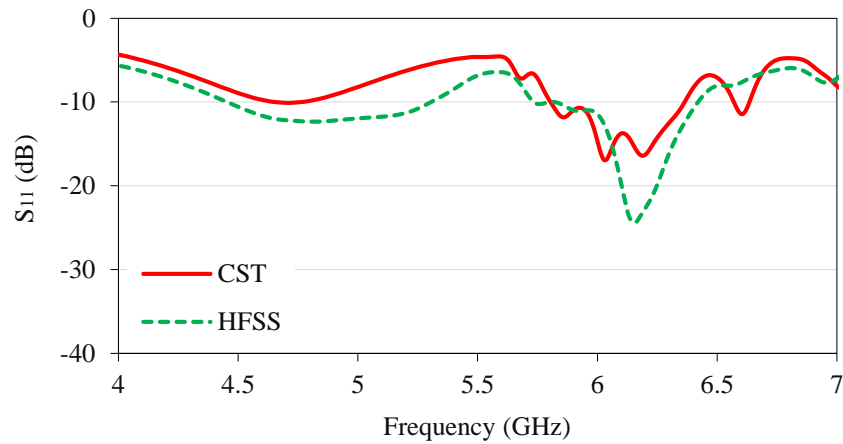


Fig. A2: S_{11} of simulation and three fabricated AMC antennas in free-space.

For the validation verification of the antenna simulations, ANSYS high frequency structure simulator (HFSS) software [130] was used to compare the simulation results of CST MWS for monopole and AMC antennas. Results are compared to those given by CST MWS software, and shown in Fig. A3. Similar performance in terms of -10 dB input impedance bandwidth can be seen from the two simulations. A slight shift in the resonance frequency was observed in case of monopole antenna from 5.63 GHz using CST MWS software to 5.35 GHz using ANSYS HFSS software. The discrepancies between ANSYS HFSS and MWS CST results are basically due to the difference in the computation methods and discretization. CST MWS is based on finite integration technique (FIT) while ANSYS HFSS is based on finite element method (FEM).



(a)



(b)

Fig. A3: Simulated S_{11} by CST MWS and HFSS for (a) monopole and (b) AMC antennas.

We searched in literature and found out that similar problem of simulation-measurement discrepancies was addressed for textile antennas. A CPW-fed textile UWB disc monopole antenna was designed using conductive Nylon fabric-Nora and dielectric acrylic fabric [131]. The antenna prototype and S_{11} results are shown in Fig. A4. Discrepancies in S_{11} results were observed when comparing simulated and measured S_{11} of the two fabricated CPW textile prototypes, *i.e.*, MCPW1 and MCPW2. Authors attributed these discrepancies mostly to manufacturing problems. In particular, two main parameters were discussed. First, since only a simple cutting tool was used, the definition of conductor edges might not be precise. Second, since the antenna was composed

of several pieces of the conductive textile, it was not easy to ensure all dimensions were correct during the attachment to the dielectric. For example, distance between the central line and ground plane, measures 0.5 mm , as shown in Fig. A4(a). The paper did not report any simulation or measurement results to support these suggestions. On the other hand, results of radiation patterns at different studied frequencies showed that a good agreement between simulation and measurement results was observed, with small discrepancies within an acceptable level. These findings are similar to the results obtained in our design in terms of radiation properties agreement between simulation and measurement results.

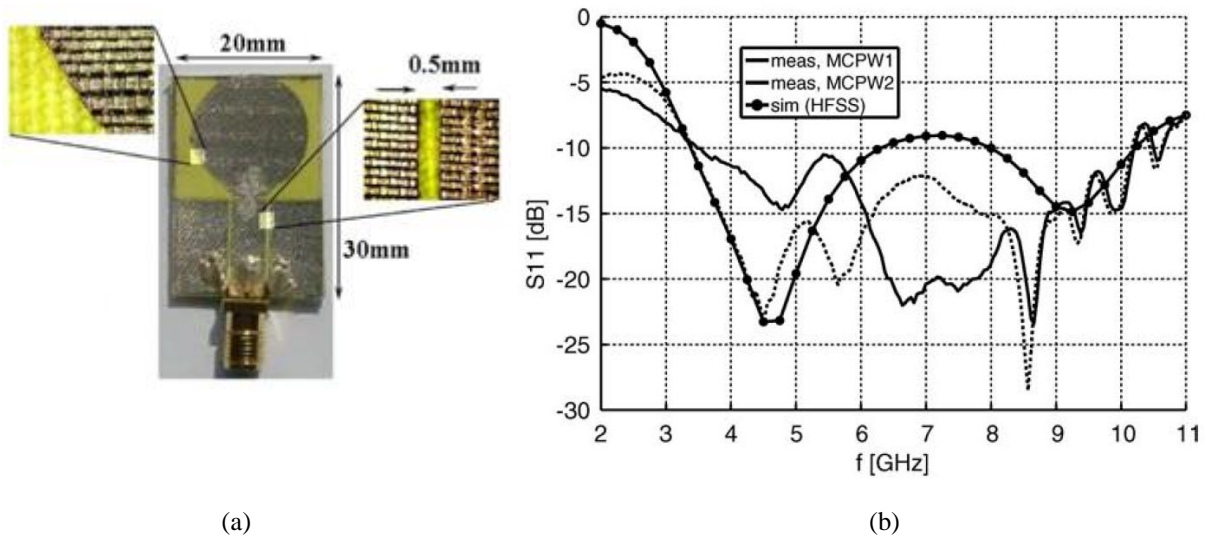


Fig. A4: CPW-fed textile UWB disc monopole antenna; (a) photograph and (b) S_{11} results. MCPW1, MCPW2: two prototypes of this textile antenna [131].

Three different structures of UWB antennas for wearable applications were fabricated and tested [132]. Antennas were made of Jeans and copper tape materials as the dielectric and conductive materials, respectively. Prototypes of antennas 1, 2, and 3 are shown in Fig. A5. Antenna 1 is a circular UWB antenna with small radius, antenna 2 is a circular UWB antenna with large radius, and antenna 3 is a circular UWB antenna with center hole. Discrepancies were observed in S_{11} results shown in Fig. A6. It is worth mentioning that there is no explanation or

investigation reported in the paper regarding the observed discrepancies and the rest of the studies were carried out based on these prototypes.

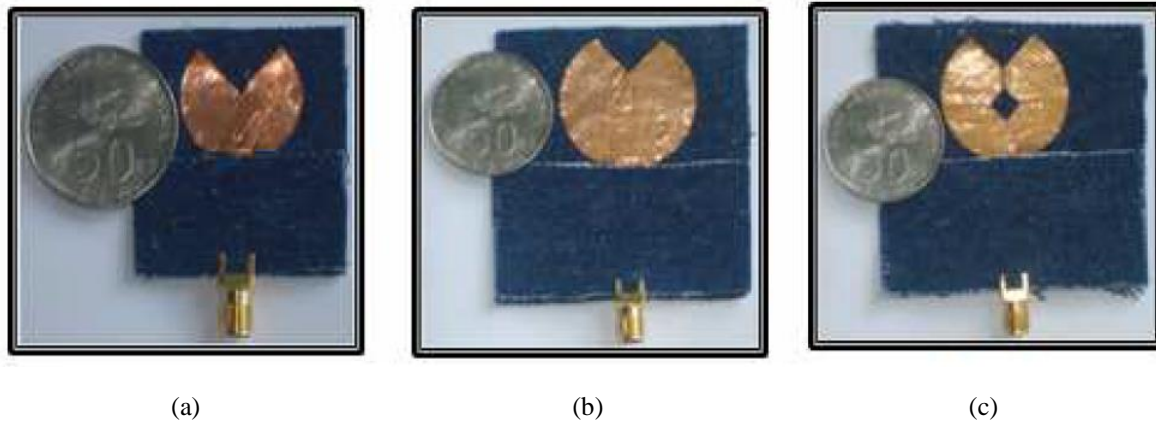


Fig. A5: UWB antenna prototypes: (a) antenna 1, UWB wearable antenna with small radius, (b) antenna 2, UWB wearable antenna with large radius, and (c) antenna 3, UWB wearable antenna with center hole [132].

Two antennas were constructed using felt fabric sandwiched between a ground plane and a slotted radiating patch [133]. Two different conductive materials were used; copper textile and Shieldit Super conductive fabric. Prototypes of the antennas are shown in Fig. A7. Antennas were named FLSL and SHSL using copper and Shieldit Super conductive materials, respectively. As shown in Fig. A8, discrepancies can be observed between simulated and measured S_{11} results in the free-space condition. Authors attributed these discrepancies to the slight differences in the fabricated dimensions between simulations and measurements, and the effect of the SMA connector represented by a simplified model in the simulation. The rest of the studies were carried based on these prototypes.

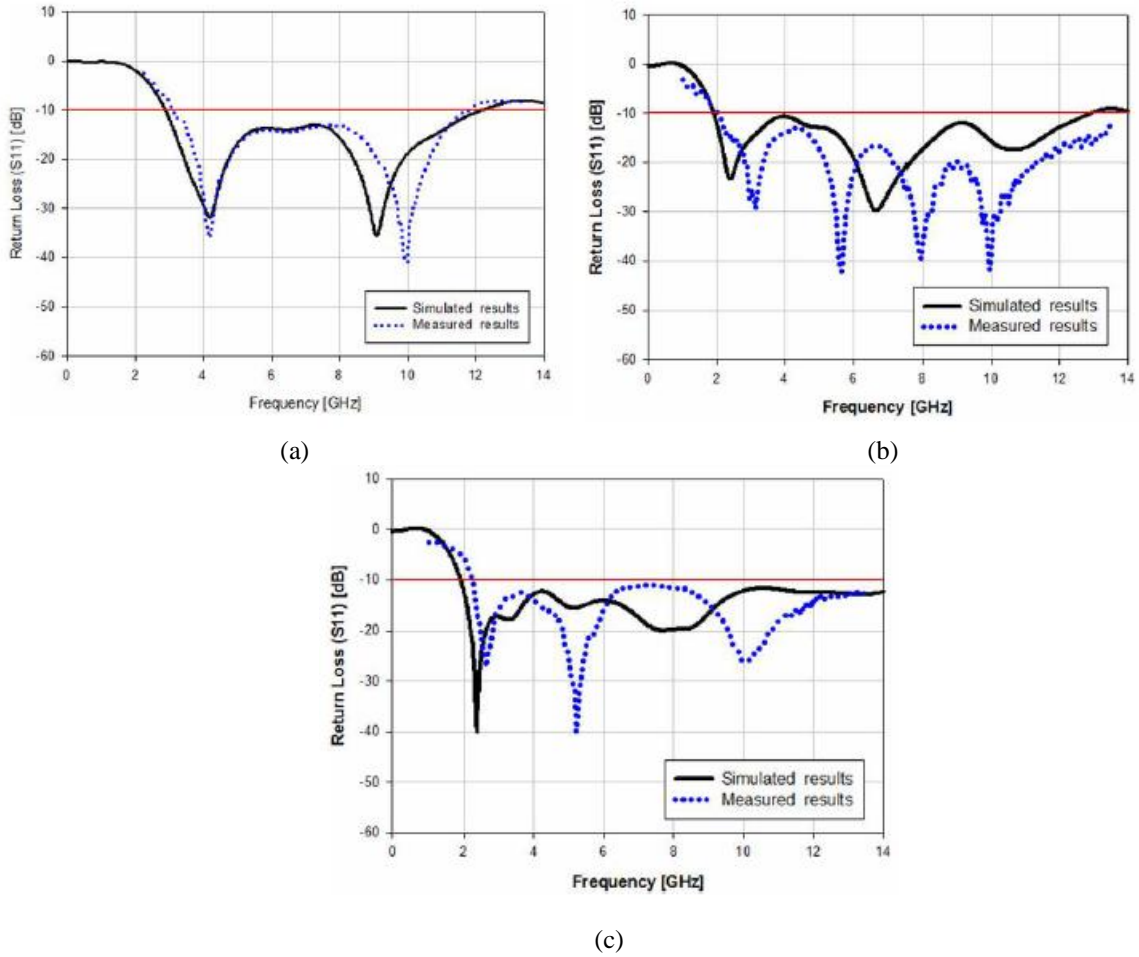


Fig. A6: Simulated and measured S_{11} of (a) antenna 1, (b) antenna 2, and (c) antenna 3 [132].

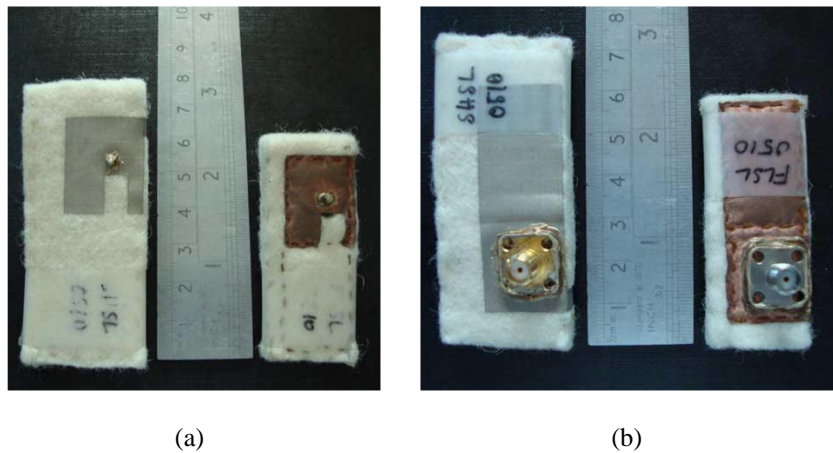
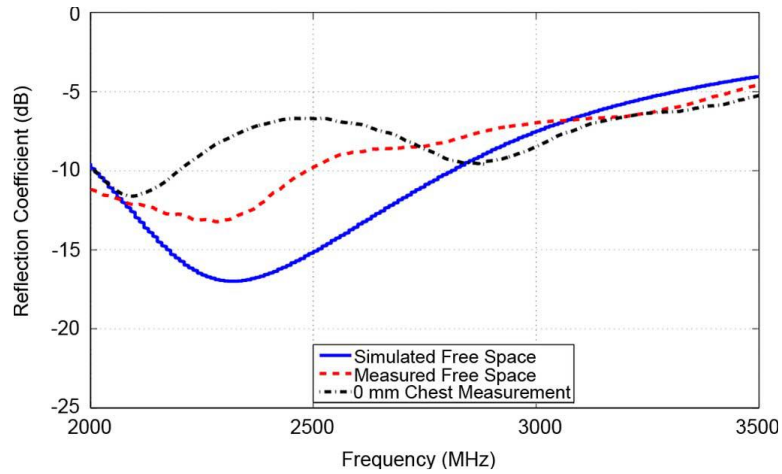
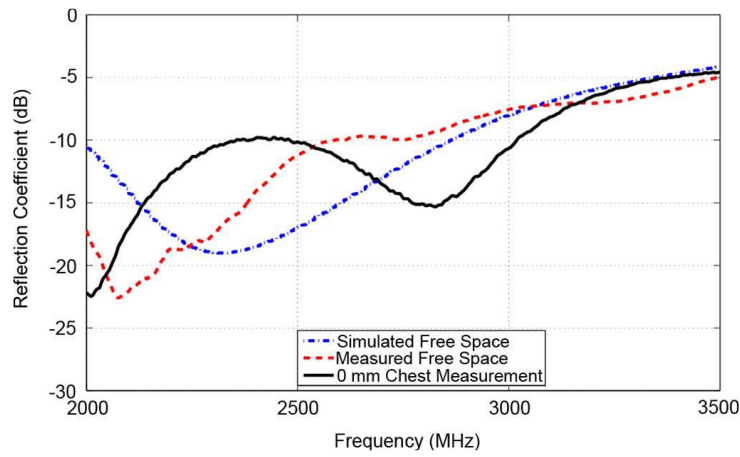


Fig. A7: Textile antennas; FLSL (right) and SHSL (left); (a) radiating elements and (b) ground planes [133].



(a)



(b)

Fig. A8: S_{11} of textile antennas; (a) FLSL and (b) SHSL [133].

A CPW fed multi-stacked patch with a full reflector is proposed, as shown in Fig. A9 [134]. The antenna consisted of a parasitic patch added beneath the radiating patch and backed with a reflector. The conductive components of the antenna, *i.e.*, radiating and parasitic patches, and reflector, were built using Shieldit Super conductive textile and the substrate layers were formed using felt fabric. Authors attributed the differences in S_{11} results shown in Fig. A10 to the fabrication tolerances, as the antenna was made by hand, and numerical errors. The rest of the studies carried out in this paper were based on the discussed prototype.

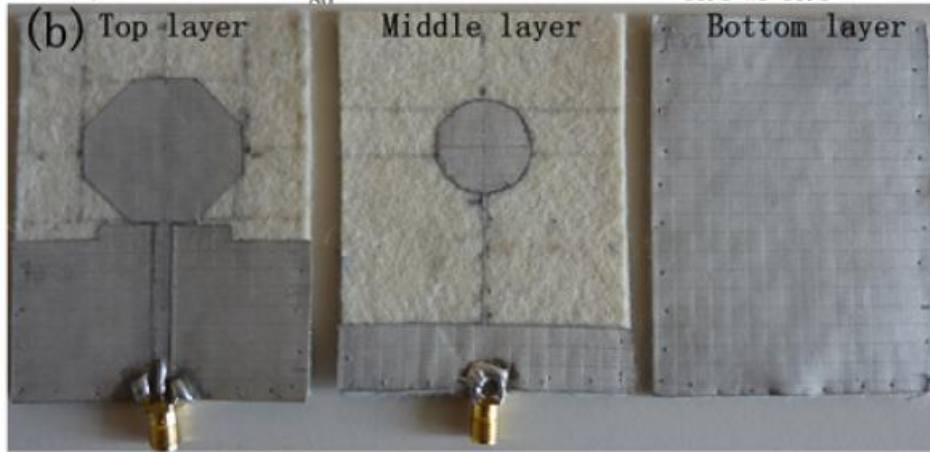


Fig. A9: CPW fed multi-stacked antenna components from left to right; radiating patch, parasitic patch, and full reflector [134].

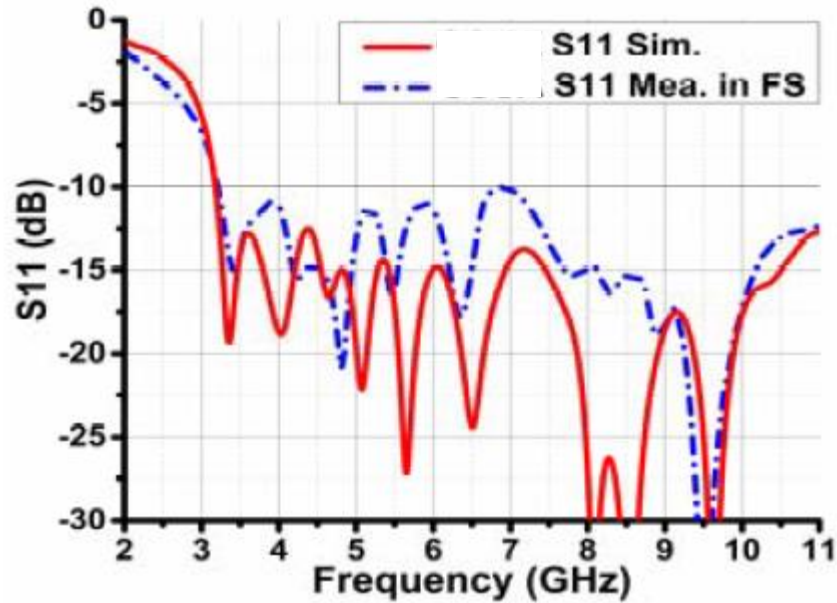


Fig. A10: Simulated and measured S_{11} of the CPW fed multi-stacked antenna in free-space (FS) [134].

A novel integrated inverted-F antenna (IIFA) with a CPW feed was proposed [135]. Initially, for testing purposes, three different materials were used to realize three different versions of the proposed antenna. Antenna 1 was made of a material of 4.4 permittivity and 0.78 mm thickness, antenna 2 was made of a material of 2.2 permittivity and 1.58 mm thickness, and antenna 3 was made of similar material as antenna 1 resonating at 5 GHz. Antenna prototypes and S_{11}

results of the three antennas are shown in Figs. A11 and A12, respectively. Authors attributed the discrepancies between simulation and measurement results to the connector solder effect on the CPW line and the ground plane since these (the line and ground plane) were parts of the antenna. The antenna was then integrated on a denim substrate using a copper tape. Antenna prototype and S_{11} results are shown in Fig. A13. A shift in the resonance frequency and a wider impedance bandwidth were observed in measurement results compared to the simulation results. There was no explanation provided by the authors on these discrepancies.

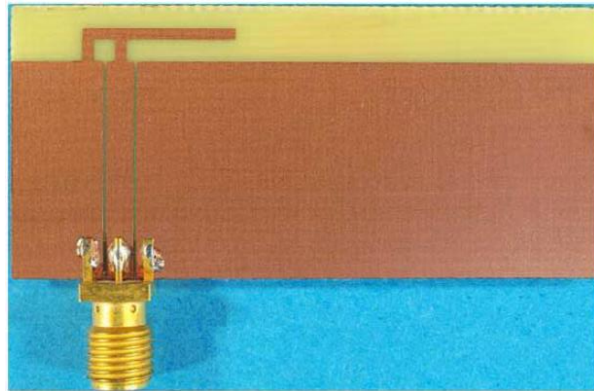


Fig. A11: IIFA antenna prototype in [135].

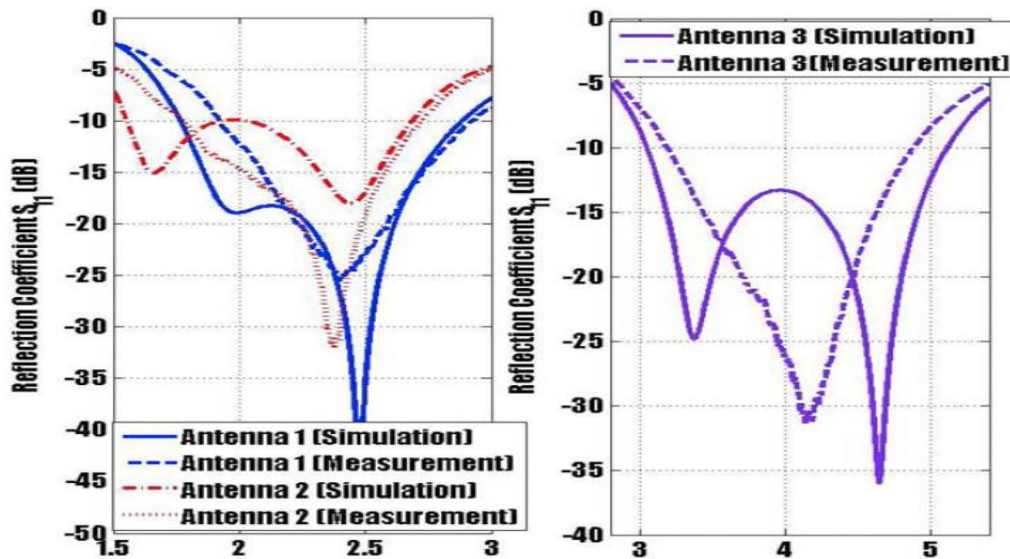
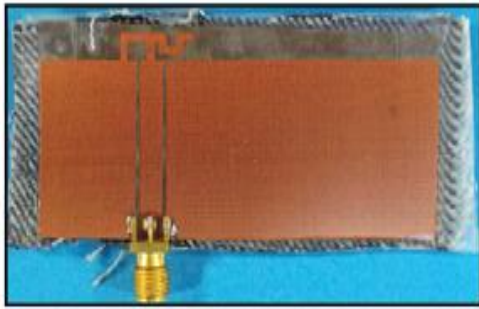
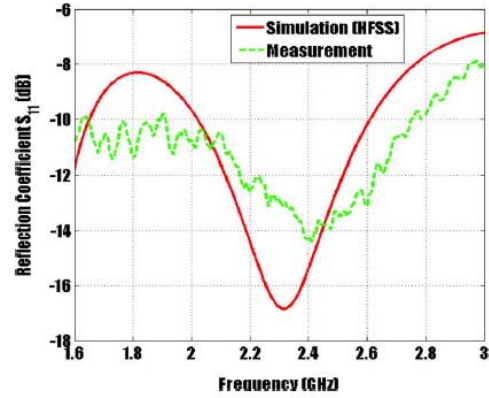


Fig. A12: S_{11} of proposed antennas in [135].



(a)

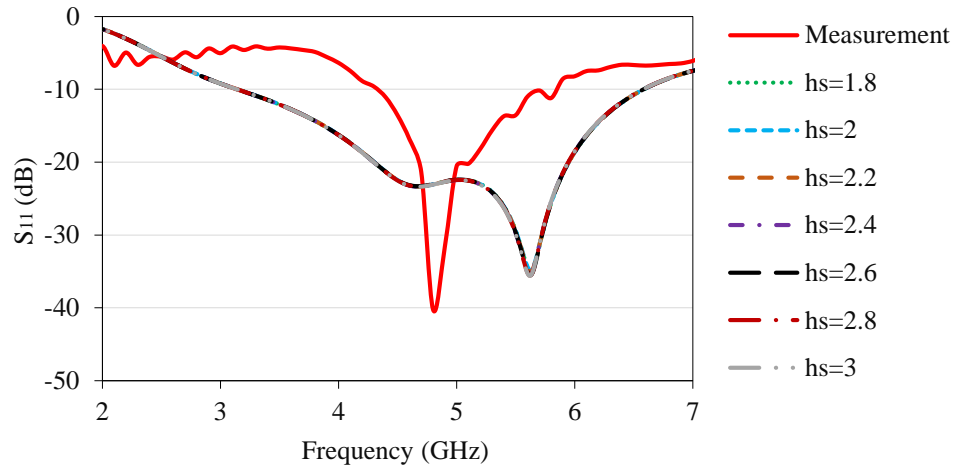


(b)

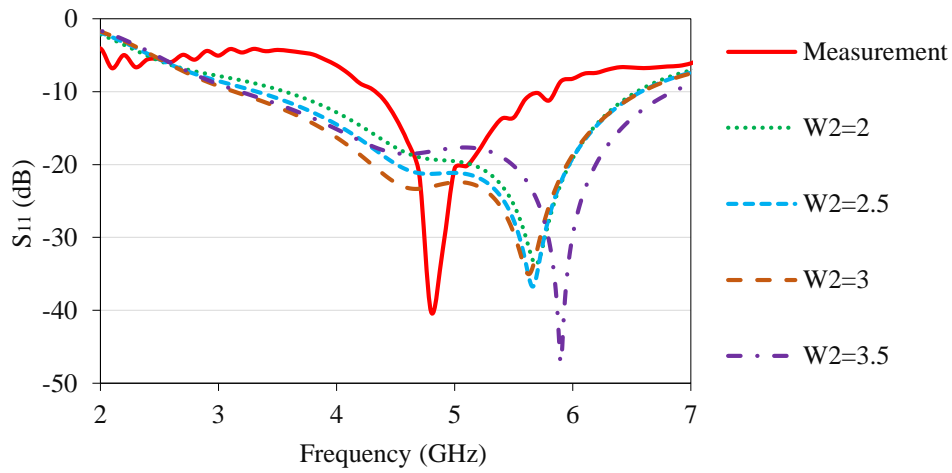
Fig. A13: Textile IIFA; (a) prototype and (b) S_{11} results [135].

After the validation of measurement and simulation procedures and a deep study in the literature, we started looking on the possible discrepancy reasons as follows:

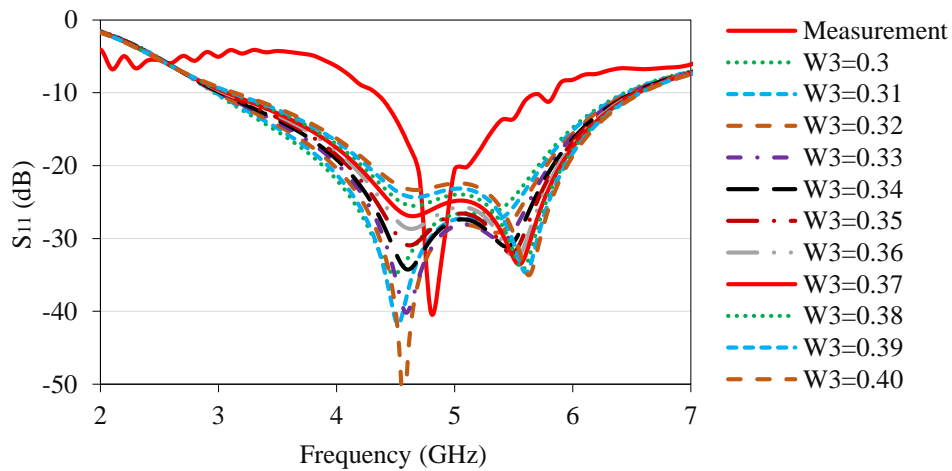
First, we looked at the discrepancy in the properties of the used textile material and dimensions of the monopole antenna simulation and measurement based prototypes. Investigations on the effects of changing these parameters on the monopole antenna performance in terms of S_{11} results were performed using CST MWS software through a parametric study. Results of changing the substrate thickness (hs), the feeding line width (W_2), the gap width between the feeding line and the ground plane in the CPW transmission line (W_3), and the material permittivity (ϵ_r) are shown in Figs. A14 and A15. Please refer to Fig. 3.5 for the monopole antenna dimension details. It is worth mentioning that similar studies were performed on the other parameters of the monopole antenna and results showed no effect on the antenna performance similar to those obtained when changing the substrate thickness (hs). In general, as a result of changing these selected parameters, two resonance frequencies at 4.6 GHz and 5.6 GHz were observed. However, none of these resonances match the measurement resonance frequency at 4.8 GHz. Furthermore, we tried a combination changes of the most design sensitive parameters, W_3 and ϵ_r , as shown in Fig. A16. Similar observation can be made for most of the tried cases.



(a)



(b)



(c)

Fig. A14: Parametric S_{11} of monopole antenna for different (a) h_s , (b) W_2 , and (c) W_3 .

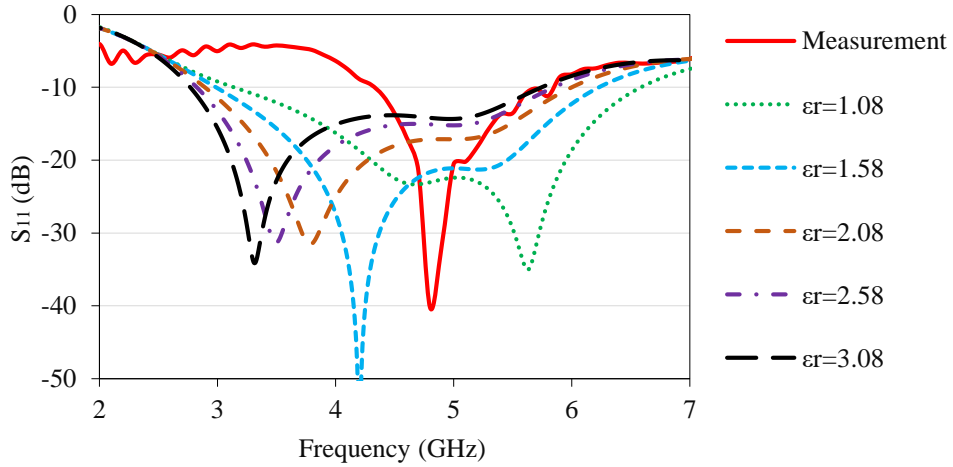
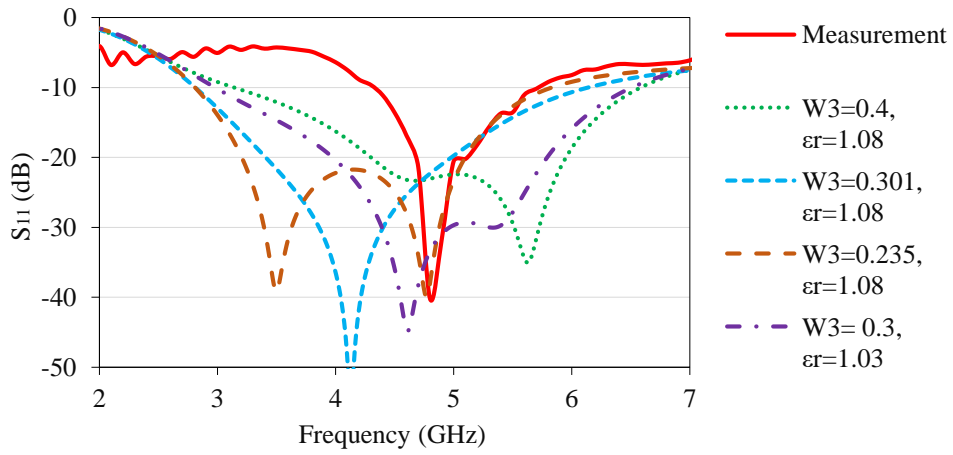
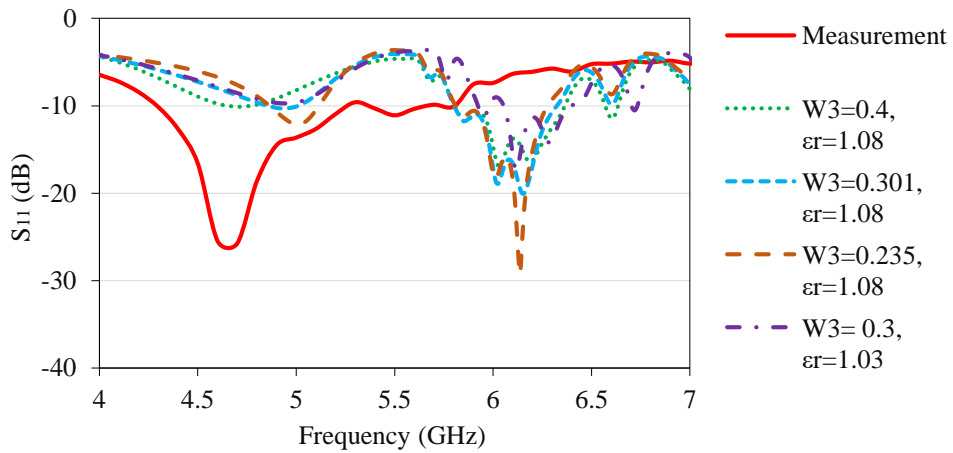


Fig. A15: Parametric S_{11} of monopole antenna for different ϵ_r .



(a)



(b)

Fig. A16: Parametric S_{11} of (a) monopole and (b) AMC antennas.

In simulations, the antenna was fed directly with a signal source, *i.e.*, through SMA connector, without using a feeding cable. However, the feeding cable was used to connect the fabricated antenna to the measurement system. According to [136], in small antennas, currents may flow back to the outer surface of the feeding cable, resulting in secondary radiation. This leads to discrepancies between simulated and measured performance of the antenna and creates uncertainties to the design of the antenna. In order to investigate effect of the cable presence on the antenna measurements, two new monopole antennas were fabricated as shown in Fig. A17, *i.e.*, the original antenna was no longer available for comparison due to oxidization of the conductive surface. S_{11} of these two newly fabricated antennas was measured using Keysight E5071C vector network analyzer (300 kHz – 20 GHz frequency operating range) for two scenarios: 1) using the feeding cable (*i.e.*, PE3VNA1801 SMA male to SMA male cable assembly is constructed with PE-VNA-R coax and the maximum VSWR is 1.25:1) and 2) directly connected to the network analyzer. Measurement setups for these two scenarios are shown in Fig. A18.

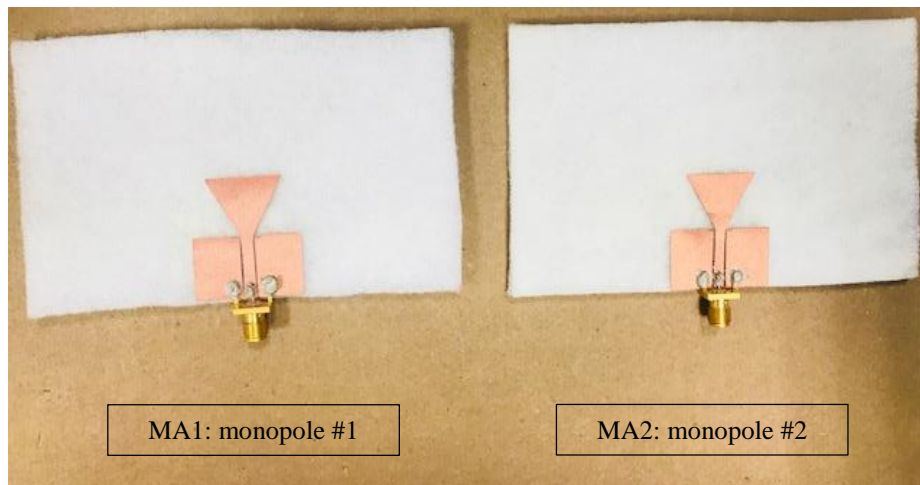


Fig. A17: New fabricated monopole antenna (MA) prototypes.

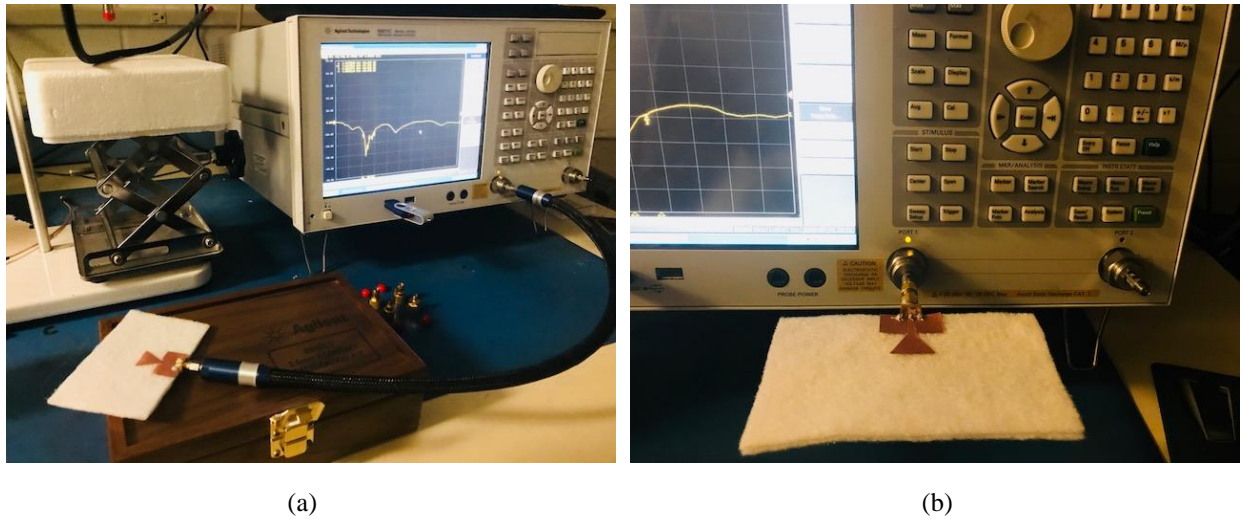


Fig. A18: S_{11} measurement setups; (a) scenario 1 (using the cable) and (b) scenario 2 (direct contact to the VNA).

S_{11} results of the two antennas are compared to the original results, denoted as “original antenna”, and the simulation result, as shown in Fig. A19. Antennas 1 and 2 were connected to the VNA through the same feeding cable used previously in the measurements. As you can see, based on measurements, a shift in the resonance frequency was observed from 4.8 GHz (original design) to 5.2 GHz (MA2), which might be attributed to the accuracy of the fabrication process. Measurement results were still similar to the original antenna, however, differences between simulation results and new set of measurement results were still observed.

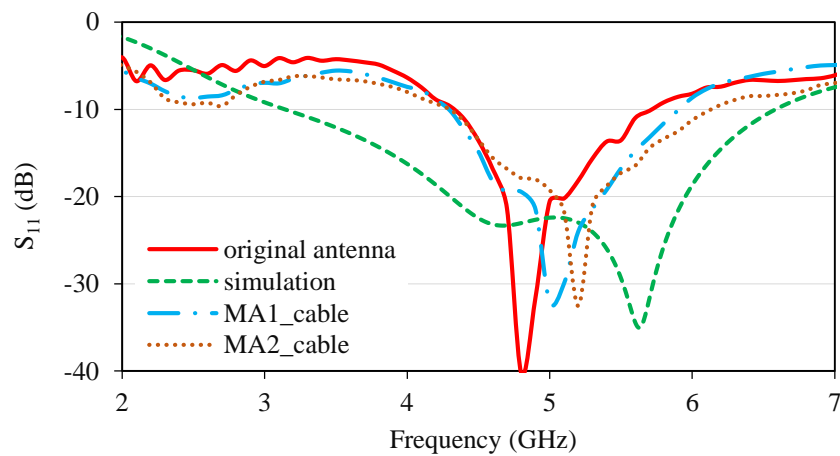


Fig. A19: S_{11} results of new fabricated monopole antennas.

In order to see the effect of the feeding cable on the measurements, results of the discussed scenarios were compared for MA1 and MA2, as shown in Figs. A20 and A21, respectively. Results show that the feeding cable has negligible effects on the measurements results. Results shown in Figs. A19, A20 and A21, confirmed the measurement and fabrication approaches followed for this design.

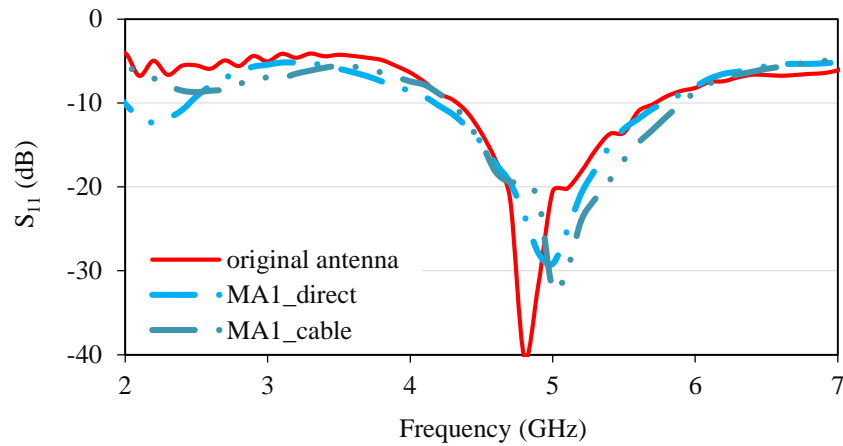


Fig. A20: S_{11} results for MA1.

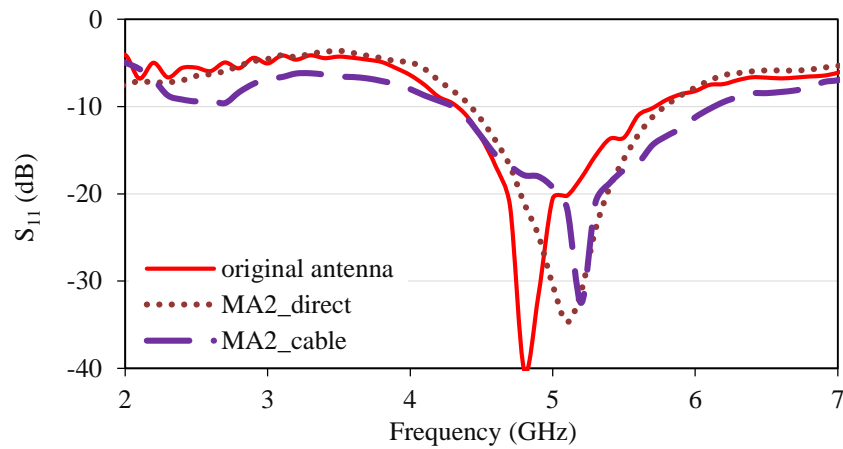


Fig. A21: S_{11} results for MA2.

Errors due the fabrication process were further investigated for the fabricated prototypes focusing on the smallest and/or most affecting parameters on the antenna performance. These parameters are shown in Fig. A22. Errors due to fabrication process are listed in Table A2 for the

original antenna and the new fabricated prototypes. S_{11} results, as shown in Fig. A23, showed they have a negligible impact on the antenna performance.

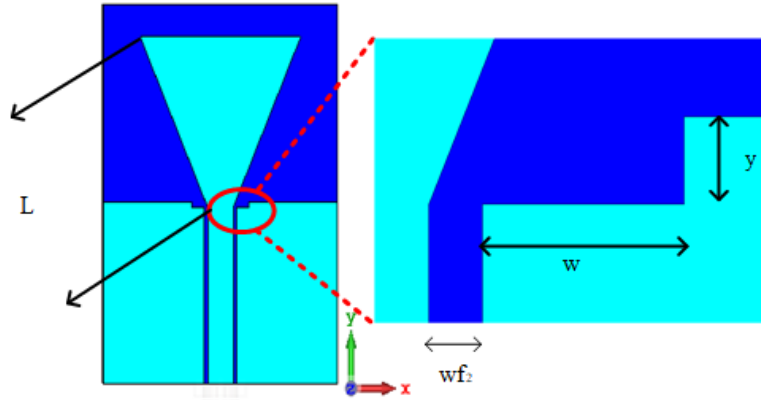


Fig. A22: Antenna parameters investigated for the fabrication accuracy.

Table A2: Errors due to fabrication process. Dimensions are in *mm*.

<i>Parameter</i>	<i>Simulation</i>	<i>Original ant.</i>	<i>Error</i>	<i>MA1</i>	<i>Error</i>	<i>MA2</i>	<i>Error</i>
wf_2	0.40	0.43	7.5%	0.42	5%	0.42	5%
L	17.44	17.04	2.2%	17.42	~ 0	17.33	~ 0
w	1.50	1.25	16%	1.38	10%	1.40	6.6%
y	0.50	0.51	~ 0	0.50	0%	0.53	6%

In order to see the effect of electro-textile material selection on the antenna performance, monopole antenna was fabricated using another electro-textile material, *i.e.*, Shieldit Super textile [52]. As summarized in Table A3, properties of the new material were compared with those for Pure Copper Taffeta electro-textile used in the design. As shown in Fig. A24, the electro-textile materials were made of individual threads. The non-continuous surface of the material, hence, might have led to a non-uniform current distribution on the textile surface. It is worth mentioning that in simulations, due to limitations, the conductive material of the antenna was modeled as a uniform surface. Two antenna prototypes named as Shieldit Super 1 and Shieldit Super 2 were fabricated using Shieldit Super material, as shown in Fig. A25(a). In order to address effect of the

non-uniform surface of the material on the antenna performance, monopole antenna was implemented using copper tape as the conductive material. Two antenna prototypes named as “Copper tape 1” and “Copper tape 2” were fabricated, as shown in Fig. A25(b).

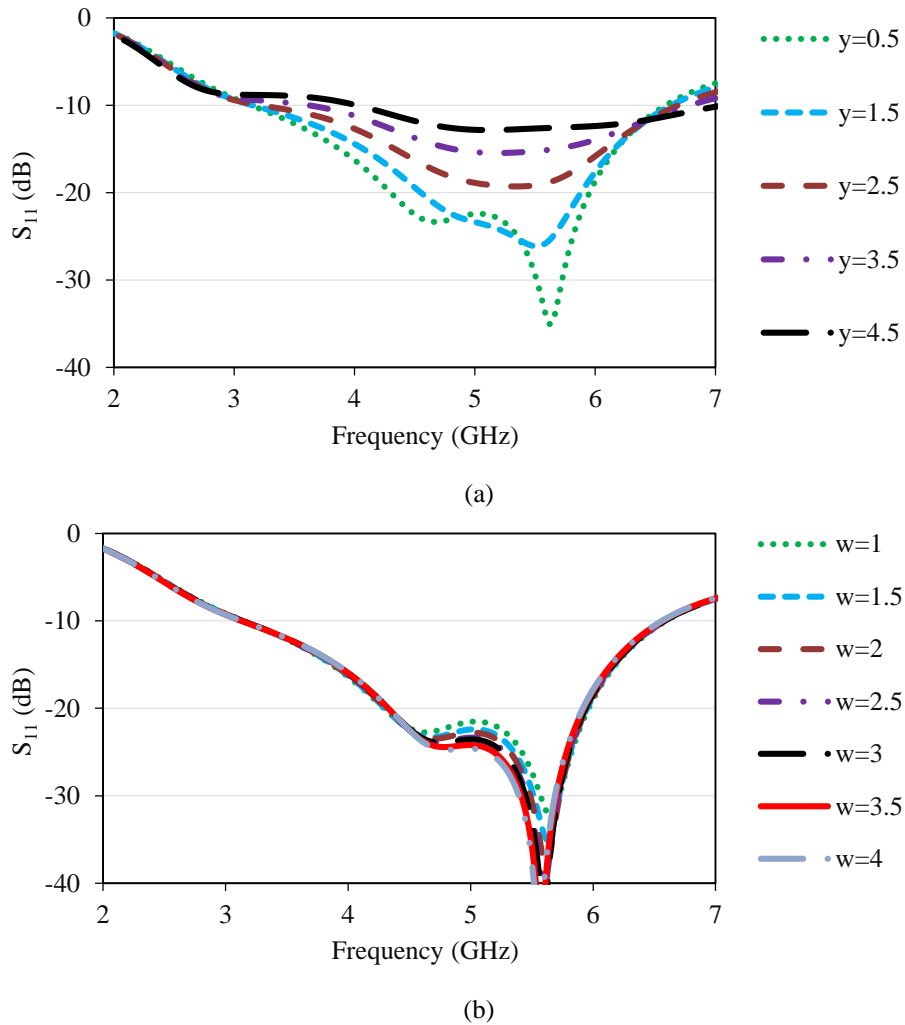


Fig. A23: S_{11} results of monopole antenna when changing; (a) y and (b) w parameters.

Table A3: Properties of electro-textiles [50].

<i>Paramater</i>	<i>Pure Copper Taffeta</i>	<i>Shieldit Super</i>
Measured resistance (<i>Ohm/sq</i>)	0.031	0.025
Surface resistance (<i>Ohm/sq</i>)	0.05	< 0.1
Conductivity (<i>S/m</i>)	2.5×10^5	6.67×10^5
Thread pitch (<i>mm</i>)	0.232	0.146
Conductive element	Cu	Ni and Cu
Thickness (<i>mm</i>)	0.08	0.17
Weight (<i>g/m²</i>)	80	230

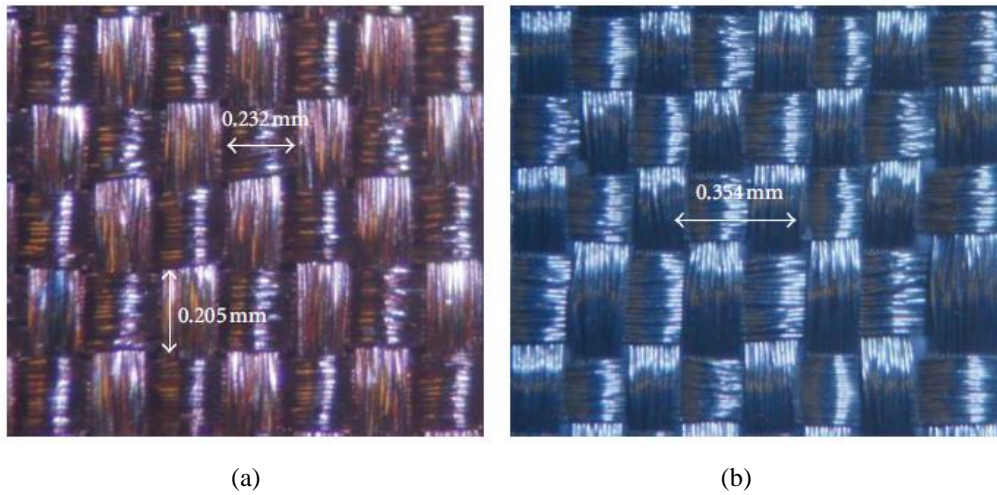


Fig. A24: Microphotographs of (a) Pure Copper Taffeta and (b) Shieldit Super fabrics [50].

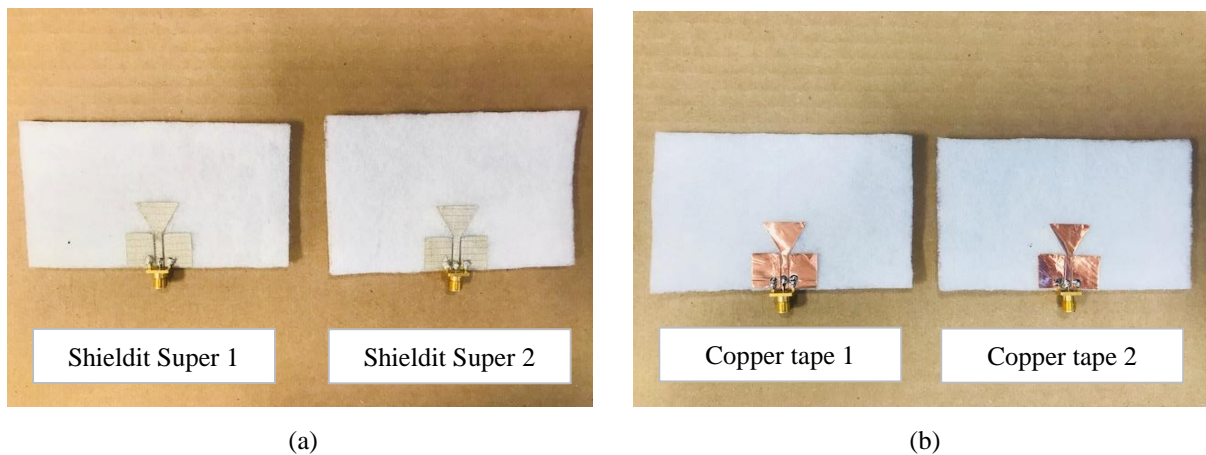


Fig. A25: Photograph of fabricated monopole antennas using (a) Shieldit Super and (b) Copper tape materials.

Fabricated antennas were tested using Keysight E5071C vector network analyzer (300 kHz – 20 GHz frequency operating range) for S_{11} measurements. Results are shown in Figs. A26 and A27 for Shieldit Super and Copper tape materials, respectively, where M1 refers to measurement results and S refers to simulation results. As can be seen in Fig. A26, a wider -10 dB input impedance bandwidth was obtained using Shieldit Super textile (4.2 GHz – 6 GHz) compared to using Pure Copper Taffeta textile (4.2 GHz – 5.6 GHz) with almost similar S_{11} response. On the other hand, using the copper tape resulted in -10 dB input impedance bandwidth (4 GHz – 6.5 GHz) closer to the simulation results (3 GHz – 6.6 GHz) spatially at the higher frequency limit, as shown in Fig. A27.

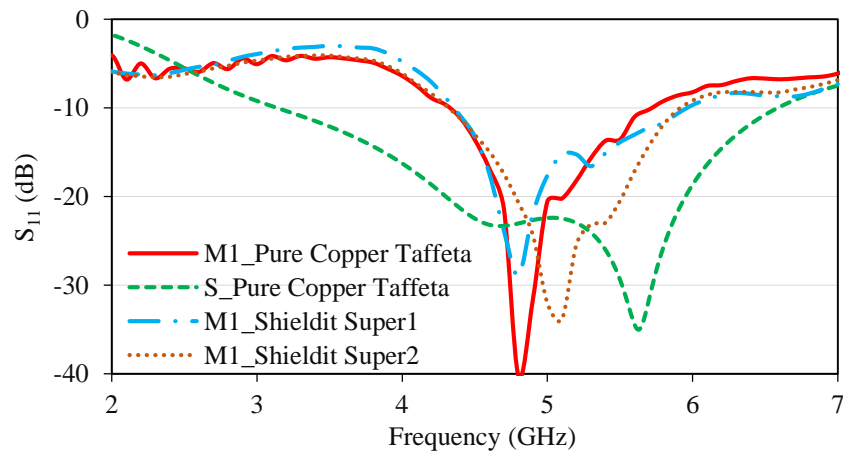


Fig. A26: S_{11} results of new fabricated monopole antennas using Shieldit Super material.

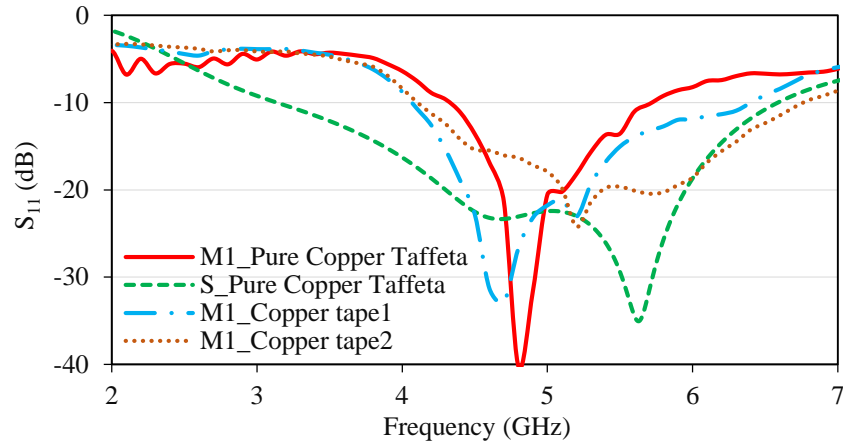
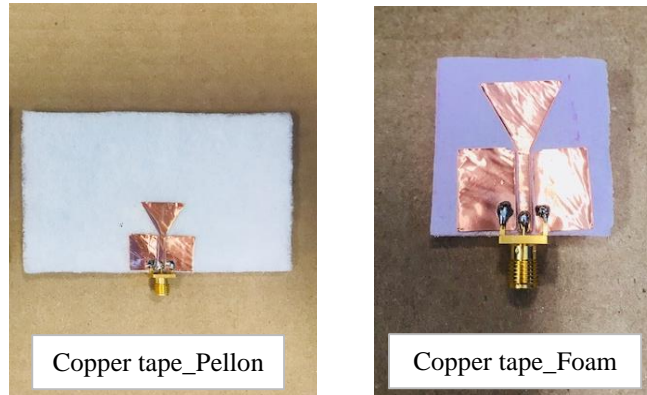


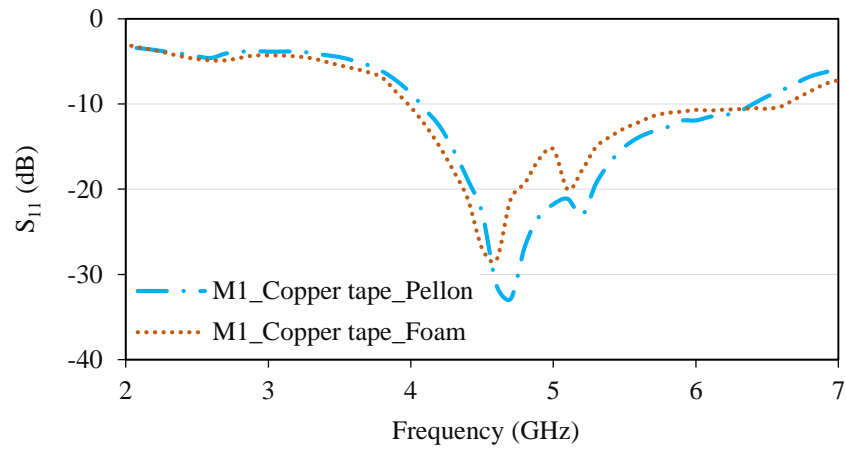
Fig. A27: S_{11} results of new fabricated monopole antennas using Copper tape material.

Another investigation was carried out to study effect of the dielectric textile on antenna performance. Dielectric textile used in the paper, *i.e.*, Pellon fabric, was replaced with foam material of similar thickness. Foam has a permittivity value close to air and similar to that for the textile substrate that we used. In both cases, copper tape was used as the conductive material. Antennas used for testing and measurement results are shown in Fig. A28. Results showed that the change of substrate material had a negligible effect on the antenna performance.

In order to further confirm measurements accuracy, all fabricated antennas were tested using another Keysight E5063A vector network analyzer (100 kHz – 18 GHz frequency operating range). The results of the second round of measurements are denoted as M4. Results showed a good agreement using both measurement setups as depicted in Fig. A29 for monopole antenna fabricated using Pure Copper Taffeta textile. Other antennas that were tested showed very similar results, but for brevity the results are not shown here.



(a)



(b)

Fig. A28: (a) Antennas using Pellon and Foam substrates and (b) S_{11} results. Where (M1) is measurement and (S) is simulation.

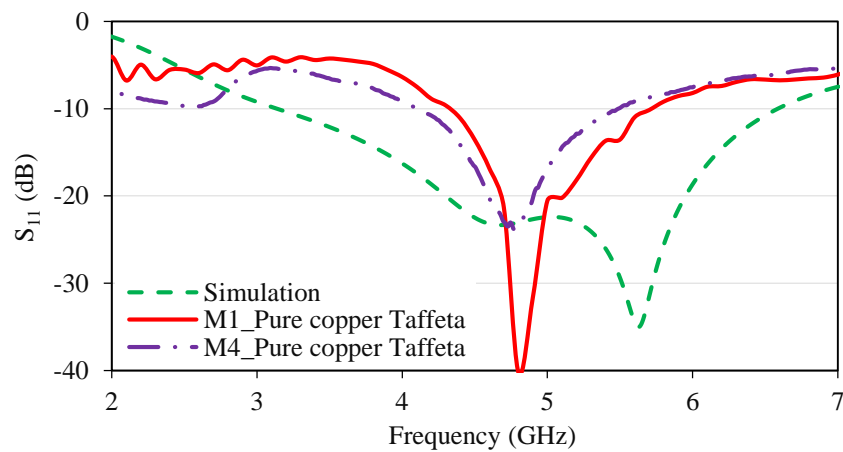


Fig. A29: S_{11} results of monopole antenna using E5071C NA (M1) and E5063A NA (M4).